Università degli Studi di Roma
"La Sapienza"

Dipartimento di Scienze di base e applicate per l'ingegneria

DOTTORATO DI RICERCA IN MODELLI MATEMATICI PER L'INGEGNERIA, ELETTROMAGNETISMO E NANOSCIENZE

CURRICULUM: SCIENZA DEI MATERIALI

XXX CICLO
ANNO ACCADEMICO: 2016 - 2017

Ionic liquids as solvents for rare-earth metals: a combined XAS and Molecular Dynamics study

Candidate:
Alessandra Serva

Supervisor:
Prof.ssa Paola D'Angelo

Contents

Chapter 1

Introduction

1.1 Ionic Liquids

Among the most exciting and successful materials developed and studied in the last 20 years, room-temperature ionic liquids (ILs) are part of those that can certainly claim one of the richest fields of applications in industry and technologies.[1, 2, 3, 4] ILs are a class of solvents entirely made by ions with melting points below 100 °C. They are usually built up by organic cations and inorganic anions and exhibit many fascinating and unique properties such as high thermal and chemical stability, non-flammability, negligible vapor pressure and the possibility of tuning their physical properties by varying the molecular structure of both the cation and the anion. Recently, a large plethora of experimental techniques have been applied to the study of ILs, showing up their unique features and, thus, explaining the huge range of applications of these materials and the call for further exploration.[5, 6, 7, 8, 9] Among possible applications, we find their use as friendly alternatives to traditional organic solvents, reaction media in organic chemistry, extraction media in analytical chemistry, lubricants, catalysts, transport media in electrochemistry and ingredients for pharmaceuticals.

Most ILs of recent interest are based on nitrogen-rich alkylsubstituted heterocyclic cations and, in particular, 1-alkyl-3-methylimidazolium cation ($[C_n mim]^+$, being n the number of carbon atoms in the alkyl chain, see Figure 1.1), accompanied by an inorganic anion ranging from simple halydes to more complex structures. Among $[C_n mim]^+$ based ILs, those having the iodide ion as counterpart have recently received considerable attention from the scientific community, as they have found to be necessary components of electrolytes in dye-sensitized solar cells (DSSCs). DSSCs are devices that provide a high light-to electric energy conversion yield,[10] whose efficiency and stability are very much dependent on the properties of the electrolyte employed in the cells.[11, 12] In this context, ILs can replace the commonly used volatile organic solvents, which essentially preclude their use in outdoor applications. The non-flammability, non-volatility and high ionic strength of alkylimidazolium iodide ILs make them the ideal nonvolatile substitutes. In particular, 1-hexyl-3-methylimidazolium iodide, $[C_6 mim]I$, shows the best

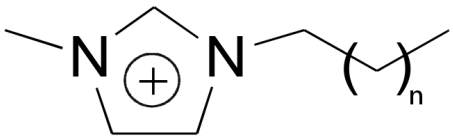

Figure 1.1: Chemical formula of 1-alkyl-3-methylimidazolium cation, $[C_n mim]^+$.

performance among the $[C_n mim]$I family (C3-C9).[13, 14] A considerable number of experimental and theoretical techniques, including Raman,[5, 9] X-ray diffraction,[5, 6, 7, 8] infrared and UV-Visible spectroscopies,[15, 16] classical and Car-Parrinello [9, 17, 18, 19, 20, 21] molecular dynamics simulations, and *ab-initio* calculations [15, 22] have been focused on the alkylimidazolium halide IL family. It was found that the association of anions and cations is predominantly given by the interaction of the halide with the three hydrogen atoms of the imidazolium ring. In particular, the hydrogen bond formed by the most "acidic" ring proton and the halide is responsible in determining the physical state of the $[C_4 mim]$X ILs, that are liquid at room temperature if X is the iodide ion, while they are solid when X is the bromide or chloride one. Indeed, going from Cl^- to I^- the C-H stretching band frequency was found to shift to higher wavenumbers as the hydrogen bonds become weaker and weaker, and the physical state of the $[C_4 mim]$X ILs from solid goes to liquid.[15] In addition to the nature of the anion, many ILs properties have also found to be influenced by the length of the lateral chain attached to the cation. $[C_n mim]^+$ based ILs are characterized by a polar positive head and an apolar alkyl tail; this means that the interactions of the head groups with the anions are dominated by electrostatic forces, while the alkyl chains mainly interact with each other through weak short-range interactions. As a consequence, there is an aggregation of the side chains, thus leading to the formation of structural domains of average size depending on the alkyl chain length, as shown in several theoretical and experimental studies.[23, 24, 25]

The exploration of microscopic properties of ILs has blossomed over the last few years and a large plethora of chemical-physical techniques have been applied to the study of ILs and, correspondingly, many peculiar and essentially unique features are showing up, thus explaining both the wide range of different applications of these materials and the call for further exploration. The most interesting features that have recently been highlighted include the occurrence of both structural and dynamic heterogeneities in these materials in their liquid state. Such features are foreseen to dramatically affect the bulk performances of ILs and accordingly a detailed understanding of their nature is necessary. In particular, in this framework, it will be interesting to understand how the choice of both the anion and the imidazolium alkyl chain can influence the short- and long-range structure, thus providing a global structural picture of the complex organization of these materials.

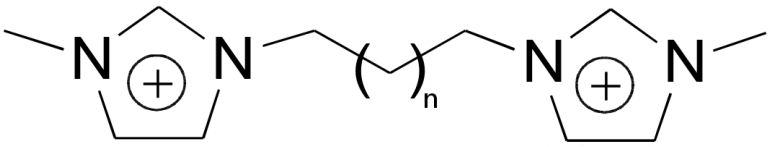

Figure 1.2: Chemical formula of 1,n-bis[3-methylimidazolium-1-yl]alkane dication, $[C_n(mim)_2]^{2+}$.

Additionally, a new family of "high stability" ILs, geminal dicationic ionic liquids (DILs), has recently been synthesized and characterized. As it can be seen in Figure 1.2, DILs have a cation consisting of two identical imidazolium rings, linked together by an alkyl chain of variable carbon number (also called spacer), that is paired with two singly charged anions.[26, 27] In contrast to monocationic ILs, each dication carries two positive unit charges, and it is structurally symmetrical in most cases. It has been found that DILs have higher thermal and chemical stability, and surface tensions and liquid ranges larger as compared to monocationic ILs.[28, 29, 30, 31] DILs expand the horizon of application for ionic liquids, since they represent a very interesting variation of the monocationic partners when used as solvents, lubricants, catalysts, separation media and electrolytes in DSSCs.[32, 33, 34, 35] Publications on this topic show that the nature of the anion has weak contributions toward bulk structure; it strongly interacts with the positively charged headgroups and, in particular, with the three hydrogen atoms of the two imidazolium rings, leaving a void of ion density around the alkyl groups.[36] Conversely, bulk structure is shown to depend principally by the choice of the alkyl spacer separating the cation charge centers, which is consistent with findings for monocationic ILs. In particular, for short alkyl-spacer DILs, the dication has no significant effect on the bulk mesostructure, while some differences can be discovered for long alkyl-spacer DILs, since the spacer chain may adopt linear or folded conformations.[37, 38] Being aware of this promising scenario, a full exploitation of the DIL properties requires a detailed understanding of their structural features at a microscopic level.

1.2 Ionic Liquid/water binary mixtures

Most ILs are hygroscopic and absorb water from the atmosphere and, therefore, traces of water are easily present in these materials. In addition, many industrial processes require a mixture of ILs and water, in which ILs are included as either the major or minor component. It has been found that the physical properties of ILs such as their polarity, conductivity and viscosity are strongly affected by the presence of water, also at very low concentration.[39, 40, 41, 42] As far as the $[C_n mim]^+$ based ILs are concerned, the water influence on their chemo-physical properties depends on different

factors such as the length of the alkyl chain, the nature of the anion and the aggregation behavior of the IL itself. Additionally, the water content of the solution can also modify the rate and selectivity of reactions carried out in ILs, that is an important task when using ILs in industrial processes, extraction and separation processes or as green solvents.[39, 43] Therefore, the knowledge of the molecular organization of ILs in the case of mixtures with water and the understanding of how the water or anion coordination geometry changes with the mixture composition is of very fundamental importance. Up to now, several theoretical and experimental investigations have been devoted to the characterization of binary mixtures of water and monocationic ILs. Using ATR-IR spectroscopy, it has been shown that in the case of ILs consisting of anions with a strong ability to form hydrogen bonds, such as $[CF_3CO_2]^-$ or $[NO_3]^-$, water molecules are mainly hydrogen bonded to the anion, even if a weak interaction of water with the most "acidic" hydrogen of the imidazolium cation is also possible.[44, 45, 46] Further studies on imidazolium based ILs having a halide ion as counterion have revealed the ability of these systems to aggregate beyond a critical aggregation concentration (CAC). The aggregation number was found to depend both on the water concentration and on the alkyl chain length. The short alkyl chain $[C_n\text{mim}]^+$ based ILs ($n \leq 4$) behave as simple salts, they form only a monolayer with no detectable aggregates if $n = 6$, while well defined and stable aggregates are found for the long alkyl chain ILs ($n \geq 8$).[47] Finally, several works have focused on the formation of tight or "solvent-shared" ion pairs between the cation and the anion in the presence of water. A Car-Parrinello study of $[C_6\text{mim}]Cl$/water mixtures has revealed the existence of "solvent-shared" ion pairs, with cations and anions that remained in close proximity over the whole simulation, sharing one or more water molecules.[48] The same findings have been observed in other studies on mixtures with water of alkylammonium chloride and bromide, where the "solvent-shared" ion pairs were able to survive under very high dilution conditions.[49, 50, 51]

Conversely, as far as the dicationic ILs are concerned, only a few studies of their water mixtures are present in the literature.[52, 53, 54, 55, 56] A comparison made between dicationic imidazolium bromide ILs with their monocationic counterparts with a long alkyl chain ($n = 10$) has shown that DILs are more thermally stable and present a 200 time about lower CAC.[56] Spontaneous aggregation of cations was also observed in solutions at low concentrations, depending on the length of the alkyl spacer; in fact, while solutions with propyl and pentyl spacers are homogeneous, those with octyl, decyl and hexadecyl ones show spatial heterogeneity, with the formation of cation aggregates where the central carbon atom of the spacer buried in the hydrophobic core and the imidazolium ring forming the hydrophilic surface.[54]

As in the case of pure ILs, despite the work already appeared in the literature, detailed experimental and theoretical studies are further needed to disentangle the structural and aggregation properties of those systems also using innovative experimental approaches. This information will be of great value in understanding the nature of molecular interactions which give rise

to the peculiar properties of IL/water solutions, for both monocationic and dicationic systems.

1.3 Ionic Liquids as solvents for rare-earth metals

As previously mentioned, ILs are considered very good solvents for a constantly increasing range of applications due to their excellent properties such as high thermal stability, low vapore pressure and favorable solvating properties for many organic and inorganic compounds. In particular, in the past few years, ILs have started to gain high interest in combination with lanthanide chemistry due to their potential applicability as solvents for the separation and purification of lanthanide, Ln(III), ions and for the reprocessing of spent nuclear fuel rods, which is a central issue in nuclear technology.[57, 58, 59, 60] The process at the basis of the separation and purification of lanthanide ions is the liquid-liquid solvent extraction, that is also of prime importance for the separation of fission products from reusable fissile material in spent nuclear fuel elements. It is based on the difference in distribution of the species of interest over two immiscible phases, being often an aqueous phase and an organic phase. Traditionally, organic solvents have been used to extract and separate Ln(III) ions from the aqueous phase, but they can have high azard, rating and low flash points, resulting in health and safety concerns. The growing awareness of safety and environmental impact related with the use of these organic solvents renders their replacement with less noxious alternatives highly desirable. In this context, ILs, having the great advantage of negligible volatility and flammability, may be the ideal alternatives for the organic phase in liquid-liquid solvent extraction systems,[57, 58, 59, 60] in accordance with the Twelve Principles of Green Chemistry. It was proposed that more than 10^{18} simple organic salts might be potential ILs, which could be prepared by varying the substitution patterns and anion choices as well as using binary, ternary and high-order suitable ILs that can be employed in the separation/extraction of Ln(III) ions. Moreover, the production of rare-earth elements in their metallic state presently relies on high-temperature molten salt technology. The same technology is also of importance for some steps in the processing of spent nuclear fuel rods. When the molten salts in these processes can be replaced by room-temperature ILs, a huge saving in energy costs can be achieved. Moreover, the redox potential of lanthanoid ions dissolved in ILs depends on the local chemical environment and coordination of the dissolved ion with the IL anion. Thus, it should be possible to use lanthanide ions dissolved in ILs to determine the IL Lewis basicity or to monitor the electron donating power of the IL anion using, for example, the Eu(III) photoluminescence. Another important issue in the use of ILs in such area is the solvent stability upon exposure to high radiation doses, and several investigations have shown that, for example, imidazolium based

ILs with nitrate or chloride anions are relatively radiation resistant with no substantial decomposition of the organic solvents.[59]

Although many studies have been devoted to ILs and their applications, only few researchers have explored so far the combination of ILs with the coordination chemistry of lanthanides.[57, 58] However, understanding the solvation properties of Ln(III) ions in ILs is fundamental to improve the efficiency of extraction procedures and to select the best performing solvents, but, despite its importance, it is still at an early state of knowledge. In particular, the molecular interactions taking place between solute and solvent, that may aid in ultimately tuning the properties of ILs for specific applications, are far from being understood. Only once a basic understanding of the dissolution and solvation of 4f-element compound in ILs had been established, the benefit for f-element chemistry could be realized.

1.4 Aim of the work

In this work a detailed investigation of the structural organization of ILs, both monocationic and dicationic, and their water mixtures will be carried out by combining X-ray absorption spectroscopy (XAS) and Molecular Dynamics (MD) simulations. Then, the same joint XAS-MD approach will be used to unravel the solvation properties of Ln(III) salts dissolved in ILs.

During the last several years the potentiality of combining XAS and MD has been well-recognized, since very accurate structural information can be obtained for disordered systems that are difficult to gain with other techniques, especially when only one method of investigation is used. XAS is a short-range order technique that may be the ideal tool to gain information on the structure of ILs or ions dissolved in ILs by directly probing the local atomic structure around a selected atom, the photoabsorber. In particular, from the analysis of the Extended X-Ray Absorption Fine Structure (EXAFS) data it is possible to obtain very accurate ion first shell distances, that are not easily achievable with other experimental techniques. However, a proper extraction of the structural parameters from the EXAFS experimental data relies on structural results obtained from theoretical simulations to be used as models in the analysis of the EXAFS data. This is particularly true when dealing with alkylimidazolium halide ILs, in which the photoabsorber atom is surrounded by different light atoms such as carbon and nitrogen. The way to obtain these models is to perform MD simulations and, in particular, Classical MD simulations. In fact, ab initio MD has high computational costs and therefore is limited both in the dimension (hundreds of atoms) of the systems and in the total simulation time (tens of picoseconds). However, this is not compatible with the intrinsic nature of ILs, that have a very high viscosity as compared to conventional liquids, and thus a proper sampling of their structural and dynamics properties require very long equilibration and simulation times (on the nanosecond scale). Thus, Classical MD simulations are the ideal theoretical method to investigate these systems. In Classical MD electrons are not explicitly treated and intra- and inter- molecular interactions

are estimated via an empirically-parametrized potential, namely "force field". Several force fields are present in the literature, but their capability to correctly describe systems that differ from those for which they were developed must be assessed. This is possible by comparing the theoretical structural results with the EXAFS experimental data. Therefore, the combined XAS-MD approach allows one on the one hand to carry out a reliable EXAFS analysis, that represents a non trivial task when the EXAFS technique is applied to the study of disordered systems. On the other hand, it allows to assess the validity of the MD potentials in providing an accurate structural description of the investigated systems. Moreover, exploiting the short-range character of the EXAFS technique and the long-range structural information derivable from the analysis of the MD trajectories, it is possible to provide a very global picture of the IL structural organization, both in proximity of the photoabsorber atom and in the longer distance range.

First, we will focus on 1-alkyl-3-methylimidazolium halides ($[C_n mim]X$, with $X = Br^-$ and I^-), with the aim of elucidating the structural changes that take place when the alkyl chain length or the anion is modified. The structural organization of one of the abovementioned ILs, $[C_6 mim]I$, will be also studied when it is combined with water, as a function of water concentration up to very high dilution. Then, we will show a systematic study of the structural behavior of 1,n-bis[3-methylimidazolium-1-yl] alkane bromide ($[C_n(mim)_2]Br_2$)/ water mixtures. In particular, we will investigate $[C_3(mim)_2]Br_2$/water solutions in a wide range of water concentrations (DIL/water molar ratio from 1:16 to 1:400) and 1:70 $[C_n(mim)_2]Br_2$/water solutions, obtained by changing the spacer chain length. In the second part of the work, the solvation structure of a light Ln(III) ion, Ce(III), dissolved in the protic IL Ethylammonium nitrate (EAN) will be investigated. To this aim we will also show a preliminary study of Ln(III) ions in water aimed at developing a new set of Ln-O Lennard-Jones parameters, from which we have extrapolated generic Ln-Ln Lennard-Jones parameters to be used in systems different from water and, in particular for Ce(III) in EAN. Before using these developed parameters in complex systems, such as EAN, we have also tested them by carrying out MD simulations of Ln(III) ions in water, but in the presence of their counterions, such as the nitrate, trifluoromethanesulfonate or bis(trifluoromethylsulfonyl)imide anions, and by assessing the theoretical results with the EXAFS experimental data.

The thesis is organized as follows. In the next two Chapters (2 and 3) we provide the basic theoretical concepts of XAS spectroscopy and MD simulations. Chapter 4 provides experimental EXAFS and theoretical MD details adopted in the study of ILs and their water solutions. Chapters 5 reports the results on pure $[C_n mim]X$ ILs, while the results on $[C_6 mim]I$/water mixtures and $[C_n(mim)_2]Br_2$/water mixtures are addressed in Chapters 6 and 7, respectively. Chapter 8 describes the development and the testing of Ln-Ln Lennard-Jones parameters, together with all of the results on the solvation properties of Ce(III) in EAN. Finally, chapter 9 gives overall conclusions.

Chapter 2

X-ray absorption spectroscopy

X-ray absorption spectroscopy (XAS) is by definition the study, or the use, of X-ray absorption versus X-ray energy. For an homogeneous isotropic sample, according to the Beer-Lambert law:

$$ln(I_0/I) = \mu x \tag{2.1}$$

there is an exponential decrease of the transmitted beam intensity I passing through a sample of thickness x due to the absorption. μ is the total linear absorption coefficient, that depends on the types of atoms and the density of the sample. Thus, a XAS spectrum, in which μ is plotted as a function of E, shows an overall decrease of the X-ray absorption with increasing energy, except at certain energies where the absorption probability suddenly increases giving rise to an absorption *edge*, as shown in Figure 2.1. Each edge occurs when the incident photon energy is equal or exceeds the binding energy of a core electron, that transits to high energy states, i.e to produce what it is now called a *photoelectron*. At this point, the photoelectron undergoes a scattering process on the surrounding atoms, producing a series of wiggles or oscillatory structures above the edge that modulate the absorption. Measurement of this fine structure can provide information on atomic species, arrangements, and bonding mechanisms. After a short time of the order of 10^{-15} s, the core-hole is filled by an electron from a higher energy state, and the corresponding energy difference is released via Auger electron emission or fluorescence X-ray. Each absorption edge has a typical energy, related to a specific atom and, in particular, to the atomic number of the atom. Thus, the edges are signatures of the chemical species of the absorbing atoms. The letter in the edge label refers to the first atomic quantum number, n, with K, L, M, N, O for n=1, 2, 3, 4, 5, respectively. The index 1 is for l=0, it is 2 and 3 for l=1, and finally, 4 and 5 for l=2. So, for example, K edge refers to the transition that excites the innermost $1s$ electron, L_1 edge is due to the excitation of the $2s$ electron, while L_2 and L_3 edges are related to the excitations of the $2p$ electrons with electronic states $^2P_{1/2}$ and $^2P_{3/2}$, respectively (see Figure 2.2). When comparing the shapes of different edges of the same element in the same material, it can be noted that K, L_1 and M_1 edges, but some differences in the broadening look very similar. In the same way, L_2, L_3, M_2, M_3, N_2,

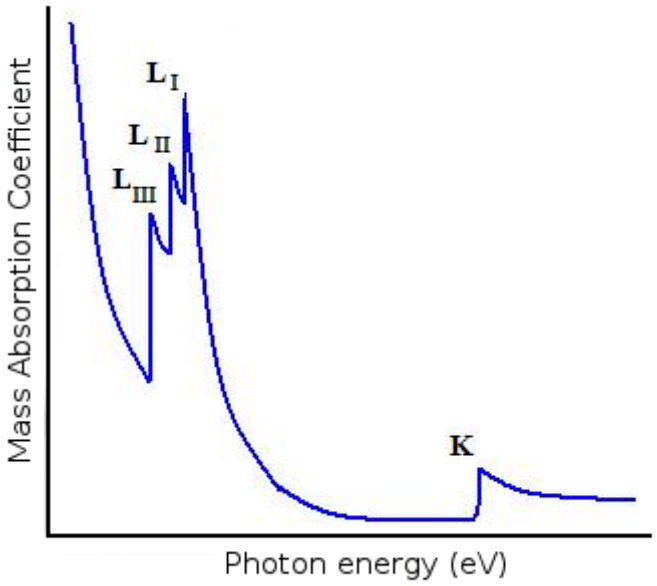

Figure 2.1: Typical XAS spectrum, showing the K, L_I, L_{II} and L_{III} absorption edges.

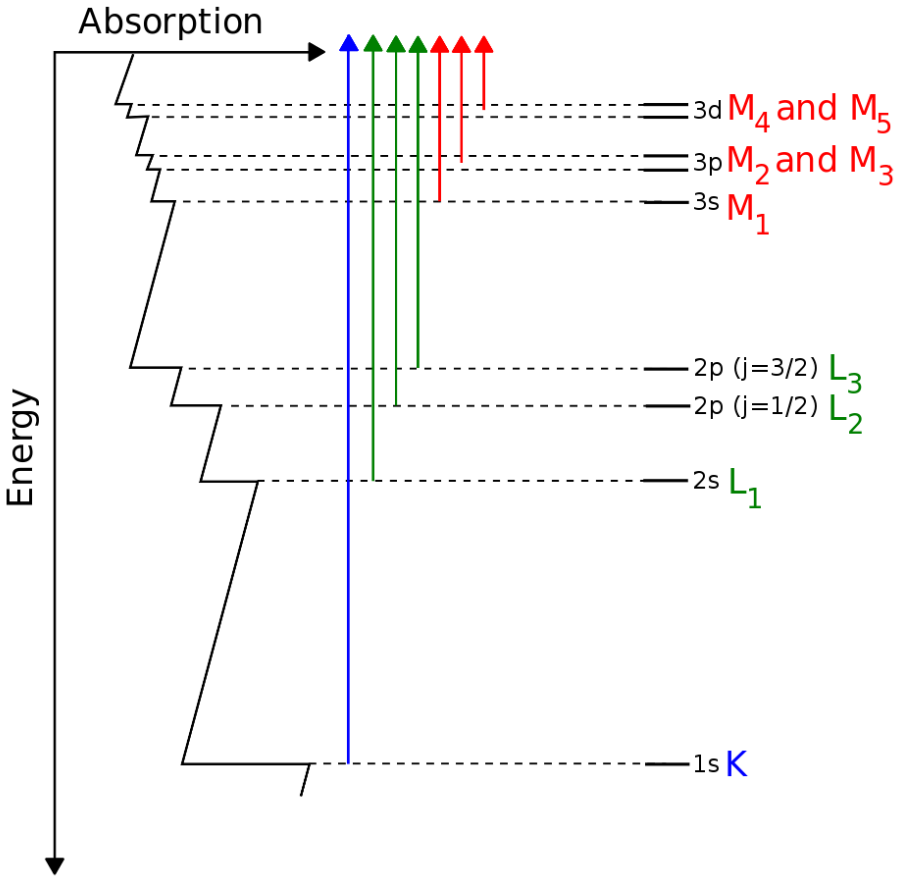

Figure 2.2: Schematic representation of the transitions taking place at the absorption edges.

N_3, up to O_2 and O_3, when they exist, look close.

In a typical XAS experiment, the absorption spectrum around the edge probed is conventionally divided into two major regions, as shown in Figure 2.3:

- X-ray Absorption Near Edge Structure (XANES) region, up to about 50 eV beyond the absorption edge;
- Extended X-ray Absorption Fine Structure (EXAFS) region at higher energies with respect to the edge, and characterized by the oscillatory modulation in the absorption coefficient.

The XANES region can be further divided into three main sub-intervals, the pre-edge region, the absorption edge and the post-edge region. The pre-edge region is characterized by a series of features due to electronic transitions from a core level to unoccupied or partially unoccupied energy levels. The energy position of the absorption edge is sensitive to the oxidation state of the photoabsorber; a change of one unit in oxidation states makes a significant change in the energy of the electronic transitions, giving a clear shift of several electron volt in the position of the edge. The XANES features are also influenced by multiple scattering effects, which depend on the three dimensional geometry of the neighboring atoms of the first shell around the photoabsorber.
The EXAFS region is located at higher energies and it is characterized by the modulation of the absorption coefficient, arising from backscattering of photoelectrons of high kinetic energy, mostly in single back scattering processes. Thus, EXAFS is independent of chemical bonding and depends on the atomic arrangement around the photoabsorber, giving information about the interatomic distances, coordination number, structural and thermal disorder around a particular atomic species.

Being an atomic probe (all atoms have core level electrons), XAS can give local structure information around almost any element in the periodic table. It can be used to study elements in any aggregation state (solid, liquid or gas) and in all kinds of environment (solids, liquids, solutions, glasses and amorphous phases). Moreover, XAS investigations can be made at trace level, giving a direct measurement of physical and chemical state of dilute species. The range that is probed by XAS is usually 4-5 Å from the photoabsorber atom,[61] and is limited by the finite lifetime of the core hole and the finite mean free path of the photoelectron. The core hole is eventually filled with an electron from a higher shell thereby emitting a fluorescence X-ray or an Auger electron while the photoelectron undergoes inelastic interactions with the surrounding material such as inelastic scattering and electron or plasmon excitation (extrinsic losses). The mean free path factor is an exponential term, describing the probability of the photoelectron travels to the backscattering atom and returns to the absorber, without inelastic scattering taking place or the core hole being filled. These features makes the XAS technique different from other experimental techniques, such as X-ray and neutron diffraction, that also provide long-range structural information.

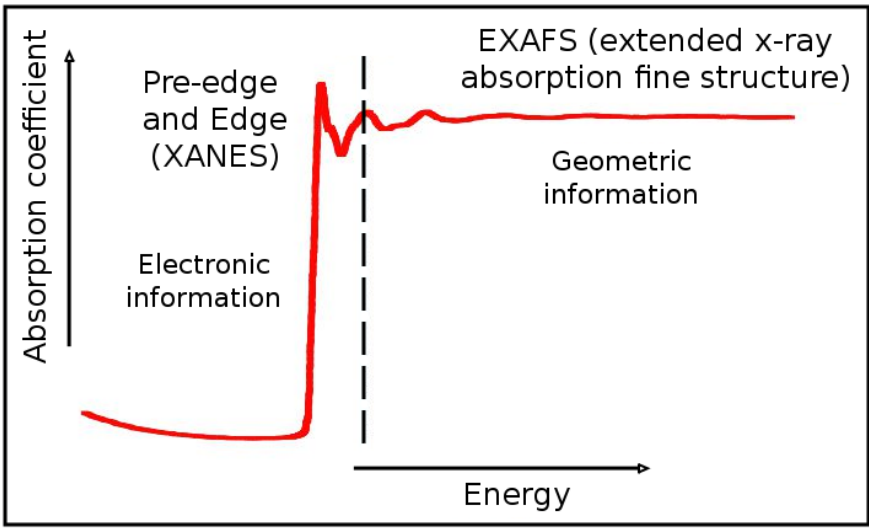

Figure 2.3: Absorption coefficient, μ(E), versus photon energy, showing the division between XANES and EXAFS regions.

Although XAS phenomenon was first observed in the early 1930's by Kronig,[62] it was not until the work of Sayers, Stern and Lytle in 1971 that XAS was shown to contain useful structural information.[63] In the intervening 50 years the phenomenon had largely been ignored due to the sheer difficulty involved in performing XAS experiments and to the lack of agreement between experiment and theory. This, however, was to change with the advent of the synchrotron, together with a corresponding improvement in the theory. In particular, Stern, in 1974, produces a semi-phenomenological expression for the EXAFS, showing that this technique could be used to obtain structural information.[64] Since this time EXAFS has been used to investigate the structure of a large variety of novel compounds.

Some years ago a unifying scheme of interpretation of the XAS spectra, based on the Multiple Scattering (MS) theory and valid for the whole energy range, has been developed.[65] In this approach, based on the Green's function formalism, the absorption cross section ($\sigma(E)$) can be factored into two terms, one of which is an atomic term ($\sigma_0^l(E)$) depending only on atomic electronic properties, and the other is a structure factor ($\chi^l(E)$), that contains all the structural information on the environment:

$$\sigma(E) \propto \sigma_0^l(E)\chi^l(E) \tag{2.2}$$

According to this MS theory, $\chi^l(E)$ is expressed by the following equation [66]:

$$\chi^l(E) = \frac{1}{(2l+1)sin^2\delta_l^0} \sum_m Im[(I + T_a G)^{-1} T_a]_{lm,lm}^{00} \tag{2.3}$$

where I is the unit matrix, G is the matrix describing the spherical wave propagation of the photoelectron from one site to another around the photoabsorber, T is the diagonal matrix describing the scattering process of the

photoelectron by the atoms located at the various sites around the photoabsorber and δ_l^0 is the phase shift of the photoabsorbing atom (located at site 0) for angular momentum l. Now, the fundamental problem in XAS calculations is the inversion of the matrix of eq. 2.3. In the EXAFS region the matrix inverse can be expanded in a series of terms, each of which corresponds to the contribution of a scattering path, i.e the matrix inverse can be written as a sum over all of the multiple scattering paths.[66] This is due to the fact that in high energy regime the series is convergent. Conversely, this expansion of the matrix inverse is not possible in the low energy region (XANES) as the series does not converge and, therefore, the structure factor has to be calculated by the exact matrix inversion. The physical reason of this difference is that in the XANES regime the electron kinetic energy is small and the scattering on the neighbouring atoms tends to be strong, while the effect of the scatterers becomes smaller at higher energies and the photoelectron is only weakly scattered.

By the middle part of 1990's, three different theory packages (EXCURVE, GNXAS and FEFF) have been developed, which enabled the application of high quality theory to XAS data analysis. The three packages share certain similarities. Each uses a cluster expansion to represent the EXAFS signal as a sum of geometric contributions and each makes two fundamental approximations. The first one is the so called Muffin-Tin approximation that was introduced as a way of solving problems of electron motion in periodic potentials. Each atom is represented by a sphere, so the potential generated by the atoms surrounding the photoabsorber is spherically averaged inside muffin-tin spheres around each atom, and averaged to a constant in the space between the spheres, the interstice, that is delimited by an outer sphere enclosing the cluster considered in the calculation. The second one is the choice of the effective optical potential in which the photoelectron moves; the most used is the advanced model for the exchange-correlation self-energy (Hedin-Lundqvist) whose imaginary part accounts for extrinsic losses.[67] It should be noted that this approximation is good in the EXAFS region, while other approximations are exploited in the XANES region.

2.1 The EXAFS technique

As previously mentioned, analysis of the EXAFS data provides fine details of the radial pair distribution functions of atoms around the photoabsorber, including distances, mean square deviations in distance, coordination numbers, and coordinating species. Because neither the theory nor the interpretation of the EXAFS makes any assumption of configurational symmetry or periodicity, EXAFS is equally applicable to all forms of condensed matter. Moreover, the physical process at the base of XAS is element specific, thus making EXAFS applicable even to dilute systems. The fundamental quantities used in the analysis of EXAFS spectra are defined as follows (see also Figure 2.4):

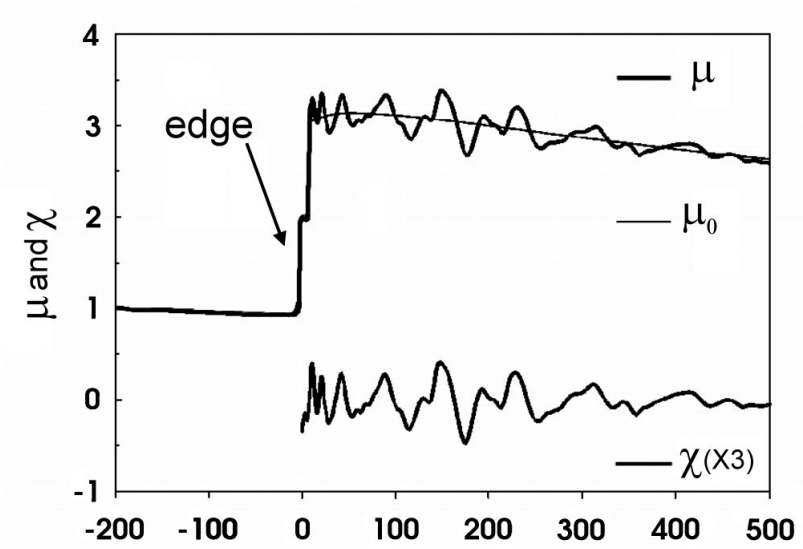

Figure 2.4: Relation between $\mu(E)$, $\mu_0(E)$ and $\chi(E)$

- $\mu(E)$ is the atomic absorption coefficient, defined as the attenuation of the X-ray beam per distance unit, which is proportional to the absorption cross section.
- $\mu_0(E)$ is the absorption coefficient of the isolated atom.
- $k = \frac{p}{\hbar} = \sqrt{\frac{2m_e}{\hbar^2}(E - E_0)}$ is the photoelectron wave number.
- $\chi(k) = \frac{\mu - \mu_0}{\mu_0}$ is the normalized oscillating part of the spectrum, which is obtained by eliminating the absorption of the isolated atom from the signal and normalizing it to unity.

A quantitative parametrization of $\chi(k)$ which has become the standard for current EXAFS analysis has been developed by Sayers et al.[63] In this formalism, the oscillatory part of the absorption coefficient can be expressed as a sum over the scattering contributions arising from the various different paths:

$$\chi(k) = S_0^2 \sum_i N_i \frac{f_i(k)}{kR_i^2} \sin(2kR_i + 2\delta_c(k) + \phi_i(k)) e^{-\frac{2R_i}{\lambda(k)}} e^{-2\sigma_i^2 k^2} \tag{2.4}$$

where S_0^2 is a phase reduction factor, the index i runs over all the different shells of neighboring atoms around the photoabsorber, $\delta_c(k)$ and $\phi_i(k)$ are the phase displacements due to the photoabsorber atom and to the scatterers, respectively. N_i is the coordination number (number of equivalent scatterers), σ_i is the average square fluctuation of the bond distances (or Debye-Waller factor) accounting for thermal and structural disorder, and f_i is the diffusion amplitude. R_i is the interatomic distance between the central atom i and the backscatterers in the ith shell. $\lambda(k)$ is the energy-dependent mean free

path, typically of few Å, determining the local character of the XAS technique. The substantial validity of this expression is due to the fact that in the high energy range the contributions of the different scattering paths can be factorized and for the special case in which only two-body paths are accounted for, the functional form of eq. 2.4 is recovered. The EXAFS phase, which directly controls the determination of the interatomic distances R_i, can be measured very accurately, and hence EXAFS provides values of distances with very high accuracy, typically of the order of 0.01 Å. Conversely, the amplitude of EXAFS is less well defined; it depends on the number of neighbour scatterers, the many-electron processes and the static and thermal disorder. Consequently, coordination numbers can be determined with an error of ±0.5. The Debye-Waller factor in eq. 2.4 accounts for the fact that, due to the thermal vibrations (thermal disorder) and to the structural variations in the interatomic distances (static or configurational disorder), the atomic positions oscillate and thus R_i is only the average value of a distance distribution. At room temperature about 99% of all molecular vibrations are in the ground state, which means that the harmonic approximation can be applied, and thus the distribution of distances between the photoabsorber and the backscattering atoms in a shell is well approximated by a Gaussian function of width proportional to the Debye-Waller factor. The term $e^{-2\sigma_i k^2}$ in eq. 2.4 then accounts for the k-dependent damping of the EXAFS oscillations. Conversely, at higher temperatures, the amplitude of the bond stretching and its vibrational movement increases, corresponding to a population increase of higher vibrational states. This means that the distribution of the distances becomes asymmetric towards the large distances, the harmonic approximation is no longer valid and the appropriate description of these systems can be performed in terms of radial distribution functions ($g(r)$). The same effect is also found for disordered systems, such as metal ions in aqueous solutions. In this cases, the $g(r)$ first peak can be modeled with Gamma-like distributions with mean distance R, standard deviation σ, and asymmetry index (third cumulant divided by σ^3) $\beta = 2p^{-\frac{1}{2}}$ that can be gradually varied in a wide range. The general expression is:

$$f(r) = N_c \frac{p^{\frac{1}{2}}}{\sigma\Gamma(p)} \left[p + \frac{r-R}{\sigma} p^{\frac{1}{2}}\right]^{(p-1)} e^{-\left[p + \frac{r-R}{\sigma} p^{\frac{1}{2}}\right]} \tag{2.5}$$

where $\Gamma(p)$ is the Euler's Gamma function for the parameter p, and N_c is the coordination number providing the correct normalization.

Thus, the $\chi(k)$ EXAFS signal contains all the structural information on the investigated system in an analogous way to the structure factor $S(q)$ in diffration techniques. However, the $S(q)$'s functions are proportional to a linear combination of M(M+1)/2 partial structure factors associated to the M atoms of the system, that are very difficult to isolate in single contributions. Conversely, the EXAFS signal depends only on the distribution functions involving the photoabsorber atom, becoming an alternative technique with a strong sensitivity to the short-range order in condensed matter. The EX-

AFS data can be also Fourier transform into R-space, providing a means to visualize different scattering contributions. Indeed, when Fourier transformed, different scattering contributions with a large difference in R_i and small values in σ_i^2 produce well separated peaks with amplitudes approximately proportional to $\frac{N_i}{\sigma_i}$. However, different k-weights might be used and a smooth window function is usually applied to account for the finite data range. Note that the Fourier Transform is a complex function and both phase and magnitude have to be considered for the full information content.

The analysis of the EXAFS data is usually performed within the Gaussian approximation obtaining average distances and coordination numbers. However, in the case of disordered systems, the experimental data contain a wider structural information that can be extracted and also the fitting parameters are often correlated, thus a more sophisticated procedure is needed to carry out a reliable EXAFS analysis. In this context, data analysis can derive strong benefit from structural information obtained from theoretical simulations which can be used as relevant models in the EXAFS fitting procedure. In particular, site-site radial distribution functions, $g(r)$'s, involving the photoabsorber atom can be computed from MD simulations and they can be used to calculate a theoretical $\chi(k)$ EXAFS signal, through the following equation:

$$\chi(k) = \int_0^\infty dr 4\pi r^2 \rho g(r) A(k,r) \sin(2kr + \phi(k,r)) \tag{2.6}$$

where $A(k,r)$ and $\phi(k,r)$ are the amplitude and phase functions, respectively, and ρ is the density of the scattering atoms. The possibility to calculate the $\chi(k)$ signal starting from the $g(r)$'s relies in the fact that the overall EXAFS signal can be written as a sum of contributions over all of the multiple scattering paths. In fact, generally, it is possible to compute $\chi(k)$ by adding a finite number of contributions associated with well defined peaks of the pair, three-body, and four-body distribution functions, and the truncation of the summation to pair distributions is usually a reasonable approximation for highly disordered systems in the EXAFS regime. However, in some cases, also three-body distribution functions should be considered, and thus the $\chi(k)$ signal can be expressed in the following integral form:

$$\begin{aligned}\chi(k) = \int_0^\infty & dr\, 4\pi r^2 \rho g(r) A(k,r) \sin(2kr + \phi(k,r)), + \\ & + \int dr_1 dr_2 d\theta\, 8\pi^2 r_1^2 r_2^2 \sin(\theta) \rho^2 g_3(r_1, r_2, \theta) \gamma^{(3)}(k, r_1, r_2, \theta)\end{aligned} \tag{2.7}$$

where the first integral term corresponds to single scattering (SS) contributions, that are dominant especially well above the absorption edge, while the second integral describes multiple scattering (MS) contributions, depending on the relative positions of two atoms around the photoabsorber one. Obviously, the MS signal is much weaker than the dominant pair contribution but, in some cases, a clear signature of a particular triplet atomic configuration is present. Note that even if the integral in eq. 2.6 and 2.7 formally

extends to infinity, there is a natural cutoff distance due to the photoelectron mean-free path. This cutoff is provided by an exponential dependence of the amplitude function $A(k,r)$ on the photoelectron mean-free path $\lambda(k)$ ($A(k,r) = f(k,r)e^{-r/\lambda(k)}/kr^2$). Similarly, the $A(k,r)$ function accounts for the monochromator resolution, that provides an effective additional damping especially in the low-k region. Thus, the symbiosis MD-EXAFS is extremely useful when complex systems containing several pair distribution functions are investigated or when MS contributions are present in the spectra, as the structural model obtained from MD simulations can represent an essential starting point for the EXAFS analysis. It should be noted that EXAFS signal of liquid samples contains very little information on the overall $g(r)$ shape and, in particular, on the second maximum and beyond. Therefore, the reliability of the final model $g(r)$ in the long-distance range is strongly dependent on the original model. Instead, the short-range shape of the $g(r)$ can be accurately probed and refined by the EXAFS data. If one is interested in long-range information, an X-ray or neutron diffraction experiment, measuring the structure factor $S(k)$, is mandatory.

The comparison between the experimental and theoretical signal is generally made by minimizing a square residual function of the type:

$$R(\{\lambda\}) = \sum_{i=1}^{N} \frac{[Y_{exp}(E_i) - Y_{theo}(E_i;\lambda_1 \dots \lambda_p)]^2}{\sigma_i^2} \tag{2.8}$$

where $Y_{exp}(E_i)$ and $Y_{theo}(E_i;\lambda_1 \dots \lambda_p)$ are the experimental and theoretical data points, N the number of data points and σ_i^2 the variance associated to each experimental datum $Y_{exp}(E_i)$. If we assume that λ_r is the set of λ parameters such as Y_{theo} is equal to the true signal and that the experimental signal ($Y_{exp}(E_i)$) is affected only by random Gaussian noise with standard deviation σ_i for each E_i energy points around the true signal, we can write:

$$Y_{exp}(E_i) = Y_{theo}(E_i;\{\lambda_r\}) + \xi_i \tag{2.9}$$

where ξ_i is the random noise for the i-point (i = 1,2,...p), with expected value $\mathrm{E}\{\xi_i\} = 0$ and covariance $\mathrm{E}\{\xi_i, \xi_j\} = \delta_{ij}\sigma_i^2$. If we substitute eq. 2.9 into eq. 2.8, we obtain:

$$R(\{\lambda\}) = \sum_{i=1}^{N} \frac{\xi_i^2}{\sigma_i^2} = \chi_p^2 \tag{2.10}$$

where χ_p^2 is a χ^2 random variable with p degrees of freedom. Note that p is the number of λ parameters on which the signal depends.

In the least-squares spirit, within a given choice for the structural model (provided by MD simulations in our approach), the optimal values for the structural parameters are the set $\{\lambda\}$=$\{\lambda_{opt}\}$ that minimizes the residual function ($\mathrm{R}(\{\lambda_{opt}\})$=$\mathrm{R}_{min}$)). The experimental signal, $Y_{exp}(E_i)$, will deviate from the signal provided by the optimal values, $Y_{theo}(E_i;\{\lambda_{opt}\})$, by the random noise ξ_i, in the same way as described in eq. 2.9, and by the difference

between λ_{opt} and λ_r. For a given structural model, with optimal values λ_{opt}, R($\{\lambda\}$) is thus described by the χ^2_p random variable shifted by the value of R in the minimum, R_{min}:

$$R(\{\lambda\}) = R_{min} + \chi^2_p \tag{2.11}$$

with $R_{min} = 0$ for λ_{opt}=λ_r.

Confidence intervals for the λ parameters can therefore be established by looking at regions in the parameter space for which $R(\{\lambda\}) < R_{min} + C$, with C depending on the confidence level of the analysis.[84]

2.2 Synchrotron

XAS experiments are generally performed at Synchrotron sources, which provide tunable X-ray beams characterized by high intensity, high degree of polarization, high degree of collimation, high brillance due to the small cross section of the electron beam and high beam stability. Charged particles (positrons or electrons) produced in the source are first accelerated in a linear accelerator or "linac" and then in a booster ring that gives them a boost in energy from millions to billions or giga electron volts; at that point they are transferred to the storage ring under high vacuum (see Figure 2.5). Here, the electrons are forced around the storage ring to follow circular paths by the magnetic field of the bending magnets. During each turn, they loose part of their energy as synchrotron radiation, that is emitted tangential to the curved sections. The energy lost in this way is re-increased as kinetic energy through a radio frequency (RF) cavity. Modern synchrotron sources also

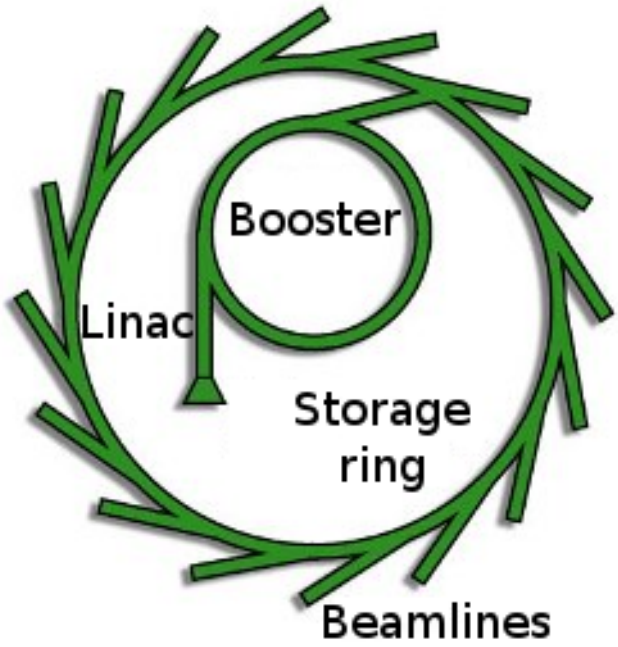

Figure 2.5: Schematic planar view of a synchrotron radiation facility.

have additional elements, so-called insertion devices, placed in the straight section between the bending magnets. These devices constitute a series of alternating magnetic fields that force the electron beam to perform either strong (wiggler) or gentle (undulator) oscillations. The wiggler emits a broad beam of incoherent radiation characterized by increased intensity and a continuous energy spectrum extending to much higher X-ray energies compared to a bending magnet. The undulator emits a narrow beam of coherent radiation the intensity of which is amplified up to 10000 times but only at certain energies.

The *first generation synchrotron facilities*, developed during 1960s and early 1970s, were only used during high energy physics experiments, and not for synchrotron radiation studies. The early-dedicated facilities, the so called *second generation synchrotron facilities*, were constructed in the mid-70s, where the synchrotron light was mainly produced by bending magnets. During the same period it was also realized that the insertion of high magnetic field devices, such as wigglers and ondulators, improved the radiation properties by several magnitudes. So, during the 80s the *third generation synchrotron facilities*, such as the European Synchrotron Radiation Facility (ESRF), were built.

Chapter 3

Molecular Dynamics

Molecular Dynamics (MD) simulations are becoming more and more an essential tool to unravel the microscopical arrangement, at the molecular level, of disordered and complex systems, like the ones investigated in the present work.

In the most common implementations MD simulations found on the Born-Oppenheimer approximation and consequent separation of the motion of nuclei and electrons. Nuclei are usually heavy enough that their motion can be described classically, maintaining in most of the cases a good description of the structural and dynamic properties of the investigated systems. In particular, this is a very good approximation for molecular systems as long as the properties studied are not related to the motion of light atoms (like the hydrogen atoms, which show quantum mechanical behaviour in certain situations such as tunneling phenomena) or vibrations with frequency ν such that $h\nu > k_B T$. The motion of the nuclei of a system composed by N particles can thus be simulated by solving the Newton's second equation of motion step-by-step [68]:

$$m\frac{\partial^2 \vec{r}}{\partial t^2} = \vec{F} \tag{3.1}$$

where m is the mass and r is the vector containing the coordinates for all the particles, i.e. in Cartesian coordinates it is a vector of length $3\mathrm{N}_{particle}$. F is the force acting on the particles, that can be expressed as the negative of the energy gradient:

$$\vec{F} = -\frac{\partial V}{\partial \vec{r}}$$

where V is the potential energy function at position $\vec{r}$.

The way V is obtained differentiates between ab-initio and Classical MD simulations. In ab-initio MD simulations the electrons are explicitly treated and V is obtained by solving the electronic Schrödinger equation. Such approach represents the most accurate but also the most computationally expensive. So, ab-initio simulations are usually limited in size and simulation time: systems of hundreds of atoms simulated for tens of picoseconds. When bigger systems and larger simulations are needed, like in the case of the viscous ILs, ab-initio simulations can not fit with the purpose of the investigation. It is

thus mandatory to use in such cases a more approximated estimation for the potential V, that allows to reduce the computational cost and to effort the dimensions and timescales needed for the investigation. Classical MD corresponds indeed to this second class of simulations, where the electrons are not explicitly treated and V is approximated via parametrized functions, known as "force fields".

3.1 Classical Molecular Dynamics

In Classical MD the force field, approximating the potential energy function V, is represented by a sum of terms, each describing the energy required for distorting a molecule in a specific fashion. In these force fields, the interactions are usually divided into bonded and non-bonded [69]:

$$V = V_{bonded} + V_{non-bonded} \tag{3.2}$$

Bonded interactions are written as a sum of various terms:

$$V_{bonded} = \sum_{bond} \frac{1}{2} k_{b_n} (b_n - b_{0n})^2 + \sum_{angle} \frac{1}{2} k_{\theta_n} (\theta_n - \theta_{0n})^2 + \\ + \sum_{dihedral} \frac{1}{2} k_{\phi_n} [1 + \cos(m_n \phi - n - \delta_n)] + \sum_{impr.dihedr} \frac{1}{2} k_{\xi_n} (\xi_n - \xi_{0n})^2 \tag{3.3}$$

- The first term describes the stretching of a covalent bond between two atom types i and j through a harmonic oscillator, with the potential being quadratic in the displacement from the minimum. k_{b_n} is the force constant, b_n the instantaneous distance and b_{0n} the equilibrium distance. The harmonic form is the simplest possible, and sufficient for determining most equilibrium geometries. In some cases, there are certain strained and crowded systems where the results from a harmonic approximation are significantly different from the experimental values, and the functional form for the potential must be improved (see for example the Morse potential [70]).

- The second term describes the bending of the bond angle formed by three atoms i, j, k, where there is a bond between i and j, and between j and k. Also in this case, the bending is modeled by a harmonic potential with force constant k_{θ_n}, instantaneous angle θ_n and equilibrium angle θ_{0n}.

- The third term is associated with a rotation around a j-k bond in a four-atom sequence i-j-k-l, where i-j, j-k and k-l are bonded, i.e it mimics the vibrations of dihedral angle (four-body) interactions. In this functional form ϕ is the angle between the ijk and jkl planes.

- The last term represents a special type of dihedral interaction, the so

called improper dihedral, which is used to force atoms to remain in a plane or to prevent transitions to a configuration of opposite chirality (a mirror image) and, in harmonic approximation, k_{ξ_n}, ξ_n and ξ_{0n} are the force constant, instantaneous and equilibrium improper dihedral angle, respectively.

Non-bonded interactions are written as a sum of two terms:

$$V_{non-bonded} = \sum_{pairs(ij)} \left[\left(\frac{C_{ij}^{(12)}}{r_{ij}^{12}} - \frac{C_{ij}^{(6)}}{r_{ij}^{6}} \right) + \frac{1}{4\pi\epsilon_0} \frac{q_i q_j}{\epsilon_r r_{ij}} \right] \tag{3.4}$$

$$\tag{3.5}$$

- The first term is the van der Waals term, describing the attraction or repulsion between atoms that are not directly bonded. This term is zero at large interatomic distances, while becomes very repulsive for short distances, as a consequence of the overlap of the electron clouds of the two atoms that repel each other. The most popular function is the *Lennard-Jones* potential, where the repulsive part is given by an r^{-12} dependence ($C_{ij}^{(12)}$ and $C_{ij}^{(6)}$ are suitable constants).

- The second term describes the interaction between point charges through the Coulomb potential (q_i and q_j are the atomic partial charges at a given distance r_{ij}). The atomic charges can be assigned by empirical rules, or by fitting to the electrostatic potential calculated by electronic structure methods.

3.1.1 Numerical integration of the equations of motion

The Newton's equations of motion are integrated numerically step-by-step. Many algorithms have been developed to do this, generally based on a Taylor expansion of the particle positions around the positions at a certain time instant t:

$$\vec{r}(t+\delta t) = \vec{r}(t) + \vec{v}(t)\delta t + \vec{a}(t)\frac{\delta t^2}{2} + O(\delta t^3) + \cdots \tag{3.6}$$

where $\vec{v}(t)$ and $\vec{a}(t)$ are the velocity and the acceleration at time t, respectively. The most commonly used method is the Verlet algorithm,[71] which is not only one of the simplest, but also usually the best. It is based on two Taylor expansions, one for positive times and the other for negative times:

$$\vec{r}(t+\delta t) = \vec{r}(t) + \vec{v}(t)\delta t + \frac{\vec{F}(t)}{2m}\delta t^2 + O(\delta t^3) + \cdots \tag{3.7}$$

$$\vec{r}(t-\delta t) = \vec{r}(t) - \vec{v}(t)\delta t + \frac{\vec{F}(t)}{2m}\delta t^2 - O(\delta t^3) + \cdots \tag{3.8}$$

Summing these two equations, we obtain:

$$\vec{r}(t+\delta t) = 2\vec{r}(t) - \vec{r}(t-\delta t) + \frac{\vec{F}(t)}{m}\delta t^2 + O(\delta t^4) \tag{3.9}$$

The estimate of the new position contains an error of the order of δt^4, where δt is the time step. Note that this algorithm does not use the velocity to compute the new position. However, we can derive the velocity from knowledge of the trajectory:

$$\vec{v}(t) = \frac{\vec{r}(t+\delta t) - \vec{r}(t-\delta t)}{2\delta t} \tag{3.10}$$

It is possible to cast the Verlet algorithm in a form that uses positions and velocities computed at equal times, and this is the so-called velocity Verlet algorithm. Another algorithm equivalent to the Verlet method is the so-called Leap-Frog algorithm,[72] that evaluates the velocities at half-integer time steps and uses these velocities to compute new positions. It is possible to derive the Leap-Frog algorithm from the Verlet scheme, by defining the velocities at half-integer time steps through the following equations:

$$\vec{v}(t - \frac{\delta t}{2}) = \frac{\vec{r}(t) - \vec{r}(t-\delta t)}{\delta t} \tag{3.11}$$

$$\vec{v}(t + \frac{\delta t}{2}) = \frac{\vec{r}(t+\delta t) - \vec{r}(t)}{\delta t} \tag{3.12}$$

From the second equation we can obtain an expression for the new positions, based on old positions and velocities:

$$\vec{r}(t+\delta t) \quad = \quad \vec{r}(t) + \vec{v}(t + \frac{\delta t}{2})\delta t \tag{3.13}$$

From the Verlet algorithm, we get the following expression for the update of the velocities:

$$\vec{v}(t + \frac{\delta t}{2}) = \vec{v}(t - \frac{\delta t}{2}) + \frac{\vec{F}(t)}{m}\delta t \tag{3.14}$$

As the Leap Frog scheme is derived from the Verlet one, it gives rise to identical trajectories. In terms of theoretical accuracy it is also of third order, as the Verlet algorithm, but the numerical accuracy is improved. Furthermore, the velocities appear directly, which facilitates a coupling to an external bath. However, the velocities are not defined at the same time as the positions, and thus kinetic and potential energy are also not defined at the same time. Hence, we cannot directly compute the total energy in the Leap-Frog algorithm. Note that both algorithms are time reversible, like the Newton's equations of motion.

3.1.2 Initial conditions and Time step

At the beginning of a MD simulation, we have to assign the initial coordinates and velocities of all particles of the system. Despite the MD trajectory

is independent on the initial configuration (after the needed amount of time to bring the system to equilibrium), in the choice of the initial set of positions and velocities it is still important to avoid unphysical distributions of positions/velocities. In order to do this, generally the crystalline structure can be used as initial configuration and, if the system to be studied is in the liquid phase, it is brought to the fusion temperature. As regards the initial velocities, they are generated by extracting the scalar components of the velocities from a Maxwellian distribution at the simulation temperature. This distribution is generated from random numbers, according to the following equation:

$$p(\vec{v}_i) = \sqrt{\frac{m_i}{2\pi k_B T}} exp\Big(- \frac{m_i v_i^2}{2k_B T}\Big)$$

where $p(\vec{v}_i)$ is the probability of the i particle to have the $\vec{v}_i$ velocity, m_i the mass and T the temperature of the system.

Another important control parameter for a simulation is the time step. The maximum time step that can be taken is determined by the rate of the fastest process in the system, and thus typically an order of magnitude smaller than the fastest process. Molecular motions, such as rotations and vibrations, occur with frequencies in the range 10^{11}-10^{14}s^{-1}, and this means that time steps of the order of femtoseconds (10^{-15}s) or less are required to model such motions with sufficient accuracy. A total simulation time of 1 nanosecond requires 10^6 time steps, and so simulation times are typically in the nano- or picosecond range.

3.1.3 Long range interactions

Non-bonded terms account for electrostatic interactions, described by the Coulomb equation, van der Waals interactions, and electron-electron repulsion. The van der Waals interactions can be described by the following equation:

$$V(r) = \frac{C_6}{r^6} + \frac{C_8}{r^8} + \frac{C_{10}}{r^{10}} \tag{3.15}$$

where r is the distance between two particles. The electron-electron repulsion depends on the (interatomic) distance in the same way of the orbital functions (e^{-r}).

In the common Lennard-Jones 12-6 formulation the van der Waals interactions are approximated considering only the $\frac{C_6}{r^6}$ term, while the electron-electron repulsion is modelled to decrease as r^{-12}, in order to minimize the cost to compute the energy contribution of the long-range interactions. More accurate force fields for the long-range interactions, like the one formulated by Buckingham, adopt more sophisticated description of van der Waals interactions and electron-electron repulsion, that are treated with the (uncatted) eq. 3.15 and with the correct exponential dependence from the distance (e^{-r}) respectively.

Generally, all the long range interactions are not calculated beyond a certain cutoff distance, r_{cut}, in order to reduce the computational cost of the

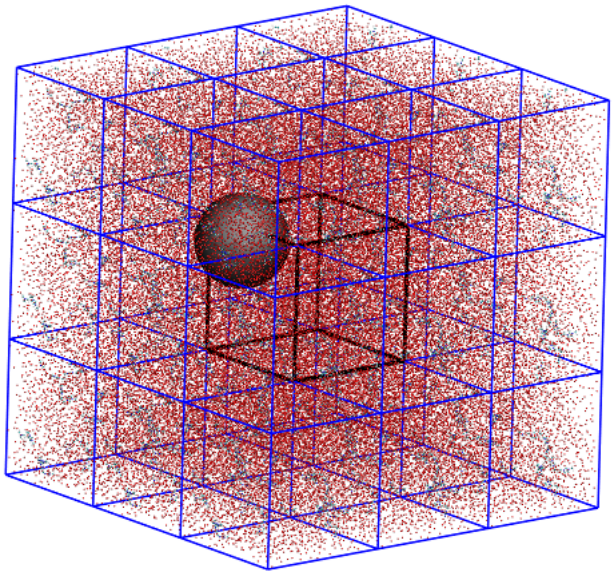

Figure 3.1: Periodic boundary conditions and *cutoff* radius.

simulation (see Figure 3.1) and because the evaluation of Coulomb interactions would lead to a non-convergent series. The choice of the r_{cut} value is constrained by a lower and upper limit. The former is given by the necessity of avoiding cutting the Lennard-Jones interactions, that go to 0 in between 9 and 12 Å, while the latter corresponds to half of the box smallest dimension, in order to not include within the cutoff two replica of the same particle. In this way van der Waals interactions and electron-electron repulsion are generally correctly accounted for. However, as regards the Coulomb interactions, truncating the interaction by using a simple cutoff distance can introduce some artifacts, giving non-physical distributions of the molecules near the cutoff distance. Several methods have been developed for treating the electrostatic interaction "exactly" (to within a numerical threshold), but with the advantage to not performing the N^2 summation over all atoms, such as the *Ewald sum* [73] and the *Particle Mesh Ewald* methods.[74, 75] The general idea is to split the interaction into two contributions, the so-called "near"- and "far" contributions. The former is obtained by embedding each point charge in a screening potential, represented by a Gaussian curve with an exactly opposing charge centered at the position of the point charge (see Figure 3.2). This means that outside the screening function, essentially given by the width of the Gaussian curve, the net charge is zero, and the interaction between these screened point charges is short-ranged and can be directly evaluated. But, in order to recover the original point charge interaction, the effect of the screening functions must be subtracted again. This compensating term is an interaction between Gaussian charge distributions and it is long-ranged. It can be evaluated in the reciprocal space by Fourier Transform methods. The only free parameter is the width of the Gaussian potential. A wide Gaussian function makes the direct-space part converge slowly, but the reciprocal-space part converge rapidly, and vice versa for a

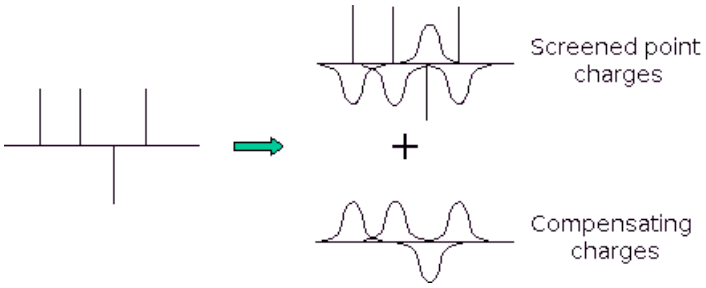

Figure 3.2: Ewald method: a set of point charges may be considered a set of screened charges minus the smoothly varying compensating background.

narrow Gaussian function. It should be noted that the Ewald method has been developed for periodic systems, such as crystals, but can also be applied to quasi-periodic models arising by applying periodic boundary conditions. The cpu time required for a fully optimized Ewald summation scales with the number of particles as $N^{\frac{3}{2}}$. In some applications we not only have the long-range interactions but short-range interactions as well. In this case it should be convenient to use the same cutoff distance for the real-space in the Ewald sum as for the short-range interactions. However, for a fixed cutoff, the calculation of the Fourier part of the Ewad sum scales as N^2, which makes the method inefficient for large systems. Several schemes for solving this problem have been proposed, such as the *Particle Mesh Ewald* method, which scales only as Nln(N).

3.1.4 Periodic boundary conditions

Periodic boundary conditions [69] are applied to prevent the outer molecules from boiling off into space and minimizing edge effects, which may produce artifacts in a finite systems. The atoms of the system to be simulated are placed in a suitable box, generally cubic, which is duplicated in all directions (the initial box is so surrounded by 26 identical cubes, which are again surrounded by 98 boxes, etc). Now if an atom leaves the central box through the right wall, its image will enter the box through the left wall from the neighbouring box. The resulting model becomes quasi-periodic, with a periodicity equal to the dimension of the box. In order to reduce the number of atoms in the simulation it is also possible to use non-cubic polyhedron, such as the dodecahedron or the truncated octahedron, which are periodically ordered and better approximate a sphere than the cubic box (see Figure 3.3). Note that the imposed artificial periodicity may cause errors when considering properties which are influenced by long-range correlations, such as for dipolar and charged systems.

3.1.5 Neighbour list

Computing all the non-bonded interactions in a MD simulation involves, in principle, a large number of pairwise calculations. The time to examine

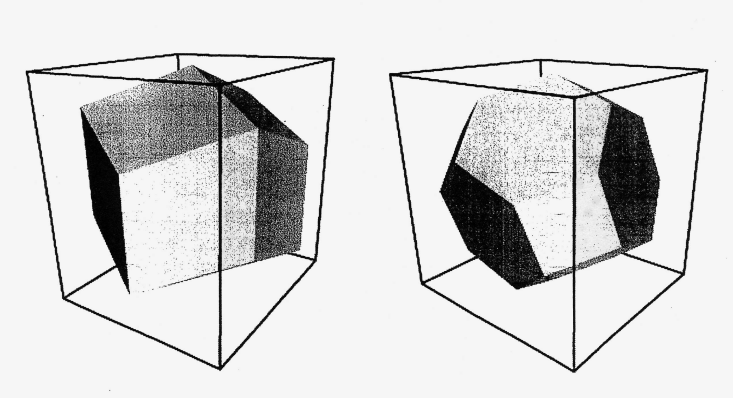

Figure 3.3: Non-cubic box: dodecahedron and truncated octahedron.

all pair separations is proportional to the number of distinct pairs ($\frac{1}{2}$N(N-1) in a N-atom system), and for each pair one must compute at least r_{ij}^2, and this still requires a lot of time. A useful tool to partially overcome this problem is to create a neighbour list: the cutoff sphere around a particular atom is surrounded by a larger sphere of radius r_{list} and, at the first step of the simulation, a list is created of all the neighbours of each atom, for which the pair separation is within r_{list}. Over the next few time steps (about 10), only pairs appearing in the list are checked in the force routine. Obviously, the choice of r_{list} is a compromise, i.e larger lists will need to be recreated less frequently, but will not give as much of a saving on cpu time as smaller lists.

3.1.6 Constraints

In Classical MD, when bonds have very high vibration frequencies (and should be treated in a quantum mechanical way rather than in the classical approximation), especially those involving hydrogen atoms, it is quite common to treat these bonds as being constrained to have fixed length. In fact, these degrees of freedom have relatively little influence on many properties. One of the most commonly used constraint method is the SHAKE algorithm [76]; it transforms at each step a set of unconstrained coordinates $\vec{r}'$ in a set of bounded coordinates $\vec{r}''$. This is equivalent to resolve a set of Lagrange multipliers on the equations of motion; being σ_k the generic equation of a constraint, we obtain:

$$\sigma_k(\vec{r}_1, \ldots, \vec{r}_K) = 0 \qquad k = 1, \ldots, K \tag{3.16}$$

$$\vec{f}_i = -\frac{\partial}{\partial \vec{r}_i}\left(V + \sum_{k=1}^{K} \lambda_k \sigma_k\right) \tag{3.17}$$

$$\vec{g}_i = -\sum_{k=1}^{K} \lambda_k \frac{\partial \sigma_k}{\partial \vec{r}_i} \tag{3.18}$$

where λ_k are the Lagrange multipliers, $\vec{f}_i$ the generalized forces, $\vec{g}_i$ the constraint forces and K the number of constraints; the SHAKE algorithm implies the iterative resolution of a system of K equations of the second order, neglecting the terms λ_k^2. This scheme is for the original Verlet algorithm, while the appropriate version for the velocity Verlet algorithm is called RATTLE. Note that the use of constraints allows longer time steps to be taken, and consequently longer simulation times to be obtained for the same computational cost.

3.1.7 Temperature and pressure control

A standard MD simulation gives rise to the NVE (microcanonical) ensemble, i.e. the energy is conserved thus constant during the simulation. Neverthless, other ensembles can be exploited (NVT, NPT), if conditions of the target system to simulate requires it. Note that all the simulations of this work have been carried out in the NVT ensemble, also called the canonical ensemble, since the necessity to reproduce the structural and dynamical properties of the investigated systems at constant room temperature. In the NVT ensemble, the temperature has a specified average (macroscopic) value, while the instantaneous observable representing the total energy of the system (i.e., the Hamiltonian H) can fluctuate. In the NPT ensemble, the pressure has (just as the temperature) a specified average value, while the instantaneous volume V of the system can fluctuate. These fluctuations vanish in the limit of a macroscopic system, but are often non-negligible for the system sizes typically considered in the simulation.

Thus, performing a MD simulation in an other ensemble than microcanonical requires to keep at least one intensive quantity constant (on average) during the simulation. A modification of the Newtonian MD scheme with the purpose of generating a thermodynamical ensemble at constant temperature/pressure is called a thermostat/barostat algorithm. Several algorithms have been developed which control the temperature and the pressure of a system. For the temperature control the Berendsen [77] and the Nosé-Hoover [78, 79] are the most extensively employed, while as regards the pressure control the most used methods are the Berendsen and the Parrinello-Rahman schemes.[80, 81]

As regards the temperature control, the use of a thermostat requires the definition of an instantaneous temperature, that will be compared to the reference temperature T_0 of the heat bath to which the system is coupled. Following the equipartition theorem, the average internal kinetic energy of a system is related to its macroscopic temperature T through the following equation:

$$E_{kin}(t) = \sum_{i=1}^{N} \frac{1}{2} m_i \vec{v}_i^2(t) = \frac{1}{2} N_{gl} k_B T(t) \tag{3.19}$$

where k_B is the Boltzmann's constant and N_{gl} the number of internal degrees of freedom of the system. Because the instantaneous temperature is

directly related to the atomic internal velocities, mantaining the temperature constant in MD simulations requires imposing some control on the rate of change of these velocities, and thus thermostat algorithms require a modification of Newton's equations.

The Berendsen [77] method for the temperature control mimics weak coupling (scale system variable in direction of desired derived value) with first-order kinetics to an external bath with given temperature T_0. The effect is that a deviation of the system temperature from T_0 is slowly corrected through the following equation:

$$\frac{dT}{dt} = \frac{T_0 - T(t)}{\tau} \tag{3.20}$$

where $T(t)$ is the system temperature and τ the time constant. This algorithm has the advantage that the strength of the coupling can be varied by varying the time costant τ; a too big τ (too weak coupling) would result in a non efficient conservation of the temperature along the simulation, while a too small τ (too strong coupling) would introduce a too strong perturbation on the velocities propagation. Consequently, a proper value of τ has to provide a good balance between these two extremes. Usually, the time constant can thus be taken quite short for equilibration runs, but much longer (about 0.5 ps) for production runs.

The Berendsen thermostat suppresses the fluctuations of the kinetic energy. This means that one does not generate a proper canonical ensemble, so rigorously the sampling will be incorrect. This error scales with 1/N, so for very large systems most ensemble averages will not be affected significantly, except for the distribution of the kinetic energy itself. However, fluctuation properties, such as the heat capacity, will be affected. A similar thermostat which does produce a correct ensemble is the velocity rescaling thermostat. The heat flow into or out of the system is affected by scaling the velocities of each particle every step, with a time-dependent factor λ:

$$\Delta E_{kin}(t) = [\lambda^2 - 1]\frac{1}{2} N_{gl} k_B T(t) \tag{3.21}$$

$$\lambda = \left[1 + \frac{\Delta t}{\tau_t}\left(\frac{T_0}{T_t} - 1\right)\right]^{-1/2} \tag{3.22}$$

where $\tau_t = \frac{\tau k_B}{2C_V}$; τ_t is different from τ since the kinetic energy change caused by scaling the velocities is partly redistributed between kinetic and potential energy. Hence, the change in temperature is less than the scaling energy.

So, in conclusion, the Berendsen weak-coupling scheme is extremely efficient for relaxing a system to the target temperature, but once the system has reached the equilibrium it might be more important to probe a correct canonical ensemble, and this is the case of the Nosé-Hoover algorithm. In fact, in the Nosé-Hoover scheme,[78, 79] the system Hamiltonian is extended by introducing a thermal reservoir and a friction term in the equations of motion. The friction parameter (also called "heat bath" variable) is a fully

dynamic quantity with its own momentum and equation of motion. In this formulation, the time derivative is calculated from the difference between the current kinetic energy and the reference temperature:

$$\frac{d^2\vec{r}_i}{dt^2} = \frac{\vec{F}_i}{m_i} - \frac{p\xi}{Q}\frac{d\vec{r}_i}{dt} \tag{3.23}$$

where the equation of motion for the friction parameter ξ is:

$$\frac{dp\xi}{dt} = \frac{1}{Q}(T - T_0) \tag{3.24}$$

where T_0 is the reference temperature and T the current instantaneous temperature of the system. The strength of the coupling is determined by the "mass parameter" of the reservoir Q in combination with the reference temperature. The difference between the weak-coupling scheme and the Nosé-Hoover algorithm is that the former produces a strongly damped exponential relaxation, while the latter approach an oscillatory relaxation. The actual time it takes to relax with Nosé-Hoover coupling is several times larger than the period of the oscillations that one selects. These oscillations (in contrast to exponential relaxation) also means that the time constant normally should be 4-5 times larger than the relaxation time used with weak coupling.

In the same spirit of the temperature coupling, the system can also be coupled to a "pressure bath". The Berendsen scheme is based on a first-order kinetic relaxation of the pressure towards a given reference pressure P_0:

$$\frac{dP}{dt} = \frac{P_0 - P(t)}{\tau} \tag{3.25}$$

where $P(t)$ is the current instantaneous pressure of the system and P_0 the reference pressure. It should be noted that although the Berendsen pressure control scheme yields a simulation with the correct average pressure, it does not yield the exact NPT ensemble.

3.2 Polarizable Molecular Dynamics

Polarization plays a key role in the energetic of molecular systems. Generally, MD studies do not treat electronic polarizability explicitly, but only implicitly using effective charges, dielectric permittivities or continuum electrostatic models. However, when dealing with high charge species, such as Ln(III) ions investigated in this work, it is well-known from the literature that explicit polarization has to be included in the classical force field. In particular, in several MD studies on Ln(III) ions in water it was found that polarizing effects should be taken into account in order to obtain an accurate determination of their hydration properties.[136, 137, 138] This is due to the fact that the high charge of Ln(III) cations has a strong polarizing effect on the surrounding water molecules. One of the goal of this work is to carry out

classical MD simulations of Ln(III) ions in a protic IL, the ethylammonium nitrate; due to the similarities of ethylammonium nitrate and water it will be fundamental to determine the importance of using a polarizable force field when carrying out MD simulations of this solvent.

If the polarization is not taken into account, the electrostatic energy corresponds only to a pure Coulomb interaction between point charges:

$$V_{elec} = \frac{1}{2} \sum_{pairs(ij)} \frac{q_i q_j}{r_{ij}} \tag{3.26}$$

In order to account for polarizability in the classical force field, one of the possible strategy is to assign isotropic polarizabilities and induce dipoles at each atom site. The polarization term, accounting for the charge-dipole and dipole-dipole energy, is described by the following equation [82]:

$$V_{pol} = \sum_{ij} [(q^i \mu_\alpha^j g^{ij}(r^{ij}) - (q^i \mu_\alpha^i g^{ji}(r^{ij})) \mathbb{T}_\alpha^{ij} - \mu_\alpha^j \mu_\beta^j \mathbb{T}_{\alpha\beta}^{ji}] + \sum_i (\frac{1}{2\alpha^i} |\mu|^2) \tag{3.27}$$

where q are the atomic point charges, μ are the induced dipoles centered on atoms, α is the atomic polarizability, T_α and $T_{\alpha\beta}$ are the charge-dipole and dipole-dipole interaction tensors and $g^{ji}(r^{ij})$ are the Tang-Toennies functions aimed at including the short range damping effects. The set of induced dipoles μ^i is treated as 3N additional degrees of freedom of the systems. The dipoles are determined at each time step by minimization of the total polarization energy and they depend on the positions of all the atoms at the corresponding time; therefore the polarization part of the potential is a many-body term.

3.3 The global MD algorithm

A general MD algorithm propagates positions and velocities of all atoms in the system starting from the initial configuration through an iterative procedure that can be decomposed in three simple steps (see the global flow scheme below): the force calculation, the numerical integration of Newton's equations of motion and the writing in an output file of the updated positions and velocities. In the iterative procedure these three actions are repeated at each MD step.

1. Input and Initial Conditions

Initial positions $\vec{r}$ of all atoms in the system.
Initial velocities $\vec{v}$ of all atoms in the system.
Potential interaction V as a function of $\vec{r}$ and $\vec{v}$.

$\Downarrow$

2. Force Calculation

The force on any atom

$$\vec{F}_i = -\frac{\partial V}{\partial \vec{r}_i}$$

is computed by calculating the force between non-bonded atom pairs:

$$\vec{F}_i = \sum_j \vec{F}_{ij}$$

plus the force due to bonded interactions (which may depend on 1-4 atoms), plus restraining and/or external forces.
The potential and kinetic energies and the pressure tensor are computed.

$\Downarrow$

3. Update configuration

The movement of the atoms is simulated by numerically solving Newton's equations of motion

$$\frac{\vec{F}_i}{m_i} = \frac{d^2\vec{r}_i}{dt^2}$$

or

$$\frac{d\vec{r}_i}{dt} = \vec{v}_i; \vec{a}_i = \frac{\vec{F}_i}{m_i}$$

$\Downarrow$

4. Output

Write positions, velocities, energies, temperature, pressure, etc.

repeat 2,3,4 for the required number of steps.

If some constraints need to be added, for example if some covalent bonds need to be freezed, the iterative procedure has to be modified in order to satisfy the required costraints. To this end, as shown in the update algorithm flow scheme, at each MD step the velocities and positions obtained from the unconstrained dynamics are rescaled in order to satisfy all the imposed constraints.

Update algorithm

Given:
Positions $\vec{r}$ of all atoms at time t,
Velocities $\vec{v}$ of all atoms at time $t - \frac{\Delta t}{2}$,
Accelerations $\frac{\vec{F}}{m}$ on all atoms at time t,
(Forces are computed disregarding any constraints)
Total kinetic energy and virial.

$\Downarrow$

1. Compute the scaling factors μ and λ

$\Downarrow$

2. Update and scale velocities:
$\vec{v}' = \lambda(\vec{v} + a\Delta t)$

$\Downarrow$

3. Compute new uncostrained coordinates: $\vec{r}' = \vec{r} + \vec{v}'\Delta t$

$\Downarrow$

4. Apply constraint algorithm to coordinates (SHAKE or LINCS algorithms);
new coordinates $\vec{r}''$

$\Downarrow$

5. Correct velocities for constraints: $\vec{v} = (\vec{r}'' - \vec{r})/(\Delta t)$

$\Downarrow$

6. Scale coordinates and box dimensions: $\vec{r} = \mu\vec{r}''$;$\mathbf{b} = \mu\mathbf{b}$

3.4 Post-processing analysis

Independently of the kind of MD simulations performed, i.e classical, polarizable, ab-initio, the trajectory obtained at the end of the simulation represents a set of microscopic configurations explored by the system in the given ensemble. With the assumption that our system explored enough the conformational space, meaning that we are on the range of validity of the ergodic hypothesis, the statistical properties of the system can be correctly evaluated as ensemble averages.

Radial, angular, combined and spatial distribution functions (vide infra) are indeed example of properties calculated averaging over all the conformations explored by the system.

Chapter 4

Methods

4.1 X-ray absorption spectroscopy

4.1.1 X-ray absorption measurements

All X-ray absorption measurements have been performed in transmission mode at room temperature at the ELETTRA Synchrotron (Italy) on the beamline 11.1,[83] that is designed to cover a wide energy range from 2.4 to 27 keV, and at the European Synchrotron Radiation Facility ESRF on the BM23 beamline (energy range 5.0 - 75.0 keV). Generally, the experimental set-up for this kind of experiments is composed of an optical apparatus, containing a monochromator and one or more mirrors, and a measurement apparatus, containing sample holders and detectors.

Monochromators. The monochromator consists of a couple of crystals, each cut parallel to the same (*hkl*) plane. The former is used to select the energy of the incident photons by means of Bragg's law ($2d_{hkl} sen\theta = n\lambda$), i.e by changing the angle of the crystals, a different energy is selected, while the latter is used to keep the outgoing beam parallel to the incident one. The double-crystal monochromator allows also to reduce high order harmonic contaminations ($n = 2, 3, 4$ .... in the Bragg's law), which have energies that may interfere with data collection, by slightly tilting the second crystal from the parallel alignment using a piezo-electric crystal. This is the so-called *detuning* procedure. The smaller is the d-spacing, the more efficient is the monochromator crystal for progressively higher energy X-ray reflection. In particular, in our experiments, we have used Si(111), Si(311) or Si(511) double-crystal monochromators, having a d-spacing of 3.1356 Å, 1.6375 Å and 1.0452 Å, respectively.

Detectors. The transmission geometry, which has been adopted in our experiments, allows to measure the direct absorption by the sample and requires the sample to be aligned perpendicular to the X-ray beam (see Figure 4.1). The most commonly used detectors for this acquisition mode are gas-filled ion chambers. The absorption is derived by measuring the intensity of the transmitted beam I_1 and that of the incident beam I_0, so at least two ion

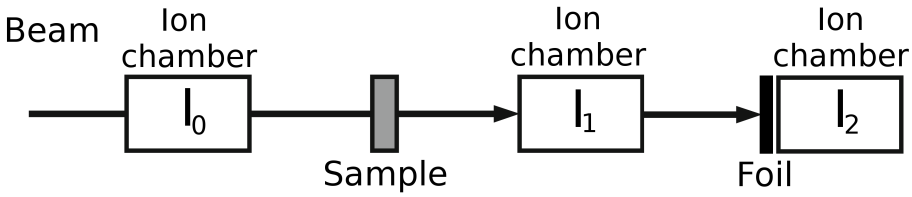

Figure 4.1: Schematic representation of the experimental setup for the XAS transmission mode.

chambers are necessary. The first chamber, filled with a gas mixture absorbing up to 20% of the incident beam, is placed before the sample, while the second one, filled with a gas mixture absorbing about 20-40% of the beam, is after the sample. Additionally, a reference metal foil of the same element is placed between the second and a third ion chamber for internal energy calibration. Several gas (N_2, Ne, Ar, Kr) or gas mixtures with He can be used, depending on the beam energy.

Also the fluorescence detection method is commonly used in XAS experiments; in this case the absorption is measured indirectly by detection of the fluorescent X-rays emitted when the core hole is filled. The intensity of the X-ray fluorescence is proportional to the number of adsorbed photons, but it is competing with other processes, such as Auger electrons. When the core hole is filled, the released energy can alternatively be used to eject Auger electrons, usually from the same shell. Therefore, the yield for emitting fluorescent X-rays varies considerably between 0 and 1, and it is higher for heavier elements.

Samples. As far as solid samples are concerned, the most common way to prepare them is to make pellets, by adding the right amount of sample powder fine grained and homogeneous to a binding/briquetting inhert agent, such as cellulose or boron nitride. The agent is added in order to make the pellet more stable and to reach a quantity of total product which is enough make the pellet. This pellet is normally held in a metal of teflon frame, between tape windows.

Liquid samples are normally measured in cells of the correct dimensions, formed by two windows that are separated by a Teflon spacer. The cell windows are transparent to X-rays and the material they are made of should not interact with the sample. They can be made of metals, polymers, ceramics or glasses and, among these, the commonly used materials are polymer films, such as polypropylene, and polymides. For our experiments, we have used the Kapton polymide film in all cases, as it is much stronger and can be used up to a temperature range of 250-320° C.

4.1.2 EXAFS data analysis

The EXAFS data analysis has been performed using the GNXAS code.[84] Selected configurations extracted from the MD simulations have been used

to calculate phase shifts, A(k,r) and ϕ(k,r), using muffin-tin potentials and advanced models for the exchange-correlation self-energy (Hedin-Lundqvist).[85] A complex potential has been used to account for inelastic losses of the photoelectron in the final state. EXAFS $\chi(k)$ theoretical signals have been calculated using eq. 2.6, where only two-body distributions have been taken into account. Indeed, as already described in Section 2.1, due to the structural disorder and to the high number of scattering atoms contributing to the total $\chi(k)$ signal, rather than using the usual discrete form of the EXAFS equation, the signal can be modelled as a function of the radial distribution functions, $g(r)$'s, calculated from MD simulations. Comparison between the experimental and theoretical curves on the one hand allows one to assess the reliability of theoretical framework used in the simulations and the structural results so obtained, on the other hand provides a useful starting model in the EXAFS analysis of disordered systems. During the minimization procedure the stuctural parameters are kept fixed, while the two non-structural ones, namely S_0^2 (which is a many-body amplitude reduction factor due to intrinsic losses) and E_0 (which aligns the experimental and theoretical energy scales) are optimized. Only in the case of Ce(III) in EAN system, a more complete analysis has been carried out, including both two-body (SS) and three-body (MS) distribution functions. The MS configurations have been extracted from the $g(r_1, r_2, \theta)$ distributions obtained from the MD simulation, and the EXAFS minimization has been carried out starting from these structural parameters and varying them less than 3% from the initial values. In all other systems, MS signals have not been taken into account for the EXAFS analysis, as their contribution has been found to be negligible. Note that more than 95% confidence intervals for the statistical errors are systematically obtained for all the least-square fits perfomed and shown in the present work.

4.2 Molecular Dynamics

4.2.1 Molecular dynamics details

As far as pure ILs and IL/water mixtures are concerned, Classical MD simulations have been carried out in the canonical ensemble (NVT) at room temperature (300 K) and atmospheric pressure using the DL_POLY package.[86] The choice of the present computational set-up is driven by the aim to investigate the properties of ILs and IL/water mixtures at ambient conditions and to compare with XAS experiments performed at 300 K and 1 atm. For all simulations, three dimensional periodic boundary conditions have been applied in order to avoid border effects that are unphysical for bulk systems. To deal with periodic boundary conditions all the atoms of the systems have been put in a cubic box. The size of each cubic simulation box has been chosen to reproduce the experimental density of the system (if available in the literature) or by equilibrating the system in the NPT ensemble at 300 K and 1 atm. In all cases the initial configuration was constructed by randomly

positioning the molecules in a very large cubic simulation box. Extensive equilibration runs were performed, comprising 10000 steps of initial energy minimization and a series of NPT runs at a very high pressure to compress the box volume and to finally reach the system experimental density. Then, the systems have been simulated in the NVT ensemble at 300 K, using a timestep of 1 fs and saving a configuration every 200 timesteps. On the one hand, the choice of the timestep is done in order to minimize the computational cost and be thus able to perform long simulations. On the other hand, an upper limit to the timestep value is fixed by the needing to correctly sample all atomic motions: the timestep has to be 20 times lower than the faster motions, i.e. the stretching of light atoms. In our simulations we systematically use the SHAKE algorithm to constrain all the bonds involving hydrogen atoms, and thus a timestep of 1 fs can be now used.

In order to obtain reliable equilibrated starting points, a first equilibration run in the NVT ensemble was carried out for each system, followed by production runs of different total time length according to each different system. The temperature was kept constant at 300 K using the Nosé-Hoover thermostat [87, 88] with a relaxation constant of 0.5 ps. As discussed in Section 3.1.7, the Nosé-Hoover thermostat and the 0.5 ps relaxation constant represent a very suitable choice to guarantee the reliability of the ensemble-average properties calculated from the simulations. A cut-off of 12 Å, larger enough for van der Waals interactions to go to zero and lower than half of the box edge length, was used to deal with nonbonded interactions, with the Ewald summation method to treat long-range electrostatic effects.[89] All the simulations have been carried out using the same general MD protocol. However, the total number of atoms, the total simulation time length and the force field employed depend on each simulated systems and they will be described in detail in the following Chapters.

As far as Ln(III) ions aqueous solutions and Ln(III) ions dissolved in ILs are concerned, a slightly different MD protocol has been adopted. In particular, for Ce(III) in EAN, we have carried out two different sets of MD simulations, the former including explicit polarization and the latter using a classical potential not including polarization effects. The MD procedure, together with the choice of the force fields, will be addressed in Chapter 8.

Force field. The force field used for IL cations was taken from Lopes and Pádua,[90, 91] which is one of the most widely used parametrizations in the area of IL modeling. In the Lopes and Pádua force field the parameters were obtained through different series of ab initio calculations concerning the geometry, force constants, torsion energy profiles and electrostatic charges distributions of the ions, and they were validated by comparison with experimental crystal structure and liquid density data. The model is transferable between different combinations of cation/anion, thus a large variety of ILs can be studied by MD simulations using this force field.

As far as the IL anions are concerned, the Br^- one was always modelled by means of the Lopes and Pádua force field, while the OPLS [92] model was em-

ployed for the I^- anion. The choice to combine Lopes and Pádua and OPLS resides on the fact that these force fields are fully compatible with each other as the former has been built starting from the latter.[90] In particular, in the case of the imidazolium based cation, the Lennard-Jones parameters for each atom type in the Lopes and Pádua force field were taken from the OPLS-AA parametrization of heterocyclic aromatic rings or aliphatic compounds.[90] It is important to stress that partial atomic charges are typically obtained from electronic structure calculations of the isolated ions in vacuum with the constraint of integer net charges of ±e on each ion, and this approach has been adopted also in the development of the Lopes and Pádua force field. However, the atomic charges can affect dynamic properties and the model with unit positive and negative charges on the cation and the anion has been found to predict slower diffusion of the ions compared to experiment, as demonstrated for example in liquid $[C_4mim][PF_6]$.[93] A possible strategy that has been proposed in the literature to overcome this problem is to employ fractional charges on the IL ions.[93] The reduction from the value of unity was rationalized as due to charge transfer between the ions and this procedure has proven to be beneficial for the simulation of transport properties. However, the advantage of the approach of Lopes and Pádua is the generality of the force field that can be used for many ILs, while if one wants to simulate the ions with reduced charges a new set of partial atomic charges has to be calculated for each cation-anion combination. The Lopes and Pádua force field [90, 91] has been also used for dicationic ILs, with a minor modification for the $[C_2(mim)_2]^{2+}$ and $[C_3(mim)_2]^{2+}$ dications, as explained later.

In the case of IL/water mixtures, the force field used for water is the SPC/E one.[94] Indeed, it is one of the most widespread model employed for water, as it appropriately reproduces the structural and dynamics properties of liquid water.[95] In such binary mixtures of ILs and water, since there are several potentials available in the literature for the IL anions, the choice of the Lennard-Jones parameters describing the anion-water interaction has been made on the basis of the comparison with the EXAFS experimental data. In fact, both the IL and water force fields present in the literature have been generally obtained and tested for the pure components, and their transferability to the mixtures has not been assessed.

Lennard-Jones parameters for all of the different atom types have been obtained using the standard Lorentz-Berthelot combining rules, in which the arithmetic average is used to calculate σ_{ij}, while the geometric average is used to calculate ϵ_{ij}:

$$\sigma_{ij} = \frac{\sigma_{ii} + \sigma_{jj}}{2} \tag{4.1}$$

$$\epsilon_{ij} = \sqrt{\epsilon_{ii}\epsilon_{jj}} \tag{4.2}$$

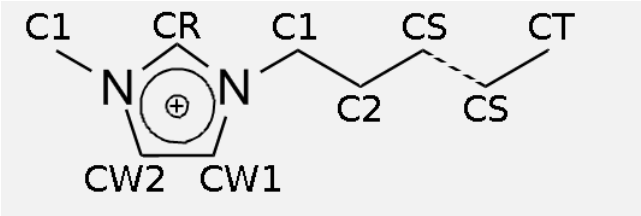

Figure 4.2: Molecular structure of 1-alkyl-3-methylimidazolium IL cation, $[C_n mim]^+$, and atom labeling as used in this work

4.2.2 Structural analysis

The structural properties of the investigated systems are described in terms of radial distribution functions, $g_{ab}(r)$:

$$g_{ab}(r) = \frac{\langle \rho_b(r) \rangle}{\rho_b^{ave}} = \frac{1}{N_a \rho_b^{ave}} \sum_{i \in a}^{N_a} \sum_{i \in b}^{N_b} \frac{\delta(r_{ij} - r)}{4\pi r^2} \tag{4.3}$$

where $\langle \rho_b(r) \rangle$ is the particle density of type b at a distance r around type a and ρ_b^{ave} is the average number density of type b particles. N_a and N_b are the number of a and b particles and r_{ij} is the distance. Now, the coordination number N of b particles around a can be calculated by integration of the $g_{ab}(r)$'s up to the first minimum, using the following equation:

$$N_b = 4\pi\rho_b \int_0^{R_{min}} g_{ab}(r) r^2 dr \tag{4.4}$$

Here R_{min} is the first minimum of the $g_{ab}(r)$ and ρ_b is the atomic density of b particles in the system. It should be noted that when evaluating the structural results obtained for systems having different densities, comparison of the $g(r)$'s can be misleading as the peak intensity strongly depends on the density and thus is not related to the number of atoms at a given distance from the reference species. Therefore, it is necessary to multiply the $g_{ab}(r)$ function by the numerical density ρ of the observed atoms b. Indeed, the $g(r)\rho$ functions allow one to appreciate the variation of the first shell coordination number as in this case the integral of the first peak is directly related to the number of atoms present in the first shell.

Combined radial/angular distribution functions, CDFs, have been calculated for pure IL systems to give information on the three-dimensional arrangement of molecules. In this analysis distances and angles stemming from a MD configuration are regarded as a 2-tuple, that is put into a two dimensional histogram. Simultaneous information on distances and angles can now be obtained. In particular, we have calculated the CDF between (i) the HCR-X distances and the ω_{HCR} angle formed by the CR-HCR and CR-X vectors and (ii) the HCR-X distances and the θ_{HCR} angle formed by the normal vector to the ring plane and the ring-center-X vector. The definition of the ω_{HCR} and θ_{HCR} angles is shown in Figures 4.3 and 4.4, respectively. Note

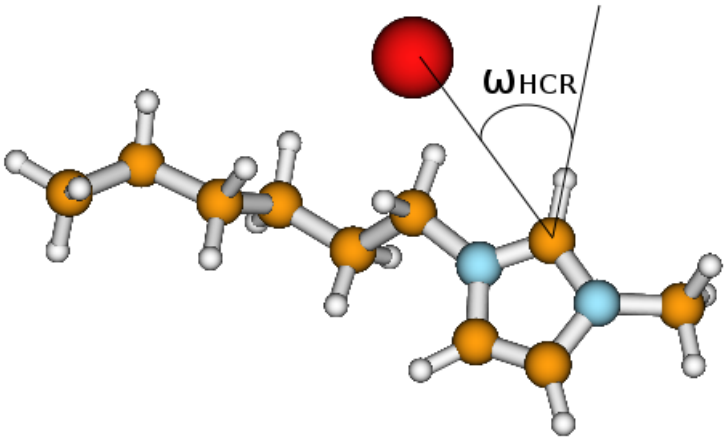

Figure 4.3: Definition of the ω_{HCR} angle used for the combined distribution function, CDF, calculation.

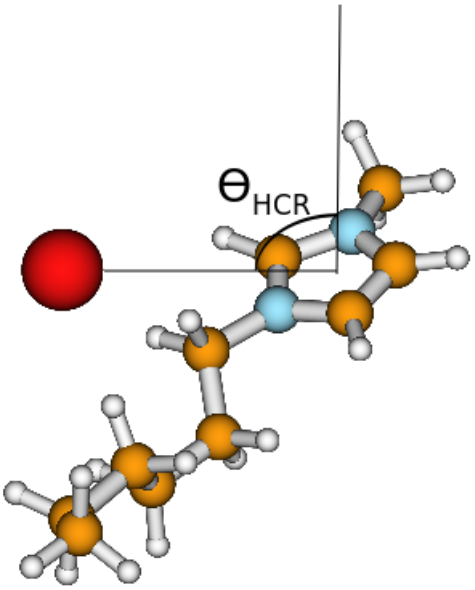

Figure 4.4: Definition of the θ_{HCR} angle used for the combined distribution function, CDF, calculation.

that the same analysis have been also computed by considering the other two hydrogen atoms (HCW1 and HCW2) of the imidazolium ring (see Figure 4.2 for atom labeling definition). Additional insight on the three-dimensional arrangement have been obtained from the calculation of the spatial distribution functions, SDFs. The 3D-isosurfaces are surfaces that pass through all areas with the same probability, i.e surfaces in which the density of the observed species is constant.

Moreover, in order to characterize the long-range organization of the systems, the X-ray theoretical structure factors $S(q)$ have been calculated from

the MD simulations using the following equation:[96, 49]

$$S(q) = \frac{\sum_{a=1}^{N}\sum_{b=1}^{N} x_a x_b f_a(q) f_b(q) H_{ab}(q)}{[\sum_{a=1}^{N} x_a f_a(q)]^2} \tag{4.5}$$

where x_a and x_b are the fractions of atomic species a and b, q is the momentum transfer, $f_a(q)$ and $f_b(q)$ are the atomic X-ray scattering factors of species a and b. Finally, $H_{ab}(q)$ is the partial structure factor, defined in terms of radial distribution functions, $g_{ab}(r)$, through the Fourier integral:

$$H_{ab}(q) = 4\pi\rho_0 \int_0^{r_{max}} r^2 (g_{ab}(r) - 1) \frac{sin(qr)}{qr} dr \tag{4.6}$$

where ρ_0 is the total number density of the system and r_{max} is the integration cutoff, choosen as half the box edge length.
The radial distribution functions and structure factors have been calculated using in-house written codes, while combined and spatial distribution functions have been performed using the TRAVIS software.[97]

Additionally, in the case of Ce(III) in EAN system we have developed a new tool to calculate CDFs giving information on the orientation of a given nitrate anion around the Ce(III) cation and on the geometry of the Ce(III) first coordination shell. Given three sets of particles (a, b, c), the CDF can be evaluated by means of the following equation:

$$P(r, \theta) = \sum_{t}^{N_t} \sum_{i}^{N_a} \sum_{j}^{CN} \sum_{k \neq j}^{CN} \frac{\delta(r_{ij} - r, \theta_{jik} - \theta)}{2 N_t N_a \rho_b V(r, \theta)} \tag{4.7}$$

where N_t is the number of time steps of the MD simulation, ρ_b is the average number density of b particles, r_{ij} is the a-b distance, θ_{jik} is the b-a-c angle, CN is the coordination number of a particle and $V(r, \theta)$ is the volume unit at distance r and angle θ. This new approach revealed itself to unambiguously assess the geometry of metal complexes existing in liquid media, and it has been also used to identify the geometry of Ln(III) first shell complexes in water.

Chapter 5

Structural properties of 1-alkyl-3-methylimidazolium halide ionic liquids

The knowledge of the IL structure is a topic of active research, and numerous experimental and theoretical techniques have been employed to this end. One of the most important structural information is the relative position between anion and cation comprising the bulk liquid. In previous investigations on various imidazolium-based ILs it has been found that the structure of ILs changes depending on the type of anions, such as Br^- and BF_4^-.[19, 98, 99] By contrast several theoretical and experimental studies have proposed that the structural differences are very small for different anion types.[100, 101, 102] Thus, this issue is still unresolved and further studies are needed to understand the relative position between the IL anion and cation. For these reasons, in the first step of this work, we have decided to study two alkylimidazolium-based ILs having two different halide ions (Br^- and I^-) as counterparts, namely 1-hexyl-3-methylimidazolium bromide ([C_6mim]Br) and 1-hexyl-3-methylimidazolium iodide ([C_6mim]I). It is also well-known from the literature that the anion-cation interactions can be influenced by the length of the lateral chain attached to the imidazolium ring of the cation and, in order to address this issue, we have investigated in the second step of the work four alkylimidazolium-based ILs with different alkyl chain length, but having the same anion as counterpart, namely [$C_n$mim]Br (with n = 5, 6, 8, 10). Figure 5.1 shows the molecular structure of the $[C_n\text{mim}]^+$ IL cation, together with the atom labeling used to describe the structural results.

5.1 Experimental Methods

X-ray absorption measurements. [$C_n$mim]Br (with n = 5, 6, 8, 10) and [C_6mim]I ILs were purchased from Iolitec GmbH with a stated purity of $>$ 99%. They were dried in vacuum for about 48 h and the final water content measured by Karl-Fischer titration was found to be between 200 and 300 ppm for the different samples. The Br K-edge XAS measurements of

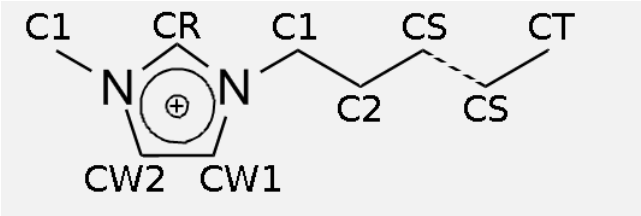

Figure 5.1: Molecular structure of 1-alkyl-3-methylimidazolium IL cation, $[C_n mim]^+$. CR is the carbon atom of the imidazolium ring between the two nitrogen atoms, while CWs are the two ring carbon atoms bonded to each other and to a nitrogen atom. C1 refers to the first carbon atom in the alkyl side chain, C2 to the second carbon atom, CSs are the carbon atoms located at least two bonds from the ring, and CT is the terminal carbon atom of the side chain.

$[C_n mim]$Br ILs were performed in transmission mode at room temperature at the ELETTRA Synchrotron (Italy) on the beamline 11.1.[83] Spectra were recorded using a Si(111) double crystal monochromator slightly detuned during data acquisition, putting the samples in cells with Kapton windows. The storage ring was running at 2 GeV energy with an optimal storage beam current between 300 and 130 mA.

The I K-edge XAS spectrum of $[C_6 mim]$I was collected in transmission mode at room temperature at the BM23 beamline of the European Synchrotron Radiation Facility ESRF. In this case the monochromator was equipped with two flat Si(311) crystals and to reduce harmonic contamination, which is weak at the I K edge, the crystals were kept slightly detuned with a feedback system. The storage ring was operating at 2 GeV with a typical beam current of 310 mA. The $[C_6 mim]$I sample was placed in a cell with Kapton windows and a Teflon spacer of 1 mm under nitrogen flux.

Molecular Dynamics details. Classical MD simulations of $[C_n mim]$Br (with $n = 5, 6, 8, 10$) and $[C_6 mim]$I have been carried out in the NVT ensemble at 300 K using the DL_POLY package,[86] for a total production time of 10 ns. The Lopes and Pádua force field has been used for the $[C_n mim]^+$ cations and for Br^-,[90, 91] while the OPLS model was employed for the I^- ion.[92] The simulated cubic boxes were composed in all cases of 500 ion pairs and the box edge lengths employed were 53.53 Å, 55.05 Å, 58.02 Å, 61.28 Å, and 56.90 Å for $[C_5 mim]$Br, $[C_6 mim]$Br, $[C_8 mim]$Br, $[C_{10} mim]$Br and $[C_6 mim]$I, respectively. These values have been chosen to reproduce the experimental density of the investigated systems, with the exception of $[C_{10} mim]$Br for which the box edge length has been obtained by equilibrating the system in the NPT ensemble at 300 K and 1 atm for about 5 ns. All the details of the MD protocol employed have been already described in Chapter 4.

5.2 $[C_6 mim]$Br *vs* $[C_6 mim]$I: the effect of the halide on the IL structure

2D organization of IL ion pairs. In order to shed light on the structural properties of $[C_6 mim]$Br and $[C_6 mim]$I, we have calculated the radial

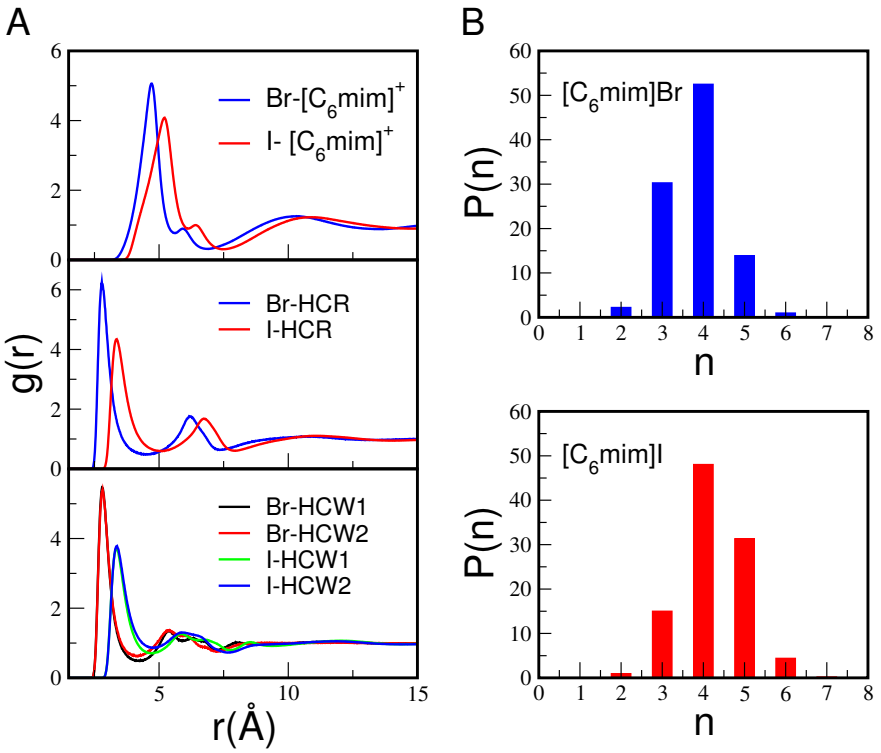

Figure 5.2: (A) Radial distribution functions, $g(r)$'s, and (B) instantaneous X-[C_6mim]$^+$ coordination number (n) distributions, expressed in percentage, calculated from the MD simulations of [C_6mim]Br and [C_6mim]I. In the (A) panels the following $g(r)$'s are reported: X-[C_6mim]$^+$ $g(r)$'s calculated between the X$^-$ ion and the ring geometrical center of the [C_6mim]$^+$ cation (top), X-HCR $g(r)$'s (middle), X-HCW1 and X-HCW2 $g(r)$'s (bottom). HCR, HCW1 and HCW2 are the three hydrogen atoms of the imidazolium ring.

distribution functions, $g(r)$'s, of a selected subset of atoms from the MD trajectories. All of the calculated $g(r)$'s are shown in Figures 5.2 and 5.3, while the first peak positions (r), the coordination numbers (N) and the cutoff distances used in the calculation of N are listed in Table 5.1. Note that in all cases the cutoff distance has been chosen as the position of the $g(r)$ first minimum. The general ordering of anions and cations can be evinced from the X-[C_6mim]$^+$ $g(r)$'s, calculated between the halide ion (X) and the ring geometrical center of the imidazolium cation, and shown in the top (A) panel of Figure 5.2. The X-[C_6mim]$^+$ $g(r)$'s show a well-defined first coordination shell in both [C_6mim]Br and [C_6mim]I ILs, and the first peak maximum is at 4.73 and 5.21 Å for the Br$^-$ and the I$^-$ ions, respectively. The fact that the I$^-$ ion coordinates the cation at longer distances as compared to the Br$^-$ one is not surprising given the ionic radii difference of the two ions. Moreover, inspection of Table 5.1 reveals that also the X-[C_6mim]$^+$ coordination number increases in going from the Br$^-$ to the I$^-$ ion. The N value represents the average number of imidazolium cations that are in the first coordination shell of the halide ion. However, it is also possible to define an instantaneous X-[C_6mim]$^+$ coordination number, as the number of anions around the [C_6mim]$^+$ cation at a distance shorter than the X-[C_6mim]$^+$ $g(r)$ first minimum at a given simulation step, and to analyze its variation along

	Br-Y			I-Y		
Y	r(Å)	N	cutoff(Å)	r(Å)	N	cutoff(Å)
$[C_6mim]^+$	4.73	3.7	5.60	5.21	4.2	6.13
HCR	2.79	1.5	4.47	3.34	1.8	5.00
HCW1	2.80	2.2	4.20	3.35	1.4	4.75
HCW2	2.80	2.2	4.20	3.37	1.6	4.86
H1	2.97	6.3	4.09	3.53	7.6	4.60
H2	3.08	1.9	4.23	3.60	2.2	4.70
CR	3.63	1.5	4.50	4.10	1.8	5.06
CW	3.70	2.5	4.34	4.22	3.4	4.94
C1	3.76	6.9	6.21	4.25	8.1	6.82
C2	3.92	1.3	4.56	4.43	4.0	6.98
N	4.16	6.6	5.51	4.69	6.9	6.10

Table 5.1: Structural parameters of the radial distribution functions, $g(r)$'s, calculated from the MD simulations of $[C_6mim]Br$ and $[C_6mim]I$. r is the position of the $g(r)$ first peak maximum, while N is the coordination number calculated by integration of the $g(r)$ up to the cutoff distance, chosen as the $g(r)$ first minimum. The cutoff distances used in the calculation of N are also reported.

the simulation time. The probabilities (in percentage), $P(n)$, for the different coordination numbers to be observed in the simulation are reported in the (B) panels of Figure 5.2 and show that the most probable configuration is a 4-coordinated species for both $[C_6mim]Br$ and $[C_6mim]I$ ILs. However, the Br-$[C_6mim]^+$ and I-$[C_6mim]^+$ instantaneous coordination numbers fluctuate in the range 2-6, and the distribution is shifted towards larger n values for $[C_6mim]I$; the second favored configurations are a 3-coordinated and a 5-coordinated species for bromide and iodide ions, respectively.

A more specific description of the interactions taking place between anions and cations can be gained by calculating all of the X-$[C_6mim]^+$ site-site $g(r)$'s. From this analysis it has been found that the anion forms the strongest interactions with the three hydrogen atoms of the imidazolium ring, HCR and HCWs (see Figure 5.1 for atom labeling). The X-HCR and X-HCWs $g(r)$'s are depicted in the middle and bottom (A) panels of Figure 5.2, respectively. In all cases the $g(r)$'s show a sharp first shell peak, followed by other lower intensity peaks, and the Br-H* $g(r)$'s (with H*=HCR, HCW1, HCW2) are found at shorter distances as compared to the I-H* ones. Moreover, the X-HCR $g(r)$ first peak is more structured and its intensity slightly higher with respect to the X-HCW $g(r)$ first peaks in both $[C_6mim]Br$ and $[C_6mim]I$ ILs. This is due to the fact that HCR is the most acidic hydrogen atom of the imidazolium ring and it forms the strongest hydrogen bonds with the halide ion. This result is in line with the ability of the HCR atom to promote hydrogen bonds, as it has been previously pointed out in the literature. The hydrogen bond formed between HCR and the anion has been found to influence the IL macroscopic properties, and variations of the IL viscosities and melting

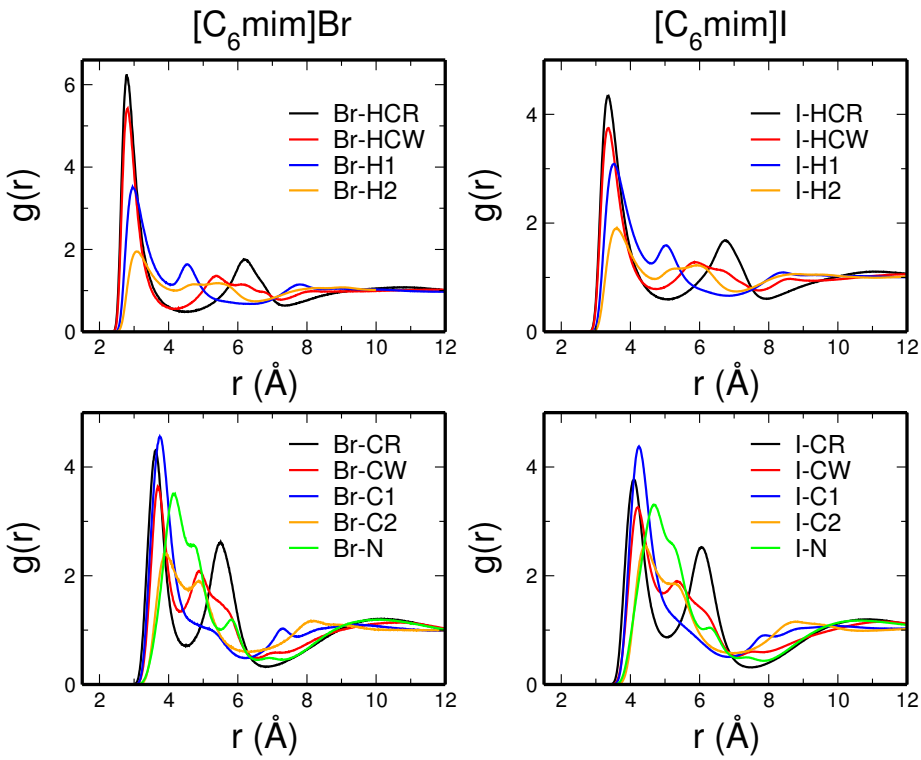

Figure 5.3: Radial distribution functions, $g(r)$'s, calculated from the MD simulations of [C$_6$mim]Br and [C$_6$mim]I. In the upper panels the X-H* $g(r)$'s are reported, while in the lower panels the X-C* and X-N $g(r)$'s.

points occur when the HCR atom is substituted by a methyl group.[103] As regards the X-HCW1 and X-HCW2 $g(r)$'s, they are practically identical at low distances, while some slight differences arise in the longer distance range. A last remarkable observation is that the presence of a second peak in the X-H* $g(r)$'s (more defined when considering the interaction with the HCR atom and oscillating in the case of the X-HCW1 and X-HCW2 $g(r)$'s) can be ascribed to halide ions interacting with hydrogen atoms on the opposite side of the imidazolium cation with respect to the hydrogen atom used in the $g(r)$ calculation, and not as the consequence of a second shell interaction.

EXAFS analysis of [C$_6$mim]I. The EXAFS spectra of liquid [C$_6$mim]Br and [C$_6$mim]I have been collected at room temperature and the experimental data have been analyzed starting from the $g(r)$'s calculated from the MD simulations. In fact, as described in Chapter 2, $\chi(k)$ EXAFS theoretical signals can be calculated by introducing the MD $g(r)$'s in eq. 2.6. Now, the comparison between the experimental and theoretical data allows us on the one hand to properly interpret the experimental spectra and, on the other hand, to assess the capability of the MD potentials to correctly reproduce the structural properties of the investigated systems. All the site-site $g(r)$'s involving the halide ion (that is the photoabsorber atom) are shown in the left panels of Figure 5.3 for the [C$_6$mim]Br and in the right ones for the [C$_6$mim]I. Note that all the $g(r)$'s involving the Br^- ion are shifted towards shorter distances

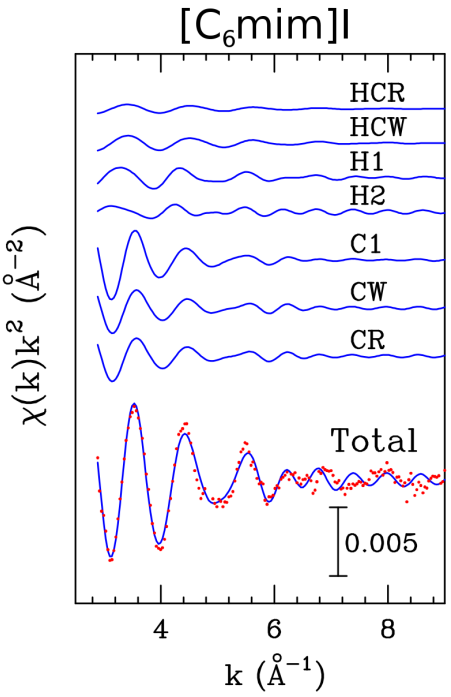

Figure 5.4: Comparison between the EXAFS experimental spectrum of [C_6mim]I (dotted red line) and the theoretical signal (solid blue line) calculated from the MD I-HCR, I-HCW, I-H1, I-H2, I-C1, I-CW and I-CR $g(r)$'s.

as compared to the I-X ones, and this strongly influences the amplitude of the EXAFS signal. Here, we report the EXAFS analysis of [C_6mim]I only, while that of [C_6mim]Br will be show in the following section together with the EXAFS analysis of the other [$C_n$mim]Br (with n = 5, 8, 10) ILs. The total $\chi(k)$ theoretical signal for [C_6mim]I has been calculated starting from the I-HCR, I-HCW, I-H1, I-H2, I-C1, I-CW and I-CR $g(r)$'s. The contribution associated with the C2, CS, CT and N atoms has been neglected, as the amplitude of the signals associated with high distance shells (above 4 Å) has been found to be negligible. Least-square fits of the EXAFS spectrum have been performed in the range k = 3.0 - 9.2 Å^{-1}, keeping fixed the MD structural parameters during the analysis. The minimization procedure has been applied only to the non-structural parameters to improve, as far as possible, the agreement between the experimental and theoretical spectra. In particular, from the minimization procedure, E_0 has been found to be 8 eV above the first inflection point of the spectrum, while S_0^2 is 0.9. The EXAFS analysis is shown in Figure 5.4: the first seven curves from the top are the I-H* and I-C* theoretical signals, while the remainder of the Figure shows the comparison between the experimental and total theoretical signals. As it can be seen, the agreement between theory and experiment is good, proving the correctness of the employed force field. This result is very significant since the combined use of EXAFS and MD represents a very strict test of the force field validity and, without such a comparison, the reliability of the structural results obtained from the simulations is hardly provable. Note that for k values higher than 7 Å^{-1} the signal to noise ratio is quite low being the

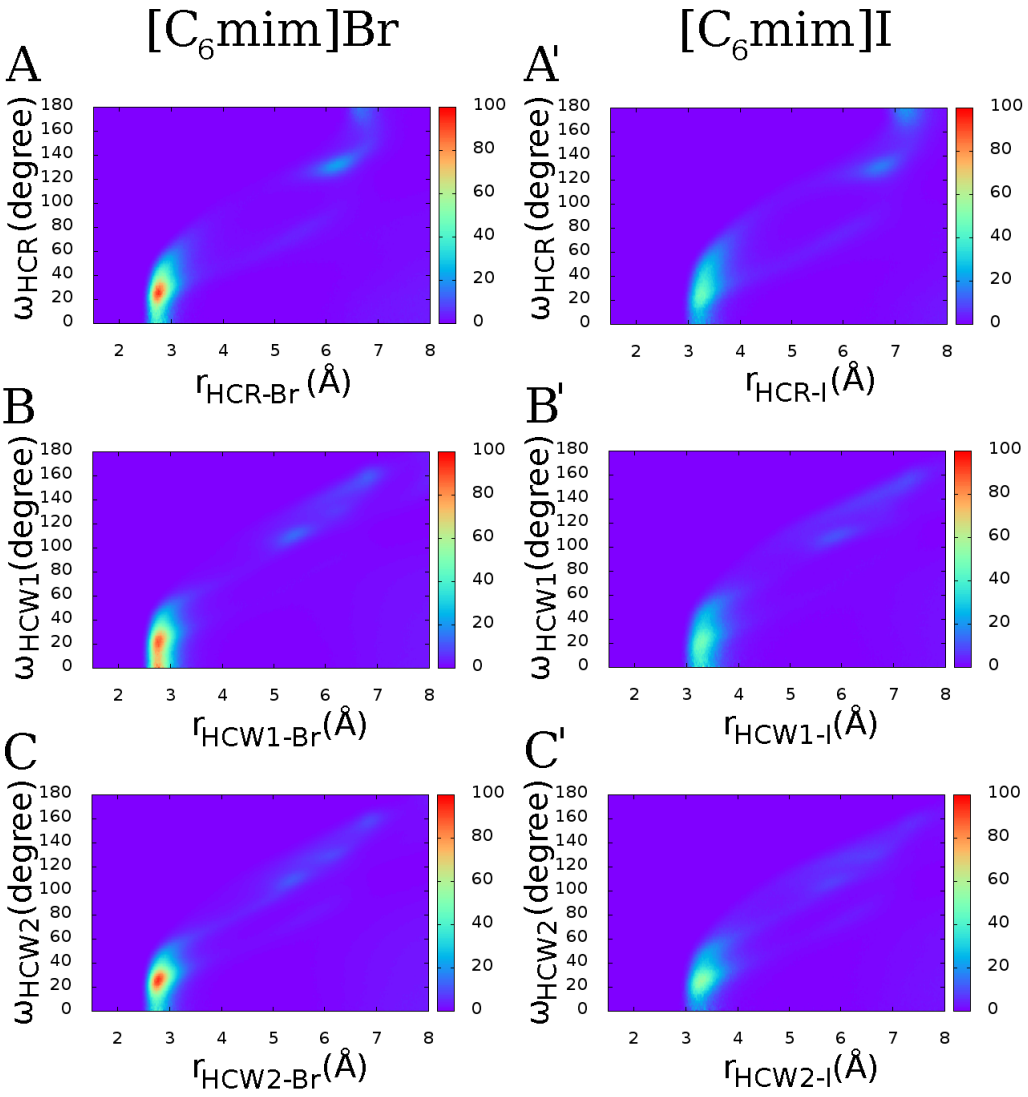

Figure 5.5: Combined distribution functions (CDFs) calculated from the MD simulations of [C6mim]Br (A, B, C) and [C6mim]I (A′, B′, C′). All the CDFs combine the H*-X distance with the ω angle formed between the C*-H* and C*-X vectors. (A,A′) H* = HCR and C* = CR. (B,B′) H* = HCW1 and C* = CW1. (C,C′) H* = HCW2 and C* = CW2.

amplitude of the scattering signal of the hydrogen and carbon atoms that are quite distant from the anion very low.

3D organization of IL ion pairs. Once the validity of the MD structural results has been proved for both [C6mim]Br (vide infra) and [C6mim]I on the basis of the comparison with the EXAFS experimental data, we have focused on the three-dimensional organization of the ions by calculating combined (CDFs) and spatial (SDFs) distribution functions from the MD trajectories. As described in the "Methods" chapter, CDFs are obtained by combining radial and angular distribution functions, giving simultaneous information on distances and angles. All of the calculated CDFs are depicted in Figures 5.5 and 5.6 for both [C6mim]Br (left panels) and [C6mim]I (right

panels). In particular, Figure 5.5 shows the CDFs between the H*-X $g(r)$ and the distribution function of the angle, ω, formed between the C*-H* and the C*-X vectors (see Figure 4.3 for angle definition). Note that H* = HCR, HCW1, HCW2 and C* = CR, CW1, CW2. As regards [C_6mim]Br IL, the CDF involving the HCR atom (panel A) shows a region of maximum intensity at a distance of about 2.8 Å and angles between 20° and 40°, corresponding to a configuration in which the Br^- ion is not located in front of the CR-HCR direction but forms an angle of about 30° with this direction. By contrast, when considering the HCW1 atom, the CDF (panel B) shows a larger region of maximum intensity (at a distance of 2.8 Å and angles between 0° and 30°) as compared to the CDF for the HCR atom, suggesting that the Br^- ion is forced towards the CW1-HCW1 direction, as a consequence of the steric hindrance of the hexyl chain in proximity of the HCW1 atom. Finally, the CDF for the HCW2 atom (panel C) is different from that of HCW1, while it is very similar to the HCR one. This means that, as in the case of the HCR atom, the bromide ion prefers to be tilted to about 30° with respect to the CW2-HCW2 direction. As far as the CDFs for [C_6mim]I are concerned (panels A′, B′ and C′ of Figure 5.5), we can see that the general trend is very similar to the one obtained for the Br^- ion: in fact, for both HCR and the two HCWs atoms, the regions of highest intensity are found at longer distances (about 3.3 Å), but the angle range is comparable. All together these results indicate that both the Br^- and the I^- ions arrange in a similar way with respect to the directions of the C*-H* bonds of the imidazolium ring. However, all of the CDFs involving the I^- ion have a much lower intensity as compared to the Br^- ones, meaning that the radial/angular correlation is lower due to the weaker interactions between the iodide ion and the three hydrogen atoms of the cation imidazolium ring.

The second type of CDFs, reported in Figure 5.6, is obtained by combining the H*-X $g(r)$ and the distribution function of the angle, θ, formed between the normal vector to the imidazolium ring plane and the intermolecular ring geometrical center-X vector (see Figure 4.4 for angle definition). This analysis gives information on the position of the anion with respect to the imidazolium ring plane, that can not be established from the previous calculated CDFs. Panels A, B and C of Figure 5.6 show the CDFs obtained for the HCR, HCW1 and HCW2 atoms of [C_6mim]Br, respectively. In the case of the HCR atom, we can see the highest correlation for the angles range 60°-120°, while for HCW1 and HCW2 atoms the region of maximum intensity is between 70° and 110°. This means that, in proximity of HCW1 and HCW2, the Br^- ion is more likely to form lower angles with the imidazolium ring plane. Note that in this case the CDFs concerning the two HCWs atoms are very similar to each other. Conversely, the CDFs calculated from the MD simulation of [C_6mim]I (panels A′, B′ and C′ of Figure 5.6) show more marked differences in going from the HCR to the HCWs atoms. In particular, when the iodide ion interacts with HCR, a symmetric function has been found, with two high intensity regions (the former between 40° and 70°, and the latter between 110° and 140°) and a minimum at 90°, clearly indicating that the

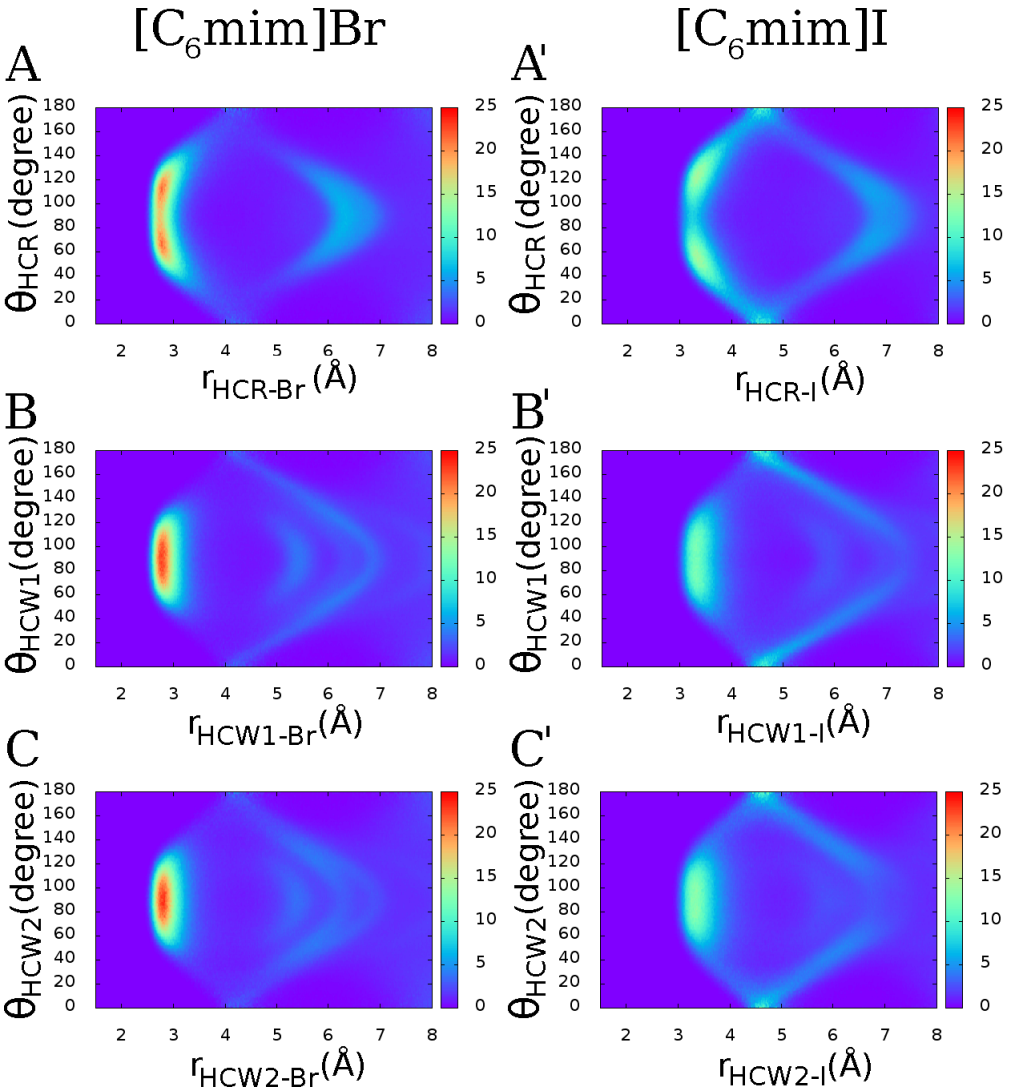

Figure 5.6: Combined distribution functions (CDFs) calculated from the MD simulations of [C_6mim]Br (A, B, C) and [C_6mim]I (A′, B′, C′). All the CDFs combine the H*-X distance with the θ angle formed between the normal vector to the imidazolium ring plane and the intermolecular ring geometrical center-X vector. (A,A′) H* = HCR. (B,B′) H* = HCW1. (C,C′) H* = HCW2.

anion prefers not to be coplanar with the plane of the imidazolium ring but to be above and below the plane itself. By contrast, in the case of HCW1 and HCW2, the I^- ion has the same probability of being either coplanar to the ring plane or not. In this case the anion forms with the plane angles up to about 20°. As previously noted for the CDFs concerning the ω angle, the CDFs of the I^- ion have lower intensity as compared to the Br^- ones.

Additional information on the 3D arrangement of anions with respect to the cation can be obtained from the SDFs shown in Figure 5.7, in which the isodensity surfaces of Br^- and I^- ions are colored orange and blue, respectively. Note that to properly compare the SDFs obtained for [C_6mim]Br and [C_6mim]I, we have reported the SDFs using the same absolute densities for both ILs. As expected, the association between anions and cations is

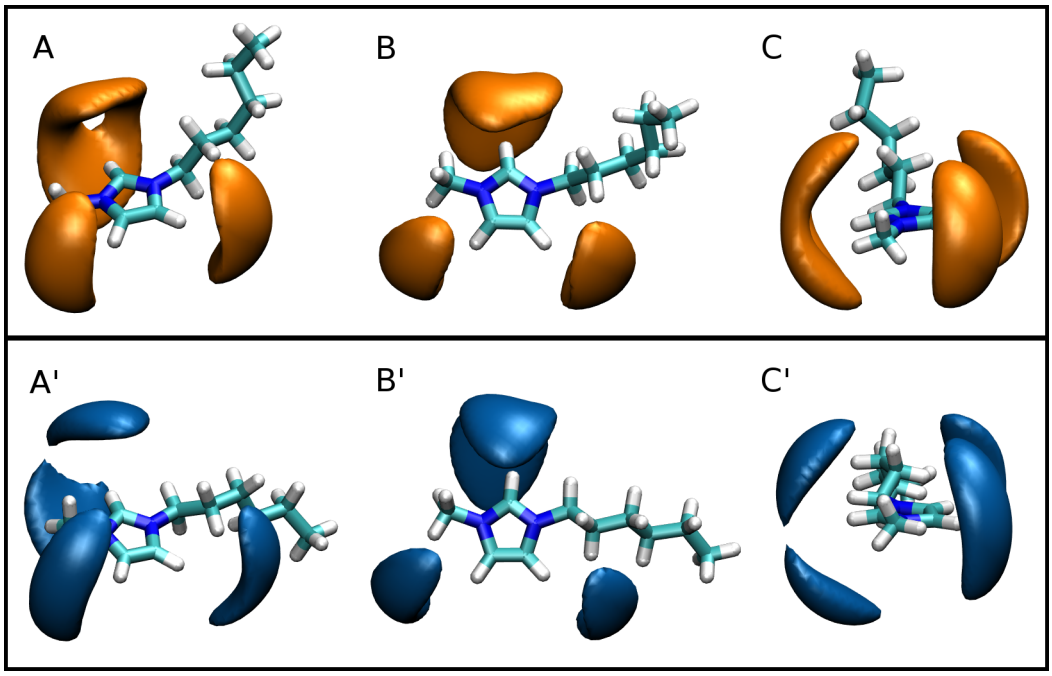

Figure 5.7: Spatial distribution functions (SDFs) of the halide ion around the $[C_6mim]^+$ cation calculated from the MD simulations of $[C_6mim]Br$ (A, B, C) and $[C_6mim]I$ (A′, B′, C′). The Br^- and I^- isosurfaces are colored orange and blue, respectively. (A, B, C) and (A′, B′, C′) represent three different orientations of the same SDF.

predominantly driven by interactions of both halide ions with the three hydrogen atoms of the imidazolium ring. However, the very interesting result is that the spatial arrangement of the Br^- and I^- ions in the proximity of the most acidic hydrogen atom of the imidazolium ring (HCR) is different: Br^- has the same probability to be above and below the ring plane or coplanar with the ring plane itself, while the I^- ion prefers not to be coplanar with the imidazolium ring plane. Conversely, the arrangement of both anions in the vicinity of the HCW1 and HCW2 atoms is very similar. Moreover, it can be noticed that the halide distributions near HCR are broader as compared to the ones near HCWs, and that halide ions interacting with HCR can occupy regions of space near the normal vector to the ring plane that are inaccessible to the anions in the proximity of HCWs atoms. All these findings are in line and confirm the results obtained from the CDF analysis. Finally, near HCW2 the anion isosurfaces are shifted towards the methyl group, while near HCW1 the steric hindrance of the hexyl chain hinders the approach of the anion.

It is interesting to observe that previous MD studies of alkylimidazolium-based ILs having the Cl^- ion as counterpart have revealed that, as in the case of Br^- and I^- ions, the chloride ion preferentially interacts with the three hydrogen atoms of the cation imidazolium ring.[29, 9, 104, 105, 98] In particular, the SDFs of the Cl^- ion around the cation look very similar to the ones found for the Br^- ion, while showing some differences with I^-. The different structural organization of Br^- and Cl^- as compared to I^- can be explained on the basis of their different ionic radii: Br^- and Cl^- ions are smaller and prefer to be located in the ring plane, while the larger I^- ion does not fit well in the

imidazolium plane and it is preferentially located above and below the plane itself.

5.3 [$C_n$mim]Br ILs: the effect of the alkyl chain length

The combined MD-EXAFS analysis on [C_6mim]Br and [C_6mim]I has revealed similarities and differences on the ion 3D arrangements. In particular, the structural organization of the Br^- and the I^- ions was found to differ near the most acidic hydrogen atom of the imidazolium ring, HCR. We are now interested in understanding how the anion-cation interactions are influenced by the length of the lateral chain attached to the imidazolium ring of the cation. To this end we have investigated four [$C_n$mim]-based ILs (with n = 5, 6, 8, 10) having the same anion (the bromide ion) as counterpart.

Short-range organization around the Br^- ion. The local coordination in [$C_n$mim]Br ILs as a function of the alkyl chain length (n = 2, 4, 6, 8, 10) has been experimentally studied by XAS spectroscopy.[106] Note that at room temperature the first two members of the series, [C_2mim]Br and [C_4mim]Br, are solid, while the others are liquid. It was found that all the members of the series, from the butyl to the decyl derivatives, have identical XAS spectra, thus indicating that the local arrangement around the Br^- ion is the same independently from the alkyl chain length, and that the structural organization of the [C_4mim]Br crystal phase is preserved also in the liquid phase at a local level. However, since XAS is a short-range-order technique that allows us to only probe the local structure around the photoabsorber atom, we have decided to also carry out MD simulations of [$C_n$mim]Br (with n = 5, 6, 8, 10) ILs. Indeed, the simulations give the possibility on the one hand to confirm the local organization emerged from the experimental data and, on the other, to obtain long-range structural information, thus providing a very global picture of the structural arrangement of the investigated systems. All the site-site $g(r)$'s involving the Br^- ion have been calculated from the MD trajectories and we show, as an example, the results obtained for [C_6mim]Br (see left panels of Figure 5.3). Starting from the MD $g(r)$'s we have calculated the EXAFS $\chi(k)$ theoretical signals associated with all the atoms around the Br^- ion, which is the photoabsorber atom, up to a cut-off distance of 4 Å through eq. 2.6. It is interesting to note that in this case the Br-C2 and Br-N $g(r)$ first peaks are below 4 Å and so the C2 and N atoms provide a detectable contribution to the EXAFS signal, contrary to what was observed in the case of [C_6mim]I. This is due to the fact that the bromide ion coordinates the cation at shorter distances as compared to the I^- one. The Br-Y $g(r)$'s used in the EXAFS analysis are shown in Figure 5.8 for all the [$C_n$mim]Br ILs, together with the calculated $\chi(k)$ theoretical signals. Note that, in order to properly compare different IL systems having different densities, the $g(r)$'s have been multiplied by the numerical density of the observed

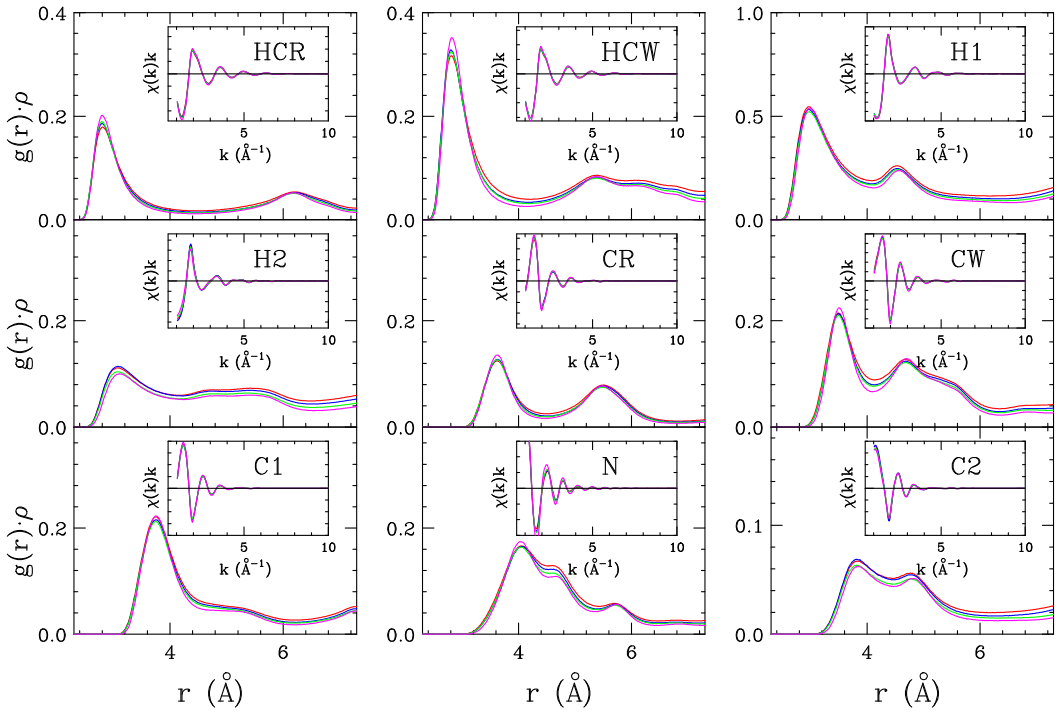

Figure 5.8: Br-Y radial distribution functions multiplied by the numerical density of the observed atoms, $g(r)\rho$'s, calculated from the MD simulations of [C_5mim]Br (red), [C_6mim]Br (blue), [C_8mim]Br (green) and [C_{10}mim]Br (magenta). The insets show the corresponding $\chi(k)$ theoretical signals obtained from the MD $g(r)$'s.

atoms, ρ. It can be seen that the Br-Y $g(r)\rho$'s are very similar for all the [$C_n$mim]Br ILs, while the EXAFS signals are identical. These results are in agreement with the previous XAS investigation [106] and confirm that the local coordination around the bromide ion is not influenced by the length of the alkyl chain. The presence of local ordered structures in [$C_n$mim]X ILs has been already suggested in the literature,[107] but here, for the first time, it has been demonstrated by using an experimental technique that directly probes the local coordination around the Br^- ion, in conjunction with MD simulations. Note that, since there is a similar short-range organization of anions and cations for all the investigated ILs, we can reasonably extend the local structural description (CDF and SDF analysis) previously obtained for [C_6mim]Br to [C_5mim]Br, [C_8mim]Br and [C_{10}mim]Br.

The Br-HCR, Br-HCW, Br-H1, Br-H2, Br-CR, Br-CW, Br-C1, Br-C2 and Br-N $\chi(k)$ theoretical signals shown in Figure 5.8 have been used to calculate a total EXAFS theoretical signal to be compared with the experimental one. The minimization has been carried out in the k range between 2.0 and 9.3 $Å^{-1}$ and during the analysis the MD structural parameters have been kept fixed, while only the non-structural parameters have been refined. E_0 was found to be 1 eV above the first inflection point of the spectrum, while S_0^2 was found to be 0.85, in all cases. The best-fit results are shown in Figure 5.9: there is a quite good agreement between the experimental and theoretical curves in all cases, demonstrating the validity of the theoretical framework.

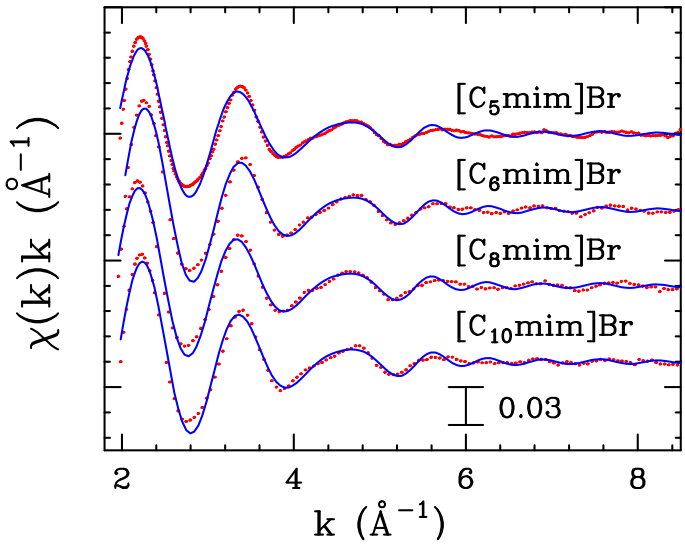

Figure 5.9: EXAFS experimental spectra (red dotted lines) of [$C_n$mim]Br (with n = 5, 6, 8, 10) ILs compared to the theoretical signals (solid blue lines) calculated from the MD $g(r)$'s.

Long-range organization. Even if the local organization around the Br^- ion, with anions and imidazolium head groups forming a local three-dimensional structure that is common to all the [$C_n$mim]Br ILs, is preserved, the length of the alkyl chain can influence the long-range organization of these systems. In order to address this issue we have calculated X-ray structure factors, $S(q)$, from the MD $g(r)$'s using eq. 4.5 and 4.6, and the results are shown in Figure 5.10. Two different regions, one above 1 $Å^{-1}$ and the other below 1 $Å^{-1}$, can be identified in the spectra. In the former region, all of the $S(q)$ curves show a very similar trend, and they are characterized by a distinct first peak in the q range 1.50 - 1.60 $Å^{-1}$, followed by two less intense peaks located at 3.65 and 5.50 $Å^{-1}$ and other less defined oscillations. These peaks are mostly due to intramolecular contributions and intermolecular short-range interactions. The fact that all of the $S(q)$ curves are very similar in this q region confirm our findings that anions and cations in [$C_n$mim]Br ILs form a short-range network that is the same regardless the length of the alkyl chain. Conversely, the $S(q)$'s are characterized by remarkable differences in the latter region (below 1 $Å^{-1}$). All the [$C_n$mim]Br ILs show a peak at this low q values, the so-called "prepeak", which is a fingerprint for the presence of long-range structural correlations. However, both the position and the intensity of this prepeak strongly depend on the alkyl chain length; in particular, the prepeak shifts towards shorter q values and its intensity becomes higher as the carbon atom number of the alkyl chain increases. The prepeak is centered at 0.45 $Å^{-1}$ for [C_5mim]Br and [C_6mim]Br, 0.31 $Å^{-1}$ for [C_8mim]Br and 0.30 $Å^{-1}$ for [C_{10}mim]Br. Similar results have been previously obtained for [C_8mim]Br from the large angle X-ray scattering experimental data in a combined MD and X-ray diffraction investigation of [C_8mim]Br and [C_8mim]Cl.[6] Moreover, similar trends of the $S(q)$ prepeak as

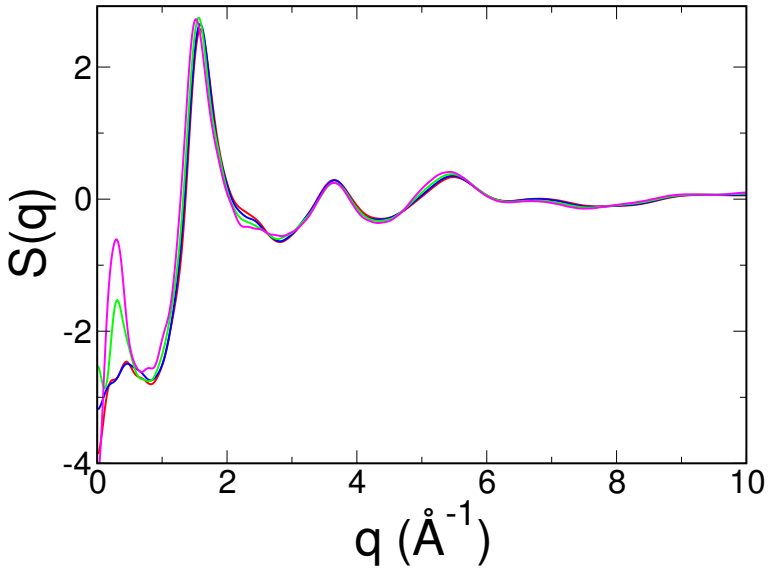

Figure 5.10: X-ray structure factors, $S(q)$, calculated from the MD simulations of [C_5mim]Br (red), [C_6mim]Br (blue), [C_8mim]Br (green) and [C_{10}mim]Br (magenta).

a function of the alkyl chain length have been found for imidazolium-based ILs with different anions both theoretically and experimentally.[19, 23, 25, 108] The understanding of the origin of this prepeak has been long debated in the literature and different explanations have been proposed. For some authors the prepeak is due to cationic tail interdigitation and the formation of micelles or more complex structures also in the case of imidazolium-based ILs with modest tail length such as [C_5mim]$^+$.[109, 110] However, recent studies by Margulis et al. and Hardacre et al. have suggested that the prepeak is a consequence of cationic anisotropy that imposes certain patterns of coordination

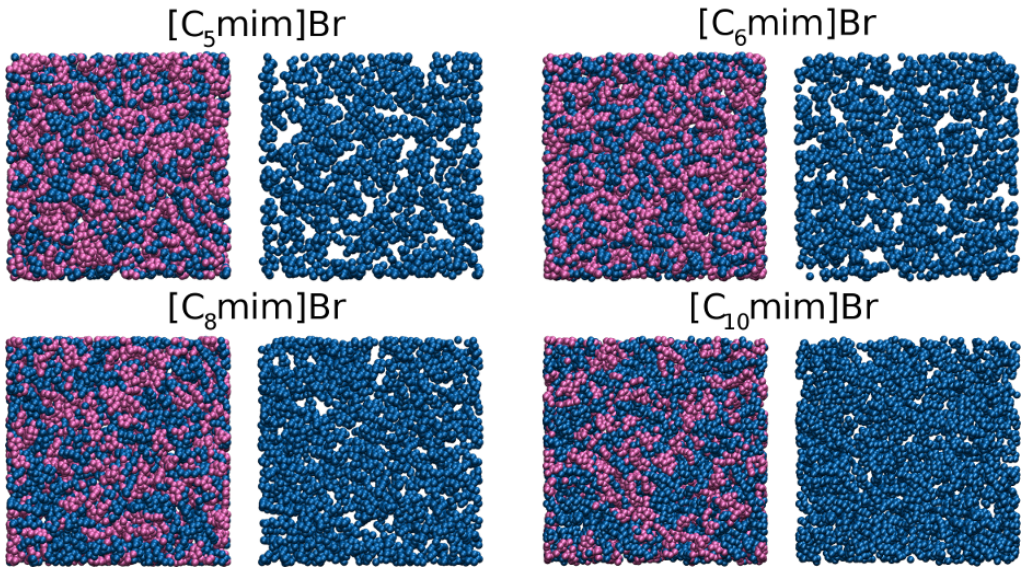

Figure 5.11: MD simulation snapshots of the [$C_n$mim]Br ILs. For each system we show the polar heads (magenta) together with the alkyl chains of the imidazolium cations (azure) on the left, while the alkyl chains only are reported on the right for better visualization.

along the direction of the longer alkyl chain and it is not due to complex long-range morphologies.[25, 108] The prepeak can be explained by much simpler considerations of solvation shell asymmetry as it emerges as a consequence of scattering contributions of the imidazolium head and not of the alkyl tails. Despite these different interpretations, the presence of a prepeak in the $S(q)$ function clearly indicates the existence of long-range structural correlations that are related to longer distances and are strengthened with increasing alkyl chain length. Due to the intrinsic amphiphilic nature of ILs the apolar alkyl tails tend to aggregate in the [$C_n$mim]Br IL family, while a tridimensional network of ionic channels is formed by imidazolium head groups and anions. In order to give a pictorial description of this behavior, we show in Figure 5.11 representative MD snapshots of the simulation boxes of [$C_n$mim]Br ILs. The hydrophilic channels crossing the box are clearly visible as white regions in the MD snapshots where only the hydrophobic portions of the systems are shown for better visualization. Moreover, with increasing alkyl chain length, the nonpolar aggregates become larger and more connected producing larger and larger separations among the polar box regions dominated by strong electrostatic forces.

Chapter 6

Monocationic imidazolium based IL/water mixtures

As already pointed out in the Introduction Chapter, among the most important applications of ILs there is their use in mixtures with water or organic solvents. For example, IL/organic solvent mixtures have been shown to have very promising performances in several areas, such as extraction of sulfur aromatic compounds from fuels and lithium-ion battery technology.[111, 112] Therefore, the knowledge of the behavior of ILs in binary liquid mixtures is important both from fundamental and applied aspects. In particular, here, the $[C_6mim]I$ IL largely characterized in the previous Chapter in its pure liquid state has been combined with water and six different $[C_6mim]I$/water mixtures have been investigated as a function of water concentration up to very high dilution, with the aim of providing a detailed microscopic characterization.

6.1 Experimental Methods

X-ray absorption measurements. $[C_6mim]I$ was purchased from Iolitec GmbH with a stated purity of $> 99\%$. The powder was dried under vacuum for 48 hours and a final water content of 200 ppm was measured by Karl-Fischer titration. $[C_6mim]I$/water mixtures with different IL/water molar ratios (1:x with x = 1, 3, 6, 12, 70, 200) were prepared by dissolving the appropriate amount of $[C_6mim]I$ in bidistilled water. A 0.1 M aqueous solution of tetramethylammonium iodide (TMAI), providing I^- ions in water, was also prepared. The I K-edge XAS spectra of the IL/water solutions, together with those of pure $[C_6mim]I$ and of a I^- aqueous solution were collected in transmission mode at room temperature at the BM23 beamline of the European Synchrotron Radiation Facility (ESRF). The samples were placed in cells with Kapton windows and Teflon spacers of 1.5 cm and during data acquisition the cells were kept under nitrogen flux to avoid contact with water. The monochromator was equipped with two flat Si(311) crystals and the storage ring was operating in 2/3 fill mode with a beam current of 200 mA after refill. The incident and transmitted fluxes were monitored by ionization

[C_6mim]I/water molar ratio	IL ion pairs	Water molecules	Simulation box edge (Å)
1:1	343	343	52.93
1:3	343	1029	53.88
1:6	216	1296	49.19
1:12	216	2592	53.84
1:70	64	4480	53.96
1:200	27	5400	55.57

Table 6.1: MD simulation details for the [C_6mim]I/water mixtures under investigation.

chambers filled with Kr gas.

Molecular Dynamics details. Classical MD simulations of [C_6mim]I/water mixtures with six different IL/water molar ratios have been performed at 300 K and 1 atm (NVT ensemble) using the DL_POLY code,[86] for a total production time of 6 ns. The simulation details (IL/water molar ratios, number of IL ion pairs, number of water molecules and edge length of the boxes) are listed in Table 6.1. Note that a 1 ns NPT run at 1 atm has been carried out to obtain an almost constant density and the final box edge length. The Lopes and Pádua force field[90, 91] was used for [C_6mim]I, while the SPC/E[94] one for water. The potential to describe the I^--water interaction was taken from the work of Reif at al.,[113] as in a combined EXAFS-MD investigation this interaction potential has been found to provide a very good description of the structural properties of iodide in aqueous solutions.[114] See Chapter 4 for all the details of the MD protocol employed.

6.2 I^--water interaction

EXAFS results. The I K-edge EXAFS experimental spectra of the [C_6mim]I/water mixtures with IL/water molar ratios of 1:1, 1:3, 1:6, 1:12, 1:70 and 1:200 are shown in the left panel of Figure 6.1. The experimental spectra of pure [C_6mim]I and of a 0.1 M aqueous solution of tetramethylammonium iodide providing I^- ions in water are also reported. The corresponding Fourier Transforms (FTs) calculated in the interval k = 1.5 to 8.3 $Å^{-1}$ are shown in the right panel of the Figure. The first observation is that the EXAFS spectrum of pure [C_6mim]I is different from that of the 1:1 mixture; it is characterized by a shift of the main oscillation towards a higher frequency meaning that the first neighbor distance is longer as compared to that of the 1:1 IL/water solution. Additionally, the amplitude of the spectrum is lower in comparison with all of the mixtures, thus suggesting that the interaction of the I^- ions with the surrounding atoms is weaker. This means that also when only one water molecule per ion pair is added to the pure IL the EXAFS spectrum is modified and, as a consequence, a variation of the local coordina-

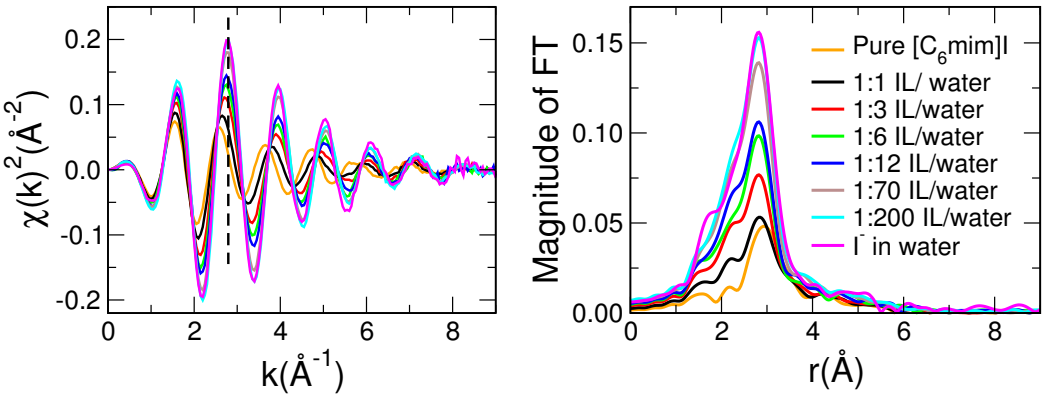

Figure 6.1: Left panel: experimental EXAFS spectra of the [C_6mim]I/water mixtures with IL/water molar ratios of 1:1, 1:3, 1:6, 1:12, 1:70 and 1:200, together with the EXAFS spectra of pure [C_6mim]I and of a 0.1 M aqueous solution of tetramethylammonium iodide providing I^- ions in water. Right panel: non-phase-shifted Fourier Transforms of the EXAFS experimental data.

tion around the I^- ion occurs. Thus, these results are a clear indication that water molecules tend to preferentially interact with the I^- ion also at very low water content. Moreover, going from low to high dilution conditions, the EXAFS data show a trend in the amplitude of the spectra, that increases at higher water concentrations, while no change in the frequency of the signals is observed. These findings indicate that the first shell water distance around the I^- ion is the same for all of the mixtures, while the number of water molecules around the anion increases with increasing water concentration. Note that the EXAFS spectrum of the 1:200 IL/water mixture is almost identical to that of I^- in aqueous solution, thus suggesting that the I^- ion is fully hydrated in this solution.

MD results. To rationalize these results, we have carried out MD simulations of the [C_6mim]I/water mixtures. The I-O and I-HW $g(r)$'s calculated from the MD trajectories are shown in panels A and C of Figure 6.2, respectively, while the first peak positions r and the coordination numbers N, together with the cutoff distances used in the calculation of N, are listed in Tables 6.2 and 6.3. Note that O and HW refer to the oxygen and hydrogen atoms of water molecules, respectively. In all cases, a well-defined first peak can be observed in the I-OW $g(r)$'s, revealing the presence of a preferential interaction of the water molecules with the anions. This sharp first peak is also found in the less diluted mixture with a 1:1 IL/water molar ratio, thus meaning that the single water molecole per ion pair interacts with the I^- anion. Moreover, two well-defined peaks are found in the I-HW $g(r)$'s, the former at shorter and the latter at longer distances as compared with the I-O first maximum peak. This means that only one of the two hydrogen atoms of the water molecules is oriented towards the iodide ion, while the second one interacts with other species of the system. In order to compare different mixtures having different densities, the I-O and I-HW $g(r)$'s have been multiplied by the numerical densities ρ of the oxygen and hydrogen atoms, respectively.

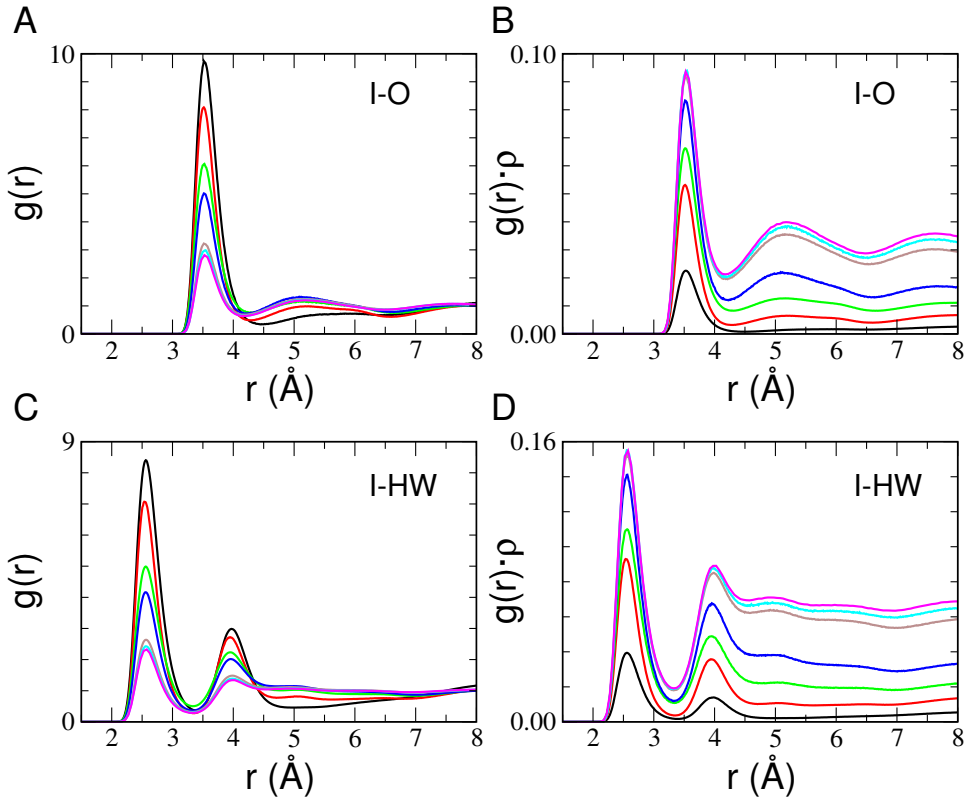

Figure 6.2: I-Water radial distribution functions, $g(r)$'s, and radial distribution functions multiplied by the numerical density of the observed atom, $g(r)\rho$'s, calculated from the MD simulations of the 1:1 (black), 1:3 (red), 1:6 (green), 1:12 (blue), 1:70 (brown) and 1:200 (cyan) [C_6mim]I/water mixtures. The I-O and I-HW $g(r)$'s and $g(r)\rho$'s (magenta) obtained from the MD simulation of the I^- ion in aqueous solution (see Ref [114]) are also reported. (A, C): I-O and I-HW $g(r)$'s. (B, D): I-O and I-HW $g(r)\rho$'s.

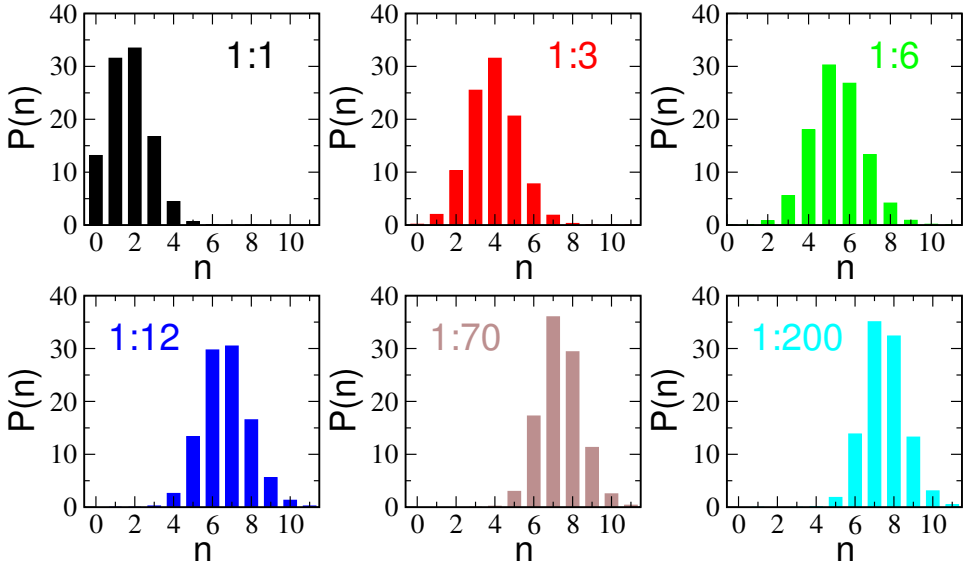

Figure 6.3: Instantaneous I-O coordination number distribution, $P(n)$, obtained from the MD simulations of [C_6mim]I/water mixtures with different molar ratios.

	r(Å)					
	1:1	1:3	1:6	1:12	1:70	1:200
I-O	3.52	3.52	3.52	3.52	3.52	3.52
$[C_6mim]^+$-I	5.31	5.35	5.39	5.45	5.51	5.51
$[C_6mim]^+$-O	4.48	4.48	4.48	4.53	4.53	4.53
HCR-O	2.61	2.61	2.64	2.65	2.67	2.67
CT-CT	4.01	4.02	4.05	4.05	4.07	4.07
CT-O	3.73	3.73	3.73	3.80	3.80	3.80

Table 6.2: Position of the $g(r)$ first peak, r, obtained from the MD $g(r)$'s of the $[C_6(mim)]I$/water mixtures with different molar ratios.

	N						cutoff (Å)
	1:1	1:3	1:6	1:12	1:70	1:200	
I-O	1.6	3.7	5.2	6.4	7.7	7.8	4.2
$[C_6mim]^+$-I	4.0	3.4	2.6	1.7	0.3	0.1	6.4
$[C_6mim]^+$-O	2.0	4.6	8.2	11.4	14.5	15.1	5.3
HCR-O	0.9	2.2	3.3	4.4	5.5	5.8	4.2
CT-CT	4.4	4.1	3.6	3.3	0.6	0.2	7.0
CT-O	0.7	2.9	4.4	7.4	16.3	18.0	5.5

Table 6.3: Coordination numbers, N, obtained from the MD $g(r)$'s of the $[C_6(mim)]I$/water mixtures with different molar ratios, together with the cutoff distances used in the calculation of N. Note that the cutoff distance has been chosen as the position of the $g(r)$ first minimum.

The I-O and I-HW $g(r)\rho$'s are shown in panels B and D of Figure 6.2, and it can be seen that there is a progressive crowding of the I^- ion first hydration shell with increasing water content, as shown also by the trend of the I-O coordination numbers listed in Table 6.3. N increases from 1.6 to 7.8 going from the 1:1 to the 1:200 IL/water solutions. It is interesting to note that the I-O coordination numbers of the 1:1 and 1:3 solutions are 1.6 and 3.7, meaning that in these systems a water molecule tends to simultaneously interact with two I^- ions. Moreover, the I-O coordination numbers for the 1:70 and 1:200 mixtures are almost identical, and also comparable to the one obtained in a previous MD simulation of I^- in pure water (see Ref [114] for all the details about the simulation), suggesting that in both cases the anion is fully hydrated and thus additional dilutions of the system do not cause significant variations of the I-O first shell coordination number. In order to analyze how the I-O coordination number varies along the MD trajectories, we have calculated an instantaneous coordination number, defined as the number of

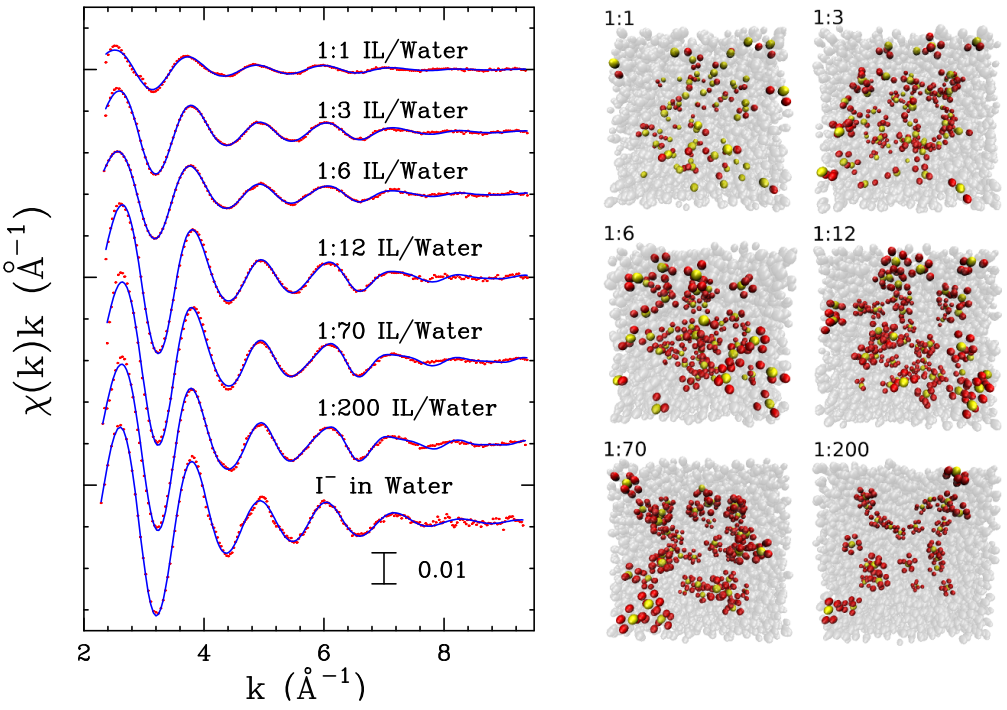

Figure 6.4: Left panel: comparison between the EXAFS experimental spectra (dotted red lines) of the [C_6mim]I/water mixtures and the theoretical signals (solid blue lines). The experimental and theoretical EXAFS data of pure [C_6mim]I and of a 0.1 M I^- aqueous solution are also shown. Note that the theoretical signals have been obtained from the MD I-O and I-HW $g(r)$'s. Right panel: MD simulation snapshots of the [C_6mim]I/water mixtures showing the oxygen atoms (red) of the water molecules belonging to the iodide ion (yellow) first hydration shell.

oxygen atoms within the I^- first hydration shell. The results are reported in Figure 6.3: for the 1:1 [C_6mim]I/water mixture n can take all values from 0 to 4, with a maximum probability of 2; for all other solutions the distribution is shifted to larger values of n, with the 7-coordinated configuration dominant for the 1:70 and 1:200 mixtures.

All these findings are in perfect agreement and confirm the EXAFS results reported above. However, as already shown for pure ILs, a direct comparison between the MD and XAS data is needed to prove the reliability of the MD potentials. The left panel of Figure 6.4 shows the $\chi(k)$ theoretical signals, calculated by introducing the MD I-O and I-HW $g(r)$'s in eq. 2.6, in comparison with the experimental data for all of the mixtures. Note that in all cases the contribution of the hydrogen, carbon and nitrogen atoms of the $[C_6mim]^+$ cation to the total $\chi(k)$ theoretical signal was found to be negligible (vide infra). The MD structural parameters have been kept fixed during the analysis and the only optimized parameters were S_0^2 and E_0, that were found equal to 0.9 and 3 eV above the first inflection point of the spectra, respectively, for all of the systems. Least-squares fits of the EXAFS data have been carried out in the range k = 2.0 - 9.1 $Å^{-1}$. The agreement between the EXAFS experimental and theoretical signals is very good in all cases, thus

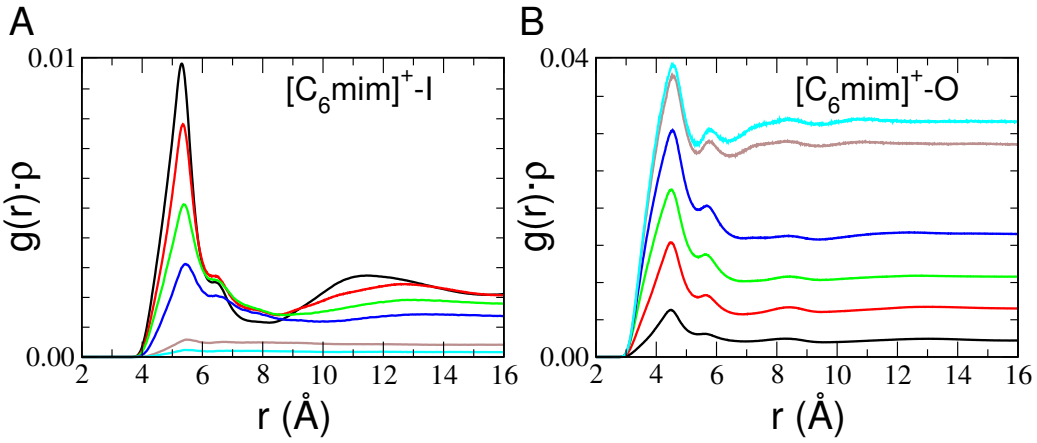

Figure 6.5: Radial distribution functions multiplied by the numerical densities of the observed atoms, $g(r)\rho$'s, obtained from the MD simulations of the 1:1 (black), 1:3 (red), 1:6 (green), 1:12 (blue), 1:70 (brown) and 1:200 (cyan) [C_6mim]I/water mixtures.
(A): [C_6mim]$^+$-I $g(r)\rho$'s calculated between the geometrical ring center of the [C_6mim]$^+$ cation and the I^- ion. (B): [C_6mim]$^+$-O $g(r)\rho$'s calculated between the geometrical ring center of the [C_6mim]$^+$ cation and the oxygen atom (O) of water molecules.

showing that the potentials used in the MD simulations correctly describe the structural properties of all the solutions.

Finally, to gain visual insights into the I^--water interactions, in the right panel of Figure 6.4 we reported selected MD snapshots, where a sample of I^- ions with their first shell water molecules is shown for all of the mixtures. As it can be seen, the water molecules are mainly coordinated with the I^- ion, also in the case of the 1:1 solution, where water molecules acting as bridge between two anions can be found. Moreover, going from low to high dilution conditions, the I^- ion hydration shell becomes more and more populated, reaching the saturation limit for the 1:70 and 1:200 mixtures, in which each anion is fully hydrated.

6.3 Cation-I and Cation-Water interactions

Besides interacting with water molecules, the I^- ions are also coordinated with the imidazolium cations as shown by the [C_6mim]$^+$-I $g(r)\rho$'s calculated between the geometrical ring center of the cation and the I^- anion (see panel A of Figure 6.5). In particular, a strong cation-anion correlation is found in the mixtures with low water content, as revealed by the existence of a distinct first shell peak in the $g(r)\rho$'s, while for the 1:70 and 1:200 solutions the [C_6mim]$^+$-I $g(r)\rho$'s are broad and featureless and also the coordination numbers become close to zero (see Table 6.3). This means that, in the less diluted mixtures up to the 1:12 one, all of the imidazolium cations form pairs with the anion. Conversely, in the 1:70 and 1:200 mixtures a small percentage of ions only exist as ionic pairs. A different behavior was found in a previous MD study of [C_4mim]Br/water mixtures as a function of wa-

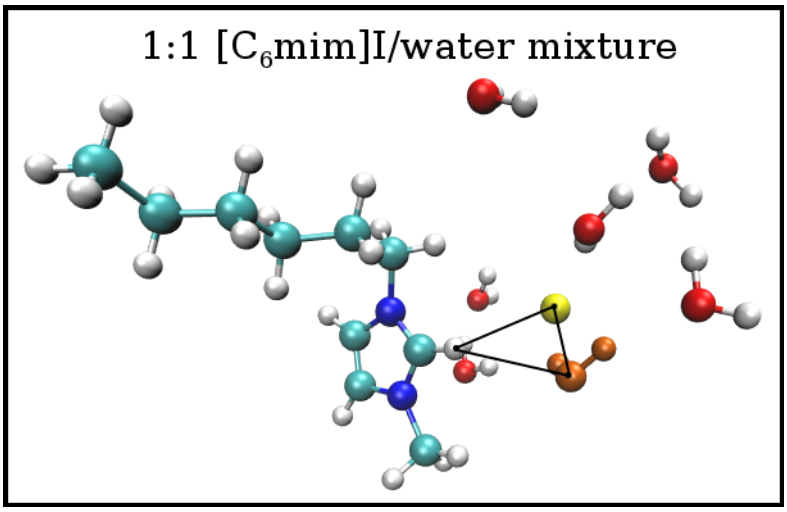

Figure 6.6: Representative snapshot extracted from the MD simulation of the 1:200 [C_6mim]I/water mixture, showing an example of cation-water-anion arrangement where one water molecule (orange) belonging to the anion first coordination shell acts as a bridge between the cation and the anion.

ter concentration, where ionic pairs were observed also in more concentrated IL/water solutions.[51] The different result can be explained by the fact that halide ions have different relative polarizabilities, which play a predominant role in determining the nature of interactions taking place in IL/water mixtures. It is also interesting to note that, in the most diluted mixture (1:200 IL/water molar ratio), although the I^- ion is surrounded on average by 7.8 water molecules, the $[C_6mim]^+$-I first shell distance does not significantly increase as compared to the 1:1 IL/water solution (see Table 6.2). This is because a complex network of interactions between cations, anions and water takes place, in which water molecules belonging to the I^- ion first hydration shell can simultaneously interact with the imidazolium cation. The water molecules act as bridge between the anion and the cation, thus allowing the anion to remain in proximity of the cation. Figure 6.6 shows an example of this cation-water-anion arrangement, that has been extracted from the MD simulation of the 1:200 IL/water mixture.

Panel B of Figure 6.5 shows the $[C_6mim]^+$-O $g(r)\rho$'s, calculated between the geometrical ring center of the $[C_6mim]^+$ cation and the oxygen atom of water molecules. As expected, a distinct peak can be observed in all cases, revealing the existence of a first coordination shell of water molecules also around the cation. However, the cation-water interaction is weaker as compared to the I^--water one. The first shell $[C_6mim]^+$-O $g(r)\rho$ peaks are less defined and less pronounced in comparison with those of the I-OW and I-HW $g(r)\rho$'s. Moreover, by evaluating all of the $[C_6mim]^+$-O site-site $g(r)$'s, it has been found that water molecules are preferentially located around the three hydrogen atoms of the imidazolium ring and, in particular, around HCR which is the most acidic one. The HCR-O $g(r)\rho$'s, reported in Figure 6.7, show a distinct first shell peak in all cases, with a coordination number different from zero also for the 1:1 IL/water mixture (see Table 6.3). This is due

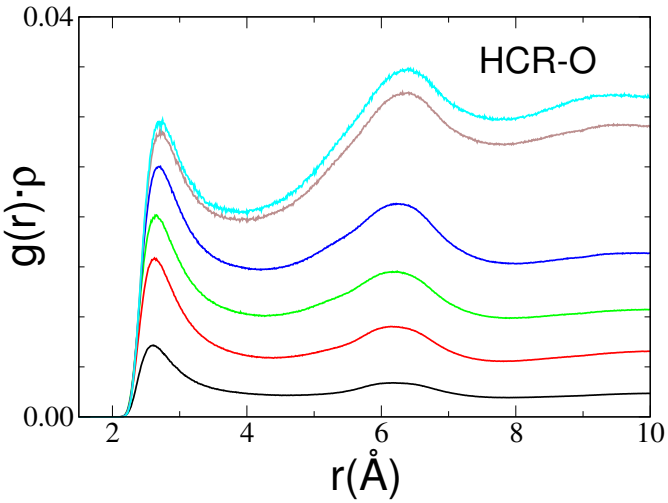

Figure 6.7: HCR-O radial distribution functions multiplied by the numerical densities, $g(r)\rho$'s, calculated from the MD simulations of the 1:1 (black), 1:3 (red), 1:6 (green), 1:12 (blue), 1:70 (brown) and 1:200 (cyan) [C_6mim]I/water mixtures. HCR is the most acidic hydrogen atom of the imidazolium cation, and O is the oxygen atom of water molecules.

to the ability of the HCR atom to promote hydrogen bonds, as previously pointed out in several investigations on IL/water solutions.[45, 46, 115]

The three-dimensional arrangement of anions and water around the imidazolium cations can be identified through the SDF functions, depicted in Figure 6.8. Note that the SDFs have been calculated from the MD simulations with different water concentration using the same absolute densities for the different IL/water mixtures. The I^- ion isosurfaces (yellow) are prefer-

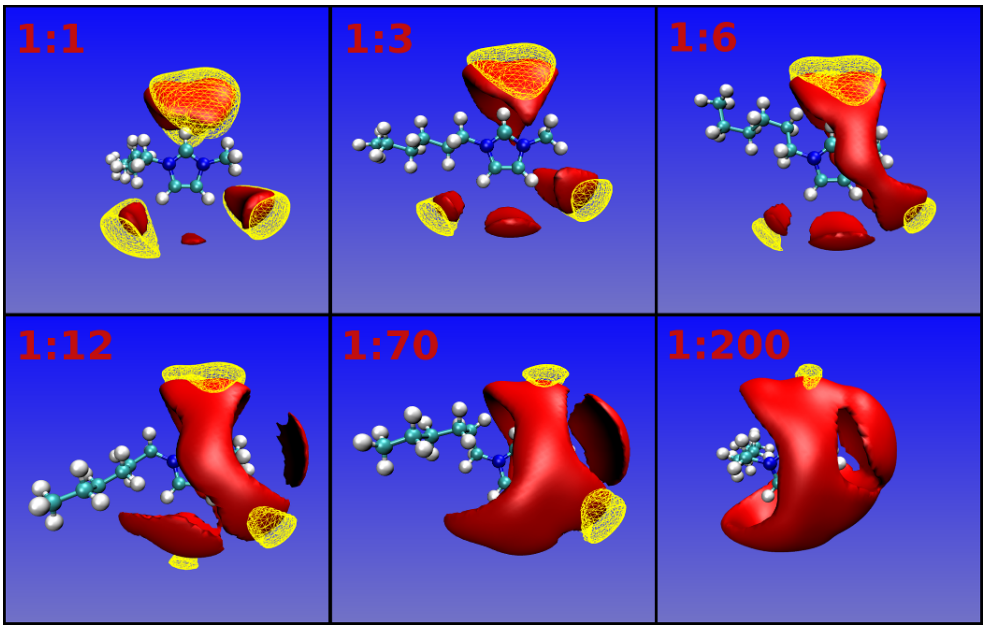

Figure 6.8: Spatial distribution functions (SDFs) of the oxygen atoms of water molecules (red) and I^- ions (yellow) around the $[C_6mim]^+$ cation calculated from the MD simulations of the [C_6mim]I/water mixtures. The same absolute densities have been used for all the mixtures.

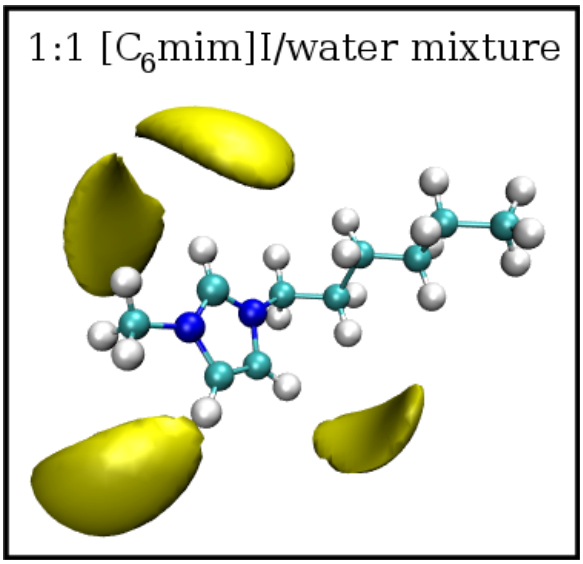

Figure 6.9: Spatial distribution function (SDF) of the I^- ions (yellow) around the $[C_6mim]^+$ cation calculated from the MD simulation of the 1:1 $[C_6mim]I$/water mixtures.

entially located around the three hydrogen atoms (HCR and HCWs) of the imidazolium ring. From the SDFs for the 1:1 and 1:3 IL/water solutions it is clear that the strongest interaction occurs between the anion and HCR, which is the most acidic hydrogen atom of the imidazolium ring. Moreover, in proximity of the HCWs atoms the I^- isosurfaces are shifted towards the lateral chains, and the shift is less pronounced on the side of the hexyl chain as a result of its steric hindrance. It is also interesting to note that the I^- ion near the HCR atom is not coplanar with the imidazolium ring plane, while near the HCWs atoms it has the same probability of being or not being coplanar with the plane (see Figure 6.9). Similar results have been found in MD simulations of pure $[C_4mim]I$ [116] and $[C_6mim]I$ ILs (see Chapter 5), and in a combined DFT and UV-vis, IR investigation of $[C_4mim]X$.[15] Going from low to high dilution condition, the probability of finding the I^- ions around the imidazolium ring decreases and, in the IL/water mixture with 1:200 molar ratio, only the anion isosurface near HCR can be observed. As concerns the cation-water SDFs, the isosurfaces of water molecules (red) are found in proximity of the three hydrogen atoms of the imidazolium ring, even if they tend to wrap the cation and to become more and more disordered and unstructured as the water concentration increases.

6.4 EXAFS sensitivity towards the cation atoms

The analysis of the MD simulations has shown that the I^- ions are well organised around both the water molecules and the cation in all the solutions. However, as previously described, the cation atoms have been found to provide a negligible contribution to the EXAFS spectra. To shed light into this issue it is useful to compare the structural properties of the $[C_6mim]I$/water

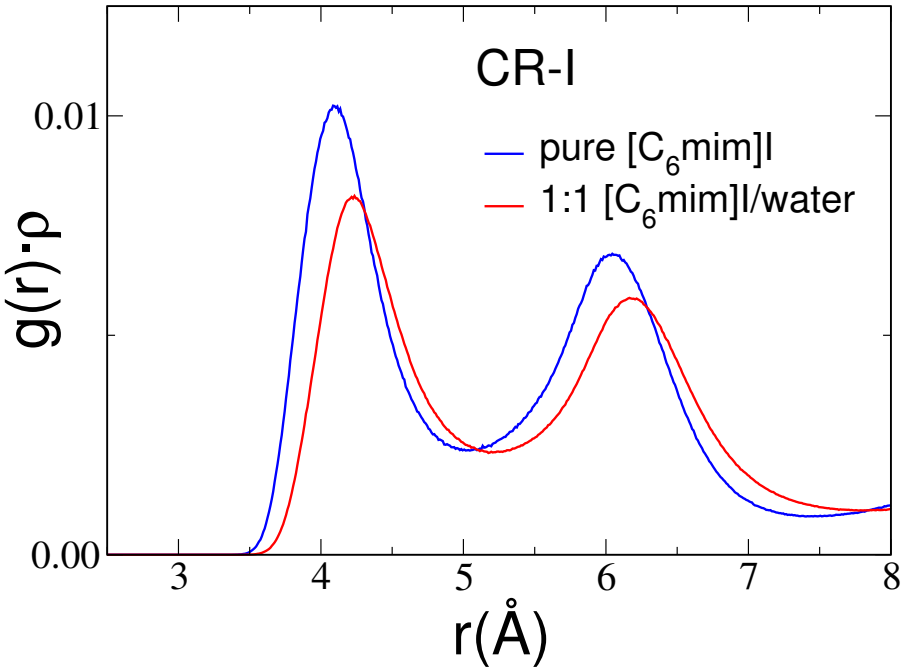

Figure 6.10: CR-I radial distribution functions multiplied by the numerical densities, $g(r)\rho$'s, calculated from the MD simulations of pure [C_6mim]I (blue) and of the [C_6mim]I/water mixture with molar ratio of 1:1 (red).

mixtures studied here with those of pure [C_6mim]I (see Chapter 5) where the EXAFS theoretical signals associated with the imidazolium cation have been found to be non negligible. So, we have compared the $g(r)\rho$'s between the $[C_6mim]^+$ and the I^- ions, focusing in particular on the CR-I, CW-I and N-I $g(r)\rho$'s. In fact, the carbon and nitrogen atoms have a higher scattering factor than the hydrogen ones and they are expected to give a more detectable contribution to the EXAFS signal. As a general trend, the cation-anion $g(r)\rho$'s for the IL/water mixtures are more unstructured and shifted towards larger distances as compared to pure [C_6mim]I. Figure 6.10 shows, as an example, the CR-I $g(r)\rho$'s for pure [C_6mim]I and for the 1:1 [C_6mim]I/water solution. Note that we have choosen this mixture as, at this very low water amount, the amplitude of the EXAFS signals associated with the cation would be larger. We can see that the CR-I first shell peaks are found at 4.10 and 4.23 Å and the coordination numbers (up to 5.06 Å) are 1.8 and 1.4 for pure [C_6mim]I and for the 1:1 [C_6mim]I/water mixture, respectively. This means that in the solutions, due to the presence of water molecules between the imidazolium cations and the I^- ions, the EXAFS signals associated with the cation atoms is less intense. Moreover, looking at Figure 6.4, it can be seen that the overall intensity of the EXAFS experimental data of the [C_6mim]I/water mixtures is about one order of magnitude larger as compared to pure [C_6mim]I, as the interactions between the I^- ions and water are very strong and provide a more intense EXAFS signal in which the imidazolium cation contributions are hardly detectable.

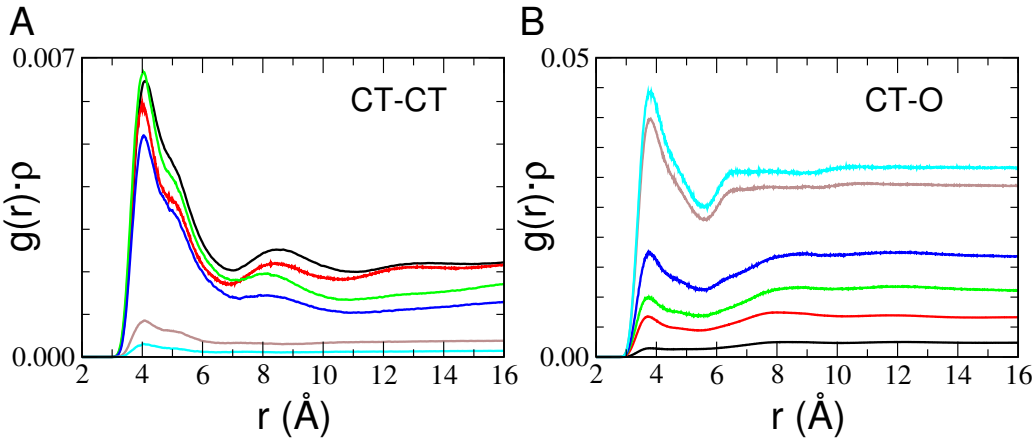

Figure 6.11: CT-CT and CT-O radial distribution functions multiplied by the numerical densities of the observed atoms, $g(r)\rho$'s, calculated from the MD simulations of the 1:1 (black), 1:3 (red), 1:6 (green), 1:12 (blue), 1:70 (brown) and 1:200 (cyan) [C_6mim]I/water mixtures. CT is the terminal carbon atom of the hexyl chain attached to the cation, while O is the oxygen atom of water molecules.

6.5 Long-range structural organization

In Chapter 5 we have seen that long chain alkylimidazolium based ILs can be organized in polar and apolar domains as a consequence of the alkyl tail aggregation. This typical structural organization can also take place when ILs are combined with water as it has been already observed in water mixtures of imidazolium based ILs having the bromide ion as counterion.[117, 118] The first indication of the presence of tail-tail aggregation arises from the analysis of the intermolecular CT-CT $g(r)\rho$'s, reported in panel A of Figure 6.11. We refer to CT as the terminal carbon atom of the hexyl chain. All of the $g(r)\rho$'s are characterized by a distinct first peak around 4.0 Å, suggesting clustering of the hexyl chains. However, the terminal methyl group of the hexyl chain also interacts with water, as evidenced by the presence of a peak at low distances in the CT-O $g(r)\rho$'s (see panel B of Figure 6.11) and by the CT-O coordination number, listed in Table 6.3. N increases with increasing dilution, and it remains different from zero also for the two most concentrated solution (0.7 and 2.9 for the 1:1 and 1:3 IL/water mixtures, respectively). These findings suggest that the alkyl chains are not completely segregated in hydrophobic domains in line with a previous NMR investigation of [C_6mim]Br and [C_8mim]Br/water mixtures.[119]

To better shed light on the long-range organization and the tail-tail aggregation it is extremely useful to compute the X-ray structure factors, $S(q)$, from the MD trajectories using eq. 4.5 and 4.6. Figure 6.12 shows the $S(q)$ functions plotted against the momentum transfer q for all of the mixtures. The oscillations above 1 $Å^{-1}$ are mostly due to intramolecular interactions, as well as to intermolecular short-range contributions existing in the solutions. In particular, when increasing water content (1:70 and 1:200 IL/water mixtures), a clear change of the $S(q)$ signal occurs in this q region as the water contribution becomes predominant. However, the very important re-

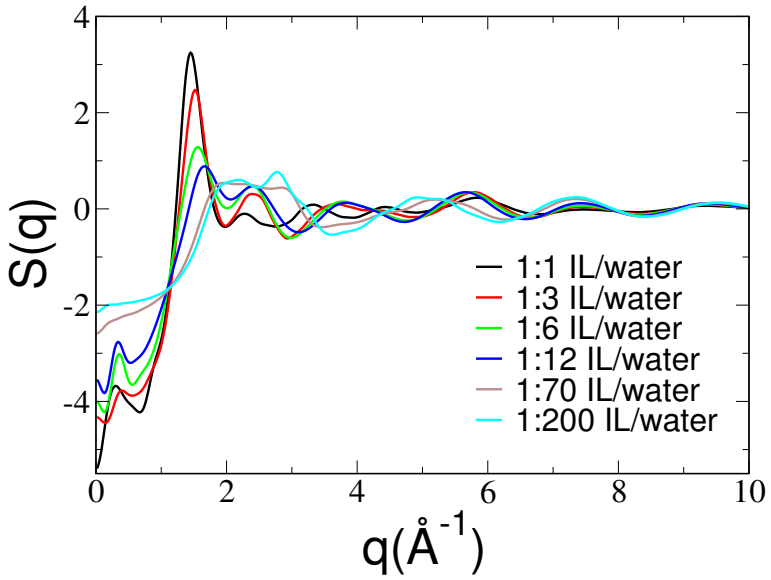

Figure 6.12: X-ray structure factors, S(q), calculated from the MD simulations of the [C_6mim]I/water mixtures with different molar ratios.

sult is the presence of the so-called "prepeak", in the q region below 1 Å^{-1}, which reflects the presence of long-range structural correlations. This peak is well defined for the [C_6mim]I/water mixtures with molar ratios ranging from 1:1 to 1:12, then it becomes less pronounced and finally disappears with increasing water content. No aggregation of the hexyl chains is found for the 1:200 IL/water mixtures, in agreement with the experimental CAC value determined for [C_6mim]I (250.3 mmol/l) [120] that corresponds to an IL/water molar ratio between 1:70 and 1:200. To gain visual insights into this behavior, we report in the left panels of Figure 6.13 representative MD snapshots in which only the hexyl chain (cyan) are shown. For the most concentrated IL/water solutions (molar ratios from 1:1 to 1:12) the existence of long-range structural correlations can be evidenced, even if the alkyl chains are not completely segregated in apolar domains as expected for micelle-like structures. Conversely, in the IL/water mixtures with molar ratios of 1:70 and 1:200 the hexyl chains exist as isolated units, completely separated from each other.

It is also interesting to note that the water molecules in the solutions tend to aggregate and form clusters as the water concentration increases. As already shown in previous works,[51, 42] this behavior is due to the presence of an extended hydrogen bond network between water molecules and anions and, at higher water concentrations, also between water molecules and cations. In the right panels of Figure 6.13 we show some MD snapshots, where the IL cations and anions are colored blue, while water molecules are highlighted. It can be seen that in the 1:1 IL/water mixture water molecules are isolated, while in the 1:3, 1:6 and 1:12 solutions the existence of string-like water clusters are visible, as previously found in the literature.[42] The characteristic string-like shape of these clusters is due to the directional nature of the water-water hydrogen bonds. In the 1:70 IL/water solution apolar domains are still present while in the most concentrated one (molar ratio of 1:200) no partic-

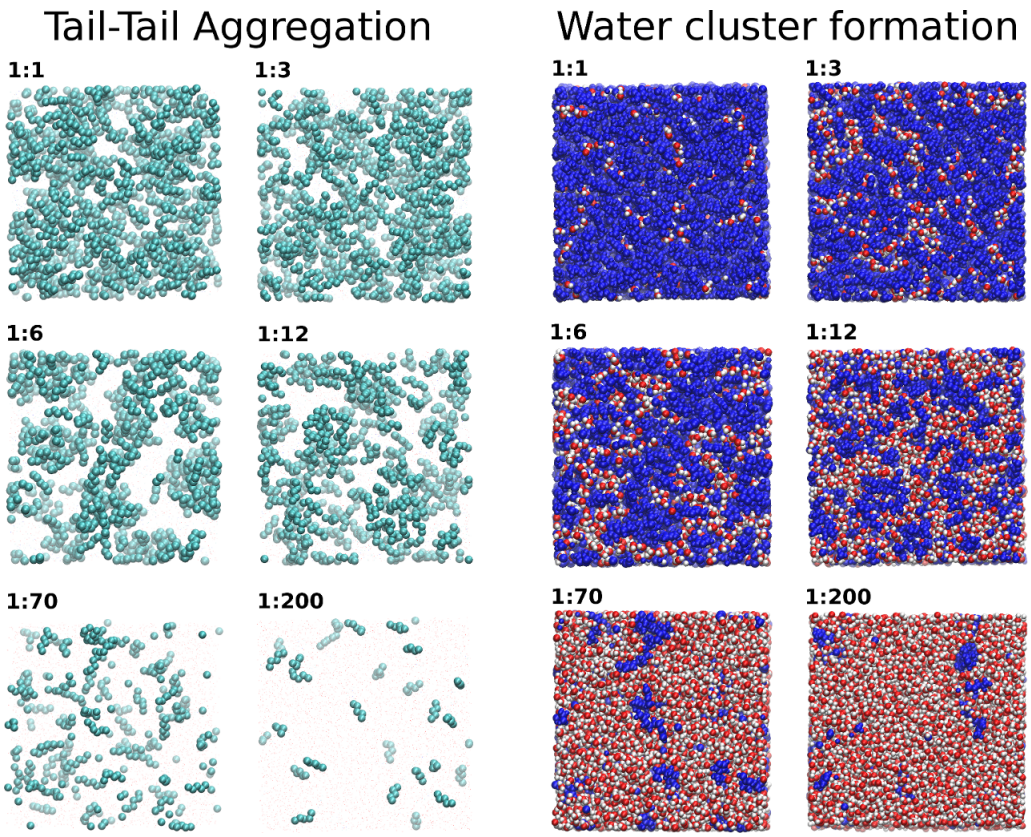

Figure 6.13: MD simulation snapshots of the $[C_6mim]I$/water mixtures. Left panels: apolar components (hexyl chains) colored in cyan. Right panels: the IL ion pairs are colored blue, while the water molecules are highlighted.

ular aggregation can be observed, and the water clusters percolate through the sample.

Chapter 7

Dicationic imidazolium-based IL/water mixtures

In this Chapter we move from monocationic to dicationic imidazolium-based ILs, as it was found that they possess wider liquid range, higher melting point, better chemical and thermal stability compared to the conventional monocationic ILs and they show affinity for self-aggregation in aqueous and polar media. For these reasons, dication-containing ILs are a class of materials with a growing portfolio of possible applications as solvents, catalysts, liquid crystals or high temperature lubricants/heat transfer fluids. They also have potential applications in nano technology, as carriers for therapeutic DNA, gene-delivery agents and modulators for the growth of 2D Langmuir films or nanorods.[121, 122, 123]

By combining MD simulations and XAS spectroscopy we will provide a detailed microscopic characterization of binary mixtures of water and a typical family of such DILs, the 1,n-bis[3-methylimidazolium-1-yl] alkane bromide ($[C_n(mim)_2]Br_2$) (see Figure 7.1). In particular, we will investigate $[C_3(mim)_2]Br_2$/water solutions in a wide range of water concentrations (DIL/water molar ratio from 1:16 to 1:400) and 1:70 $[C_n(mim)_2]Br_2$/water solutions, obtained by changing the spacer chain length.

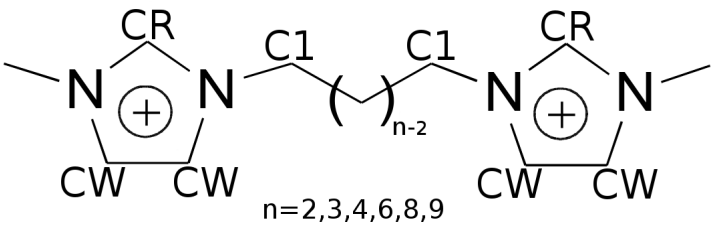

Figure 7.1: Molecular structure of 1,n-bis[3-methylimidazolium-1-yl]alkane dication, $[C_n(mim)_2]^{2+}$, and atom labeling used in the work.

7.1 Experimental Methods

X-ray absorption measurements. $[C_n(mim)_2]Br_2$ (with n = 2, 3, 4, 6, 8, 9) ILs were synthesized at room temperature by reacting two molar equiv of 1-methylimidazole and one molar equiv of 1,n-dibromoalkane, according to the synthesis procedure of Ref [26]. All DILs were dried under vacuum for about 36 hours and the final water content measured by Karl-Fischer titration was between 150 and 300 ppm for the different samples. $[C_3(mim)_2]Br_2$/water mixtures with different molar ratios (1:x with x = 16, 28, 40, 70, 200 and 400) and 1:70 $[C_n(mim)_2]Br_2$/water mixtures with different spacer chain lengths (n = 2, 3, 4, 6, 8, 9) were prepared by adding the proper amount of $[C_n(mim)_2]Br_2$ to bidistilled water. It is important to note that DIL/water molar ratio of 1:x means that there are x water molecules per ion pair, and x/2 water molecules for each Br^- ion. A 0.1 M RbBr aqueous solution was also prepared, choosing the Rb^+ as counterion as it is known that it does not form ion pairs with Br^- inside the solution at the concentration used. The Br K-edge spectra of all DIL/water solutions, of pure $[C_3(mim)_2]Br_2$ and of a Br^- aqueous solution were measured at room temperature in transmission mode at the Elettra Synchrotron (Italy) on the beamline 11.1.[83] The monochromator was equipped with a Si(111) double crystal and the storage ring was operating at 2 GeV with a storage beam current between 300 and 200 mA.

Molecular Dynamics details. Classical MD simulations of the $[C_3(mim)_2]Br_2$/water mixtures with six different molar ratios and 1:70 $[C_n(mim)_2]Br_2$/water mixtures with six different spacer chain lengths have been carried out in the NVT ensemble, at 300 K, using the DL_POLY package,[86] for a total production time of 6 ns. The simulation details for the $[C_3(mim)_2]Br_2$/water mixtures and for the 1:70 $[C_n(mim)_2]Br_2$/water mixtures are collected in Tables 7.1 and 7.2, respectively. The number of ion pairs and water molecules used in each simulation depends on the mixture and computational feasibility. Note that a 1 ns NPT run at 1 atm has been carried out to obtain an almost constant density and the final box edge length. The force field used for $[C_n(mim)_2]Br_2$ DILs was taken from Lopes and Pádua,[90, 91] with a minor modification for the $[C_2(mim)_2]^{2+}$ and $[C_3(mim)_2]^{2+}$ dications of the partial atomic charges of the spacer chain in order to preserve the total charge +2 and the atomic charge symmetry of the spacer between the two imidazolium rings. In particular, for $[C_2(mim)_2]^{2+}$, we distributed the residual charge to the only two carbon atoms of the spacer chain and to their corresponding hydrogen atoms (+0.05e on each carbon atom and +0.04e on each hydrogen atom). So we obtained a final partial charge of -0.12e and +0.13e for the carbon and hydrogen atoms of the spacer, respectively. For the $[C_3(mim)_2]^{2+}$ dication we adopted the modification introduced by Yeganegi et al.[36] The SPC/E [94] model was used for water molecules. The potential to describe the Br^--water interaction was taken from the OPLS force field,[92] for which we obtained the best agreement between the EXAFS experimental data and the theoretical signal for the 1:70 $[C_3(mim)_2]Br_2$/water solution (vide infra).

$[C_3(mim)_2]Br_2$/water molar ratio	DIL ion pairs	Water molecules	Simulation box edge (Å)
1:16	216	3456	57.49
1:28	125	3500	53.66
1:40	125	5000	58.51
1:70	64	4480	54.30
1:200	27	5400	55.67
1:400	16	6400	58.25

Table 7.1: MD simulation details for the $[C_3(mim)_2]Br_2$/water mixtures with different molar ratios performed in this work.

n	DIL ion pairs	Water molecules	Simulation box edge (Å)
2	64	4480	54.15
3	64	4480	54.30
4	64	4480	54.51
6	64	4480	54.92
8	64	4480	55.35
9	64	4480	55.54

Table 7.2: MD simulation details for the 1:70 $[C_n(mim)_2]Br_2$/water mixtures as a function of the spacer chain length (n) performed in this work.

All the details of the MD protocol employed are described in Chapter 4.

Moreover, a MD simulation of the Br^- ion in aqueous solution has been also carried out adopting the same MD protocol as the one employed for the DIL/water mixture simulations. The system was composed of 1 Br^- ion and 819 water molecules, and a homogeneous background charge was added to preserve the neutrality of the solution.

7.2 1:x $[C_3(mim)_2]Br_2$/water mixtures: effect of the water concentration

EXAFS results. The Br-K edge spectra of the $[C_3(mim)_2]Br_2$/water mixtures with 1:16, 1:28, 1:40, 1:70, 1:200 and 1:400 molar ratios (extracted with a three-segmented cubic spline function) are shown in the left panel of Figure 7.2, together with the experimental data of pure $[C_3(mim)_2]Br_2$ and of a 0.1 M Br^- aqueous solution, while the corresponding Fourier Transforms,

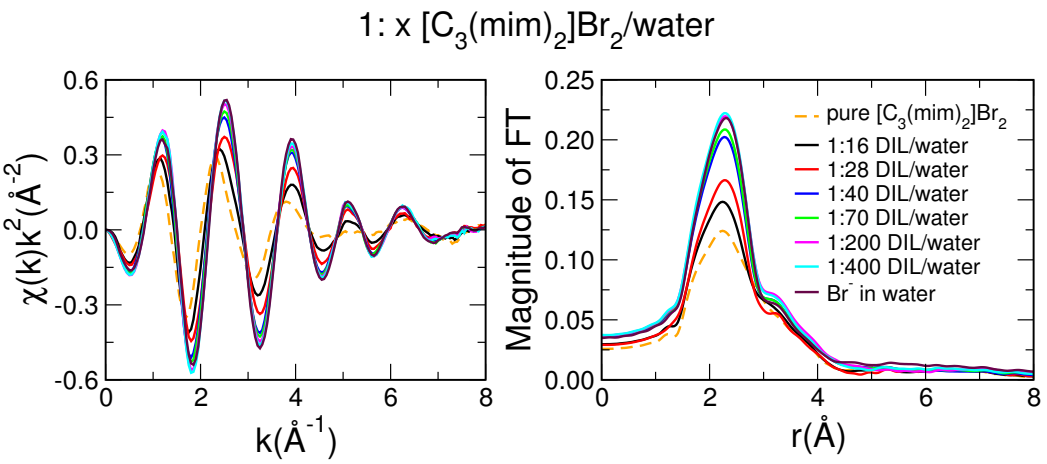

Figure 7.2: Left panel: EXAFS spectra of the $[C_3(mim)_2]Br_2$/water mixtures with 1:16, 1:28, 1:40, 1:70, 1:200 and 1:400 DIL/water molar ratios, together with the spectra of pure $[C_3(mim)_2]Br_2$ and of a 0.1 M Br^- aqueous solution. Right panel: Fourier Transforms of the experimental data.

FTs, (calculated in the interval $k = 0.7$ to 12 $Å^{-1}$) are reported in the right panel of the Figure. The first evidence is that the EXAFS spectrum of pure $[C_3(mim)_2]Br_2$ has a lower amplitude as compared to all the DIL/water solutions. This result suggests that water molecules have a high affinity with the Br^- ion and enter its coordination sphere also for the most diluted mixture with a 1:16 DIL/water molar ratio. Moreover, when looking at the EXAFS data of the DIL/water solutions, higher EXAFS amplitudes are found at higher water concentrations. The same trend can be also found in the FTs of the experimental data: the FT peak position is always the same, while its intensity increases with increasing water content. All these features indicate that the Br^- ion mainly interacts with water molecules at the same distance and its hydration shell becomes more structured and crowded when more water is added to the solution. These results are similar to those reported in a recent EXAFS-MD study of monocationic $[C_4mim]Br$/water mixtures in a wide range of water concentrations,[51, 124] where it was found that the Br^- first coordination shell becomes more populated as the water concentration increases. A similar behavior has been also evidenced from the investigation of monocationic $[C_6mim]I$/water mixtures as a function of water concentration up to very high dilution, reported in Chapter 6. It was found that the water molecules preferentially interact with the anion (in this case the iodide ion), also at very diluted conditions. Finally, the last remarkable observation is that the EXAFS spectrum of the 1:400 DIL/water solution is almost identical to that of Br^- in aqueous solution.

MD results. In order to gain complementary information to the EXAFS experimental evidences, we have performed MD simulations on the $[C_3(mim)_2]Br_2$/water mixtures and then compared the experimental and theoretical results. However, as described in the Introduction, a proper choice of the force field is mandatory for a correct description of the investigated systems. For the $[C_n(mim)_2]Br_2$ DILs and water we used the Lopes and Pádua

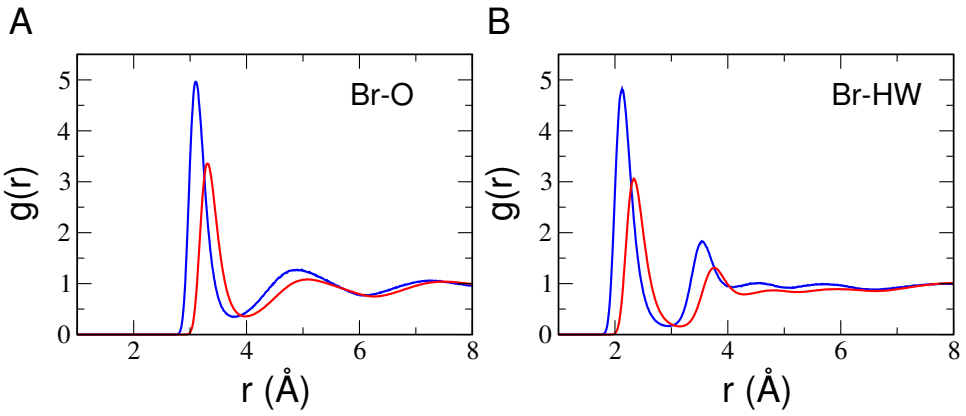

Figure 7.3: Br-Water radial distribution functions, $g(r)$'s, calculated from the MD simulations of the 1:70 $[C_3(mim)_2]Br_2$/water mixture using either the Lopes and Pádua (CL&P) (blue lines) or the OPLS (red lines) Lennard-Jones parameters.

(CL&P) [90, 91] and SPC/E [94] force fields, respectively, since they were well-known to correctly reproduce the structural and dynamics properties of both systems. Conversely, as regards the Br^--water interaction, there are several potentials available in the literature, whose reliability has to be assessed by comparison with the experimental data.

The Br-water potential. In order to chose the best-performing Lennard-Jones parameters for the Br^--water interaction, we have first carried out two MD simulations of the 1:70 $[C_3(mim)_2]Br_2$/water mixture using either the CL&P or the OPLS[92] parameters for the Br^- ion in combination with the SPC/E water model. As shown in Figure 7.3, the Br-O and Br-HW $g(r)$'s, where O and HW refer to the oxygen and hydrogen atoms of water molecules, strongly depend on the employed potential. In particular, the Br-O first shell peaks are found at 3.10 and 3.33 Å for the CL&P and OPLS potentials, respectively. Starting from the Br-O and Br-HW $g(r)$'s and using eq. 2.6 we have calculated the $\chi(k)$ EXAFS theoretical signals for both the MD simulations carried out using either the CL&P or the OPLS Lennard-Jones parameters. Note that the theoretical signals associated with the carbon, nitrogen and hydrogen atoms of the dication were found to be negligible. The explanation of this issue is the same to the one we did in Chapter 6 for monocationic $[C_6mim]I$/water mixtures. The EXAFS analysis is shown in Figure 7.4: the first two curves from the top are the Br-HW and Br-O theoretical signals, while the remainder of the Figure shows the total theoretical signal in comparison with the experimental data. It is clear that the agreement between the experimental and calculated spectra is good only for the OPLS parameters, since a marked shift of the main oscillation appears when using the CL&P force field. This shift is due to the short average Br-O and Br-HW first shell distances as compared with the EXAFS experimental data. Bearing in mind these results, we have decided to use the OPLS Lennard-Jones parameters to describe the Br^--water interaction.

Once the Br^--water potential has been chosen, we have carried out the

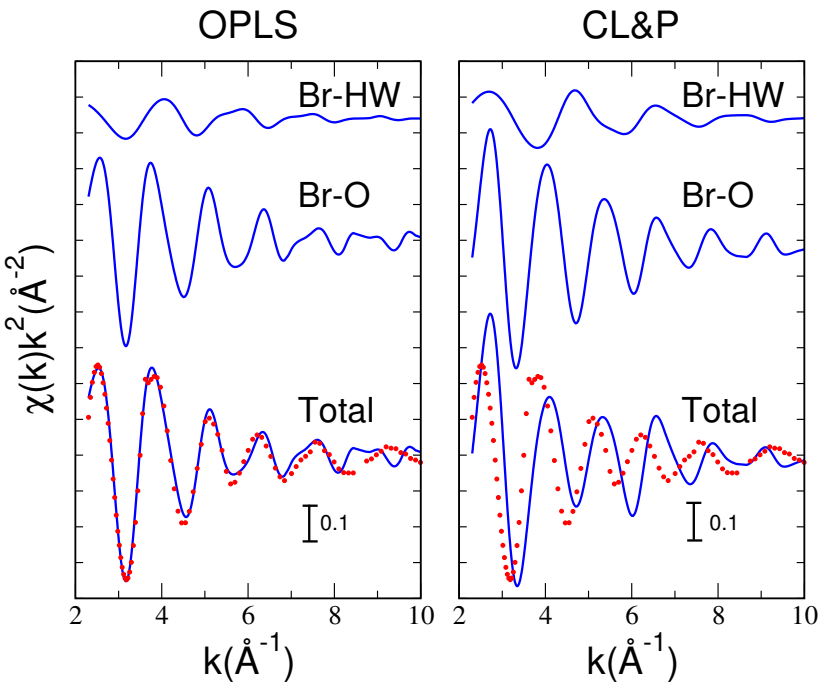

Figure 7.4: EXAFS experimental spectra (dotted red line) of the 1:70 $[C_3(mim)_2]Br_2$/water mixture compared with the theoretical signals (solid blue line), calculated from the MD Br-O and Br-HW $g(r)$'s using either the Lopes and Pádua (CL&P) or the OPLS Lennard-Jones parameter values.

MD simulations of all the $[C_3(mim)_2]Br_2$/water mixtures and the most relevant $g(r)$'s have been computed from the MD trajectories. The upper panel of Figure 7.5 shows the Br-O and Br-HW $g(r)$'s, while the corresponding Br-O and Br-HW $g(r)$'s multiplied by the numerical density of the O and HW atoms, $g(r)\rho$'s, are reported in the lower panel of the same Figure. Both the Br-O and Br-HW $g(r)$'s show very sharp and distinct first peaks centered at 3.33 and 2.35 Å, respectively, as strong anion-water interactions take place in the solutions, in agreement with the EXAFS experimental results. Note that the position of the Br-O first maximum, as it can be seen in Table 7.3, is the same for all the DIL/water solutions, thus proving that the first shell distance of the water molecules around the Br^- ion does not change with increasing water concentration. As regards the Br-HW $g(r)$'s, two distinct peaks are found, the former at shorter and the latter at longer distances as compared with the Br-O $g(r)$ first peak. This is due to the fact that the first-shell water molecules orient only one hydrogen atom towards the anion, in line with the ability of the Br^- ion to form strong hydrogen bonds.[125] Additionally, looking at the Br-O and Br-HW $g(r)\rho$'s, that allows to directly compare different mixtures having different densities, we can see a trend of the peak intensity that increases significantly with increasing water concentration. Indeed, the Br-O coordination number changes from 4.4 to 6.5 in going from the 1:16 to 1:400 DIL/water solutions (see Table 7.4). It is interesting to note that the value obtained for the 1:400 mixture is slightly lower as compared to the

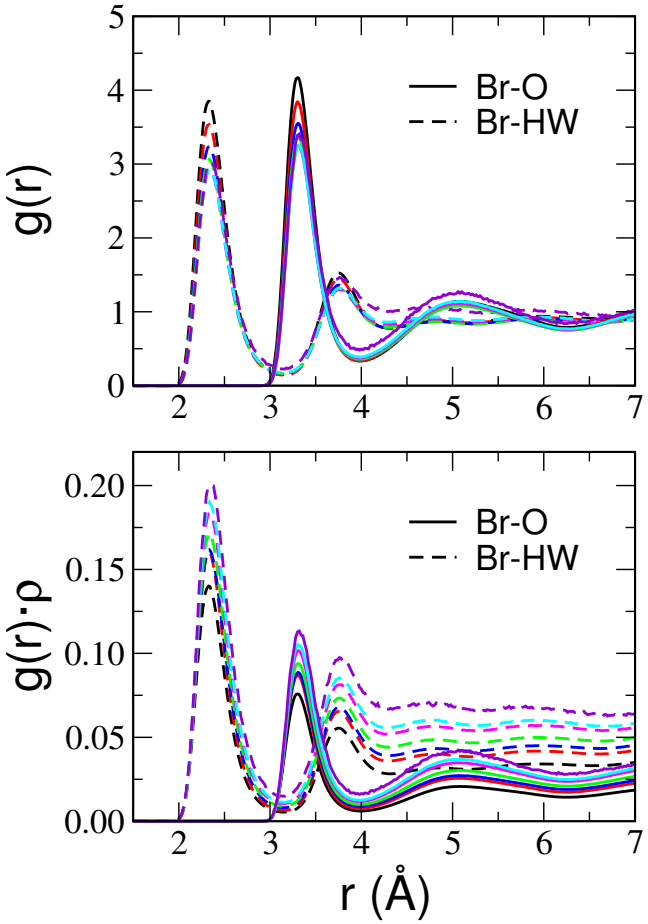

Figure 7.5: Br-Water radial distribution functions, $g(r)$'s, and radial distribution functions multiplied by the numerical density of the observed atom, $g(r)\rho$'s, calculated from the MD simulations of the 1:16 (black), 1:28 (red), 1:40 (blue), 1:70 (green), 1:200 (magenta) and 1:400 (cyan) $[C_3(mim)_2]Br_2$/water mixtures. Upper panel: Br-O (solid lines) and Br-HW (dashed lines) $g(r)$'s. Lower panel: Br-O (solid lines) and Br-HW (dashed lines) $g(r)\rho$'s. The Br-O and Br-HW $g(r)$'s and $g(r)\rho$'s (magenta) obtained from the MD simulation of the Br^- ion in aqueous solution are also reported.

one calculated from the MD simulation of Br^- ion in aqueous solution. This result suggests that the Br^- ion is not fully hydrated in the most diluted mixture, as interactions between dications and anions also persist when water is added in great excess. This difference has not been observed in the EXAFS experimental data shown in Figure 7.2, due to the low sensitivity of the EXAFS spectroscopy towards slight changes in the coordination number of the atoms around the photoabsorber one.

To directly compare the theoretical and experimental data, $\chi(k)$ theoretical signals have been calculated using eq. 2.6, starting from the MD Br-O and Br-HW $g(r)$'s for all of the $[C_3(mim)_2]Br_2$/water solutions and adopting the same procedure described above. Figure 7.6 shows the comparison between the EXAFS experimental data and the theoretical ones obtained from the MD simulations for all of the mixtures. The theoretical and experimental EXAFS signals of a 0.1 M Br^- aqueous solution are also reported. In all cases

	r(Å)						
$[C_3(mim)_2]Br_2$/water molar ratio	1:16	1:28	1:40	1:70	1:200	1:400	Br^- in water
Br-O	3.33	3.33	3.33	3.33	3.33	3.33	3.33
$[C_3(mim)_2]^{2+}$-O	4.55	4.55	4.55	4.55	4.55	4.55	
$[C_3(mim)_2]^{2+}$-Br	4.81	4.82	4.82	4.82	4.82	4.82	
HCR-O	2.74	2.75	2.75	2.75	2.75	2.75	
HCW-O	2.83	2.85	2.85	2.85	2.85	2.85	
HCR-Br	2.89	2.90	2.90	2.90	2.90	2.90	
HCW-Br	2.92	2.93	2.93	2.93	2.93	2.93	

Table 7.3: Position of the $g(r)$ first peak, r, obtained from the MD simulations of the $[C_3(mim)_2]Br_2$/water mixtures with different molar ratios, together with that of the Br^- ion in aqueous solution.

	N(Å)							cutoff (Å)
$[C_3(mim)_2]Br_2$/ water molar ratio	1:16	1:28	1:40	1:70	1:200	1:400	Br^- in water	
Br-O	4.4	5.1	5.4	5.8	6.3	6.5	7.3	4.0
$[C_3(mim)_2]^{2+}$-O	10.7	12.3	12.7	13.4	14.3	14.7		5.3
$[C_3(mim)_2]^{2+}$-Br	2.7	2.2	2.0	1.6	1.1	0.9		5.8
HCR-O	4.3	4.9	5.1	5.3	5.7	5.9		4.3
HCW-O	4.9	5.8	6.0	6.3	6.7	6.9		4.3
HCR-Br	1.1	0.9	0.8	0.7	0.5	0.4		4.5
HCW-Br	0.9	0.7	0.6	0.5	0.3	0.2		4.5

Table 7.4: Coordination number, N, and cutoff distances obtained from the MD $g(r)$'s of the $[C_3(mim)_2]Br_2$/water mixtures with different molar ratios, together with the structural parameters of the Br^- ion in aqueous solution. Note that the cutoff distance has been chosen as the position of the $g(r)$ value first minimum.

the theoretical data match very well the EXAFS experimental spectra, thus proving the validity of the MD results. Once again, we can notice that the amplitude of the EXAFS spectra increases with increasing water content, as more and more water molecules are accomodated in the Br^- first shell.

Although the Br^- ions are preferentially coordinated to water molecules, an interaction between anions and dications also takes place, as shown by the strong dication-anion correlation found in all the simulated mixtures. The $[C_3(mim)_2]^{2+}$-Br $g(r)\rho$'s, calculated between the geometrical center of one of the two rings of the dication and the Br^- ion, are shown in panel A of Figure

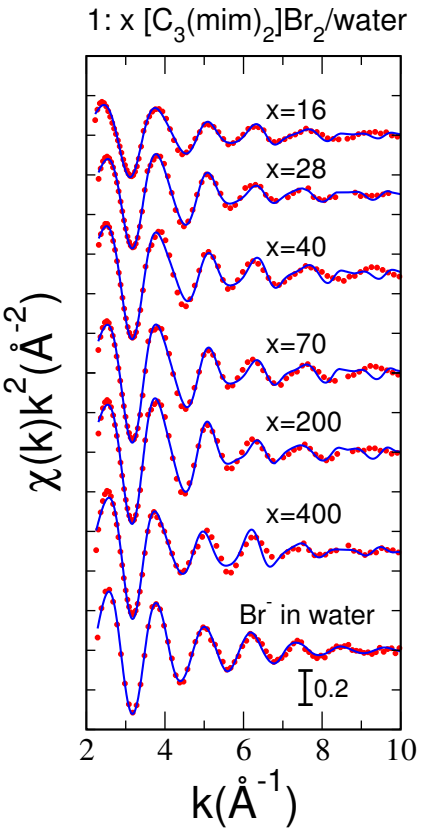

Figure 7.6: EXAFS experimental spectra (dotted red line) of the $[C_3(mim)_2]Br_2$/water mixtures compared with the theoretical signals (solid blue line) calculated from the MD Br-O and Br-HW $g(r)$'s. The EXAFS experimental spectrum of a 0.1 M Br^- aqueous solution in comparison with the theoretical signal is also shown.

7.7. Note that identical results have been obtained by choosing for the $g(r)$ calculation the geometrical center of the other imidazolium ring or both geometrical ring centers. Moreover, by calculating all of the $[C_3(mim)_2]^{2+}$-Br site-site $g(r)$'s it has been found that the Br^- ions are preferentially located around the HCR and HCW hydrogen atoms of the imidazolium rings. The HCR-Br and HCW-Br $g(r)\rho$'s are reported in panels B and C of Figure 7.7, respectively. Similar results have been found in a MD investigation of pure $[C_n(mim)_2]X_2$ DILs with X = Br^-, $BF4^-$ and $PF6^-$.[36] As regards the nature of the interaction between the hydrogen atoms of the cation and the anion in alkylimidazolium based ILs, it is now well-recognized that it is due to the formation of hydrogen bonds, that can affect the properties and the physical states of ILs.[126] Finally, as expected, the dications also interact with water molecules. The dication-water interaction is weaker as compared to the Br^--water one, as shown by the less defined and less pronounced first shell peak of the $[C_3(mim)_2]^{2+}$-O $g(r)\rho$'s (panel A′ of Figure 7.7). Also in this case, only one of the two ring geometrical centers of the $[C_3(mim)_2]^{2+}$ dication has been taken into account. Moreover, as found for the Br^- ions, the water molecules are mainly associated with the HCR and HCW hydrogen atoms of the imidazolium rings. The HCR-O and HCW-O $g(r)\rho$'s are depicted in

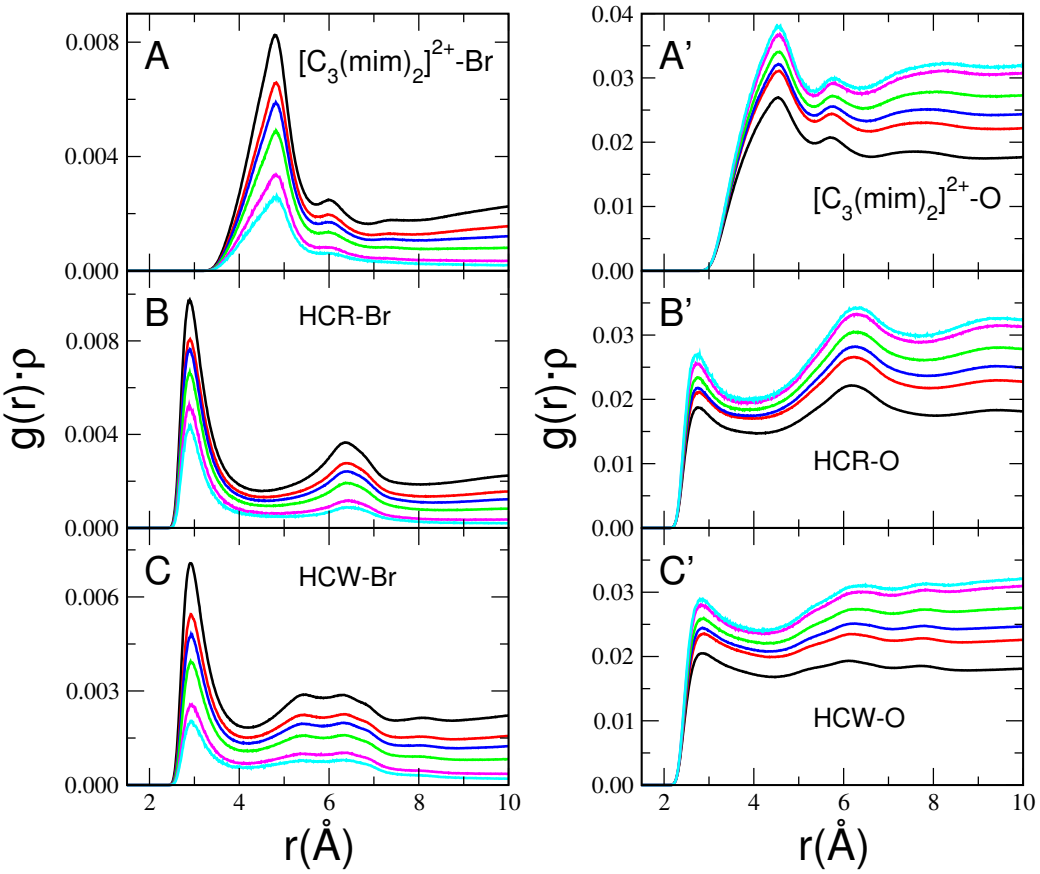

Figure 7.7: Radial distribution functions multiplied by the numerical density of the observed atom, $g(r)\rho$'s, calculated from the MD simulations of the 1:16 (black), 1:28 (red), 1:40 (blue), 1:70 (green), 1:200 (magenta) and 1:400 (cyan) $[C_3(mim)_2]Br_2$/water mixtures. Note that in the calculation of the $[C_3(mim)_2]^{2+}$-Br and $[C_3(mim)_2]^{2+}$-O $g(r)\rho$'s only one of the two ring geometrical centers of the $[C_3(mim)_2]^{2+}$ dication has been taken into account.

panels B′ and C′ of Figure 7.7, respectively. All of the $[C_3(mim)_2]Br_2$/water solutions show a first distinct peak in the HCR-O and HCW-O $g(r)\rho$'s, and the HCR-O and HCW-O coordination numbers increase with increasing water content (see Table 7.4).

Figure 7.8 shows the 3D-organization of the Br^- ions (yellow isosurfaces) and water molecules (blue isosurfaces) around one of the two imidazolium rings of the $[C_3(mim)_2]^{2+}$ dication. The isosurfaces around the other ring have been omitted, for clarity. Note that we have used the same absolute densities for all of the mixtures. Going from low to high diluted solutions there is a clear evolution of the dication environment that progressively loses bromide ions to accomodate more and more water molecules. In particular, the Br^- ions are mainly found in proximity of the three hydrogen atoms of the imidazolium ring, with an almost identical spatial arrangement around them. The anion can be both in the imidazolium ring plane and above or below the plane itself. This result is in line with previous investigations of pure $[C_n(mim)_2]X_2$ DILs [36] and DILs/water mixtures.[54] As far as the dication-water interaction is concerned, the water molecule distribution is

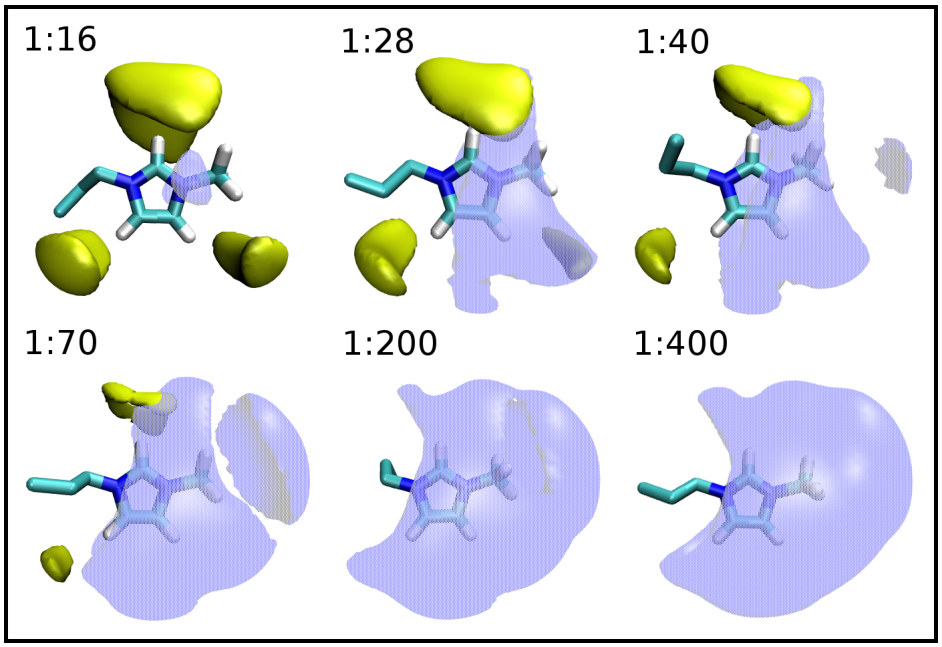

Figure 7.8: Spatial distribution functions (SDFs) of Br^- ions (yellow) and oxygen atoms of water molecules (blue) around one of the two rings of the $[C_3(mim)_2]^{2+}$ dication calculated from the MD simulations of the $[C_3(mim)_2]Br_2$/water mixtures. Note that the hydrogen atoms of the spacer and the second imidazolium ring have been omitted, for clarity.

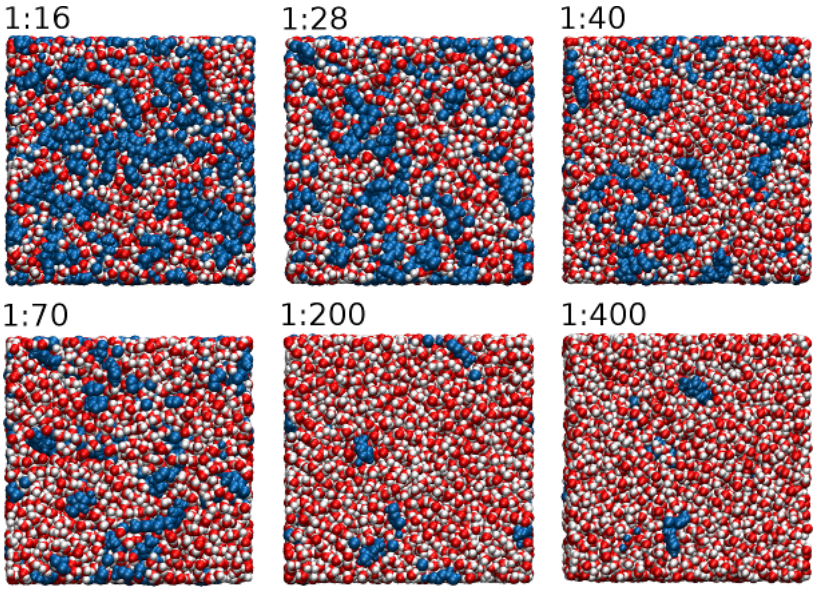

Figure 7.9: MD simulation snapshots of the $[C_3(mim)_2]Br_2$/water mixtures in which the water molecules are highlighted and the DIL ion pairs are colored blue.

less site-specific as compared with the Br^- isosurfaces, and much more unstructured and broadened with increasing dilution.

It is also interesting to observe that water molecules in the mixtures tend to aggregate and form water clusters. A pictorial description of this be-

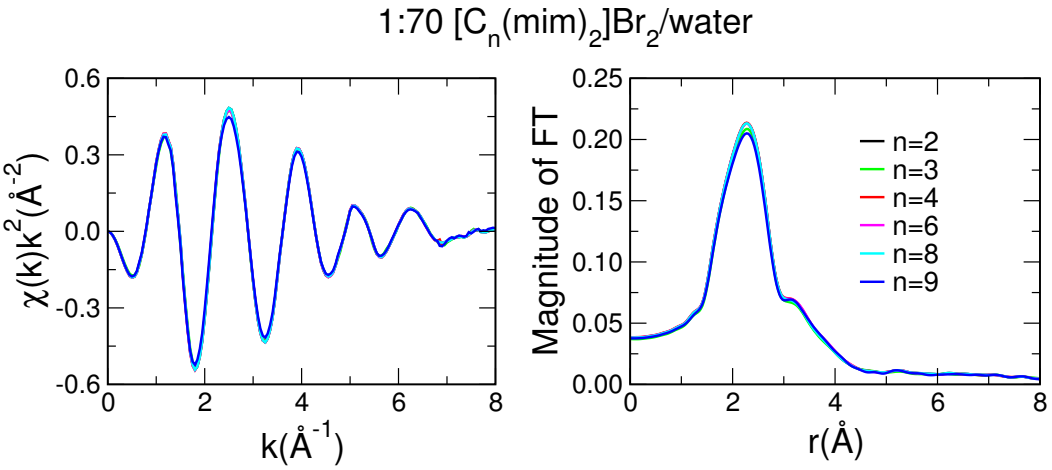

Figure 7.10: Left panel: EXAFS experimental spectra of the 1:70 [C_n(mim)$_2$]Br$_2$/water mixtures with a spacer of 2, 3, 4, 6, 8 and 9 carbon atoms. Right panel: Fourier Transforms of the experimental data.

havior is given in Figure 7.9, where some MD snapshots are reported in which water molecules are highlighted. String-like clusters are visible in the [C_3(mim)$_2$]Br$_2$/water mixtures with 1:16 and 1:28 molar ratios, as already observed in water solutions of monocationic [C_6mim]I IL (see Chapter 6). Then, with increasing water content very large clusters are formed percolating through the sample. Moreover, due to the short length of the spacer no aggregates among the dications are found and the water clusters are able to cross the simulation boxes from one side to the other in all the mixtures.

7.3 1:70 [C_n(mim)$_2$]Br$_2$/water mixtures: effect of the spacer length

The EXAFS experimental data of the [C_3(mim)$_2$]Br$_2$/water mixtures as a function of water concentration in conjunction with the MD results have revealed that water molecules are preferentially coordinated with the bromide ion, whose first coordination shell becomes more and more populated going from the 1:16 to the 1:400 DIL/water mixture, and that a complex network of interactions among dications, anions and water molecules takes place. We are now interested in understanding how the interactions between DIL ion pairs and water molecules in DIL/water mixtures are influenced by the length of the spacer chain. To this end we have collected the EXAFS experimental spectra of [C_n(mim)$_2$]Br$_2$/water mixtures having the same constant DIL/water molar ratio of 1:70 and varying n from 2 to 9, and then we have carried out MD simulations of the same solutions. The EXAFS experimental spectra, extracted with a three-segmented cubic spline function, are shown in Figure 7.10, together with the FTs calculated in the interval $k = 0.7$ to 12 Å^{-1}. As it can be seen, both the EXAFS and FT signals are almost identical for all the solutions. These findings are in line with the results obtained from the MD simulations. In fact, the Br-O and Br-HW $g(r)\rho$'s, depicted in panel

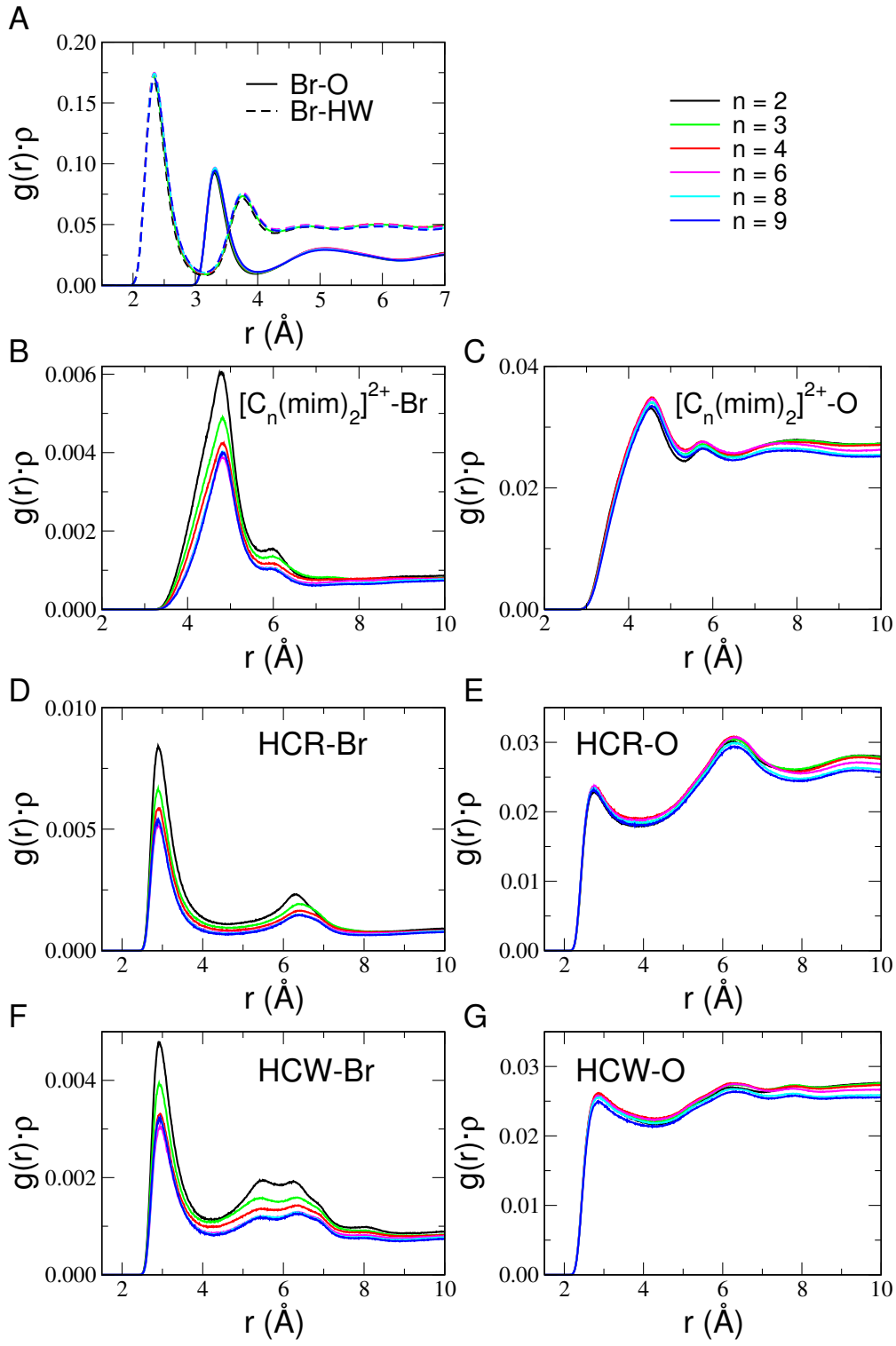

Figure 7.11: Radial distribution functions multiplied by the numerical density of the observed atoms, $g(r)\rho$'s, calculated from the MD simulations of the 1:70 $[C_n(mim)_2]Br_2$/water mixtures with different spacer chain lengths (n). Note that in the calculation of the $[C_n(mim)_2]^{2+}$-Br and $[C_n(mim)_2]^{2+}$-O $g(r)\rho$'s only one of the two ring geometrical centers of the $[C_n(mim)_2]^{2+}$ dication has been taken into account.

	r(Å)					
n	2	3	4	6	8	9
Br-O	3.33	3.33	3.33	3.33	3.33	3.33
$[C_n(mim)_2]^{2+}$-O	4.55	4.55	4.55	4.55	4.55	4.55
$[C_n(mim)_2]^{2+}$-Br	4.82	4.82	4.82	4.82	4.82	4.82
HCR-O	2.75	2.75	2.75	2.75	2.75	2.75
HCW-O	2.85	2.85	2.85	2.85	2.85	2.85
HCR-Br	2.90	2.90	2.90	2.90	2.90	2.90
HCW-Br	2.93	2.93	2.93	2.93	2.93	2.93

Table 7.5: Position of the $g(r)$ first peak, r, obtained from the MD simulations of the 1:70 $[C_n(mim)_2]Br_2$/water mixtures with different spacer chain length (n).

	N						cutoff (Å)
n	2	3	4	6	8	9	
Br-O	5.5	5.8	5.9	6.0	6.0	6.0	4.0
$[C_n(mim)_2]^{2+}$-O	13.1	13.4	13.7	13.6	13.3	13.2	5.3
$[C_n(mim)_2]^{2+}$-Br	1.9	1.6	1.4	1.2	1.2	1.2	5.8
HCR-O	5.2	5.3	5.5	5.4	5.3	5.3	4.3
HCW-O	6.2	6.3	6.4	6.3	6.2	6.1	4.3
HCR-Br	0.8	0.7	0.6	0.5	0.5	0.5	4.5
HCW-Br	0.6	0.5	0.5	0.4	0.4	0.4	4.5

Table 7.6: Coordination number, N, and cutoff distances obtained from the MD $g(r)$'s of the 1:70 $[C_n(mim)_2]Br_2$/water mixtures with different spacer chain length (n). Note that the cutoff distance has been chosen as the position of the $g(r)$ value first minimum.

A of Figure 7.11, look very similar and the Br-O coordination number only varies from 5.5 to 6.0 in going from $n = 2$ to $n = 9$ (see Tables 7.5 and 7.6 for the position of the $g(r)$ first maximum and the coordination numbers, respectively). The MD results are in agreement with the experimental data, as the error in the determination of coordination numbers is ±0.5 when the EXAFS technique is applied to the investigation of disordered systems. Also in this case, EXAFS $\chi(k)$ theoretical signals have been calculated by introducing the Br-O and Br-HW $g(r)$'s in eq. 2.6, using the procedure described previously. The comparison between the experimental and theoretical curves is shown in Figure 7.12 for all of the mixtures under investigation. The experimental spectrum matches the theoretical one in all cases proving again the validity of the MD potential and the reliability of the structural results.

Panel B of Figure 7.11 shows the $[C_n(mim)_2]^{2+}$-Br $g(r)\rho$'s, calculated between one of the two ring geometrical centers of the $[C_n(mim)_2]^{2+}$ dication

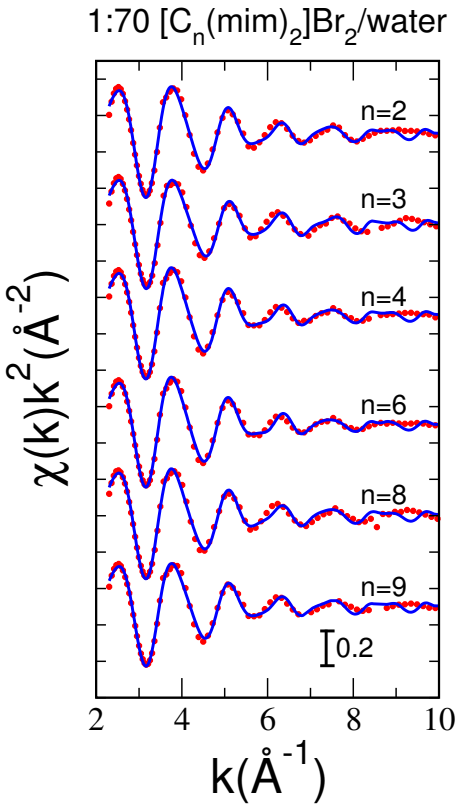

Figure 7.12: EXAFS experimental spectra (dotted red line) compared with the theoretical signals (solid blue line) calculated from the MD simulations of the $[C_n(mim)_2]Br_2$/water mixtures with a constant DIL/water molar ratio of 1:70.

and the bromide ions. All the $g(r)\rho$'s feature a sharp peak centered at 4.82 Å, indicating that the Br^- ion first shell distance around the dication is the same independently from the spacer length. Conversely, the $[C_n(mim)_2]^{2+}$-Br coordination number slightly decreases from 1.9 to 1.2 with increasing the spacer chain length, thus suggesting that there is a reduction of the Br^- ion organization around the dication. The site-site HCR-Br and HCW-Br $g(r)\rho$'s are shown in panels D and F of Figure 7.11, respectively. A similar finding has been previously observed in a MD investigation of $[C_n(mim)_2]Br_2$/water mixtures as a function of the spacer chain length.[54] The result can be explained by the fact that for the $[C_n(mim)_2]Br_2$/water mixtures with $n = 2$, 3, 4 a single bromide ion can simultaneously interact with the two rings of the same dication, forming a bridge between them. To provide visual insights, two representative MD snapshots extracted from the 1:70 $[C_3(mim)_2]Br_2$/water solution are shown in Figure 7.13, as an example. A remarkable observation is that in some cases the Br^- ion interacts with the HCR atoms of the two rings of the same $[C_3(mim)_2]^{2+}$ dication, but there is also the possibility for the anion to interact with the HCR atom of one imidazolium ring and the HCW atom of the other ring. Conversely, when the spacer is long (n $\geq$ 6), the Br^- ion can interact only with one of the two imidazolium rings as the spacer chain does not allow the simultaneous interaction of Br^- with both

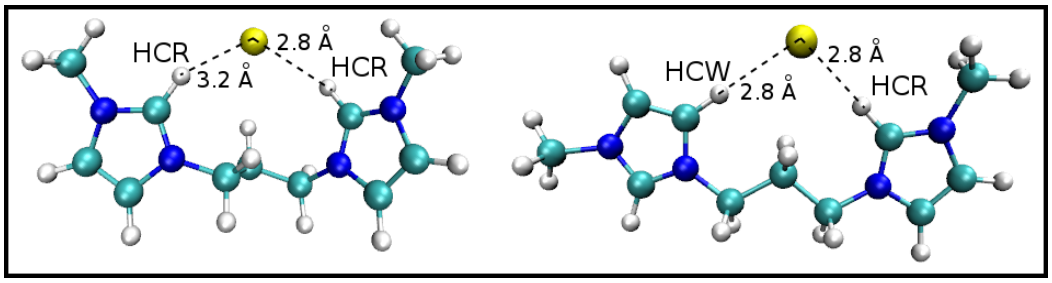

Figure 7.13: Simultaneous interaction of the Br^- ion (yellow) with the two imidazolium rings of the same $[C_n(mim)_2]^{2+}$ dication, as found in representative snapshots of the 1:70 $[C_3(mim)_2]Br_2$/water mixture simulation.

rings. Finally, in panel C of Figure 7.11 we provided the $g(r)\rho$'s between the geometrical center of one of the two rings of the $[C_n(mim)_2]^{2+}$ dications and the oxygen atoms of water molecules. A first distinct peak at 4.55 Å can be seen for all the 1:70 $[C_n(mim)_2]Br_2$/water solutions, and inspection of Table 7.6 shows that the $[C_n(mim)_2]^{2+}$-O coordination number is about 13. Also in this case, from the analysis of the $[C_n(mim)_2]^{2+}$-O site-site $g(r)$'s, it has been found that the water molecules preferentially coordinate the HCR and HCW hydrogen atoms of the imidazolium rings. The HCR-O and HCW-O $g(r)\rho$'s are depicted in panels E and G of Figure 7.11, respectively.

Figure 7.14 shows the C1-C1 intramolecular $g(r)$'s calculated from the MD trajectories of the 1:70 $[C_n(mim)_2]Br_2$/water mixtures (with n going from 3 to 9), where the two C1 atoms are the first and last carbon atom of the spacer (see Figure 7.1). This analysis allows one to understand which type of conformation (linear or folded) is assumed by the spacer chain. The theoretical distance of a linear (non-folded) conformation of the alkyl chain

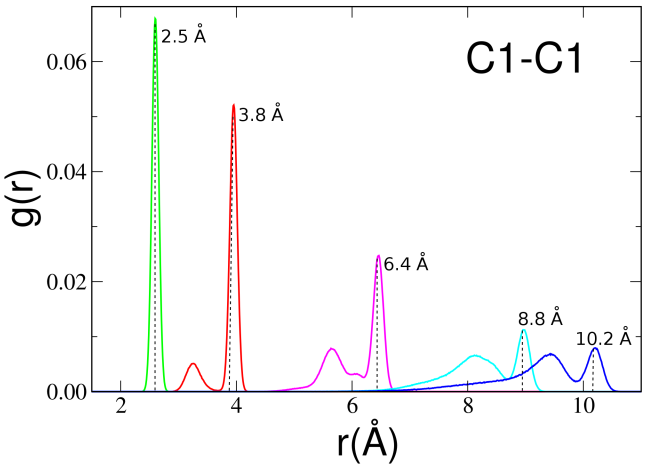

n	% linear	% folded
3	100	0
4	88	12
6	62	38
8	37	63
9	33	67

Figure 7.14: Left: intramolecular C1-C1 radial distribution functions, $g(r)$'s, obtained from the MD simulations of the 1:70 $[C_n(mim)_2]Br_2$/water mixtures with a spacer chain of 3 (green), 4 (red), 6 (magenta), 8 (cyan) and 9 (blue) carbon atoms. The dashed black lines represent the theoretical distances of a linear conformation of the spacer chain.
Right: percentage probability of the linear and folded conformations obtained from the MD C1-C1 $g(r)$'s.

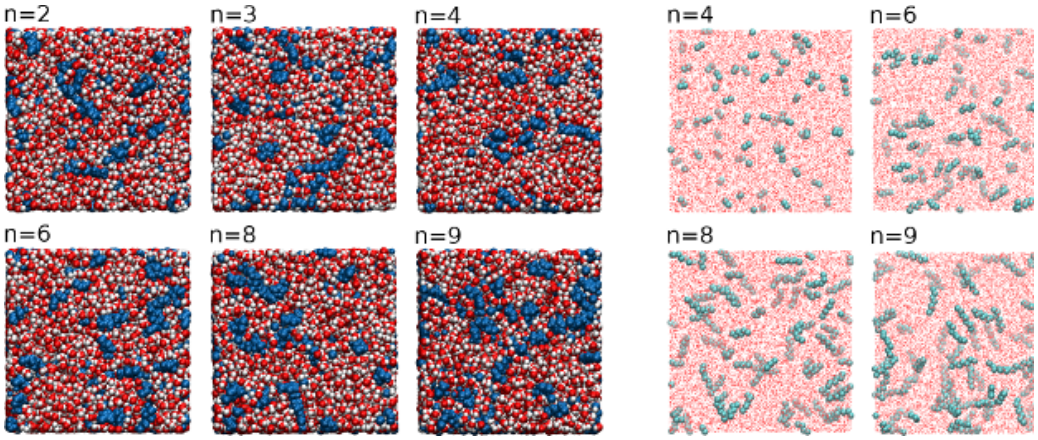

Figure 7.15: MD simulation snapshots of the 1:70 [C_n(mim)$_2$]Br$_2$/water mixtures. (Left panels) Water cluster formation: the water molecules are highlighted, while the DIL ion pairs are colored in blue. (Right panels) Aggregation behavior: the spacer chains are colored in cyan while all of the other atoms of the system are represented as red dots.

is marked by a dashed black line in the Figure for each system. For $n = 3$ the $g(r)$ shows only one defined sharp peak, centered at 2.5 Å, while two peaks can be seen in all other systems. This means that the linear conformation is the only possible one for the [C_3(mim)$_2$]Br$_2$ DIL, while both linear and folded conformations are found when n $\geq$ 4. We have also calculated the percentage probability of the two conformations multiplying the $g(r)$'s by $4\pi r^2$ and then integrating it. The obtained values indicate that the probability of finding the spacer in the linear conformation decreases with increasing the spacer length, and for the [C_8(mim)$_2$]Br$_2$ and [C_9(mim)$_2$]Br$_2$ DILs the most probable conformations are the folded ones.

In Chapter 6 we have seen that long chain monocationic imidazolium based ILs undergo aggregation behavior beyond a critical aggregation concentration (CAC) and form micelle-like structures. It is now interesting to see if dicationic ILs behave in a similar way to their monocationic counterparts. It should be noted that dicationic ILs possess lower CAC values as compared to monocationic ILs having an equal ratio of hydrophilic to hydrophobic portions.[55] In order to address this issue we have reported in Figure 7.15 (right) some MD snapshots of the simulation boxes, where the polar regions (imidazolium rings, Br^- ions and water molecules) are represented as red dots, while the spacer chains are highlighted. No evidence of the aggregation of the spacer chains has been found with increasing the number of carbon atoms of the chain. In fact, the spacer chains exist as isolated units, completely separated from each other in all the solutions. A different result has been obtained from a MD study of 1:25 and 1:50 [C_8(mim)$_2$]Br$_2$/water mixtures where a few dimers and trimers are present.[54] The difference can be ascribed to the higher water concentration of our solutions. Finally, it is interesting to observe the molecular state of water in the solutions by looking at Figure 7.15 (left). Due to the high amount of water, very large clusters of water molecules are formed in all the solutions percolating through the

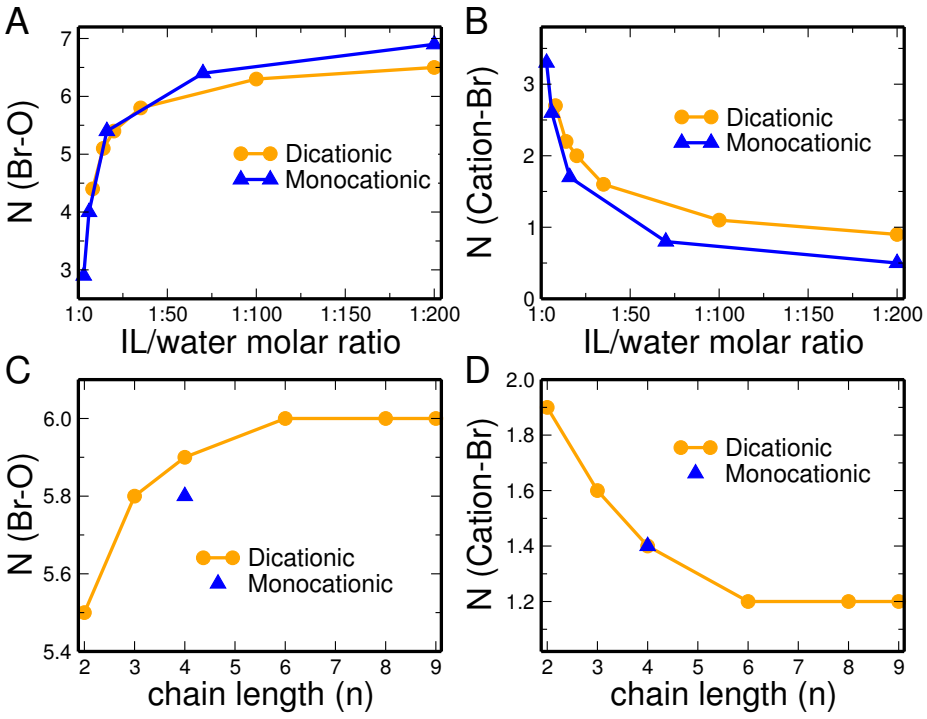

Figure 7.16: Br-O (A) and Cation-Br (B) coordination numbers obtained from the MD simulations of the $[C_3(mim)_2]Br_2$/water (orange circles) and $[C_4mim]Br$/water (blue triangles) mixtures with different molar ratios. The DIL/water molar ratios have been divided by a factor of two. Br-O (C) and Cation-Br (D) coordination numbers obtained from the MD simulations of the 1:70 $[C_n(mim)_2]Br_2$/water mixtures (orange circles) with different spacer length (n). The coordination numbers extrapolated for a 1:35 $[C_4mim]Br$/water mixture are also shown as blue triangles.

sample.

7.4 Monocationic *vs* dicationic ILs

A very interesting issue when dealing with DILs is the comparison with their monocationic counterparts. In particular, in this work, we have decided to compare the structural properties of the $[C_n(mim)_2]Br_2$/water mixtures together with the properties of aqueous solutions of a monocationic IL, namely $[C_4mim]Br$, in a wide range of water concentration (IL/water molar ratios of 1:3, 1:6, 1:16, 1:70 and 1:200), previously studied by our group of research (all the experimental and MD details can be found in Ref [124] and [51]). In panels A and B of Figure 7.16 we show the Br-O and the Cation-Br coordination numbers, respectively, obtained from the $[C_3(mim)_2]Br_2$/water mixtures and $[C_4mim]Br$/water mixtures with different molar ratios. The Cation-Br coordination numbers refer to the interaction between the bromide ion and the geometrical center of the $[C_4mim]^+$ cation ring for the monocationic system, or one of the two ring geometrical centers of the $[C_3(mim)_2]^{2+}$ for the dicationic one. It should be noted that we have divided by a factor of two the molar ratios of the DIL/water solutions to properly compare the different

concentrations of the solutions. This means that the DIL/water molar ratio in the Figure corresponds to the number of water molecules per subunit of the $[C_n(mim)_2]Br_2$ DIL, which is formed by a single imidazolium ring and a single Br^- ion. As it can be seen, the Br-O coordination numbers increase as the water concentration increases for both monocationic and dicationic ILs, while the Cation-Br coordination numbers decrease. However, we can notice that the Br-O coordination numbers of monocationic and dicationic ILs are substantially the same for low amount of water, while they are different under high dilution conditions. In fact, the bromide ions are coordinated by a lower number of water molecules in the dicationic systems as compared to the monocationic ones. This result can be explained by looking at the Cation-Br coordination numbers: they are always higher in the DIL systems, and the difference between monocationic and dicationic IL/water solutions becomes more pronounced with increasing water concentration. This is due to the fact that when the DIL has a short spacer chain a Br^- ion can simultaneously interact with the two rings of the same dication, with a consequent increase of cation-anion interactions as compared to monocationic ILs. In this way, the bromide ion, accomodating more cations in its first solvation shell, coordinates less water molecules in comparison with the monocationic systems. Clearly, the difference is more pronounced at high water content, as the number of cations able to interact with the anions is very low.

As expected, also the spacer length can influence the structural properties and the Br^- coordination of the investigated systems. Panels C and D of Figure 7.16 show the Br-O and the Cation-Br coordination numbers, respectively, calculated from the MD simulations of the 1:70 $[C_n(mim)_2]Br_2$/water mixtures as a function of the spacer length (n = 2, 3, 4, 6, 8, 9). Inspection of the Figure reveals that the Br-O coordination numbers increase with increasing n, while the Cation-Br coordination numbers decrease, reaching a plateau for n $\geq$ 6. In order to understand how the structural properties of the DILs are influenced by the spacer with respect to their monocationic counterparts, we have shown the Br-O and Cation-Br coordination numbers of a $[C_4mim]Br$/water mixture in panels C and D of Figure 7.16, respectively. To be comparable with the DIL/water mixtures with 1:70 molar ratio, these coordination numbers have been extrapolated from the data sets of panels A and B for an IL/water molar ratio of 1:35. Also in this case the Br-O coordination number trend can be explained as a consequence of the variation of dication-Br interactions that take place when the spacer length is modified. The Cation-Br coordination numbers for the 1:70 $[C_n(mim)_2]Br_2$/water solutions with n = 2, 3 are larger than the one obtained for the monocationic IL/water mixture. As mentioned before, in DILs with short spacer chain the Br^- ion can simultaneously interact with both rings of the same dication, thus leading to an increase of the cation-anion interactions. When n = 4 the Cation-Br coordination numbers in monocationic and dicationic ILs are identical, and finally for n = 6, 8, 9 they keep a constant value that is slightly lower with respect to the one obtained for the monocationic IL. These findings suggest that long spacers in dicationic ILs slightly hamper the interactions

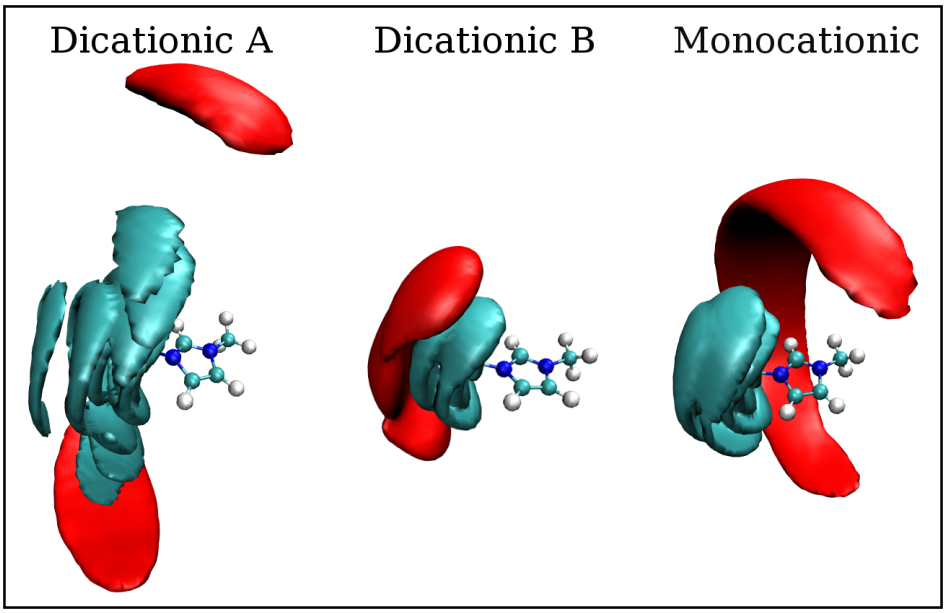

Figure 7.17: Intramolecular spatial distribution functions (SDFs) of the spacer (cyan) and of one imidazolium ring (red) around the other one obtained from the MD simulations of the 1:70 $[C_9(mim)_2]Br_2$/water (Dicationic A) and 1:70 $[C_3(mim)_2]Br_2$/water (Dicationic B) mixtures. The SDFs for the spacer chain have been computed by taking into account all of the carbon atoms, while for the imidazolium ring the geometrical center has been considered. SDFs of the butyl chain (cyan) and of the cation imidazolium rings (red) with respect to the imidazolium ring of one reference cation computed from the MD simulation of $[C_4mim]Br$/water mixture with a 1:16 molar ratio (Monocationic).

between cations and anions. In order to get visual insights, we have calculated the intramolecular SDFs of the spacer chain and of one imidazolium ring around the other ring of the $[C_n(mim)_2]^{2+}$ dication, that has been taken as the reference system (see Figure 7.17). Note that all of the chain carbon atoms have been included in the calculation of the spacer SDF, while for the imidazolium ring it has been considered the imidazolium ring geometrical center. As regards the 1:70 $[C_n(mim)_2]Br_2$/water mixture with $n = 9$ (Dicationic A), the two imidazolium rings tend to position themselves above and below each other forming π-π stacking interactions, with the spacer extending perpendicularly to the imidazolium ring plane. As a consequence, on the one hand the spacer slightly hampers the approach of the bromide ion towards the imidazolium ring due to its steric hindrance, and on the other it repels water molecules due to its hydrophobic character. This peculiar internal arrangement undertaken by the dication can explain the reduction of interactions between dications and anions found in the 1:70 $[C_n(mim)_2]Br_2$/water mixtures with a long spacer ($n \geq 6$). Conversely, for the water solutions of $[C_n(mim)_2]Br_2$ with a short spacer chain (Dicationic B), both the spacer and the second imidazolium ring are found in a wide region of space on the lateral side of the ring plane and not perpendicular to it. Now, in order to compare these structural results with those of monocationic ILs, we have computed the SDFs of the butyl chain and of the cation imidazolium rings with respect

to the imidazolium ring of one reference cation for the $[C_4mim]Br$/water mixture with 1:16 molar ratio (Monocationic). As it can be seen, the butyl chains are found to extend laterally to the imidazolium ring, and the imidazolium rings of other cations are located in a wide region of space encircling, on one side, the central ring. These different structural properties of dicationic ILs in comparison with their monocationic counterparts could be the reasons of their increased stability and other peculiar distinguishing features.

Chapter 8

Ionic Liquids as solvents for rare-earth metals

Lanthanoids, which form the f-block of the periodic table (the "southern island", according to the definition of Atkins), are the most extended series of chemically similar metal ions. These elements were first classified as "rare-earth" due to the fact that obtained by reasonably rare minerals. However, this can be misleading since the lanthanide elements have a practically unlimited abundance. The pure metals of lanthanoids have very little use. However, the alloys of metals can be very useful; for example the alloys of Cerium have been used for metallurgical applications due to their strong reducing abilities. They can be also used for ceramic purpose, to improve the intensity and color balance of arc lights, or as contrast agents in magnetic resonance imaging for medical diagnosis. Moreover, lanthanoids can be employed for nuclear purposes: the oxides can be used as diluents in nuclear fields, the metals can be used for structural-alloy-modifying components of reactors. The hydrides can be used as hydrogen-moderator carriers. Eu is a radiation sources, while other elements, such as Tm, can be used as portable X-ray sources.[127, 128, 129, 130] Lanthanoids are almost always present in the +3 oxidation state, which is the most stable state, but they can also have an oxidation state of +2 or +4. The progressive filling of the 4f orbitals from La(III) to Lu(III) is accompanied by a smooth decrease in ionic radius with increase in atomic number, as a consequence of the increasingly strong nuclear attraction for the electrons in the diffuse f orbitals. These orbitals are shielded by the surrounding filled 5s and 5p ones, leading to very small crystal field splittings in the lanthanide complexes. This means that the coordination properties of the Ln(III) ions do not depend on differences in the electronic structure of the cation, but on the electrostatic and steric nature of the ligands.

As illustrated in the Introduction Chapter (see Section 1.3), ILs have been recently considered in several processes involving Ln(III) ions, such as liquid-liquid extraction, separation and purification, and nuclear waste management, due to their many unique properties and their "green characteristics".[57, 58, 59, 60] Thus, understanding the solvation properties of Ln(III) ions in ILs is

fundamental to improve the efficiency of extraction procedures and to select the best performing solvents. In particular, in this work, we will investigate the solvation properties of a light lanthanoid (III) ion, the Ce(III), in a protic IL namely Ethylammonium nitrate (EAN) by combining Classical MD simulations and XAS spectroscopy.

It is well-known that Classical MD simulations require interaction potentials between all the particles concerned. However, while in the literature there is a large variety of force fields for ILs, we did not find Lennard-Jones interaction potentials for the Ce(III) cation to be combined with the Lennard-Jones parameters of all other atoms of the system. So, we have first developed new Ce-Ce Lennard-Jones parameters starting from the optimization of the interaction potentials of Ce(III) ion in water, in order to correctly reproduce the structural properties of the Ce(III) hydration complexes. To this end, we have compared the structural results obtained from Classical MD simulations with EXAFS experimental data, as the combined MD-XAS approach has revealed to be particularly well-suited to assess whether the interaction potentials used in the simulations are able to provide a reliable structural description of the systems. In this context, we also extended the optimization procedure to the entire lanthanoid series, and this is the first time that a new set of Lennard-Jones parameters to be used in Classical MD simulations of Ln(III)-containing systems has been developed for the entire series. The availability of non-polarizable force field for Ln(III) ions and, in particular, in the Lennard-Jones formulation, is well recognized in the literature, as this force field can be easily applied for the study of a large variety of Ln(III)-containing systems, ranging from inorganic to bioinorganic chemistry, that is beyond the scope of this work. In the former case (inorganic chemistry) it is interesting to study the interactions that take place between Ln(III) ions and inorganic anions, such as carbonate, perchlorate and nitrate anions, as Ln(III) ions can form different complexes in which these anionic ligands replace the solvent molecules. In the latter case (bioinorganic chemistry), Ln(III) ions can be combined with proteins for several applications, such as live cell imaging studies of protein activity and interactions or for the development of lanthanide-based biosensors. As an example, a recent MD investigation of uranyl uptake by proteins has demonstrated the necessity of having a non-polarizable interaction potential to study the cation-protein binding process.[131] In conclusion, our developed parameters can be combined with force-field parameters available in the literature in order to obtain pair potentials involving Ln(III) ions in other disordered systems, as the most straightforward way to study Ln(III) ions in complex liquid media is to carry out Classical MD simulations without polarizing effects, in which the interactions among all atoms are described by means of computationally efficient Lennard-Jones interaction potentials.

8.1 Development of Ln-Ln Lennard-Jones interaction potentials

8.1.1 Experimental Methods

X-ray absorption measurements. 0.2 M Ln(III) aqueous solutions were obtained by dissolving in freshly distilled water the stoichiometric amount of hydrated trifluoromethanesulfonates $[Ln(H_2O)_n](CF_3SO_3)_3$ (in which Ln = La, Ce, Pr, Nd, Sm, Eu, Gd, Tb, Dy, Ho, Er, Tm, Yb, Lu). In order to avoid hydrolysis, trifluoromethanesulfonic acid was used to acidify the solution to about pH=1. At the low concentration used in the experiments, there are about 277 water molecules for each Ln(III) ion in the solution, so that ion-water clusters involving more than one lanthanide ion are not expected to be present. The spectra were collected at the Ln K-edge in transmission geometry, on the BM23 beam line at the European Synchrotron Radiation Facility of Grenoble. The storage ring was operating in 16-bunch mode with a typical current of 80 mA after refill. A Si(511) double-crystal monochromator was used for the data acquisition, with the second crystal detuned by 20% for harmonic rejection. The aqueous solutions were kept in cells with Kapton film windows and Teflon spacers ranging from 2 to 3 cm depending on the sample. Internal energy calibration was made when possible with a foil of the corresponding lanthanoid metal.

Molecular Dynamics details. Classical MD simulations of Ln(III) aqueous solutions (in which Ln = La, Ce, Pr, Nd, Sm, Eu, Gd, Tb, Dy, Ho, Er, Tm, Yb, Lu) have been carried out in the NVT ensemble at 300 K (the Nosé-Hoover thermostat was used to control the temperature [87, 88]) by means of the DL_POLY code.[86] Two different sets of simulations were performed using the SPC/E model for water,[94] and either Lennard-Jones or Buckingham potentials to describe the van der Waals interactions between the Ln(III) ion and the water molecules. The Lennard-Jones or Buckingham potential parameters were developed in order to reproduce the structural properties of Ln(III) solvation complexes in water, as discussed in the Results section. Note that in analogy with the SPC/E water model, the van der Waals interactions involving hydrogen atoms of water molecules were set to zero. As regards the Ln(III)-water electrostatic interactions, they were modelled by including Coulombic interactions between the 3+ charge on the cation and the partial atomic charges of the SPC/E model on the water molecule. The systems were composed of 1 Ln(III) ion and 819 water molecules in a 29.1 Å edge cubic box, replicated using periodic boundary conditions. The box volume has been chosen to reproduce the water density (996.557 g/L) at temperature and pressure conditions of 300 K and 1 atm, respectively. Note that using this box volume the number density of oxygen atoms in our simulation boxes (0.0333 $Å^{-3}$) is identical to the one previously used in Ref [132] to carry out MD simulations of Ln(III) aqueous solutions where explicit polarization was included in the classical force field. Long-range electrostatic interactions were calculated through the particle mesh Ewald method,[89] while a cut-off

of 9 Å was adopted for the nonbonded ones. All of the simulations have been carried out for 10 ns, after an equilibration run of 3 ns, using a time step of 1 fs and saving a configuration every 25 timesteps.

8.1.2 Results

The Ln(III)-water interaction potentials have been developed in order to correctly reproduce the structural properties of Ln(III) hydration complexes (radial distribution of water molecules around the Ln(III) ions, coordination number trend along the series and geometry of the first-shell complexes). To this end we have decided to directly compare the structural results derived from the MD simulations with the EXAFS experimental data, as this combined MD-EXAFS approach has revealed to be a powerful tool to check the performance of a classical force field. In particular, the force-field parameters have been refined in order to reproduce the Ln(III)-water EXAFS experimentally inferred first-shell peak mean distances, as they represent the most accurate structural information that can be obtained from this experimental technique. Indeed, the Ln-O average distances have been recently determined from an improved analysis of the EXAFS experimental data and, starting from these mean distances, a new set of ionic radii for Ln(III) ions in aqueous solution has been also derived.[132] However, it is important to stress that, in order to properly compare the Ln-O first-shell mean distances obtained from the simulations with those determined from the EXAFS analysis, the first peak of the Ln-O MD $g(r)$'s has been modeled with gamma-like distribution functions, using eq. 2.5. Note that the calculated R values are the average distances of the distributions that are shifted toward larger values with respect to the maximum of the $g(r)$'s because of the shell asymmetry.

In the first step of the work we have used the Ln-O mean distances to refine a set of Ln-O Lennard-Jones potentials, given by the following equation:

$$V_{LnO}^{LJ}(r) = 4\epsilon_{LnO}\left[\left(\frac{\sigma_{LnO}}{r}\right)^{12} - \left(\frac{\sigma_{LnO}}{r}\right)^{6}\right] \tag{8.1}$$

where the first term is a steep repulsive term describing the Pauli repulsion due to the overlap of the electronic clouds, while the second one is a smoother attractive term, representing the London dispersion forces. In this formalism, $V_{LnO}^{LJ}(r)$ depends on two parameters: (i) ϵ_{LnO}, which is the potential well depth and it represents a measure of how strongly the two interacting particles attract each other; (ii) σ_{LnO}, the distance at which the intermolecular potential is zero, giving a measurement of how close two nonbonding particles can get. Even if the Lennard-Jones potential is not the most faithful representation of the potential energy surface, its use is widespread due to its simple form, computational efficiency and excellent transferability characteristics. In fact, it can be easily generalized to be used in combination with commonly available force fields. Initial σ_{LnO} and ϵ_{LnO} values for the development of the Lennard-Jones potentials were taken from the ones previously used to describe the interaction between the Nd(III) ion and the oxygen

	Lennard-Jones Ln-O		Lennard-Jones Ln-Ln	
Ln	σ_{LnO}	ϵ_{LnO}	σ_{LnLn}	ϵ_{LnLn}
La	3.310	0.4308	3.454	0.2855
Ce	3.285	0.4308	3.404	0.2855
Pr	3.268	0.4308	3.369	0.2855
Nd	3.229	0.4308	3.292	0.2855
Sm	3.174	0.4308	3.182	0.2855
Eu	3.143	0.4308	3.120	0.2855
Gd	3.117	0.4308	3.068	0.2855
Tb	3.090	0.4308	3.014	0.2855
Dy	3.068	0.4308	2.970	0.2855
Ho	3.043	0.4308	2.919	0.2855
Er	3.029	0.4308	2.892	0.2855
Tm	3.017	0.4308	2.868	0.2855
Yb	3.007	0.4308	2.847	0.2855
Lu	2.997	0.4308	2.828	0.2855

Table 8.1: σ_{LnO} (Å) and ϵ_{LnO} (kJ/mol) Lennard-Jones parameters developed to describe the Ln-O interaction potentials. The σ_{LnLn} and ϵ_{LnLn} Lennard-Jones parameters for Ln-Ln interactions, obtained from the Ln-O parameters using the Lorentz-Berthelot mixing rules, are also reported.

atom of water molecules in a MD study of concentrated aqueous solutions of lanthanide salts.[133] Starting from these values, the optimization procedure involved the following three steps:

(i) Refinement of the σ_{LnO} and ϵ_{LnO} parameters for the first element of the series, the La(III) ion. In particular, we modify only the σ_{LnO} in order to reproduce the La-O EXAFS experimentally inferred mean first-shell distance.[132]

(ii) Initial guess for the σ_{LnO} parameters of the other Ln(III) ions. In this step, being the trend of Ln(III) ionic radii in aqueous solution very regular and nearly linear,[132] we have assumed that also the σ_{LnO} values decreased linearly in going from La(III) to Lu(III) ion. So, σ_{LnO} parameters have been calculated by scaling the σ_{LnO} value optimized for La(III) by the ionic radius difference between the La(III) and a given Ln(III) ion.

(iii) Optimization of the σ_{LnO} values, obtained in the previous step, on the basis of the Ln-O EXAFS experimentally inferred first-shell peak mean distances.

	N	R(Å)	σ^2(Å^2)	β
La-O	9.2	2.600	0.006	0.64
Ce-O	9.0	2.569	0.006	0.57
Pr-O	9.0	2.549	0.005	0.52
Nd-O	8.9	2.523	0.005	0.52
Sm-O	8.9	2.488	0.005	0.57
Eu-O	8.9	2.469	0.006	0.61
Gd-O	8.8	2.454	0.006	0.65
Tb-O	8.7	2.438	0.006	0.69
Dy-O	8.7	2.424	0.007	0.74
Ho-O	8.5	2.403	0.007	0.79
Er-O	8.3	2.390	0.007	0.80
Tm-O	8.1	2.373	0.006	0.78
Yb-O	8.0	2.359	0.006	0.73
Lu-O	7.9	2.346	0.005	0.68

Table 8.2: Ln-O first shell structural parameters of Ln(III) ions in aqueous solution obtained from the MD simulations carried out using the Lennard-Jones interaction potentials. N is the coordination number, R is the Ln-O average distance, σ^2 is the Debye-Waller factor, and β is the asymmetry parameter.

All the optimized Ln-O Lennard-Jones parameters are listed in Table 8.1. Note that the ϵ_{LnO} value refined for La(III) has been kept fixed through the series. The structural parameters obtained from the fitting procedure of the MD Ln-O $g(r)$'s by means of eq. 2.5 are collected in Table 8.2. If we look at Table 8.2 and Table 8.3, where the Ln-O first-shell structural parameters determined from the EXAFS analysis of Ref [132] are reported, it can be seen that the theoretical average distances calculated from the MD simulations are almost identical to the experimentally inferred ones for all of the Ln(III) aqua ions. This result is even more evident when plotting both theoretical and experimentally-inferred Ln-O mean distances as a function of the atomic number (see Figure 8.1). Note that, due to the lanthanoid contraction, the distances decrease smoothly with increasing atomic number.

Even if we were interested in developing Ln-Ln Lennard-Jones parameters to be used in Classical MD simulations of Ln(III)-containing systems, such as Ce(III) nitrate in the protic IL ethylammonium nitrate, we have decided to also develop a set of Buckingham interaction potentials describing the non-electrostatic interaction between the Ln(III) ions and the water molecules. In fact, previous works have shown that the Lennard-Jones potentials can in

	N	R(Å)	σ^2(Å^2)	β
La-O	9.1	2.600	0.010	0.47
Ce-O	9.0	2.570	0.010	0.48
Pr-O	9.0	2.550	0.011	0.49
Nd-O	9.0	2.525	0.010	0.50
Sm-O	9.0	2.490	0.010	0.52
Eu-O	9.0	2.470	0.009	0.55
Gd-O	9.0	2.455	0.009	0.59
Tb-O	9.0	2.440	0.008	0.61
Dy-O	9.0	2.425	0.008	0.64
Ho-O	8.9	2.405	0.008	0.65
Er-O	8.9	2.390	0.007	0.65
Tm-O	8.8	2.375	0.007	0.52
Yb-O	8.7	2.360	0.008	0.47
Lu-O	8.2	2.345	0.007	0.44

Table 8.3: Ln-O first shell structural parameters of Ln(III) ions in aqueous solution obtained from the EXAFS analysis of Ref [132]. N is the coordination number, R is the Ln-O average distance, σ^2 is the Debye-Waller factor, and β is the asymmetry parameter.

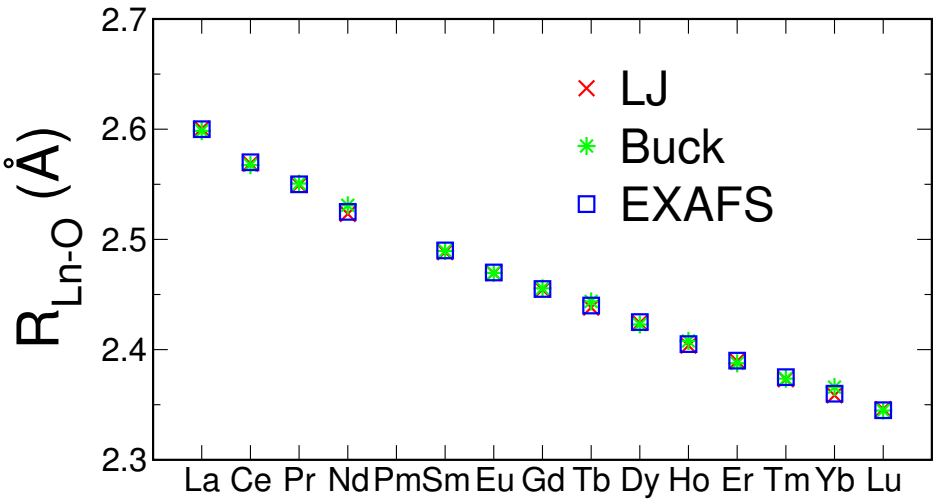

Figure 8.1: Ln-O first-shell average distances of Ln(III) ions in aqueous solutions obtained from the EXAFS experimental data (blue squares) compared with those obtained from the MD simulations carried out using either the Lennard-Jones (red crosses) or the Buckingham (green stars) interaction potentials.

some cases provide too structured Ln(III) hydration shells.[134] The Buckingham parameters can be, for example, used to describe specific interactions involving Ln(III) ions and oxygen-containing species, while treating the other interactions by means of the more standard Lennard-Jones potentials. The Buckingham potential is composed by a long range attractive term with $1/r^6$ behavior and a short range repulsive term modeled via an exponential function, that is more physical as compared to the Lennard-Jones repulsive term:

$$V_{LnO}^{Buck}(r) = A_{LnO}e^{-r/\rho_{LnO}} - \frac{C_{LnO}}{r^6} \tag{8.2}$$

In this formalism, three parameters enter to determine the energy values: A_{LnO}, which represents the height of the Buckingham repulsion, ρ_{LnO} and C_{LnO}. As in the case of the Lennard-Jones potentials, the development of the Buckingham potentials involved three steps:

(i) Refinement of the A_{LnO}, ρ_{LnO} and C_{LnO} parameters for the La(III) ion in order to obtain a La-O mean first-shell distance identical to the one obtained from the EXAFS experimental data.[132] As starting point, we have decided to convert the La-O Lennard-Jones potential into the Buckingham one using the DREIDING method, thus obtaining the initial A_{LnO}, ρ_{LnO} and

	Buckingham Ln-O		
Ln	A_{LnO}	ρ_{LnO}	C_{LnO}
La	318418	0.294276	2007.88
Ce	318418	0.291276	2007.88
Pr	318418	0.289276	2007.88
Nd	318418	0.286776	2007.88
Sm	318418	0.281340	2007.88
Eu	318418	0.278879	2007.88
Gd	318418	0.277327	2007.88
Tb	318418	0.276146	2007.88
Dy	318418	0.274384	2007.88
Ho	318418	0.273195	2007.88
Er	318418	0.271888	2007.88
Tm	318418	0.270863	2007.88
Yb	318418	0.270276	2007.88
Lu	318418	0.268776	2007.88

Table 8.4: A_{LnO} (kJ/mol), ρ_{LnO} (Å), and C_{LnO} (Å^6 kJ/mol) Buckingham parameters developed to describe the Ln-O interaction potentials.

	N	R(Å)	σ^2(Å^2)	β
La-O	9.0	2.598	0.012	0.54
Ce-O	8.9	2.567	0.010	0.53
Pr-O	8.9	2.551	0.010	0.55
Nd-O	8.8	2.531	0.011	0.57
Sm-O	8.8	2.489	0.012	0.68
Eu-O	8.7	2.469	0.013	0.74
Gd-O	8.6	2.456	0.013	0.78
Tb-O	8.5	2.444	0.013	0.81
Dy-O	8.3	2.423	0.013	0.83
Ho-O	8.2	2.408	0.013	0.83
Er-O	8.0	2.388	0.012	0.80
Tm-O	7.9	2.374	0.011	0.77
Yb-O	7.9	2.366	0.011	0.75
Lu-O	7.7	2.345	0.010	0.65

Table 8.5: Ln-O first shell structural parameters of Ln(III) ions in aqueous solution obtained from the MD simulations carried out using the Buckingham interaction potentials. N is the coordination number, R is the Ln-O average distance, σ^2 is the Debye-Waller factor, and β is the asymmetry parameter.

C_{LnO} values (see equations 31' and 32' of Ref [135]). Note that we used a scaling parameter (ζ) value of 13.772. Starting from these values, we have modified only the ρ_{LnO} value on the basis of the experimentally-inferred La-O mean first shell distance.[132]

(ii) Initial guess for the ρ_{LnO} parameters of the other Ln(III) ions calculated by scaling the ρ_{LnO} refined for La(III) and taking into account the decrease of ionic radii along the series.

(iii) Optimization of the ρ_{LnO} parameters on the basis of the Ln-O EXAFS experimentally inferred mean distances, while keeping fixed through the series the A_{LnO} and C_{LnO} values refined for La(III).

The optimized Buckingham parameters are listed in Table 8.4, while the Ln-O structural parameters obtained from the fitting procedure are collected in Table 8.5. Also in this case, the Ln-O first-shell mean distances calculated from the MD simulations and those determined from the EXAFS analysis are almost identical for the whole Ln(III) series (see Figure 8.1).

Figure 8.2 shows the optimized Lennard-Jones σ_{LnO} and Buckingham ρ_{LnO} parameters plotted as a function of the Ln(III) ion atomic number. Both σ_{LnO} and ρ_{LnO} decrease in going from La(III) to Lu(III) ion, as a con-

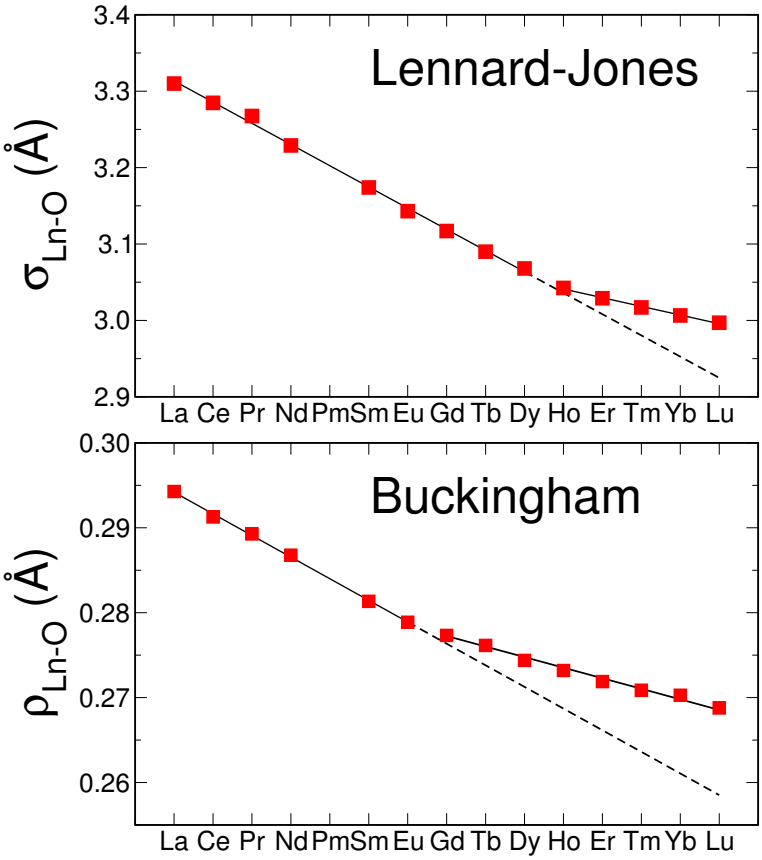

Figure 8.2: Lennard-Jones σ_{LnO} (upper panel) and Buckingham ρ_{LnO} (lower panel) parameters developed in this work to describe the Ln-O interaction potential.

sequence of the lanthanoid contraction. Moreover, two different linear trends are found: (i) for the Lennard-Jones potential the turning point from one slope to the other is between Dy(III) and Ho(III) ions, while for the Buckingham one is found between Eu(III) and Gd(III) ions. This change of slope can be due to the decrease of the Ln-O coordination number across the series, accompanied by a change in the first-shell hydration structure. The contraction of the hydration complexes with increasing atomic number leads to an increase of the repulsion among the first-shell water molecules. However, for the last elements of the series, due to the reorganization of the first hydration shell, there is a lower increase of water-water repulsion going from one Ln(III) ion to the subsequent one and, as a consequence, a lower decrease of the σ_{LnO} or ρ_{LnO} values is sufficient, for heavier lanthanoid ions, to obtain a given contraction of the Ln-O first shell mean distance.

In order to assess the validity of the optimized Lennard-Jones and Buckingham parameters, it is important not only to compare the Ln-O theoretical mean distances with the experimentally inferred ones, but also the Ln-O $g(r)$'s, as they give information on the radial distribution of water molecules around the Ln(III) ion. The full Ln-O $g(r)$'s calculated from the MD simulations carried out using either the Lennard-Jones or Buckingham parameters

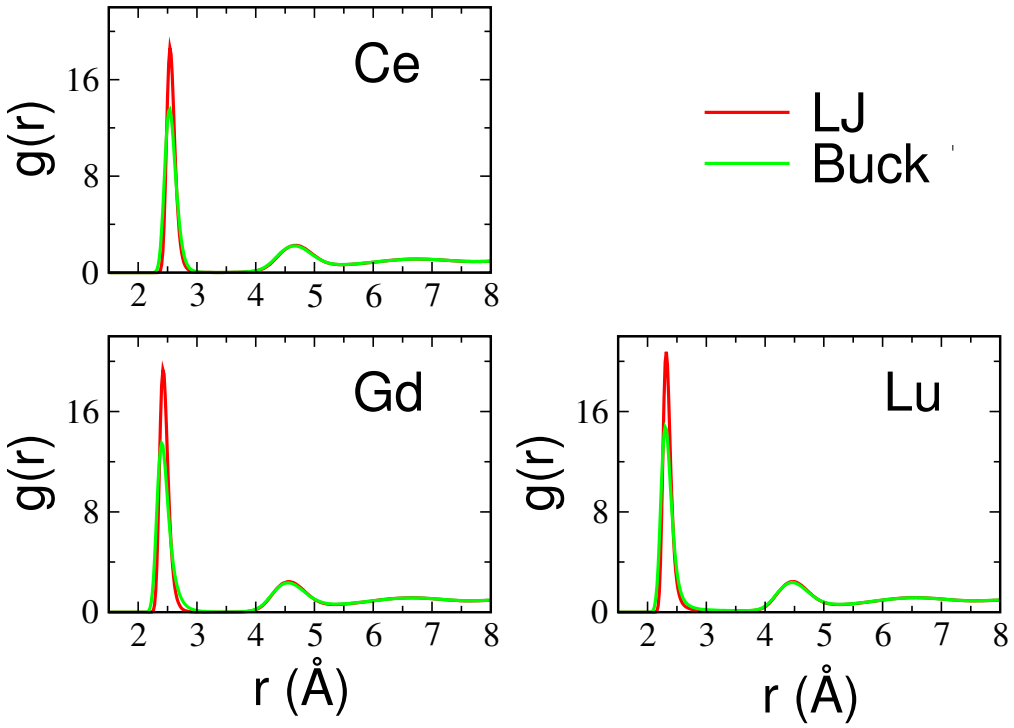

Figure 8.3: Ln-O $g(r)$'s obtained from the MD simulations of Ce(III), Gd(III) and Lu(III) ions in aqueous solution carried out using either the Lennard-Jones (red) or the Buckingham (green) interaction potentials.

are shown in Figure 8.3 for three ions taken at the beginning (Ce), in the middle (Gd) and at the end (Lu) of the series. All of the calculated $g(r)$'s show two distinct peaks, the former in the Ln-O distance range between 2.2 and 2.7 Å and the latter, which is well separated from the former one, between 4.0 and 5.0 Å. As discussed later in the work, the first peak of the Ln-O $g(r)$'s obtained using the Lennard-Jones potential shows some differences as compared to the one obtained with the Buckingham potential, while beyond the first solvation shell the Ln-O $g(r)$'s are almost identical for both van der Waals potentials. The first peak of the MD Ln-O $g(r)$'s has been compared with the $g(r)$ first peak obtained from the EXAFS analysis in Figure 8.4 for all of the Ln(III) ions. Note that the EXAFS $g(r)$'s have been calculated as gamma-like distributions (eq. 2.5) by using the N, R, σ^2 and β parameters obtained from the EXAFS data analysis of Ref [132] and listed in Table 8.3. As a general trend, the Ln-O $g(r)$'s obtained from both the Lennard-Jones and Buckingham interaction potentials are in good agreement with the EXAFS experimentally inferred ones. However, it is interesting to observe that the quality of the agreement is different for different Ln(III) ions. In fact, with the exception of the cases in which the agreement between experiment and theory is perfect, the Lennard-Jones and Buckingham $g(r)$'s are slightly more or less structured as compared to the EXAFS ones, respectively. In particular, for the first elements of the series (La, Ce, Pr, Nd), the Lennard-Jones $g(r)$'s are too structured than the EXAFS ones, while the Ln(III) first hy-

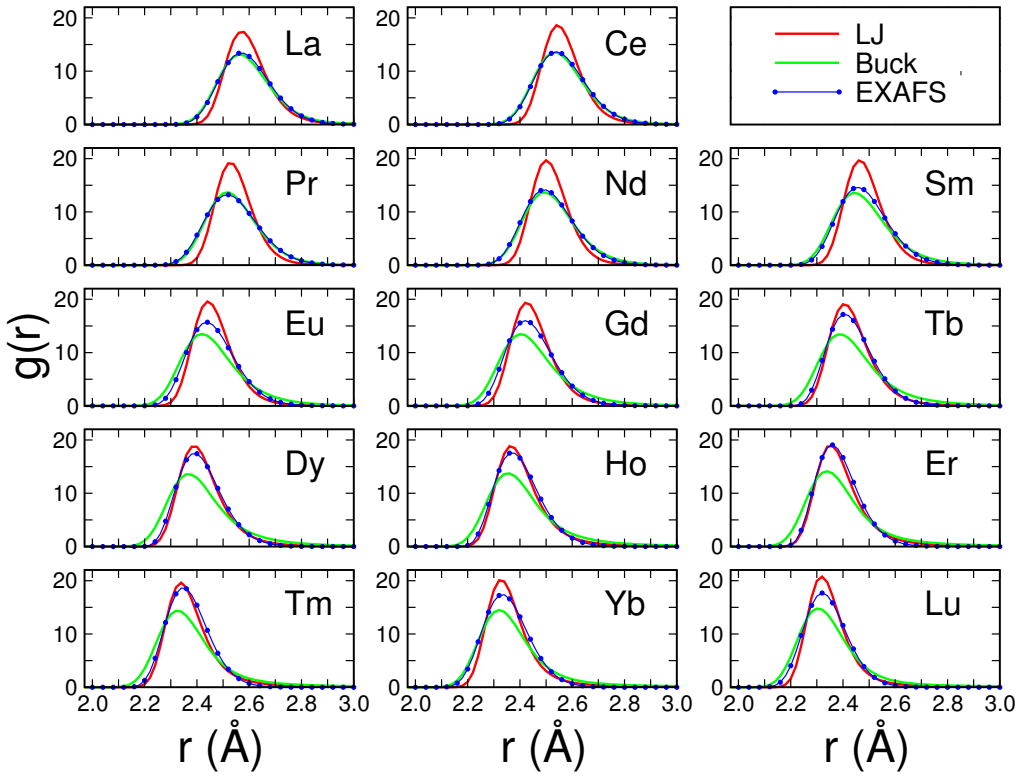

Figure 8.4: First-shell peak of the Ln-O $g(r)$'s obtained from the EXAFS data analysis (blue) compared with those obtained from the MD simulations carried out using either the Lennard-Jones (red) or the Buckingham (green) interaction potentials.

dration shells obtained from the Buckingham potentials are identical. Then, with increasing atomic number, the Lennard-Jones description becomes more and more accurate, and the Lennard-Jones $g(r)$'s of the Ln(III) ions from Tb to Tm are coincident with the EXAFS experimentally-inferred ones, while the Buckingham $g(r)$'s become less structured.

It is well-known that the optimal approach to carry out an accurate determination of the structural and dynamic properties of lanthanide ions in aqueous solutions is by including explicit polarization in the classical force field.[136, 137, 138] MD simulations with explicit polarization were carried out in Ref [132], starting from the new set of Ln(III) ionic radii in aqueous solution determined from the EXAFS analysis. The Ln-O $g(r)$'s calculated from the polarizable MD together with those obtained from the EXAFS experimental data are shown in Figure 8.5. The $g(r)$'s have been calculated as gamma-like distributions starting from the N, R, σ^2 and β parameters listed in Table 8.3 and Table S4 of Supporting Information of Ref [132]. As it can be seen, the MD $g(r)$'s match the EXAFS curves with a similar accuracy all along the series. Moreover, the agreement between the theoretical and experimental $g(r)$'s is comparable to the one obtained from our MD simulations carried out without including explicit polarization, thus supporting the validity of our new sets of interaction potentials.

The Ln-O coordination numbers calculated from the integration of the

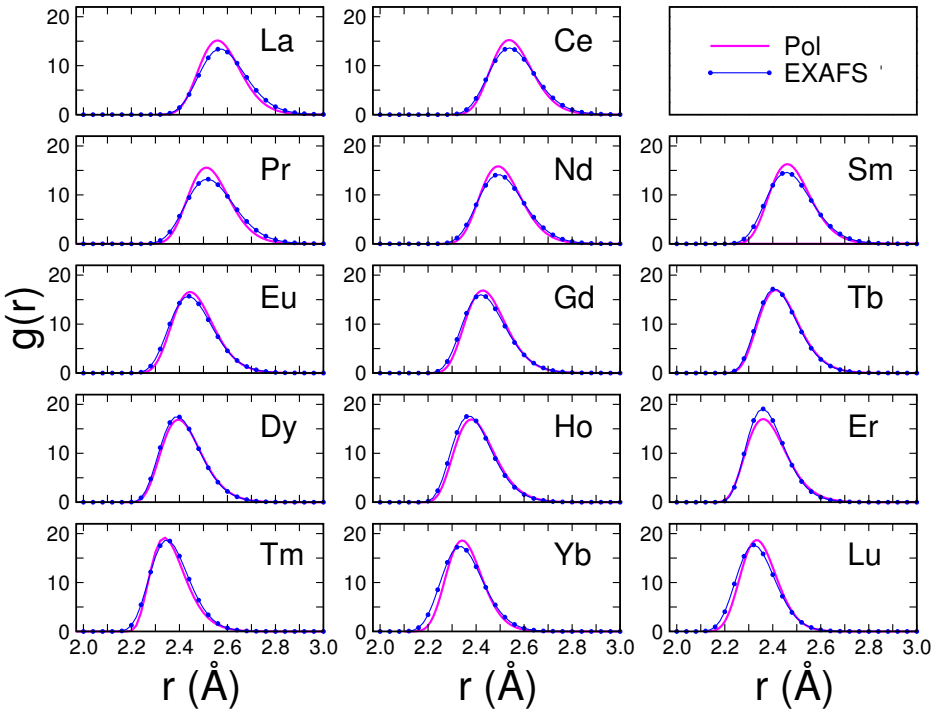

Figure 8.5: First-shell peak of the Ln-O $g(r)$'s obtained from the EXAFS data analysis (blue line) compared with those obtained from the polarizable MD simulations (magenta line) published in Ref [132].

Ln-O MD $g(r)$ first peak are plotted in Figure 8.6, together with those obtained from the EXAFS experimental data of Ref [132]. It can be seen that the coordination numbers change smoothly across the series from about 9 for the light Ln(III) ions to 8 for the heaviest ones, in accordance with the previous literature, and the agreement between the MD and EXAFS results is good. The biggest differences are found for La(III) and Ce(III) ions, where the Lennard Jones values are slightly higher than the experimental ones, and for the Lu(III) ion, where both the Lennard-Jones and Buckingham potentials give a coordination number that is 0.2 higher than the EXAFS one. However, the agreement between theory and experiment is satisfactory, as the error on the determination of the coordination numbers is about ± 0.5 when the EXAFS spectroscopy is applied to the study of Ln(III) ions in aqueous solutions.[132] Non-integer coordination numbers indicate that the Ln(III) ions transit among structures having a different number of water molecules during the simulation time, and it is interesting to calculate the percentage of these structures in the course of the simulation. The result of this analysis (see Figure 8.7) reveals that the favored configuration is a 9-coordinated species for all of the Ln(III) ions, with the exception of Lu(III). Moreover, 10-fold complexes are also found for La, Ce, Pr and Nd, whose percentage decreases with increasing atomic number. Note that the percentages of 10-fold structures of La(III), Ce(III) and Pr(III) ions obtained from the Lennard-Jones simulations are higher in comparison with those calculated from the EXAFS

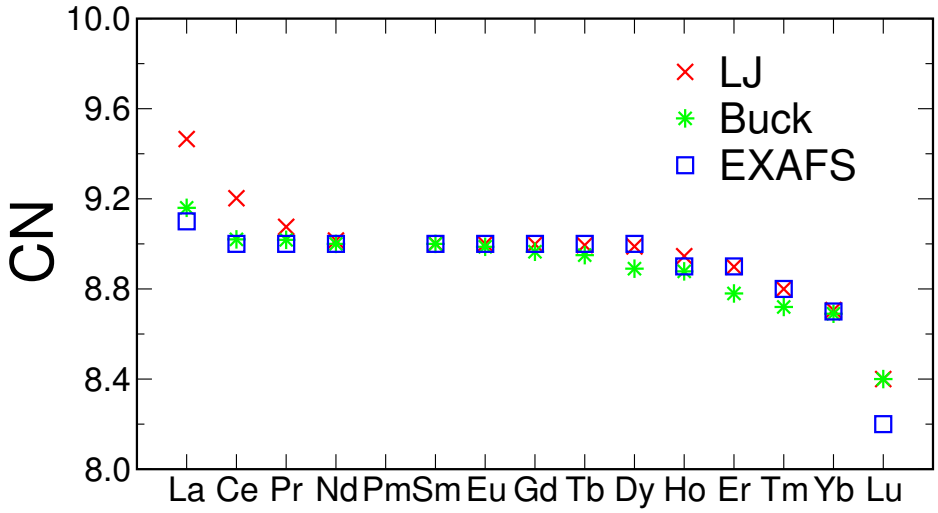

Figure 8.6: Ln-O first-shell average coordination numbers of Ln(III) ions in aqueous solution obtained from the EXAFS experimental data in Ref [132] (blue squares) compared with those obtained from the MD simulations carried out using either the Lennard-Jones (red crosses) or the Buckingham (green stars) interaction potentials developed in this work.

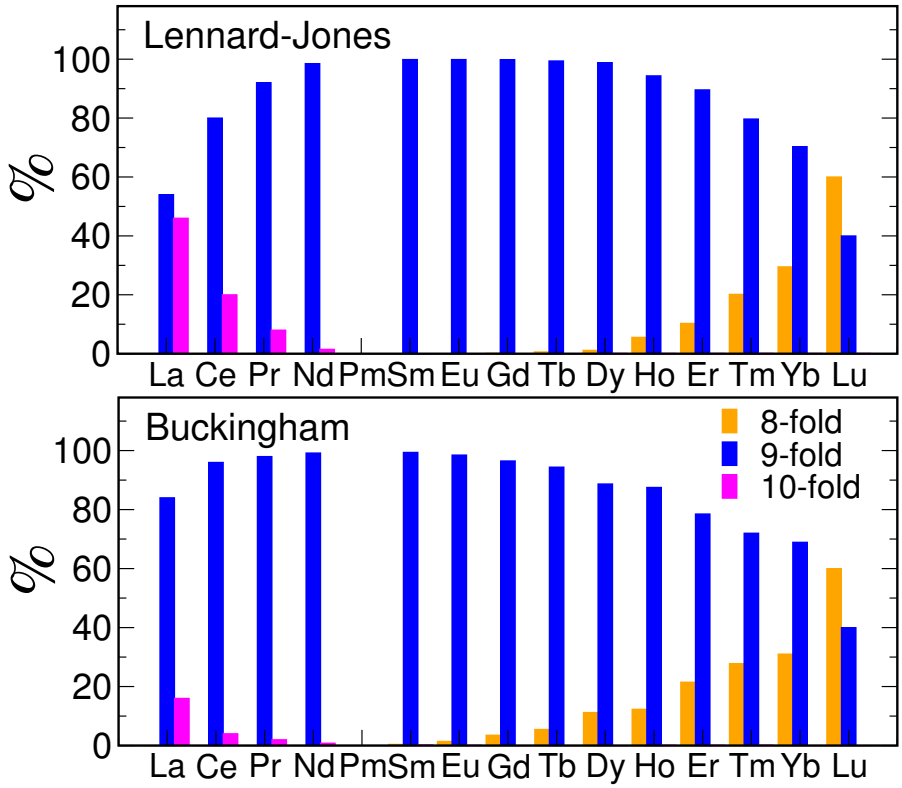

Figure 8.7: Percentages of first-shell hydration structure with a coordination number of 8 (orange), 9 (blue) and 10 (magenta) obtained from the MD simulations of Ln(III) ions in aqueous solution carried out using either the Lennard-Jones (upper panel) or the Buckingham (lower panel) interaction potentials.

	n_l^{SAP}		θ^{SAP}	n_θ^{SAP}
l_1	16	θ_1	74.9	16
l_2	4	θ_2	118.5	4
l_3	8	θ_3	141.6	8
l_4	-	θ_4	-	-
l_5	-	θ_5	-	-
l_6	-	θ_6	-	-

Table 8.6: List of parameters for an ideal SAP polyhedron: number of O-O distances (n_l), O-Ln-O angle theoretical values (θ_n) and number of angles (n_θ).

	n_l^{TTP}		θ^{TTP}	n_θ^{TTP}
l_1	12	θ_1	69.4	12
l_2	6	θ_2	75.3	6
l_3	3	θ_3	90.3	3
l_4	3	θ_4	120.0	3
l_5	6	θ_5	134.8	6
l_6	6	θ_6	138.7	6

Table 8.7: List of parameters for an ideal TTP polyhedron: number of O-O distances (n_l), O-Ln-O angle theoretical values (θ_n) and number of angles (n_θ).

analysis and from the very accurate MD simulations where the polarization was included in the classical force field.[132] The percentage of 9-coordinated species decreases going from lighter to heavier lanthanide ions and, finally, the predominant hydration complex for Lu(III) is a 8-fold species.

A further check of the reliability of the potentials developed here has been obtained by the calculation of the three-dimensional structures of Ln(III) ions in aqueous solutions, that have been at the center of a long-lasting debate. According to most investigations, $[Ln(H_2O)_9]^{3+}$ structures present a tricapped trigonal prism (TTP) geometry, as found in solid and liquid state both experimentally and theoretically, while for $[Ln(H_2O)_8]^{3+}$ structures the most probable geometry is the square antiprism (SAP) one.[137, 139, 140] A regular SAP is a 3D uniform polyhedron bounded by 2 squares and 8 triangles, having 16 edges and 8 vertices. It is characterized by 3 groups of vertex pairs, meaning 3 different O-O distance values: (i) l_1^{SAP}, the side of the polyhedron (this group is comprised of 16 vertex pairs); (ii) l_2^{SAP}, the diagonal of the square faces (this group counts 4 pairs); (iii) l_3^{SAP}, the distance between a vertex of a square face and one of the farthest vertices of the opposite square (this group counts 8 pairs). The number of O-O distances (n_l) together with the O-Ln-O angle theoretical values (θ_n) and the number of angles (n_θ) are

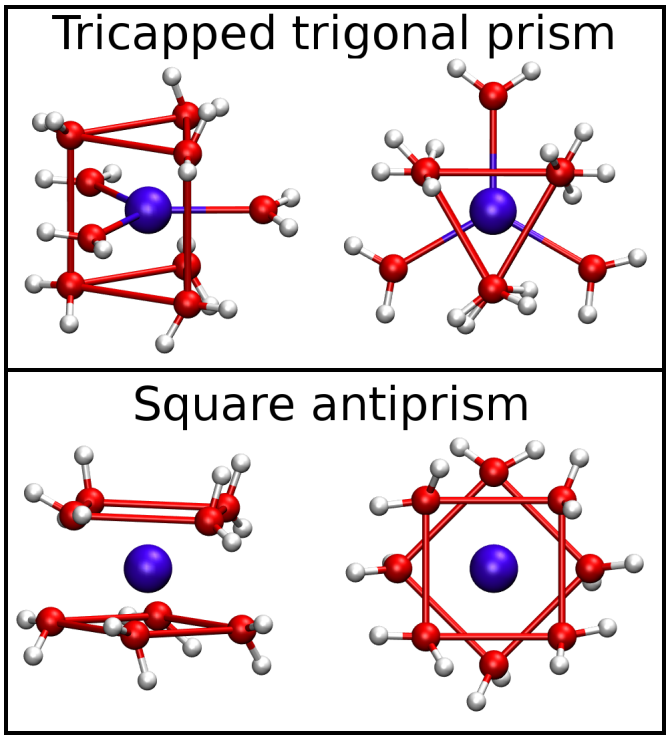

Figure 8.8: First-shell coordination structures of Ln(III) ions in aqueous solutions: tricapped trigonal prism (TTP) geometry (upper panel) and square antiprism (SAP) geometry (lower panel). Both side and top views are shown.

listed in Table 8.6. As far as the TTP geometry is concerned, the quadrilateral faces of the prism should have a square shape if the polyhedron was regular. However, in many crystal structures the prism is found to be distorted into having rectangular faces, with an height longer than the side of the triangular faces. This kind of TTP polyhedron is characterized by 6 groups of vertex pairs. The prism-prism vertex pairs form the 6 sides of the triangles (l_2^{TTP}), the 3 long sides of the rectangles (l_3^{TTP}) and the 6 diagonals of the rectangular faces (l_5^{TTP}). A capped vertex has 4 shorter distances (l_1^{TTP}) with the vertices of the capped rectangular face (12 pairs for the 3 capping vertices), 2 longer distances (l_6^{TTP}) with the farthest vertices of the prism (6 pairs) and 3 long distances (l_4^{TTP}) with the other capping vertex. See Table 8.7 for the full list of parameters. Note that for the calculation of the theoretical angles, the a parameter (where a is the ratio between the height of the prism and the side of the triangular faces) has been set to 1.61, as the value found in the crystal structure of $[Ln(H_2O)n](CF_3SO_3)_3$.[141] A representation of the SAP and TTP polyhedra is shown in Figure 8.8. In order to identify the geometry of Ln(III) ion first solvation shells, we have developed a new tool based on the calculation of the CDF functions, that are obtained by combining radial and angular distribution functions (see also the Methods Chapter). In particular, we have evaluated the CDF that combines the Ln-O distances and the O-Ln-O angles, where only the oxygen atoms belonging to the first coordination shell of the Ln(III) ion have been accounted for in the calcula-

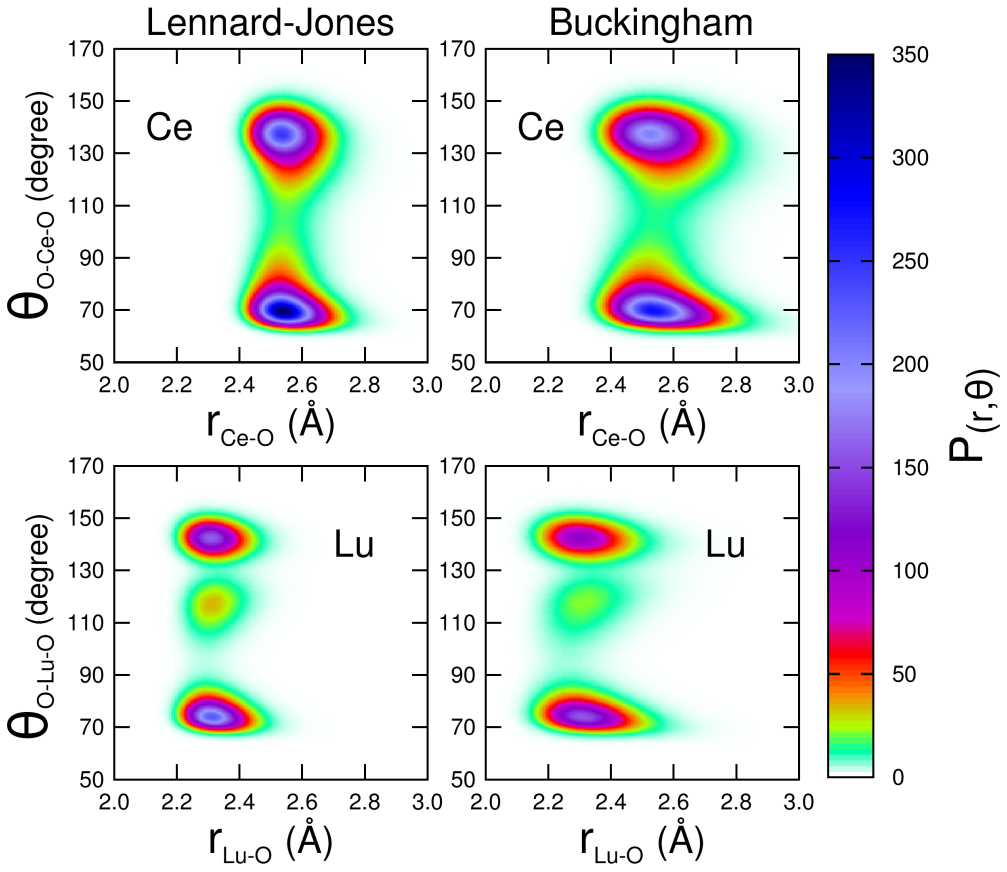

Figure 8.9: Upper panels: combined distribution functions (CDFs) between the Ce-O distances and O-Ce-O angles calculated for the 9-fold configurations only extracted from the MD simulations of the Ce(III) ion in aqueous solution. Lower panels: combined distribution functions (CDFs) between the Lu-O distances and O-Lu-O angles calculated for the 8-fold configurations only extracted from the MD simulations of the Lu(III) ion in aqueous solution.

tion. This CDF is the ideal tool to highlight the symmetry of ion coordination complexes in solutions and it is much more informative than common angular distribution functions (ADFs), that have generally been used in the past to determine the coordination geometry of an ion in solution. In fact, the ADF analysis in many cases is not able to distinguish among different polyhedra having similar internal angle values. Two ions at the beginning (Ce(III)) and at the end (Lu(III)) of the series have been chosen for this analysis, as they have a dominant percentage of 9-fold and 8-fold complexes, respectively (see Figure 8.7). We have extracted from the Ce(III) simulation configurations containing 9-fold coordinated Ce(III) ions only, and from the Lu(III) simulation configurations containing 8-fold coordinated Lu(III) ions, and we have computed the CDFs over these two different sets. The results of this analysis are shown in Figure 8.9 for both Lennard-Jones and Buckingham interaction potentials. The CDF for the Ce(III) ion (upper panels of Figure 8.9) features two peaks, which are both centered at a Ce-O distance of 2.57 Å and O-Ce-O angles of 70° and 135°. In both simulations the form of the distri-

butions, with the characteristic L-shape of the low angle peak, is consistent with a TTP polyhedron, in agreement with the results previously reported for the light Ln(III) ions.[137, 139, 140] Conversely, in the case of Lu(III) ion three peaks are found in the CDF (lower panels of Figure 8.9), centered at a Lu-O distance of 2.35 Å and O-Lu-O angles of 75°, 118° and 145°, in line with the existence of a SAP geometry of water molecules around the Lu(III) ion.[137, 139, 140] It is interesting to note that the CDFs calculated from the Buckingham simulations are much wider as compared to the Lennard-Jones ones for both Ce(III) and Lu(III) ions, thus suggesting that in the former case the first hydration shell is more disordered and unstructured, in agreement with the $g(r)$ results.

To finally validate our force-field parameters, we have also directly compared the EXAFS experimental data with the MD results, by calculating $\chi(k)$ theoretical signals starting from the MD $g(r)$'s and using eq. 2.6. Note that the theoretical models contain both the Ln-O and Ln-H signals, as the Ln-H interactions have been found to provide a detectable contribution to the EXAFS spectra of lanthanoid ions in aqueous solutions.[141] Least-squares fits of the EXAFS raw experimental data have been carried out in the range $k = 2.4$ - 14.0 Å^{-1} and two non structural parameters have been optimized, namely E_0 (core ionization threshold energy) and S_0^2. The results are shown in Figure 8.10 for both the MD simulations carried out using the Lennard-Jones (left panels) and the Buckingham (right panels) interaction potentials. The agreement between the experimental data and the MD simulations is very good for all the elements of the series. Taking into account the accuracy of the EXAFS spectroscopy in determining the first-shell coordination distances, this result is a very strict test of the reliability of the new sets of Lennard-Jones and Buckingham parameters developed in this work. However, some observations can be made looking at the reported residual curves. In particular, as far as the Lennard-Jones potential is concerned, the experimental data show a phase-shift with respect to the $\chi(k)$ theoretical signals, at k values higher than 10 Å^{-1} for the first and the last elements of the series (see Figure 8.10). An oscillation in the high k region is found in the residual curves, and it is known to be due to a wrong shape of the radial distribution around the photoabsorber atom.[142] This result is in line with the $g(r)$'s reported in Figure 8.4, where it was found that the Lennard-Jones Ln-O $g(r)$'s are too structured and have a different shape in comparison with the $g(r)$'s obtained from the EXAFS experimental data. Conversely, when considering the Buckingham potential, the residual curves show an oscillation in the low k region starting from the Eu(III) ion. This finding is in agreement with the $g(r)$'s shown in Figure 8.4 and it is due to a slight difference in the $g(r)$ first peak position betweeen the theoretical and experimental distributions. In fact, the Buckingham MD $g(r)$'s are shifted toward shorter distances with respect to the EXAFS ones, while the shape and the wideness of the curves are very similar.

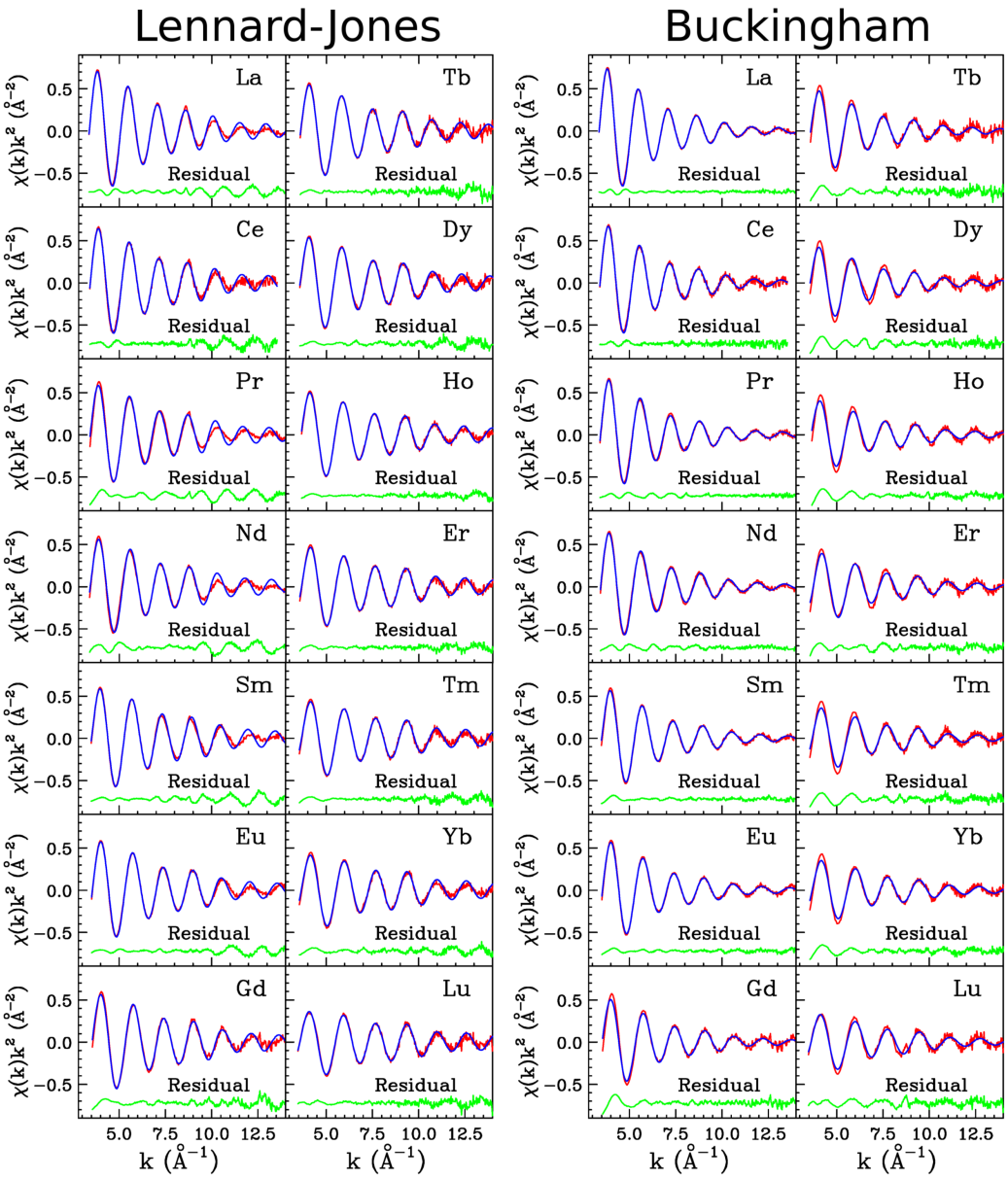

Figure 8.10: Comparison between the EXAFS experimental spectra (red dotted line) of Ln(III) ions in aqueous solutions and the $\chi(k)$ theoretical signals (solid blue line) calculated from the Ln-O and Ln-H $g(r)$'s obtained from the MD simulations using either the Lennard-Jones (left panels) or the Buckingham (right panels) interaction potentials. The residual curves are also shown in green.

Further tests to optimize the potential interactions

We have made many attempts to improve the description of the radial distributions of water molecules around the central Ln(III) ion by changing the potential parameters (both the σ_{LnO} and ϵ_{LnO} Lennard-Jones values and the A_{LnO}, ρ_{LnO} and C_{LnO} Buckingham ones). It was clear that the shape of the radial distribution curve obtainable with a given potential is inherent to the form of the potential itself and it cannot be modified by only changing

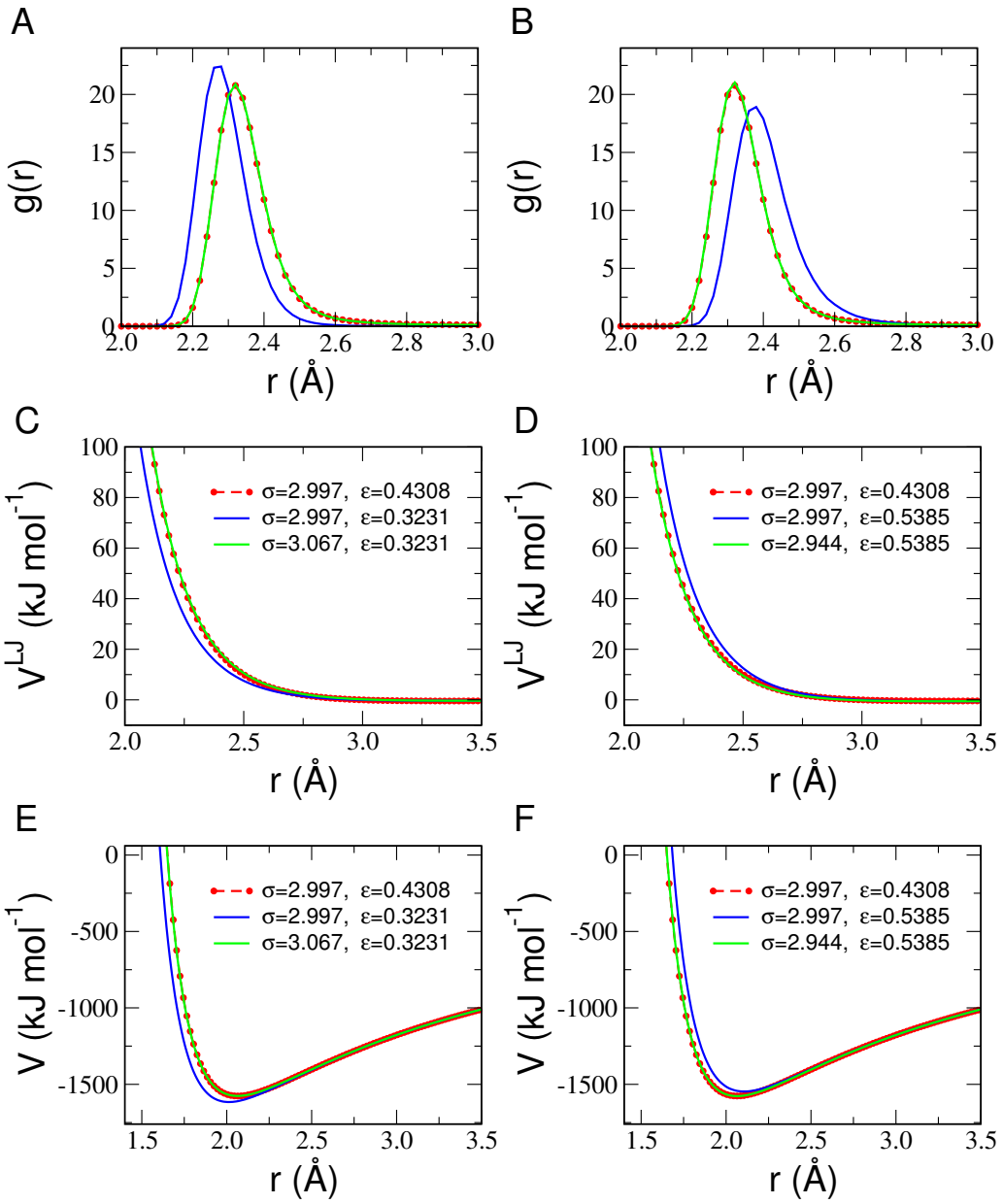

Figure 8.11: (A, B): First peak of the Lu-O $g(r)$'s calculated from the MD simulations carried out using different combinations of σ_{LnO} and ϵ_{LnO} Lennard-Jones parameters. (C, D): Lennard-Jones potential curves obtained using different combinations of σ_{LnO} and ϵ_{LnO} parameter values. (E, F): Total Lu-O non bonded potentials (Lennard-Jones potential plus Coulombic interaction) corresponding to different Lennard-Jones parameter combinations.

the interaction potential parameters. In fact, it was not possible to obtain a better agreement between the experimental and theoretical results than the one obtained with our sets of parameters.

Another important point concerning the development of Lennard-Jones and Buckingham interaction potentials is that there may exist different combinations of σ_{LnO} and ϵ_{LnO} or A_{LnO}, ρ_{LnO} and C_{LnO} parameters providing similar potential curves, and thus giving the same best agreement with the

EXAFS experimental data. In order to better explain this issue we have carried out, as an example, several MD simulations of Lu(III) ion in water where we have first reduced or augmented the ϵ_{LnO} value of a 25% of its value reported in Table 8.1, keeping fixed the σ_{LnO} parameter. The Lennard-Jones potential curves corresponding to these combinations of parameters are depicted in panels C and D of Figure 8.11, respectively. Hence, in this way, we have obtained a different Lu-O $g(r)$, shifted towards either shorter or longer distances with respect to the initial one, as shown in panels A and B of Figure 8.11. Then, by modifying the σ_{LnO} value we have re-obtained in both cases a Lu-O $g(r)$ identical to the initial one. To have an idea on how the Lu-O $g(r)$ is related to the parameter values, panels E and F show the total Lu-O nonbonded potential curves, obtained by summing the Coulombic interaction between the 3+ charge of the cation and the partial atomic charge of the oxygen atom of water molecules to the Lennard-Jones potential. It is evident that the total Lu-O functions obtained using different combinations of σ_{LnO} and ϵ_{LnO} values and corresponding to almost identical Lu-O $g(r)$'s are very similar. This means that there are different combinations of the σ_{LnO} and ϵ_{LnO} Lennard-Jones parameters providing identical distributions of water molecules around the Lu(III) ion and, as a consequence, providing the same degree of agreement with the EXAFS data. Among all the possible choices, we have arbitrarily decided to keep fixed the ϵ_{LnO} Lennard-Jones parameter along the whole series (or the A_{LnO} and C_{LnO} parameters for the Buckingham potential) and optimize only the σ_{LnO} and ρ_{LnO} values. However, as there are many possible combinations of the potential parameters providing identical Ln-O $g(r)$'s and therefore identical agreement with the EXAFS experimental data, obtaining a good agreement with the EXAFS results does not exclude the existence of other parameter combinations that can give reliable structural properties of Ln(III) ion in aqueous solution resulting in the same degree of agreement.

In conclusion, these new sets of Ln-O Lennard-Jones and Buckingham parameters allowed us to properly account for the structural properties of Ln(III) ions in water, such as the radial distribution of water molecules around the central cation, the hydration number trend along the series, that smoothly decrease with increasing atomic number, and the geometry of the first-shell hydration complexes. Now, starting from the new set of σ_{LnO} and ϵ_{LnO} values and the Lennard-Jones parameters of the SPC/E water model, and using the Lorentz-Berthelot combination rules (see eq. 8.3 and 8.4), it is possible to obtain generic σ_{LnLn} and ϵ_{LnLn} parameters describing the Ln-Ln pair interactions.

$$\sigma_{LnLn} = 2\sigma_{LnO} - \sigma_{OO} \tag{8.3}$$

$$\epsilon_{LnLn} = \frac{\epsilon_{LnO}^2}{\epsilon_{OO}} \tag{8.4}$$

The extrapolated σ_{LnLn} and ϵ_{LnLn} are listed in Table 8.1 for all of the elements of the series.

8.2 Testing the transferability of the Ln-Ln Lennard-Jones interaction potentials

As previously mentioned, the new set of Ln-Ln Lennard-Jones parameters can be used in combination with force fields available in the literature for studying the coordination of Ln(III) ions in different disordered systems, going from inorganic to bio-organic to organic systems. Indeed, the Lennard-Jones potential has the advantage to be a very computationally efficient interaction potential and it can be readily used to perform Classical MD simulations without explicit polarization. However, the capability of a given potential to reproduce the structural properties of systems different from that for which it has been developed can not be ascertain "a priori" and it has to be verified case by case. Thus, before using our Ln-Ln Lennard-Jones parameters in a complex/disordered system, which is a diluted solution of $Ce(NO_3)_3$ in the protic IL Ethylammonium nitrate, we have tested them in water.

In particular, we have investigated the structural and dynamic properties of two Ln(III) ions, La(III) and Dy(III), in water, but in the presence of their counterions, which are the triflate (TfO^-), bis(trifluoromethylsulfonyl)imide (Tf_2N^-) and nitrate (NO_3^-) ions (see Figure 8.12). Generally, MD simulations of Ln(III) ions in water have been performed under infinite dilution conditions, which means one Ln(III) cation immersed in bulk water, adding a homogeneous background charge to preserve the neutrality of the solution. However, the presence of a counterion can influence the coordination structure and dynamics of the Ln(III) ion, also in high dilution conditions, as the one studied in this work. The TfO^- has been chosen as a counterion because it is known as a non-complexing anion and triflate-based salts are generally used to dissolve Ln(III) ions in water and organic solvents. The Tf_2N^- is one of the most common anion used in combination with organic cations to form a large variety of ILs and, finally, the NO_3^- is interesting to be studied as in some nitrate-metal salts solutions it was shown that the anion readily form complexes and the question arises as to whether these complexes also occur with La(III) and Dy(III) aqueous solutions.

Even if it is well known that the optimal approach to carry out an accurate determination of the structure and dynamics of Ln(III) aqueous solutions is by including explicit polarization in the classical force field, we

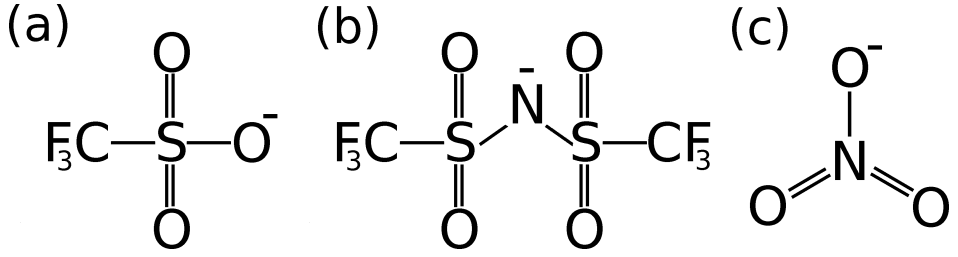

Figure 8.12: Schematic molecular structure of the (a) triflate (TfO^-), (b) bis(trifluoromethylsulfonyl)imide (Tf_2N^-) and (c) nitrate (NO_3^-) anions.

have demonstrated in the previous section that a good description of their solvation properties can be also obtained by using classical MD simulations without polarizing effects and describing the interactions among atoms by means of appropriate interaction potentials.

8.2.1 Experimental Methods

X-ray absorption measurements. 0.1 M Ln(III) aqueous solutions were obtained by dissolving in freshly distilled water the stoichiometric amount of $Ln(TfO)_3$, $Ln(Tf_2N)_3$ and $Ln(NO_3)_3$ (in which Ln = La and Dy). The spectra were collected at the La and Dy K-edge in transmission geometry, on the BM23 beam line at the European Synchrotron Radiation Facility of Grenoble (ESRF). The storage ring was operating in 16-bunch mode with a typical current of 80 mA after refill. A Si(511) double-crystal monochromator was used for the data acquisition, with the second crystal detuned by 20% for harmonic rejection. The aqueous solutions were kept in cells with Kapton film windows and Teflon spacers. Internal energy calibration was made with a foil of the corresponding lanthanoid metal.

Molecular Dynamics details. Classical MD simulations of 0.1 M $Ln(TfO)_3$, $Ln(Tf_2N)_3$ and $Ln(NO_3)_3$ (in which Ln = La and Dy) aqueous solutions, corresponding to a 1:555 molar ratio, have been performed in the NVT ensemble at 300 K by means of the Gromacs package.[143] The rigid SPC/E model[94] was used for water molecules, while the force field for the TfO^-, Tf_2N^- and NO_3^- anions was taken from Lopes and Pádua.[90, 144] As far as the La(III) and Dy(III) cations are concerned, we considered standard point charge 3+ and Lennard-Jones parameters (σ_{LnLn} and ϵ_{LnLn}) previously developed by us in order to obtain accurate structural properties of La(III) and Dy(III) in pure water (see Table 8.1 of Section 8.1). All the Lennard-Jones cross terms between different atom types have been calculated using the Lorentz-Berthelot mixing rules, with the exception of the specific interaction of the Ln(III) cation with the oxygen atoms of NO_3^- ions. In this case, the σ_{OO} and ϵ_{OO} values for the oxygen atoms were taken from the SPC/E model.[94]

The systems were composed of 5 Ln(III) cations, 15 anions and 2775 water molecules in a cubic box, created by randomly assigning initial positions to all ions and molecules and then equilibrated under NPT conditions in order to obtain the final starting configuration. Then, at the end of the equilibration, a final NVT run at 300 K was performed for 3 ns. The production simulations were carried out for 20 ns using a 1 fs time step and saving a configuration every 100 timesteps. The Nosé-Hoover thermostat,[87, 88] with a relaxation constant of 0.5 ps, was used to control the system temperature. Long-range interactions have been evaluated by the particle-mesh Ewald method,[89] while the cut-off of the nonbonded interactions was set to 9 Å. Periodic boundary conditions have been applied in order to simulate bulk material.

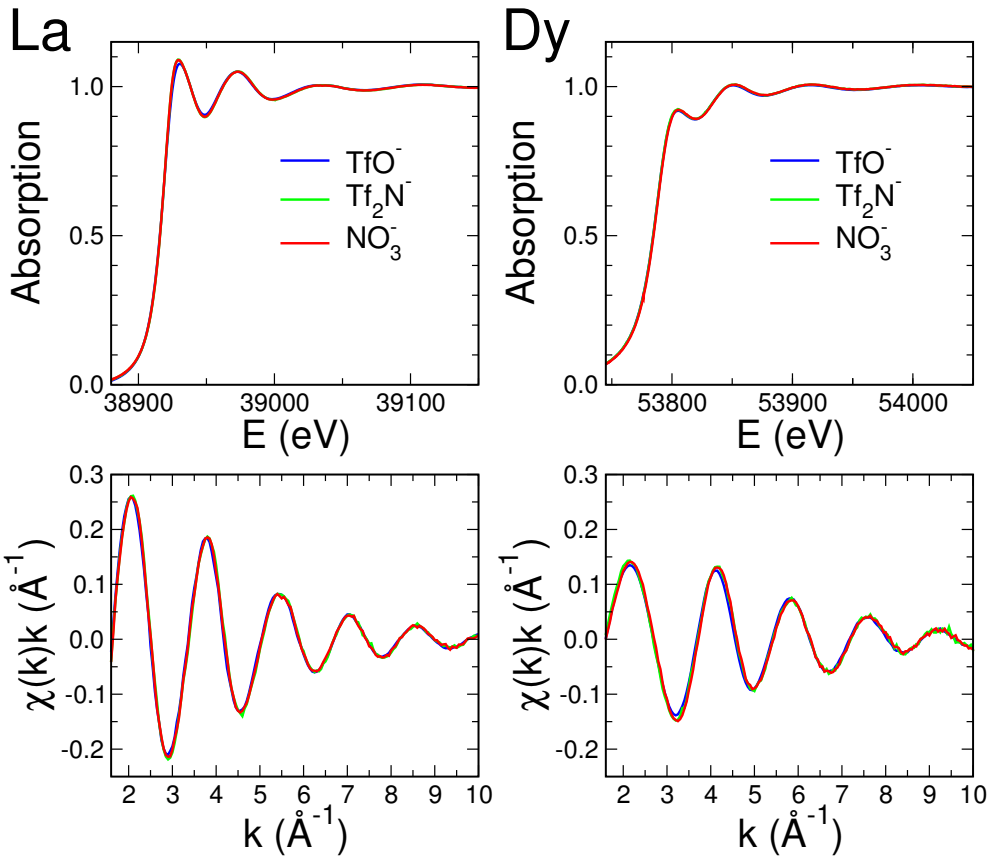

Figure 8.13: Upper panels: La and Dy K-edge X-ray absorption spectra of the 0.1 M $La(TfO)_3$ and $Dy(TfO)_3$ (blue lines), $La(Tf_2N)_3$ and $Dy(Tf_2N)_3$ (green lines), and $La(NO_3)_3$ and $Dy(NO_3)_3$ (red lines) aqueous solutions. Lower panels: corresponding EXAFS signals of the experimental data.

8.2.2 Experimental results: XAS data

XAS is a short range technique that gives information on the local environment around the photoabsorber atom, which is in our case the La(III) or Dy(III) ion. The La and Dy K-edge spectra of the 0.1 M salt aqueous solutions collected at room temperature are shown in the upper panels of Figure 8.13. It can be seen that for both La(III) and Dy(III) ions, the spectra are identical in all the energy range. The similarity of the XAS features gives a first indication that, despite the type of counterion (TfO^-, Tf_2N^- or NO_3^-), the local coordination around the La(III) or Dy(III) ion is similar in all of the investigated aqueous solutions. These results are confirmed by the EXAFS spectra extracted with a three segmented cubic spline, shown in the lower panels of Figure 8.13. As already observed for the X-ray absorption near-edge structure (XANES) data, the EXAFS signals of all of the aqueous solutions are identical. These findings suggest that only water molecules enter the La(III) and Dy(III) first coordination shell, whereas the anions do not bind directly to the cations but probably occur in the second coordination shell of the cations or in the bulk water.

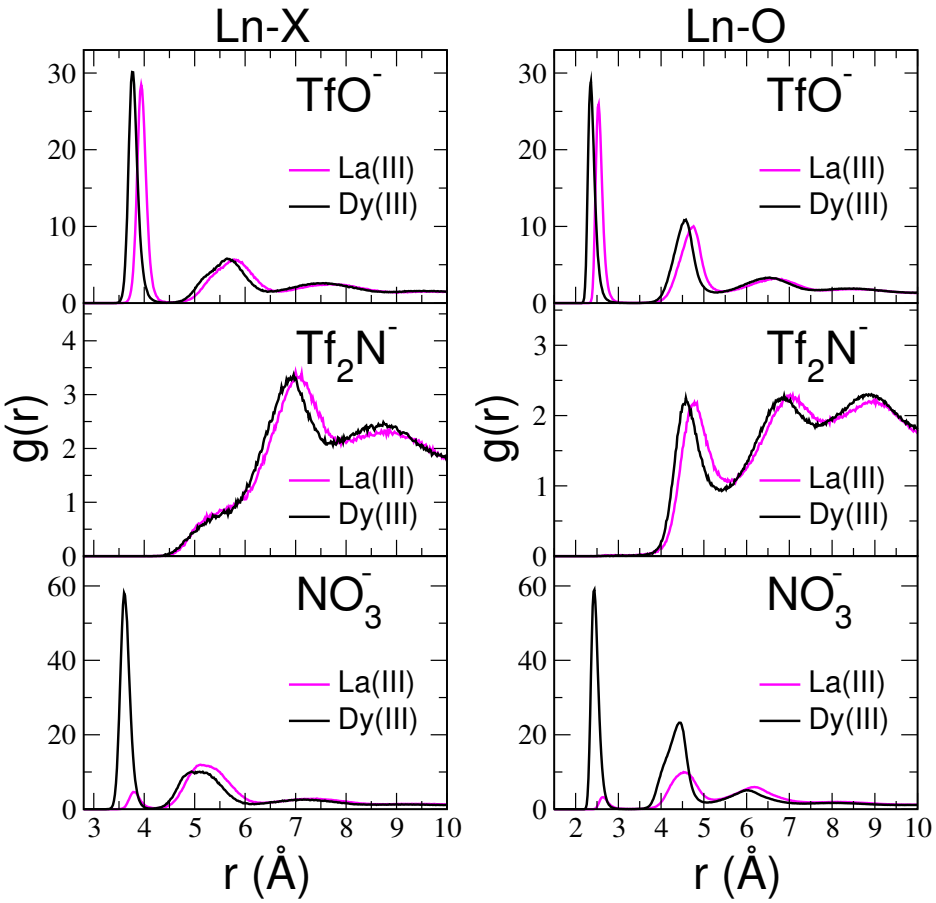

Figure 8.14: Ln-X (left panel) and Ln-O (right panel) radial distribution functions, $g(r)$'s, calculated from the MD simulations of 0.1 M $Ln(TfO)_3$ (top), $Ln(Tf_2N)_3$ (middle) and $Ln(NO_3)_3$ (bottom) aqueous solutions. Note that X = S for the TfO^- anion and X = N for Tf_2N^- and NO_3^- anions, while O is the oxygen atom of the anions.

8.2.3 Ln(III) salts: inner-/outer-sphere complexation

In order to better shed light on the structural properties of Ln(III) salts in water, we have carried out MD simulations of $Ln(TfO)_3$, $Ln(Tf_2N)_3$ and $Ln(NO_3)_3$ (Ln = La and Dy) aqueous solutions, as described in detail in the Experimental Method section. Now, the first important question when studying Ln(III) salts is if they form inner-sphere associated complexes in water. Indeed, when dealing with salt association processes in solution it is very important to properly sample the phase space visited by the system. In particular, if the salt dissociation/association process is slow and the simulation time is too short, the initial conditions can bias the results that are obtained from the calculations. To this end we have simulated large simulation boxes containing 5 Ln(III) cations, 15 anions and 2775 water molecules, and the initial configurations were constructed by randomly positioning the ions and water molecules; after an NPT equilibration, the systems were equilibrated

for 3 ns in the NVT ensemble and production runs were then collected for a long simulation time of 20 ns. Now, in order to investigate the complexation properties of Ln(III) salts in water we have calculated the $g(r)$'s between the La(III) and Dy(III) cations and the anions, that are shown in Figure 8.14. In particular, the left panel of the Figure shows the Ln-X $g(r)$'s, in which we have chosen the sulfur atom, S, as observed atom for the TfO^- anion, and the nitrogen atom, N, for the Tf_2N^- and NO_3^- anions. The $g(r)$ peak positions r and the coordination numbers CN are listed in Table 8.8 for all of the solutions.

$Ln(TfO)_3$ salts. The TfO^- anions are considered as non-complex forming species and they are often used as counterions for structural studies of the hydration properties of Ln(III) ions in water.[142, 141] The Ln-S $g(r)$'s calculated from our MD simulations of the $Ln(TfO)_3$ aqueous solutions show a first shell peak with maximum at 3.90 and 3.80 Å for the La(III) and Dy(III) ions, respectively, followed by a second shell peak and some less-defined oscillations beyond. However, inspection of Table 8.8 reveals that the Ln-S first shell coordination numbers, obtained by integrating the $g(r)$ first peak up to the first minimum, are very low for both ions (0.2) meaning that the $Ln(TfO)_3$ salts are substantially dissociated in water. This result is in agreement with the common assumption that the TfO^- anions does not form ion pairs with lanthanides in aqueous solution, and also with two NMR investigations, the former carried out on $Ln(TfO)_3$ in water for the entire lanthanide series,[145] the latter on $Dy(TfO)_3$ aqueous solutions,[146] where it was found that the TfO^- anion does not enter the Ln(III) first coordination shell. A similar result has also been obtained for the La(III) ion in a recent combined DFT and Raman scattering study.[147]

$Ln(Tf_2N)_3$ salts. The analysis of our MD simulations shows that $Ln(Tf_2N)_3$ salts are fully dissociated in water. Indeed, looking at the Ln-N $g(r)$'s of Figure 8.14, calculated between the La(III) and Dy(III) cations and the Tf_2N^- anions, only a broad low intensity peak at long Ln-N distances can be found. The Tf_2N^- anions approach the La(III) and Dy(III) cations many times in the course of the simulations, but they never enter the Ln(III) first solvation shell.

$Ln(NO_3)_3$ salts. At variance with our findings on $Ln(TfO)_3$ and $Ln(Tf_2N)_3$ aqueous solutions, where the two Ln(III) cations have shown very similar structural properties, $La(NO_3)_3$ and $Dy(NO_3)_3$ salts in water behave differently from one another. Indeed, the Ln-N $g(r)$'s, calculated between the La(III) and Dy(III) cations and the NO_3^- anions, show a different trend: the La-N $g(r)$ features a low intensity first shell peak with maximum position of 3.80 Å, while for Dy(III) a much more intense first shell peak with maximum at 3.61 Å is found. Indeed, the Ln-nitrate first shell coordination number obtained for La(III) is very low, while in the case of the Dy(III) ion a larger number of nitrate ions enter the cation first coordination sphere (0.5). The coordination number obtained for the La(III) ion is consistent with the results of a recent DFT and Raman study, where it was found that, in dilute La(III) nitrate aqueous solutions, only a small percentage of nitrate ions coordinate La(III) in its first coordination shell.[147] The results are also in line with

La(III)								
system	$r^{(1)}_{La-OW}$	$CN^{(1)}_{OW}$	$r^{(2)}_{La-OW}$	$CN^{(2)}_{OW}$	$r^{(1)}_{La-X}$	$CN^{(1)}_{X}$	$r^{(2)}_{La-X}$	$CN^{(2)}_{X}$
water	2.57	9.5	4.71	17.9				
TfO^-	2.57	9.3	4.71	16.8	3.90	0.2	5.80	0.4
Tf_2N^-	2.57	9.5	4.71	17.1			7.00	0.5
NO_3^-	2.57	9.5	4.71	17.0	3.80	0.04	5.20	0.8
Dy(III)								
system	$r^{(1)}_{Dy-OW}$	$CN^{(1)}_{OW}$	$r^{(2)}_{Dy-OW}$	$CN^{(2)}_{OW}$	$r^{(1)}_{Dy-X}$	$CN^{(1)}_{X}$	$r^{(2)}_{Dy-X}$	$CN^{(2)}_{X}$
water	2.39	9.0	4.54	16.6				
TfO^-	2.39	8.8	4.53	15.6	3.80	0.2	5.65	0.4
Tf_2N^-	2.39	9.0	4.52	15.9			6.90	0.5
NO_3^-	2.39	8.5	4.54	15.3	3.61	0.5	5.00	0.6

Table 8.8: Structural parameters of the radial distribution functions, $g(r)$'s, calculated from the MD simulations of La(III) and Dy(III) salts aqueous solutions, together with those of La(III) and Dy(III) ions in pure water. Position (Å) of the first, $r^{(1)}_{Ln-OW}$, and second, $r^{(2)}_{Ln-OW}$, Ln-OW $g(r)$ peaks, and coordination numbers of the first, $CN^{(1)}_{OW}$, and second, $CN^{(2)}_{OW}$, Ln(III) hydration shells. Position (Å) of the first, $r^{(1)}_{Ln-X}$, and second, $r^{(2)}_{Ln-X}$, Ln-X $g(r)$ peaks (X = S for the TfO^- anion and X = N for the Tf_2N^- and NO_3^- anions) and coordination numbers of anions that are in the first, $CN^{(1)}_X$, and in the second, $CN^{(2)}_X$, Ln(III) ion coordination shells.

the low association constant values of Dy(III) and other Ln(III) nitrate salts determined by solvent extraction techniques and microcalorimetry.[148, 149] Moreover, the presence of a single peak in our Ln-N $g(r)$'s indicates that a single nitrate coordination mode takes place in both La(III) and Dy(III) nitrate aqueous solutions, i.e. the monodentate one, with only one oxygen atom pointing towards the central Ln(III) ion, as already found by Duvail et al. from MD simulations of Nd(III) and Dy(III) nitrates in water.[150]

8.2.4 La(III) and Dy(III) first coordination shell

MD simulations of La(III) salt aqueous solutions have shown that very little first shell association takes place between the La(III) cation and triflate, Tf_2N^- and nitrate counterions. Indeed, the La(III) ion is mainly coordinated, in its first solvation shell, by water molecules, as evidenced by the La-OW and La-HW $g(r)$'s that are reported in the upper panel of Figure 8.15 (OW and HW refer to the water oxygen and hydrogen atoms). All of the La-OW and the La-HW $g(r)$'s show very sharp and structured first shell peaks, as

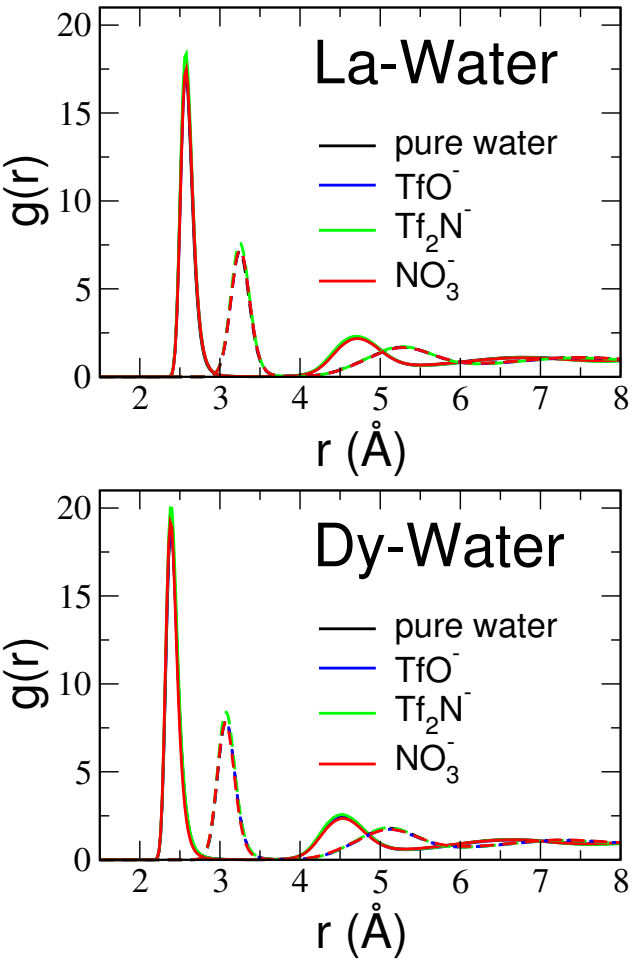

Figure 8.15: Upper panel: La-OW (solid lines) and La-HW (dashed lines) radial distribution functions, $g(r)$'s, obtained from the MD simulations of 0.1 M $La(TfO)_3$ (blue), $La(Tf_2N)_3$ (green) and $La(NO_3)_3$ (red) aqueous solutions. OW and HW are the oxygen and hydrogen atoms of the water molecules. Lower panel: Dy-OW (solid lines) and Dy-HW (dashed lines) radial distribution functions, $g(r)$'s, obtained from the MD simulations of 0.1 M $Dy(TfO)_3$ (blue), $Dy(Tf_2N)_3$ (green) and $Dy(NO_3)_3$ (red) aqueous solutions. The La-OW and Dy-OW $g(r)$'s (black solid line), and the La-HW and Dy-HW $g(r)$'s (black dashed line) calculated from the MD simulations of La(III) and Dy(III) in pure water are also shown.

strong cation-water interactions are present and the neat separation between the La-OW and the La-HW $g(r)$ first peak indicates that the water molecules are strongly oriented due to the electrostatic field of the La(III) ion. But the very interesting result is that the La-Water $g(r)$'s calculated for the three different anions are very similar to each other and also similar to the La-Water $g(r)$'s calculated from the MD simulation of La(III) ion in pure water (reported in Section 8.1). As previously described, this simulation has been carried out in the infinite dilution approximation with a single La(III) ion immersed in bulk water and using the same interaction potential parameters adopted here. Inspection of Table 8.8 shows that the La-OW mean distance is the same in all systems (2.57 Å), independently of the counterion, with

about 9.5 water molecules in the La(III) first coordination shell. The only exception is for the $La(TfO)_3$ aqueous solution in which the La-OW first shell coordination number is slightly lower (9.3). This means that when the anion does not coordinate the La(III) ion in its first coordination shell, the number of water molecules forming the La(III) ion hydration complex is identical to the La-OW coordination number found in pure water. When a small percentage of anions are located in the La(III) first coordination shell, i.e. in the triflate solution, the cation hydration number slightly decreases in such a way that the total coordination number (water molecules plus anions) remains unchanged. Since the cation-anion interactions take place between the lanthanide ion and the oxygen atoms of the anion (O), it is useful to look at the La-O $g(r)$'s, shown in the right panel of Figure 8.14. It can be seen that the La(III) ion coordinates the oxygen atoms of the NO_3^- and TfO^- anions at longer and shorter distances (2.65 and 2.53 Å), respectively, as compared to the La-OW first shell distance, and the La-O coordination numbers are 0.04 and 0.2 for the nitrate and triflate salts in water. Note that a longer distance of the nitrate oxygen atoms with respect to the water oxygen has been previously found in an EXAFS investigation of lanthanide nitrate salts in water.[151] All together these findings show that the La(III) ion always coordinates 9.5 oxygen atoms in its first solvation shell. In particular, in the solutions containing Tf_2N^- and NO_3^- ions, the 9.5 oxygen atoms belong only to the water molecules, while in the case of the TfO^- anion a very low percentage belongs to the anion. We have also analyzed the geometry of the first hydration shell of oxygen atoms surrounding the La(III) ion by calculating the combined distribution functions (CDFs) that, as described in Section 8.1, allows one to identify the first shell symmetry of an ion in solution. In particular, we have extracted from the La(III) simulations configurations containing 9-fold coordinated La(III) ions only, and we have calculated the CDFs between the distribution functions of the La-O distances and O-La-O angles, where O represents oxygen atoms belonging either to water molecules or to anions in the La(III) first coordination shell (see Figure 8.16). It can be seen that the CDFs obtained for the salt solutions are very similar to each other and to the one calculated for La(III) in pure water: two peaks are found, centered at a La-O distance of about 2.57 Å and O-La-O angles of 70° and 135°. In all cases, the form of the distributions, with the characteristic L-shape of the low angle peak, is consistent with a tricapped trigonal prism (TTP) geometry of the first shell cluster, in agreement with the results reported in the literature for light Ln(III) ions.[139, 137, 140] Moreover, the similarity of the CDFs indicate that the three-dimensional arrangement of the oxygen atoms in the La(III) first coordination shell is the same in all of the solutions, regardless if all oxygen atoms belong to water molecules (pure water, NO_3^- and Tf_2N^- solutions) or a small fraction of oxygen atoms belong to the anion (TfO^- solution).

Also in the case of the Dy(III) ion, the counterions have a small influence on the structure of the Dy(III) first hydration shell. Indeed, the Dy-OW and Dy-HW $g(r)$'s calculated for the three salt solutions are very similar (see the

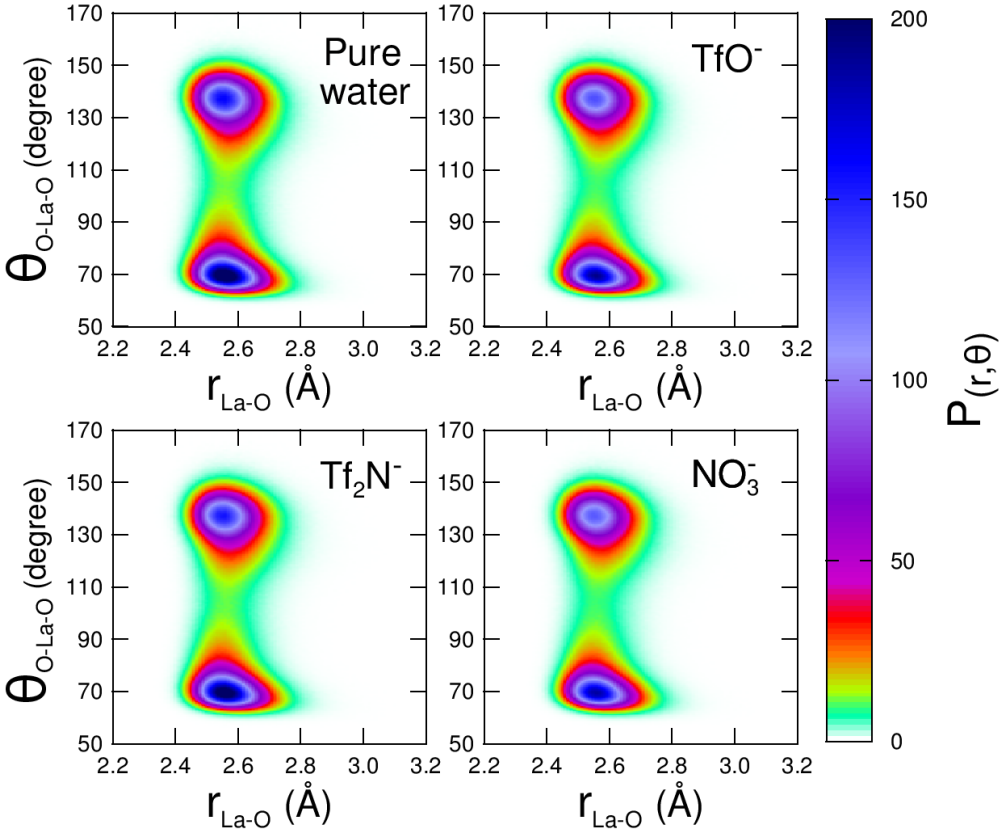

Figure 8.16: Combined distribution functions (CDFs) between the La-O distances and O-La-O angles calculated for the 9-fold configurations only extracted from the MD simulations of the 0.1 M $La(TfO)_3$, $La(Tf_2N)_3$ and $La(NO_3)_3$ aqueous solutions. The CDF calculated from the MD simulation of La(III) in pure water is also reported.

lower panel of Figure 8.15), and also similar to the Dy-Water $g(r)$'s calculated from the MD simulation of Dy(III) ion in pure water (see Section 8.1). Looking at Table 8.8, it can be seen that the Dy-OW distance (2.39 Å) is identical in all of the simulations, and it is shorter as compared to the La-OW one, as a consequence of the well-known lanthanide contraction that takes place along the series.[139] In the $Dy(Tf_2N)_3$ aqueous solution, the Dy-OW first shell hydration number is 9.0, as the one found in pure water. This value is lower than that obtained for the La(III) ion, in agreement with the decrease of lanthanide hydration numbers going from the first to the last element of the series.[139] Conversely, for the $Dy(TfO)_3$ and $Dy(NO_3)_3$ salts, a decrease in the Dy-OW first shell hydration number can bo observed, but also in this case the sum of the coordination numbers of water molecules and anions is always 9.0 (see Table 8.8). As observed for the La(III) ion, the Dy(III) ion coordinates the oxygen atoms of the NO_3^- and TfO^- anions at longer and shorter distances (2.43 and 2.35 Å), respectively, as compared to the Dy-OW first shell distance, and the Dy-O coordination numbers are 0.2 and 0.5 for the nitrate and triflate salts in water. In conclusion, our results suggest that the Dy(III) ion forms a first coordination shell composed of 9.0 oxygen atoms:

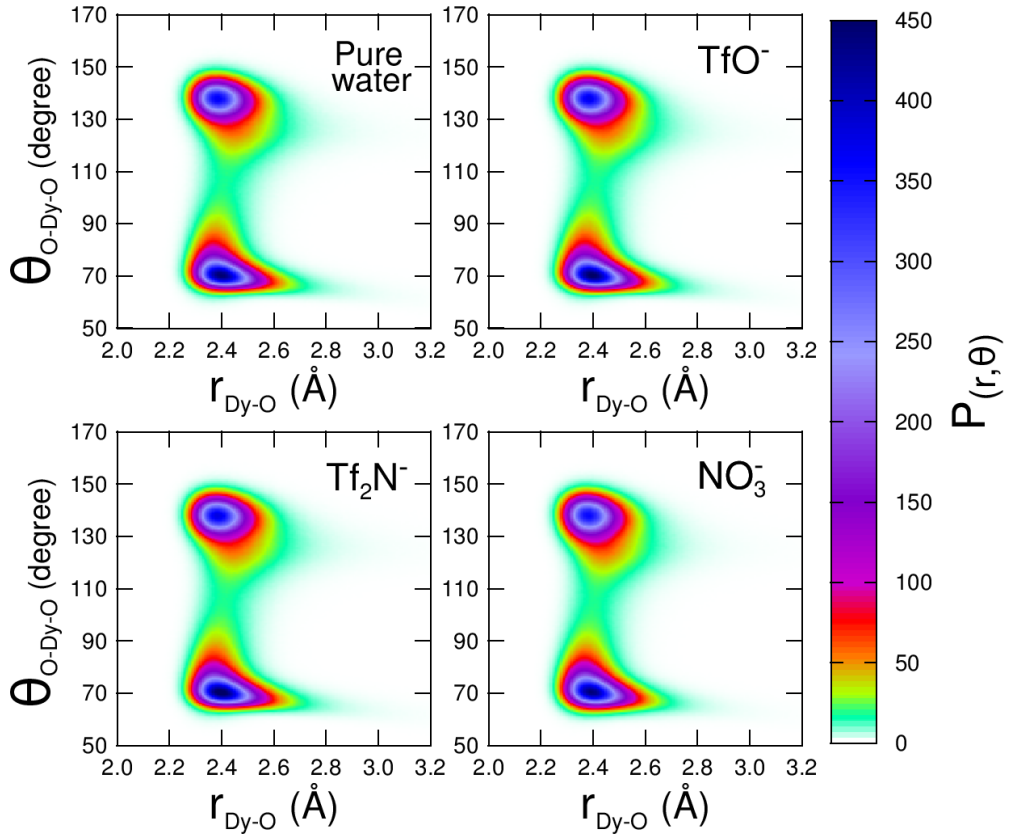

Figure 8.17: Combined distribution functions (CDFs) between the La-O distances and O-La-O angles calculated for the 9-fold configurations only extracted from the MD simulations of the 0.1 M $Dy(TfO)_3$, $Dy(Tf_2N)_3$ and $Dy(NO_3)_3$ aqueous solutions. The CDF calculated from the MD simulation of Dy(III) in pure water is also reported.

in pure water and in Tf_2N^- solutions, the nine coordinated ligands are all water molecules, while a small percentage of water molecules are replaced by TfO^- and NO_3^- counterions in Dy(III) triflate and nitrate solutions. To shed light on the three-dimensional arrangements of the oxygen atoms surrounding the Dy(III) ion, we have extracted from each Dy(III) simulation a trajectory containing 9-fold coordinated Dy(III) ions only and we have calculated the CDF combining the distribution functions of the Dy-O distances and O-Dy-O angles, where O are the oxygen atoms belonging either to water molecules or to anions in the Dy(III) first coordination shell (see Figure 8.17). As observed for the La(III) ion, the form of the CDF, with two peaks centered at a distance of about 2.39 Å and O-Dy-O angles of 70° and 135°, is consistent with the existence of a TTP geometry of the Dy(III) first coordination shell. Moreover, the geometry of the oxygen atoms surrounding the Dy(III) ion is the same in all of the salt solutions, as shown by the strong similarity of the CDFs obtained for the different systems.

A direct comparison between the MD and XAS data can be made to assess the accuracy of the theoretical framework used in the simulations. To this end $\chi(k)$ theoretical signals have been calculated by introducing the MD

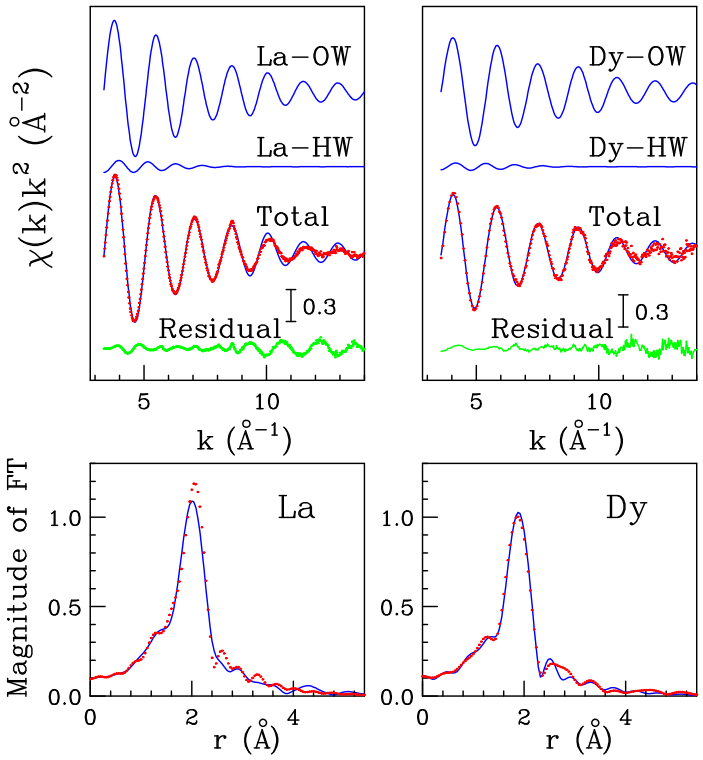

Figure 8.18: Upper panels: EXAFS experimental spectra (dotted red line) of the 0.1 M $La(TfO)_3$ (left) and $Dy(TfO)_3$ (right) aqueous solutions compared with the theoretical signals (solid blue line) obtained from the MD La-OW/La-HW and Dy-OW/Dy-HW $g(r)$'s. The residual curves are shown in green. Lower panels: non-phase-shifted corrected Fourier transforms of the experimental data (dotted red line) and of the theoretical signals (solid blue line).

La/Dy-OW and La/Dy-HW in eq. 2.6. EXAFS least-square fits have been performed in the range k = 2.4 - 14.0, with the MD structural parameters keeping fixed during the analysis. Figure 8.18 shows the EXAFS analysis results for the $La(TfO)_3$ (left panels) and $Dy(TfO)_3$ (right panels) aqueous solutions, as an example. In the upper panels, the first two curves from the top are the La/Dy-OW and La/Dy-HW theoretical signals, while the remainder of the Figure shows the total theoretical contribution in comparison with the experimental spectrum. The residual curves are also shown in green. The theoretical data (solid blue line) match very well with the experimental ones (dotted red line) proving that the structural information derived from the MD simulations is reliable, and that the chosen force field is capable of providing a correct description of the investigated systems. In the lower panels of Figure 8.18 the comparison between the nonphase-shifted corrected Fourier transforms of the experimental data and of the theoretical signals is reported and, as it can be seen, a very good agreement is found also in distance space.

Both MD simulations and EXAFS data indicate the substantially absence of inner-sphere $Ln(TfO)_3$, $Ln(Tf_2N)_3$ and $Ln(NO_3)_3$ complexes (in which Ln = La and Dy), making the three anions and, in particular, the TfO^- and

Tf_2N^- ones suitable to be used for experimental determinations of the Ln(III) structural properties in water. It is clear that they are non-complexing anions in high diluted conditions, as the one of the present investigation. In higher concentrated solutions (> 1 M) the anions could penetrate into the Ln(III) first coordination shell and form contact ion pairs due to the low number of water molecules that are not sufficient to complete the shell, as already found for example for the perchlorate ion.[147] Moreover, the very good agreement between the experimental and theoretical results allowed us to be confident that the new set of Ln-Ln Lennard-Jones interaction potential is transferable to systems different from which it has been developed.

8.2.5 La(III) and Dy(III) second coordination shell

Due to the short-range character of the XAS spectroscopy, no information can be obtained from the experimental data about the structural organization of the La(III) and Dy(III) second coordination shell and of the bulk structure of solutions. Conversely, from the analysis of the MD trajectories it is possible to provide a global picture of the structural arrangement of the investigated aqueous solutions, both in the short- and long-distance range. In particular, here, we will explore the structural and dynamic properties of the second coordination shell of both La(III) and Dy(III) ions. As far as the interaction with water molecules is concerned, it can be seen from Figure 8.15 that the second shell water molecules are at the same mean distance from the central Ln(III) ion (the Ln-OW distance is about 4.71 Å for La(III) and 4.54 Å for Dy(III)), independently from the nature of the counterion. However, the number of the second shell water molecules is slightly lower in comparison to the one obtained from the MD simulations of La(III) and Dy(III) ions in pure water (see Table 8.8). This is because some anions can enter the La(III) or Dy(III) second coordination shell, as shown by the presence of a distinct second shell peak in the La/Dy-X $g(r)$'s of Figure 8.14. For both La(III) and Dy(III) cations, the broad peak is due to the formation of solvent-separated ion pairs between the cation and the anion, and it is interesting to observe that this peak becomes more unstructured and wider in going from the NO_3^- to the TfO^- and finally to the Tf_2N^- anion. Inspection of Table 8.8 also reveals that the number of anions in this shell vary from 0.4 to 0.8 depending on both the Ln(III) ion and the nature of the anion. However, the coordination number of anions is always less than 1, suggesting that they do not have a strong influence on the structural organization of the water molecules in the La(III) and Dy(III) second solvation shell.

As previously observed, the second shell peak of the La/Dy-X $g(r)$'s has a broad shape, as the anions can be found in different orientations in the cation second coordination shell, i.e in a wide range of distances from the cation. To provide visual insights, three representative MD snapshots of the environment seen by the La(III) ion in the $La(TfO)_3$, $La(Tf_2N)_3$ and $La(NO_3)_3$ aqueous solutions are shown in Figure 8.19:

- The anion acts as monodentate ligand with only one oxygen atom point-

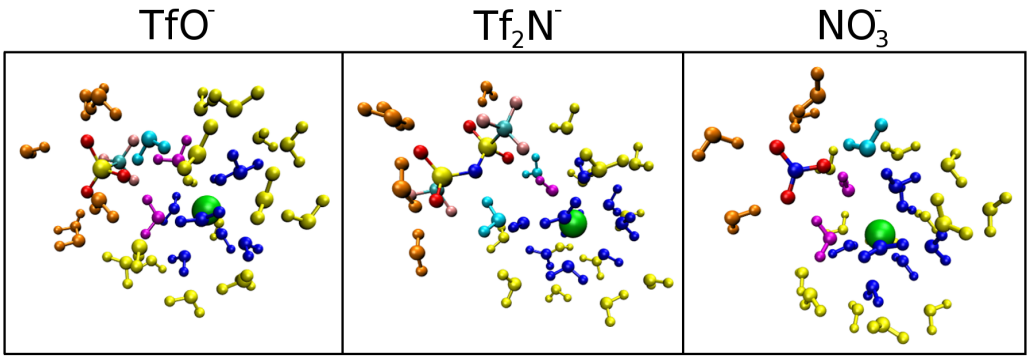

Figure 8.19: Simulation snapshots showing the anions belonging to the La(III) second coordination sphere. The La(III) first- and second-coordination sphere water molecules are colored blue and yellow, respectively, while those belonging to the anion first solvation sphere are orange. Note that the water molecules in magenta belong to both the La(III) and the anion first coordination sphere, while those colored in cyan are in the second coordination shell of the La(III) ion and in the first coordination shell of the anion.

ing toward the La(III) ion, and this oxygen atom is also coordinated with (i) two water molecules (magenta) belonging to the La(III) first solvation shell (see the TfO^- anion, left panel of Figure 8.19), (ii) one water molecule (magenta) being in the La(III) first solvation shell (see the Tf_2N^- anion, central panel of Figure 8.19).

- The anion acts as bidentate ligand with two oxygen atoms pointing towards the central La(III) ion, and they also coordinated two distinct water molecules belonging to the La(III) first hydration shell (see the NO_3^- anion, right panel of Figure 8.19).

In addition to being coordinated with the La(III) first shell water molecules, each anion can also coordinated one or two water molecules belonging to the second coordination shell of the cation (cyan water molecules in Figure 8.19). It should be noted that we have shown only three example configurations, one for each anion. However, all the three configurations are possible for all the three anions, and the same configurations also occur for the Dy(III) aqueous solutions.

From the analysis of the MD trajectories several exchanges of the anions between the cation neighborhood and the bulk have been observed. Figure 8.20 shows the instantaneous coordination number of anions in the Ln(III) second coordination shell for both La(III) (upper panels) and Dy(III) (lower panels) ions. It can be seen that, for almost the entire duration of the simulation, there is at most only 1 anion in the La(III)/Dy(III) second coordination shell, and configurations with 2 or 3 anions are very rarely. But the interesting result is that the most probable anion configuration is the zero-coordinated species, with the exception of $La(NO_3)_3$, suggesting once again the poor affinity of these anions for the two Ln(III) ions. Obviously, also several exchanges of water molecules entering and leaving the La(III)/Dy(III) second coordination shell have been observed. The exchange process rate has been evaluated

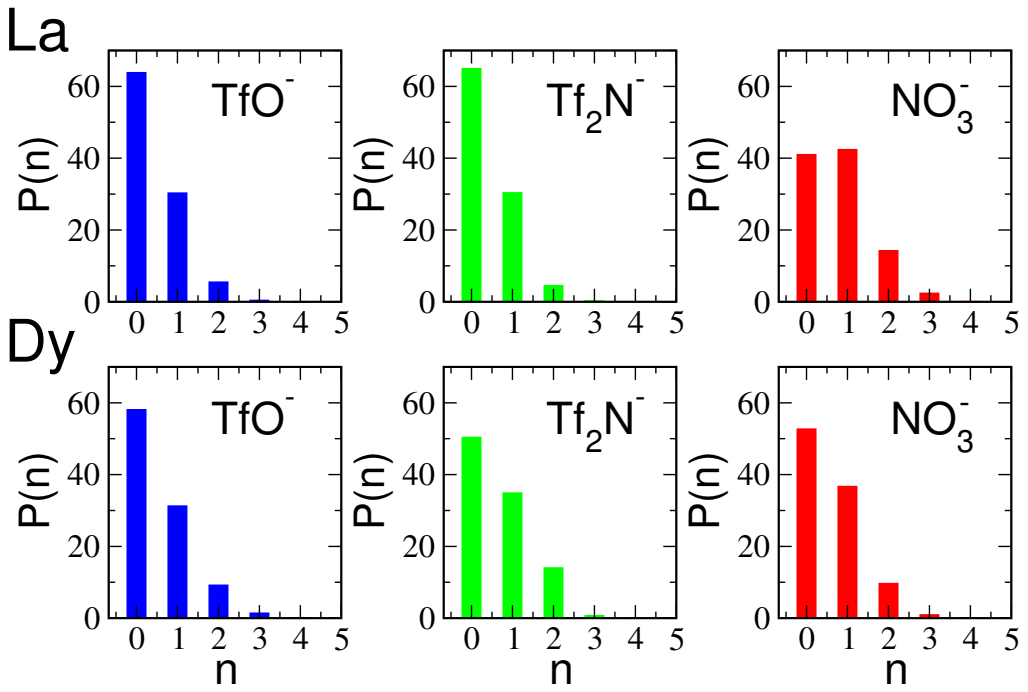

Figure 8.20: Instantaneous coordination number (n) distribution of anions belonging to the La(III) (upper panels) and Dy(III) (lower panels) second coordination shell calculated from the MD simulations of 0.1 M $La(TfO)_3$ and $Dy(TfO)_3$ (blue), $La(Tf_2N)_3$ and $Dy(Tf_2N)_3$ (green), and $La(NO_3)_3$ and $Dy(NO_3)_3$ (red) aqueous solutions.

by computing the mean residence times (MRTs) of both water molecules and anions in the cation second coordination shell.

The MRTs have been calculated using the method proposed by Impey et al. in Ref [152]. This approach is based on the calculation of the following correlation function:

$$n(t) = \frac{1}{N_t} \sum_{n=1}^{N_t} \sum_{j} P_j(t, t_n, t^*) \tag{8.5}$$

where N_t is the total number of steps of the MD simulation and P_j goes over all of the molecules j being either 0 or 1. It takes the value 1 if molecule j lies within the second coordination shell of the La(III)/Dy(III) ion at both time steps t_n and $t + t_n$, and in the interim does not leave the coordination shell for any continuous period longer than t*, otherwise it takes the value 0. At long times, $n(t)$ decays in an exponential fashion:

$$n(t) = n(0)e^{-t/\tau} \tag{8.6}$$

with a characteristic correlation time τ which defines the MRT of a molecule in the shell.[152] The MRTs of both anions and water molecules in the La(III) and Dy(III) second coordination shell are listed in Table 8.9, together with the MRTs of water molecules obtained for La(III) and Dy(III) ions in pure water. In particular, all the MRTs have been calculated using a t* of 0.5 ps. Such

	La(III)		Dy(III)	
system	$MRT^{(2)}_{WAT}$	$MRT^{(2)}_{X}$	$MRT^{(2)}_{WAT}$	$MRT^{(2)}_{X}$
water	11		14	
TfO^-	13	25	15	27
Tf_2N^-	15	23	15	22
NO_3^-	13	41	16	57

Table 8.9: Mean residence times (ps), calculated from the MD simulations of La(III) and Dy(III) salts aqueous solutions, together with those of La(III) and Dy(III) ions in pure water. In particular, $MRT^{(2)}_{WAT}$ and $MRT^{(2)}_{X}$ are the mean residence times of the water molecules and the anions in the La(III) and Dy(III) second coordination shell, respectively.

value, chosen as the minimum time to define a real exchange, corresponds to the average lifetime of a water-water hydrogen bond. In all cases the MRTs are in the order of magnitude of picoseconds, thus suggesting a flexible nature of the La(III) and Dy(III) second coordination shells. As far as the water molecules are concerned, the MRTs are quite similar for all the aqueous solutions and comparable to the ones obtained for La(III) and Dy(III) ions in pure water. The values are also of the same order of magnitude of those reported in a previous MD study of Ln(III) ions in liquid water, where a polarizable force field was employed.[137] The MRTs of anions, $MRT^{(2)}_{X}$, are bigger than those of water molecules; in particular, the calculated values for the TfO^- and Tf_2N^- ions are almost identical and smaller if compared to the nitrate one. Also in this case, our result is consistent with that obtained by Duvail et al. from a MD study of $Nd(NO_3)_3$ and $Dy(NO_3)_3$ in water.[150] The dynamic behavior is in line with the structural findings, that reveal a slightly stronger affinity of nitrates for the cation with respect to the TfO^- and Tf_2N^- anions. These last two ions seems to be organized in a more disordered and unstructured way around the cation.

8.2.6 Hydration properties of anions

Since the TfO^-, Tf_2N^- and NO_3^- ions are only weakly coordinated to the La(III) and Dy(III) ions, their coordination shells will be formed primarily by water molecules. Figure 8.21 shows several $g(r)$'s describing the interaction between anions and water molecules. In particular, in the upper and central panels the $g(r)$'s between the oxygen atom, O, of the anions and the hydrogen, HW, and oxygen, OW, atoms of water molecules are shown, while in the lower panel the S(anion)-OW $g(r)$'s for the TfO^- and Tf_2N^- anions, and

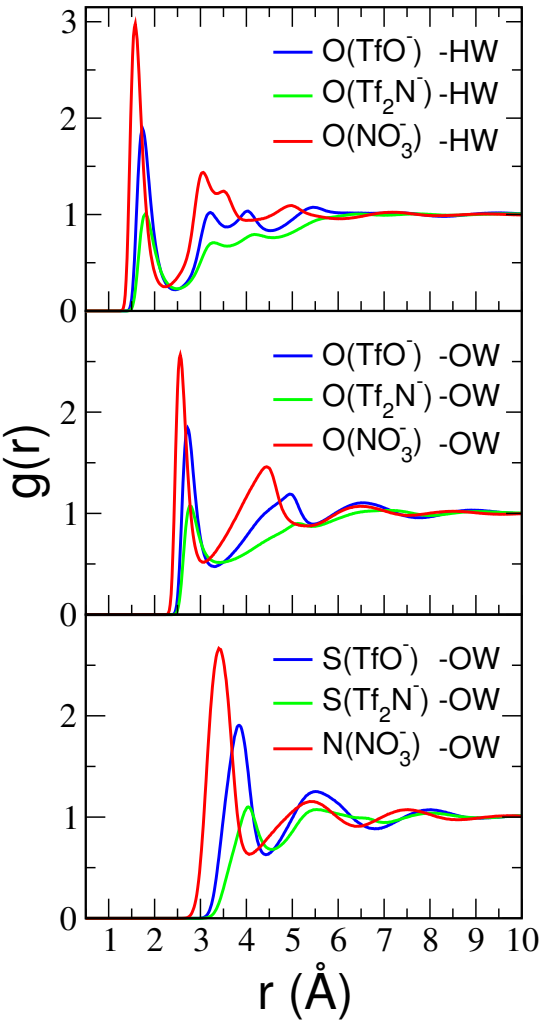

Figure 8.21: Anion-Water radial distribution functions, $g(r)$'s, obtained from the MD simulations of 0.1 M $La(TfO)_3$ (blue), $La(Tf_2N)_3$ (green) and $La(NO_3)_3$ (red) aqueous solutions. From the top to the bottom the following $g(r)$'s are reported: O(anion)-HW $g(r)$'s (upper panel), O(anion)-OW $g(r)$'s (central panel) and S/N(anion)-OW $g(r)$'s (lower panel).

the N(anion)-OW $g(r)$'s for the NO_3^- one are reported.

A first shell peak can be observed in all cases, even if this peak is well defined and more structured for the NO_3^- ion. The O(NO_3^-)-OW $g(r)$ first peak is centered at 2.56 Å, with about 2.6 water molecules around each oxygen atom of the anion, while the N(NO_3^-)-OW $g(r)$ first maximum is at 3.40 Å. These parameters are in good agreement with experimental [153] and calculated [154, 155] structural data (N-OW = 3.40 Å) of NO_3^- in liquid water, that is six to seven water molecules in the nitrate first hydration shell at a cutoff distance of 3.60 Å. The first shell peak becomes broader and less structured, and it shifts towards larger distances for the TfO^- and the Tf_2N^- ions. In particular, the O(TfO^-)-OW $g(r)$ first peak is centered at 2.72 Å, with a coordination number of 2.6, while the O(Tf_2N^-)-OW $g(r)$ first peak is centered at 2.78 Å, with a coordination number of 2.1. As regards the inter-

action of anion with the hydrogen atoms of water molecules (see the upper panel of Figure 8.21), a first distinct peak at shorter distances as compared to the O(anion)-OW $g(r)$ first maximum, and a second and less defined double peak at longer distances can be observed. This means that only one hydrogen atom of water molecules points towards the oxygen atoms of the anions, resulting in a strong hydrogen bond between the anion and water. Note that in the case of the TfO^- and Tf_2N^- anions, we have also calculated the $g(r)$'s between the carbon and fluorine atoms of the anions and the water molecules but, due to the low polarity of these sites, we have found that these atoms are very weakly coordinated with water and they are located at longer distances as compared to the sulfur and oxygen atoms. Identical results have been obtained from the analysis of the MD simulations of $Dy(TfO)_3$, $Dy(Tf_2N)_3$ and $Dy(NO_3)_3$ aqueous solutions.

The 3-D organization of the water molecules in the first solvation shell of the anion can be observed looking at the spatial distribution functions (SDFs) shown in Figure 8.22. The isodensity surfaces of the hydrogen and oxygen atoms are colored iceblue and magenta, respectively. Note that the isosurfaces around one half of the molecule only are shown for the Tf_2N^- anion, as its structure is symmetric with respect to the nitrogen atom. The strongest interaction between the anion and water molecules is with the hydrogen atoms, remarking the ability of the anions to form hydrogen bonds with water. In particular, for the TfO^- and NO_3^- ions the O(anion)-H(water) interaction is not linear along the S-O and N-O vector directions, respectively. Moreover, in the Tf_2N^- ion the distributions seem to be slightly less structured as compared to the TfO^- and NO_3^- ones, but always localized around the oxygen atoms.

All together these results reveal the strong affinity of the three anions with water. This behavior can explain why under high dilution conditions, as the one investigated in this work, the La(III) and Dy(III) salts are substantially dissociated, thus leading to a La(III) and Dy(III) first coordination shell mainly formed by water molecules. Moreover, the strongest affinity between the anions and water can be the reason of several behaviors observed in systems containing such anions. For example, the Tf_2N^- ion is a component of many room-temperature ILs,[156, 157] of fundamental interest in pure and applied chemistry. These ILs are soluble in water thanks to the favoured coordination of the Tf_2N^- anion with water.

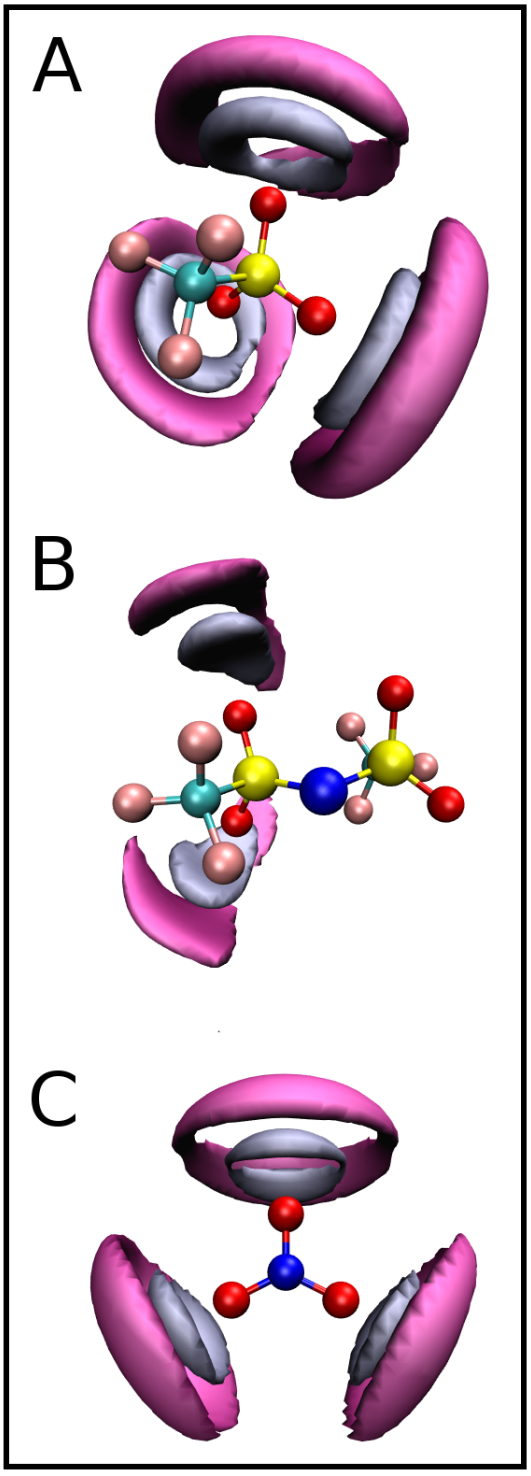

Figure 8.22: Spatial distribution functions (SDFs) of oxygen (magenta) and hydrogen (iceblue) atoms of water molecules around the TfO^- (A), Tf_2N^- (B) and NO_3^- (C) anions calculated from the MD simulations of 0.1 M $La(TfO)_3$, $La(Tf_2N)_3$ and $La(NO_3)_3$ aqueous solutions. Note that for the Tf_2N^- ion only the isosurfaces around one half of the molecule have been depicted, for clarity.

8.3 Ce(III) Nitrate in Ethylammonium nitrate

Ethylammonium nitrate (EAN) is one of the oldest ILs, known since 1914 when it was described by Walden as an IL with a melting point of 287.6 K.[158] EAN belongs to the class of protic ILs, which are formed through proton transfer from a Brønsted acid to a Brønsted base. This proton transfer gives rise to the presence of proton-acceptor and proton-donor sites, leading to the formation of a hydrogen-bond network, reminiscent to the three-dimensional hydrogen bond network of water.[159] Additionally, EAN has been identified as being able to act as self-assembly media, having a nanoscale structure that can be fitted with a bicontinuous sponge-like model. The amphiphilic nature of the cation leads to the occurrence of mesoscopic tails clustering embedded into a polar mesh.

Here we will explore the solvation properties of a diluted solution of the Ce(III) ion dissolved in EAN, by always combining MD simulations with EXAFS spectroscopy. Such solution has been taken as a model to understand the molecular interactions taking place between a lanthanoid ion and a protic IL. In fact, although EAN is the earliest discovered IL and the PIL on which most researchers have been focused up to now, there is a lack on reported results about solvation of ionic or molecular species in EAN, an essential step for almost any successful application. In particular, we have carried out MD simulations with or without including polarization effects (vide infra), and this is the first MD study where a polarizable force field has been used to describe a heavy metal ion in a protic IL. A previous MD investigation has been carried out on La(III) and Lu(III) in EAN, but it was a DFT-based MD study.[160]

8.3.1 Experimental Methods

X-ray absorption measurements. $Ce(NO_3)_3{\cdot}6H_2O$ was purchased from Sigma-Aldrich with a stated purity of 99.5% and further purification was not carried out, while Ethylammonium nitrate was purchased from Iolitec GmbH with a stated purity of $> 99\%$. A 0.05 M solution of $Ce(NO_3)_3{\cdot}6H_2O$ in ethylammonium nitrate was made by dissolving the proper amount of salt in EAN and it was sonicated under nitrogen for 10 min. The solution was kept under vacuum at 80°C for 24 hours to remove water, and a final water content of 150 ppm was measured by Karl-Fischer titration. The Ce K-edge XAS spectra of the solution were collected in transmission mode at room temperature at the beamline BM23 of the European Synchrotron Radiation Facility (ESRF). The monochromator was equipped with two flat Si(311) crystals with the second crystal detuned by 20% for harmonic rejection. The sample was kept in a cell with Kapton film windows and Teflon spacers of 2 cm. Three spectra were collected and averaged.

Molecular Dynamics details. Two classical MD simulations of a 0.05 M solution of $Ce(NO_3)_3$ in EAN, corresponding to a molar ratio of 1:224, were performed using either a non-polarizable (UPOL) or a polarizable (POL)

force field. In particular, for the UPOL-MD we used the DL_POLY code,[86] while the POL-MD was carried out by means of the FIST module of CP2K package, where the self-consistent method (SCF) was employed to propagate induced dipoles in time. Note that, in this case, the system was previously equilibrated adopting the UPOL force field. The initial configuration was constructed by randomly positioning 2 $Ce(NO_3)_3$ molecules and 448 EAN molecules within a very large cubic simulation box. Extensive equilibration runs were performed, comprising of 10000 steps of initial energy minimization and a series of NPT runs at 300 K and high pressure, until the experimental density of pure EAN [161] was reached. The box edge length obtained was 40.62 Å. Then the system was equilibrated under constant NVT conditions (T = 300 K) for 3 ns. The equilibrated system was then simulated in the NVT ensemble at 300 K, using either the UPOL or the POL force field for 1.5 ns, with a timestep of 1 fs and saving a configuration every 200 time steps. As for all other simulations of pure ILs and IL/water mixtures, the temperature was kept constant at 300 K using the Nosé-Hoover thermostat,[87, 88] with a relaxation constant of 0.5 ps. A cut-off of 12 Å was used to deal with nonbonded interactions, using the Ewald summation method to treat the long-range electrostatic effects.[89] The SHAKE algorithm [76] has been employed to constrain the stretching interactions of the hydrogen atoms. Periodic boundary conditions were used in order to mimic bulk conditions.

Additionally, a UPOL MD simulation at 300 K has been carried out on a larger cubic box system, consisting of 5 $Ce(NO_3)_3$ molecules and 1120 EAN molecules, with an edge length of 55.13 Å, for a total production time of 10 ns. Then the system was heated at 400 K, while keeping the system density equal to that of the simulation at 300 K, and simulated at 400 K for 10 ns. By selecting 4 different configurations in the simulation at 400 K, new simulations at 300 K were carried out for 10 ns. All the MD parameters chosen to simulate the smaller system were also adopted for the larger one. The MD simulation of pure EAN has been carried out using the same MD protocol and force fields employed for the $Ce(NO_3)_3$ solution. To simulate the liquid state, 1000 ionic couples were placed in a cubic box of 52.85 Å edge length, with periodic boundary conditions, and the simulation was carried out for 10 ns.

As far as the force field is concerned, the bonded interactions were described by means of the Lopes and Pádua model.[90, 91] Conversely, two different force fields were considered for the nonbonded interactions, a non-polarizable (UPOL) and a polarizable (POL) one. In both cases, we used the typical Lennard-Jones potential form to describe the non-electrostatic interaction, with the exception of the interaction between Ce(III) ion and the oxygen atoms of NO_3^- anions, which was treated with the Buckingham formalism:

$$V_{Ce-O}^{buck} = \sum_{ij} A e^{-B r_{ij}} - \frac{C}{r_{ij}^6} \tag{8.7}$$

where A, B, and C are different between the UPOL and POL force fields. The Lennard-Jones parameters for EAN were taken from Lopes and Pádua,[90, 91]

	Ce(III) (UPOL)	Ce(III) (POL)
A (kcal mol^{-1})	240000	240000
B (Å^{-1})	3.500	3.500
C (Å^6 kcal mol^{-1})	8889.8	8789.5
σ_{Ce-Ce} (Å)	3.4035	3.4035
ϵ_{Ce-Ce} (kJ mol^{-1})	0.2855	0.2855
R$_i$ (Å)	1.220	1.220

Table 8.10: Ce(III)-O interaction parameters for the Buckingham potential and Ce-Ce Lennard-Jones parameters. R$_i$ is the effective ionic radius as reported in Ref [132].

while for Ce(III) Lennard-Jones parameters we used the values developed ad hoc to reproduce the EXAFS experimental Ce-water mean distances (see Section 8.1). As regards the Ce-O Buckingham potential, the polarizable parameters were taken from the work of Martelli et al,[162] while for the non-polarizable ones we used as reference the La-O values reported in the same work and adjusted them by considering the difference in ionic radii between La(III) and Ce(III), using the same interpolation procedure adopted to develop force fields for lanthanoids(III) in water [132] and dimethylsulfoxide.[163] All the Ce(III) parameters are listed in Table 8.10.

For the non-polarizable electrostatic term, we considered standard point charges: 3+ for Ce(III), for NO_3^- anion the Lopes and Pádua force field has been adopted, while for the ethylammonium cation we used the OPLS values.[92] For the electrostatic part, in the polarizable potential we have added to the Coulomb interaction between point charges the polarization term [82]:

$$V_{pol} = \sum_{ij}[(q^i\mu_\alpha^j g^{ij}(r^{ij}) - (q^i\mu_\alpha^i g^{ji}(r^{ij}))\mathbb{T}_\alpha^{ij} - \mu_\alpha^j\mu_\beta^j\mathbb{T}_{\alpha\beta}^{ji}]+ \sum_i(\frac{1}{2\alpha^i}|\mu|^2) \quad (8.8)$$

where q are the atomic point charges, μ are the induced dipoles centered on atoms, α is the atomic polarizability centered only on O atoms,[164] T_α and $T_{\alpha\beta}$ are the charge-dipole and dipole-dipole interaction tensors and $g^{ji}(r^{ij})$ are the Tang-Toennies functions aimed at including the short range damping effects.

8.3.2 Polarizable *vs* non-polarizable MD simulations

The EAN IL shows many distinctive properties similar to that of water, such as the high polarity, the capability to form an extensive network of hydrogen bonds and the ability to promote micelle formation.[165] As regards

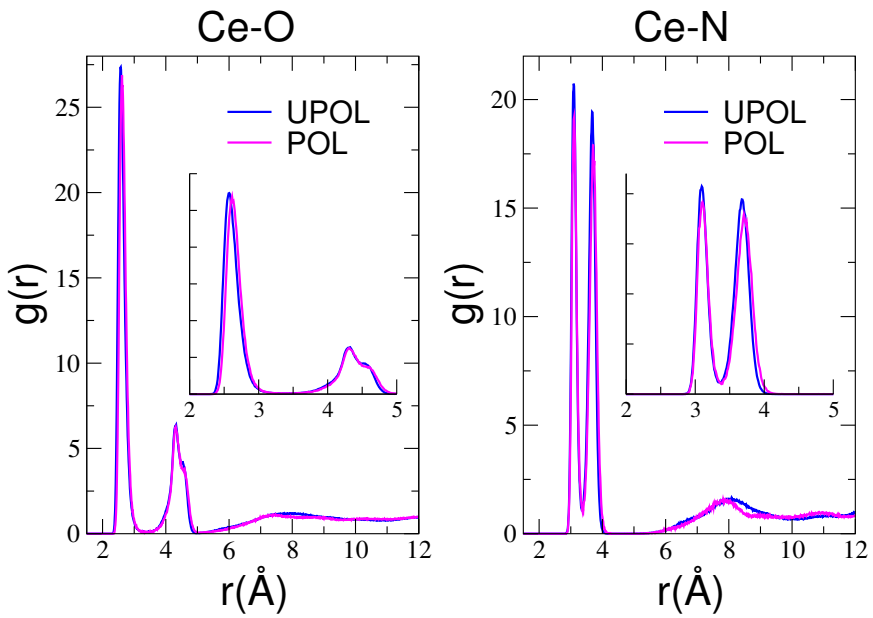

Figure 8.23: Ce-O and Ce-N radial distribution functions, $g(r)$'s, calculated from the MD simulations of $Ce(NO_3)_3$ in EAN using either the non-polarizable (UPOL) (blue line) or the polarizable (POL) (magenta line) force field.

water, it is well known that, even if it is a seemingly simple molecule, it shows a very complex behavior, arising from the delicate interplay between different kinds of interactions, such as hydrogen bonding and many body polarization effects. In particular, several MD investigations have shown that the optimal approach to carry out an accurate determination of the hydration properties of Ln(III) ions in water is by including explicit polarization in the classical force field, as the high charge of Ln(III) cations has a strong polarizing effect on the surrounding water molecules.[136, 137, 166] Due to the similarities of EAN and water, when carrying out MD simulations of EAN, one can expect that the same effects, such as polarization, that are important to describe aqueous environments, should be considered also to provide a reliable description of EAN-containing systems. However, at variance with water, EAN is entirely composed of ions and this difference could be fundamental in determining the role of polarization in the two systems. It is therefore important to understand if the MD simulations of Ln(III) ions in EAN should explicitly include polarization effects. In order to evaluate these effects on the structural properties of $Ce(NO_3)_3$ in EAN, we have carried out two MD simulations using either a polarizable (POL) or a non-polarizable (UPOL) force field, and we have compared the results obtained with the two different theoretical approaches. In particular, the MD box consisted of 2 $Ce(NO_3)_3$ and 448 EAN molecules and the simulations were carried out for 1.5 ns. Focusing first on the solvation properties of the Ce(III) ion, it was found to be coordinated only by the nitrate ions. The Ce-O and Ce-N $g(r)$'s, where O and N are the oxygen and nitrogen atoms of the NO_3^- anions, respectively, are shown in Figure 8.23, while the $g(r)$ maximum positions (R) and

	Ce-O		Ce-N			
system	R_O(Å)	N_O	R_{bi}(Å)	N_{bi}	R_{mono}(Å)	N_{mono}
UPOL	2.57	12.2	3.10	3.2	3.71	5.8
POL	2.59	12.1	3.10	3.1	3.71	5.9

Table 8.11: Position of the $g(r)$ peaks, R, and coordination number, N, obtained from the MD simulations of $Ce(NO_3)_3$ in EAN using either the non-polarizable (UPOL) or the polarizable (POL) force field. R_{bi}, R_{mono}, N_{bi}, and N_{mono} are the maximum positions and coordination numbers of the first and second peaks of the Ce-N $g(r)$, corresponding to the bidentate and monodentate coordination around the Ce(III) ion. Note that the Ce-O coordination number, N_O, has been calculated using a cutoff distance of 3.30 Å, while N_{bi} and N_{mono} have been calculated within a cutoff distance range of 0.0-3.36 Å and 3.36-4.20 Å, respectively.

coordination numbers (N) are collected in Table 8.11. The first important observation is that the results obtained from the simulations with or without explicit polarization are almost identical. Moreover, the Ce-N $g(r)$'s show two peaks of similar intensity, as two different coordinations of the nitrate molecules around the Ce(III) ion are possible. When the nitrate ion acts as monodentate ligand with only one oxygen atom pointing towards the Ce(III) ion, the Ce-N distance is about 3.7 Å, while when it acts as bidentate ligand with two oxygen atoms directed towards the cation, the Ce-N $g(r)$ maximum is shifted towards shorter distances (about 3.1 Å). Additionally, the analysis of the coordination numbers reveals that about 3 nitrate ions adopt the bidentate coordination and 6 the monodentate one, for a total of 9 NO_3^- anions surrounding the Ce(III) ion. As a consequence, the first coordination shell of the cation is formed by a total of 12 oxygen atoms.

As radial distribution functions give only information on the radial distribution of atoms around a given species, in order to provide a description of the three-dimensional structure of nitrate ions around the Ce(III) ion, we have developed a tool based on the calculation of CDF functions. Indeed, the identification of the local three-dimensional structures that are formed around ions in liquids is a difficult task, due to the thermal and structural disorder of these systems, and the most used ADF analysis in many cases is not able to distinguish among different polyhedra having similar internal angle values. Our tool revealed itself able to unambiguously assess the coordination geometry of ion complexes in liquid systems. Figure 8.24 shows the CDFs, for both the UPOL and POL MD simulations, that combine the Ce-X distances and the Ce-O-N angles, where X is either the oxygen (panels A and A′) or nitrogen (panels B and B′) atom of the nitrate anion, respectively. Panels A and B also provide distance and angle definitions used for the CDF calculation. This kind of analysis allows us to determine the geometric orientation of a single nitrate ion with respect to the Ce(III) ion. By computing

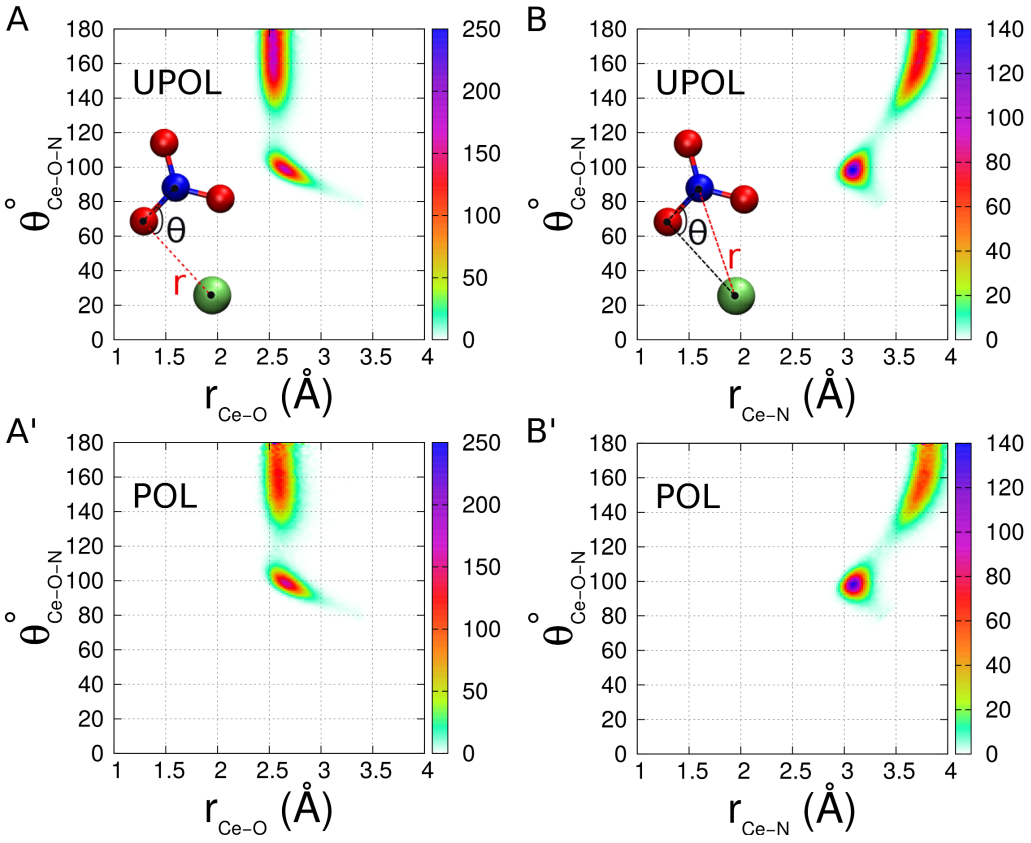

Figure 8.24: Combined distribution functions (CDFs) calculated from the MD simulations of $Ce(NO_3)_3$ in EAN carried out using either the non-polarizable (UPOL) (A,B) or the polarizable (POL) (A′,B′) force field. (A,A′): CDFs between the Ce-O distances and the Ce-O-N angles. (B,B′): CDFs between the Ce-N distances and the Ce-O-N angles. Panels A and B also show the definition of distances, r, and angles, θ, used for the CDF calculation.

the CDFs from MD simulations using either the UPOL or POL force fields, we have obtained almost identical results, confirming the previous findings. Moreover, the CDF analysis reveals that when the nitrate anions coordinate the Ce(III) ion in a bidentate mode, an ordered and stable geometry (as suggested by the quite narrow peaks) is formed with a Ce-O-N angle of 98° and Ce-O and Ce-N distances of 2.65 Å and 3.10 Å, respectively. On the contrary, the monodentate coordination gives rise to a peak located between 150° and 180° in both Ce-O and Ce-N CDFs. These peaks are broader, suggesting the formation of a more disordered structure with a higher orientational freedom. Finally, Figure 8.25 shows the CDFs calculated between Ce-O distances and O-Ce-O angles, where O are the oxygen atoms belonging to the first solvation shell of the Ce(III) ion. As described in Section 8.1, this CDF is the ideal tool to highlight the global geometry of a metal ion (in the specific case the Ce(III) ion) first solvation shell. Also in this case, the CDFs computed from the MD simulations carried out with or without including explicit polarization effects are almost identical.

Both the $g(r)$ and CDF analysis have shown that it is not necessary to

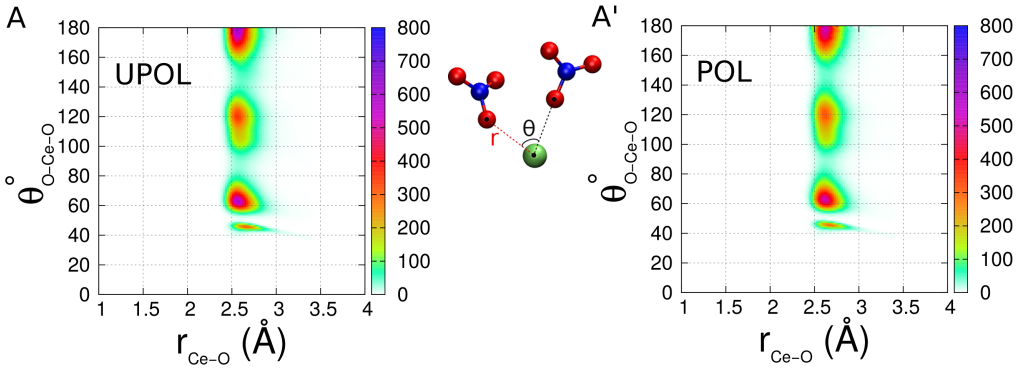

Figure 8.25: Combined distribution functions (CDFs) between the Ce-O distances and the O-Ce-O angles calculated from the MD simulations of $Ce(NO_3)_3$ in EAN carried out using either the non-polarizable (UPOL) (A) or the polarizable (POL) (A′) force field. Note that only the oxygen atoms belonging to the Ce(III) ion first solvation shell are accounted for in the calculation. The definition of the distance, r, and the angle, θ, used for the CDF calculation has been also shown.

introduce the polarization term in the classical force field to structurally characterize $Ce(NO_3)_3$ in EAN. This is an important finding since the introduction of explicit dipoles in the simulations leads to a high computational cost, posing severe limits in the simulation times achievable, as well as in the size of the simulated systems. These limits could be a problem when dealing with EAN-containing systems, or more in general with ILs, as they have a very high viscosity and their dynamics is much slower than that of conventional liquids, and it is very important to simulate the system for very long equilibration and simulation times (on the order of nanoseconds). In fact, the error associated with a poor sampling of the phase space of the system could be much larger than that arising from the neglect of polarization effects in the MD simulations.

8.3.3 Ce(III) first coordination complex: the icosahedral geometry

Once we have demonstrated that MD simulations with or without explicit polarization provide the same local three-dimensional structures around the Ce(III) ion, we have decided to enlarge both the size and the time length of the simulation using the non-polarizable force field with the aim of carrying out a better sampling of the phase space visited by our system. In particular, a MD box including 5 $Ce(NO_3)_3$ molecules was simulated for 10 ns, and the calculated Ce-O and Ce-N $g(r)$'s have been compared with the previously reported ones (see Figure 8.26). It can be seen that the Ce-O and Ce-N maximum positions are identical for both systems, while there is a difference in the relative intensity of the two Ce-N $g(r)$ peaks. This is a consequence of the different ratio between the monodentate and bidentate coordination

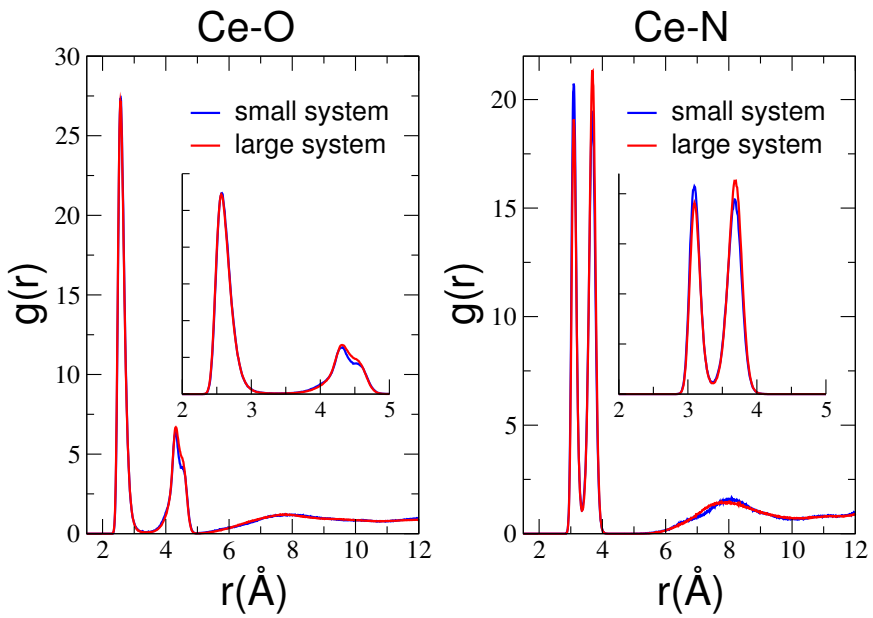

Figure 8.26: Ce-O and Ce-N radial distribution functions, $g(r)$'s, calculated from the MD simulations of $Ce(NO_3)_3$ in EAN for the box containing either 2 Ce(III) ions (blue line) or 5 Ce(III) ions (red line).

in the two systems, resulting in a 0.2 variation of the N_{bi} coordination number (see Tables 8.11 and 8.12). Indeed, in the larger system, one of the five Ce(III) ions is coordinated by 10 NO_3^- anions instead of 9. However, the first coordination shell of the cation is always formed by a total of 12 oxygen atoms.

At this point, we decided to proceed further by carrying out a MD simulation at high temperature (400 K), while keeping the system density equal to that used in the simulation at 300 K. In fact, as previously mentioned, a possible drawback of systems with a high viscosity is the slow dynamics of the ions in the MD simulations. One of the strategy to overcome this problem is to increase the temperature of the simulated system to accelerate the ion dynamics and possibly explore additional local minima of the potential energy surface. By following the trajectory of the high-temperature simulation as a function of time, we observed that some NO_3^- anions belonging to the Ce(III) second coordination shell entered the first shell. In particular, at the beginning of the simulation only one Ce(III) ion was 10-fold coordinated, after about 260 ps a second Ce(III) ion became coordinated by 10 NO_3^- anions and finally, after about 5 ns, all 5 Ce(III) cations were 10-fold nitrate coordinated. To shed light on this behaviour, we selected from the high-temperature trajectory 4 different frames to be used as starting configurations of new MD simulations carried out at low temperature (300 K). In particular, the configurations were chosen in such a way that they contained 2, 3, 4 or 5 Ce(III) ions coordinated by 10 nitrate ions, respectively (the corresponding simulations are labelled SIM1, SIM2, SIM3 and SIM4). By analyzing the trajectories, we have found that the Ce(III) ion preserves the

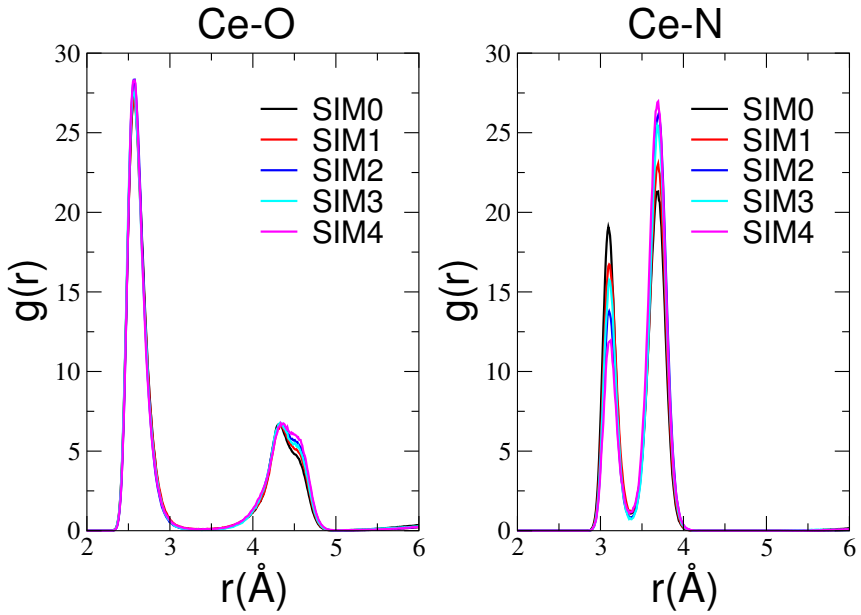

Figure 8.27: Ce-O and Ce-N radial distribution functions, $g(r)$'s, calculated from the MD simulations of $Ce(NO_3)_3$ in EAN for the box containing 5 Ce(III) ions. SIM0 is the initial simulation carried out at 300 K, while SIM1, SIM2, SIM3 and SIM4 refer to the simulations carried out at 300 K, after initial heating at 400 K, containing 2, 3, 4 or 5 Ce(III) ions coordinated by 10 NO_3^- ions, respectively.

	Ce-O		Ce-N			
system	R_O(Å)	N_O	R_{bi}(Å)	N_{bi}	R_{mono}(Å)	N_{mono}
SIM0	2.57	12.2	3.10	3.0	3.71	6.2
SIM1	2.57	12.2	3.10	2.8	3.71	6.6
SIM2	2.57	12.1	3.10	2.5	3.71	7.1
SIM3	2.57	12.0	3.10	2.2	3.71	7.6
SIM4	2.57	12.0	3.10	2.0	3.71	8.0

Table 8.12: Position of the $g(r)$ peaks, R, and coordination number, N, obtained from the MD simulations of $Ce(NO_3)_3$ in EAN using a box with 5 $Ce(NO_3)_3$ molecules. SIM0 is the initial simulation carried out at 300 K, while SIM1, SIM2, SIM3 and SIM4 are the simulations carried out at 300 K, after initial heating at 400 K, and containing 2, 3, 4 or 5 Ce(III) ions coordinated by 10 NO_3^- anions, respectively. R_{bi}, R_{mono}, N_{bi}, and N_{mono} are the maximum positions and coordination numbers of the first and second peaks of the Ce-N $g(r)$, corresponding to the bidentate and monodentate coordination around the Ce(III) ion. Note that the Ce-O coordination number, N_O, has been calculated with a cutoff distance of 3.30 Å, while N_{bi} and N_{mono} have been calculated within a cutoff distance range of 0.0-3.36 Å and 3.36-4.20 Å, respectively.

coordination adopted in the high temperature simulation also when the temperature was lowered. In other words, if Ce(III) was coordinated by 10 NO_3^- ions in the simulation carried out at 400 K, it retains this coordination when it was simulated at a lower temperature (300 K). Figure 8.27 shows the Ce-O and the Ce-N $g(r)$'s calculated from the four trajectories together with those of the initial simulation carried out at 300 K, while the structural parameters are collected in Table 8.12. The very interesting result is that the total number of oxygen atoms in the Ce(III) first coordination shell is always 12, for both the 9-fold and 10-fold nitrate coordination. This means that there is a different ratio of NO_3^- ions acting either as monodentate or bidentate ligands in the 9-fold and 10-fold nitrate coordination complexes. In particular, the monodentate/bidentate ratio is 6/3 and 8/2 for the 9-fold and 10-fold coordination, respectively. As a consequence, going from SIM1 to SIM4, the Ce-N coordination number related to the monodentate nitrate ligands (N_{mono}) increases, while that of the bidentate ones (N_{bi}) decreases. An example of the two possible clusters is depicted in Figure 8.28, where two representative MD shapshots are reported. All together our results reveal that an equilibrium between a 9-fold and 10-fold nitrate coordination exists for Ce(III) in EAN, but the first coordination shell of the cations is always formed by 12 oxygen atoms. The only difference stands in the monodentate/bidentate ratio. In particular, when the tenth NO_3^- ion enters the Ce(III) first coordination shell, it enters as monodentate ligand and one nitrate ion of the first shell switches from the bidentate to the monodentate coordination mode, so that the number of the oxygen atoms coordinating the cation does not change.

Additional insights into the global geometry of the Ce(III) first solvation shell have been gained by calculating the CDFs between Ce-O distances and

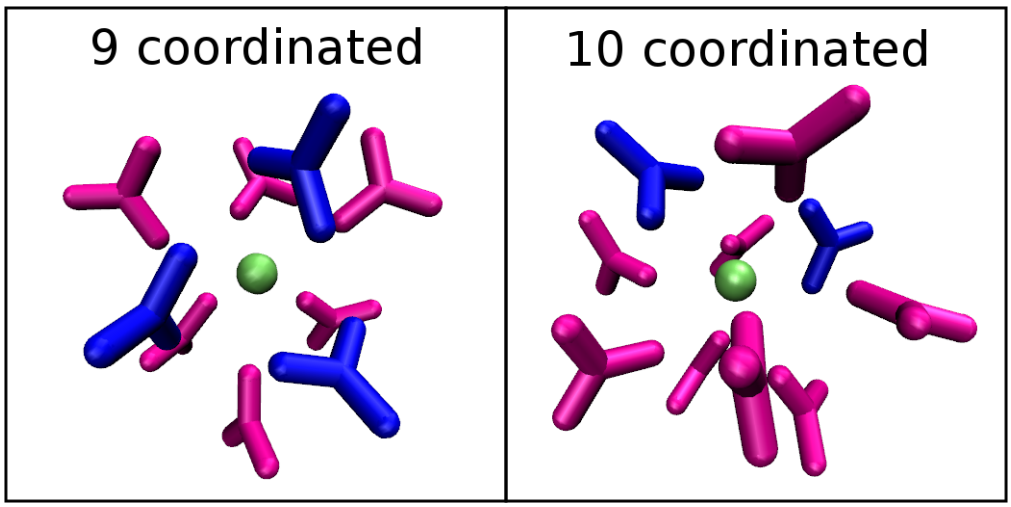

Figure 8.28: MD snapshots showing the nitrate molecules belonging to the first solvation shell of the Ce(III) ion, in the case of the 9-fold and 10-fold nitrate coordination. The nitrate molecules that are monodentate with respect to the Ce(III) ion are colored magenta, while those adopting a bidentate coordination mode are blue. The number of oxygen atoms in the Ce(III) first coordination shell is 12 in both cases.

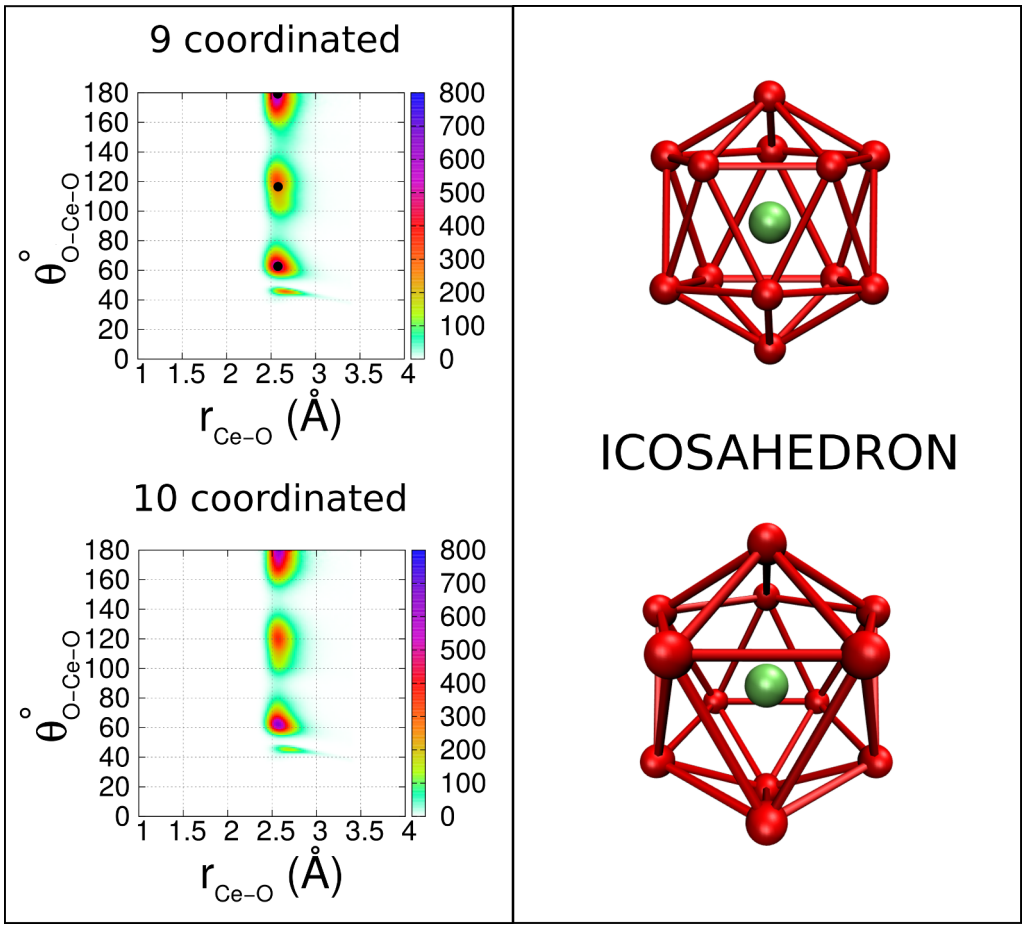

Figure 8.29: Left panel: combined distribution functions (CDFs) between the Ce-O distances and the O-Ce-O angles, calculated from the MD simulations of $Ce(NO_3)_3$ in EAN for either the 9-fold (top) or the 10-fold (bottom) nitrate coordinated Ce(III) ion. Only the oxygen atoms belonging to the Ce(III) ion first solvation shell have been included in the calculation. Note that the black spots represent the theoretical angles for the icosahedral geometry. Right panel: the icosahedron, the first solvation structure of Ce(III) ion in EAN. Two different viewpoints of the same model are shown, for clarity.

O-Ce-O angles separately for the 9-fold and 10-fold nitrate complexes. To this end, we have extracted from each simulation two sets of configurations, the former containing 9-fold coordinated Ce(III) ions only, and the latter containing 10-fold coordinated Ce(III) ions, and we have calculated the CDF over the two different sets. The CDFs are shown in the left panel of Figure 8.29 and, as it can be seen, the functions are identical in the two cases, in both the shape and the intensity of the peaks. This means that the oxygen atoms of the first coordination shell adopt the same geometry in the two different clusters. Note that identical results have been obtained for all of the simulations (SIM0 to SIM4). These findings suggest that the driving force of the solvation process is the strong electrostatic interaction between the Ce(III) ion and the oxygen atoms of the nitrate anions. A more detailed analysis of the CDFs reported in the left panel of Figure 8.29 allows us to understand if the structure adopted by the 12 oxygen atoms around the Ce(III) cation

is symmetrical and similar to that of an ideal polyhedron. Three peaks are found in the CDF, centered at a Ce-O distance of 2.57 Å and O-Ce-O angles of 63°, 116° and 180°, corresponding to that of an icosahedron. The theoretical angles of the ideal icosahedron are also marked by black spots in Figure 8.29, for the CDF obtained for the 9-fold coordinated complex, as an example. The icosahedron is a regular polyhedron that has 20 faces, 30 edges and 12 vertices. All the faces are equilateral triangles and are all congruent. An example of icosahedron from two different viewpoints is depicted in the right panel of Figure 8.29. Also by integrating the CDF peaks, we obtained a number of angles equal to those of an ideal icosahedron, that are 30, 30 and 6 for the O-Ce-O angles at 63°, 116° and 180°, respectively. Therefore, the first coordination shell of the Ce(III) ion is formed by 12 oxygen atoms arranged in an icosahedral geometry, a very regular and symmetric structure, at variance with the tricapped trigonal prism (TTP) geometry that the Ce(III) cation adopts in water. An example of the local environment around a Ce(III) ion extracted from the SIM0 simulation is shown in Figure 8.30. It can be seen that the Ce(III) cation is embedded inside the EAN polar domains via the interactions formed between the first shell NO_3^- anions and the polar heads of the ethylammonium cations. Moreover, in the Ce(III) outer shells EAN cations and nitrate anions form a three-dimensional network of polar charged domains that solvophobically exclude the ethyl chains into apolar regions.

It should be noted that our findings are slightly different from those

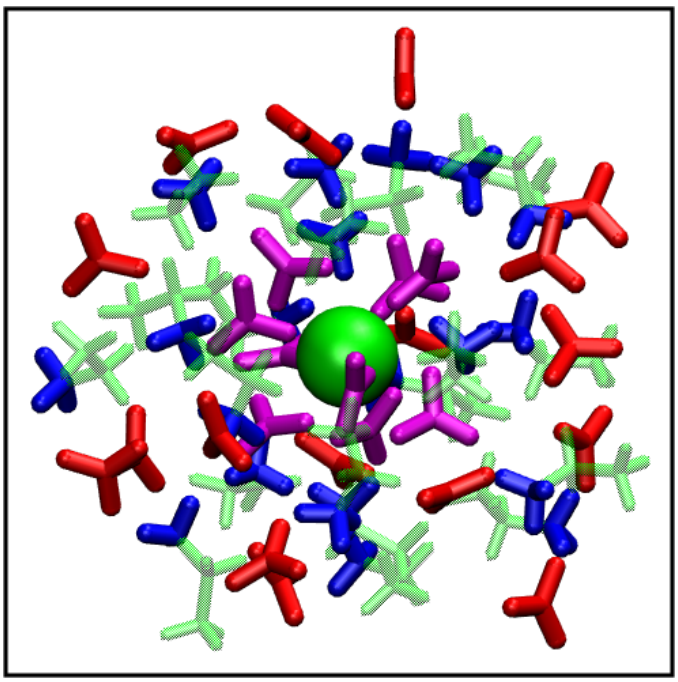

Figure 8.30: MD snapshot extracted from the SIM0 simulation showing the local environment around a Ce(III) ion (green). In particular, the nitrate ions belonging to the Ce(III) first coordination shell are colored magenta, the other nitrate ions are red, while the ethyl chains and the polar heads of the ethylammonium cations are colored in transparent green and blue, respectively.

obtained in a recent DFT-based MD investigation of La(III) and Lu(III) in EAN. In this case, for the La(III) ion, that is expected to have coordination properties similar to Ce(III), it was found a first solvation shell composed of 5 nitrate anions, all of them acting as bidentate ligands, for a total of 10 oxygen atoms in close contact with the La(III) ion.[160] However, it has to be considered that the different coordination structure found in the ab initio MD simulation could be due to the very short simulation time lengths (tens of picoseconds) and small box sizes, as well as to the fact that it is not trivial to treat heavy atoms by means of ab initio calculations. Conversely, our results are in good agreement with all of the reported crystallographic structures of Ce(III) nitrate complexes present in the literature (see for example Ref [167, 168, 169]), where it was found that the Ce atoms are surrounded by six bidentate nitrate groups, for a total of 12 oxygen atoms arranged in an icosahedral geometry with Ce-O distances ranging from 2.60-2.72 Å. Note that in solid structures also the other Ln(III) ions are coordinated by six bidentate nitrate ligands with a first shell icosahedral structure.[170, 171]

8.3.4 Influence of $Ce(NO_3)_3$ on the EAN structure

A few investigations have dealt with the structural characterization of protic IL mixtures with inorganic salts, most of which focused on Li(I) salts due to the interest in Li batteries, and depending on the salt concentration the bulk structure of the IL system has been found either to mainly mantain its macroscopic arrangement or to be significantly perturbed upon salt addition.[172, 173, 174, 175] For example, neutron diffraction and empirical structure refinement modeling have been employed by Hayes et al. to study a 1:10 $Li(NO_3)$/EAN solution, and it was found that the $Li(NO_3)$ salt weaks the hydrogen bond network formed between EAN cations and anions and it also gives rise to a disruption of the ethyl chain alignment. Conversely, MD simulations carried out by Méndez-Morales et al. on $Li(NO_3)$/EAN solutions, with a molar ratio from 1:12 up to saturation, have revealed that EAN retains its structure, even if there was a gradual disruption of the hydrogen bonds with increasing $Li(NO_3)$ concentration.

To shed light into the effect of adding $Ce(NO_3)_3$ to EAN we have carried out a MD simulation of pure EAN without explicit polarization, and we have compared the structural results obtained. In particular, the left panel of Figure 8.31 shows the H_{NH_3}-O and N_{NH_3}-N $g(r)$'s, describing the interaction between cations and anions of the EAN IL. As it can be seen, these $g(r)$'s are identical both in pure EAN and in the solution. Moreover, also the CT-CT $g(r)$'s, calculated between the terminal carbon atoms (CT) of the ethylammonium ethyl chains are identical for both systems, meaning that no reorganization of the EAN apolar domains occurs upon salt addition. Finally, we have calculated the N-$H_{NH_3}\cdots$O angular distribution functions, that are reported in the right panel of Figure 8.31. Both functions feature a peak at about 107°, reflecting the existence of bent hydrogen bonds in agreement with

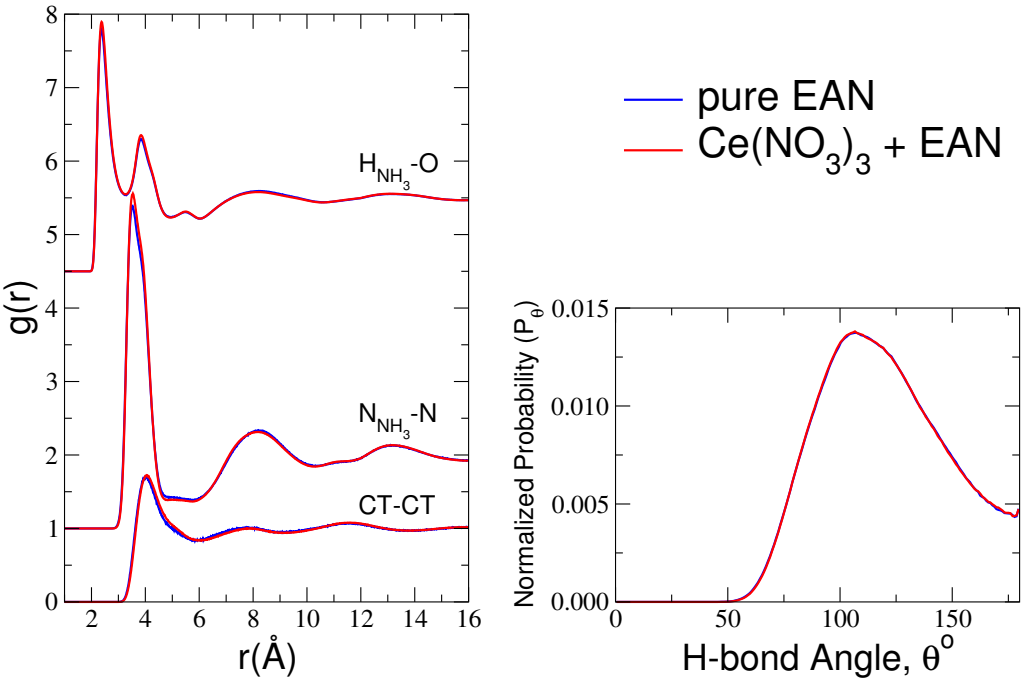

Figure 8.31: Left panel: radial distribution functions, $g(r)$'s, calculated from the MD simulations of pure EAN (blue line) and of the $Ce(NO_3)_3$ solution (red line). From top to the bottom the following $g(r)$'s are reported: H_{NH_3}-O, N_{NH_3}-N and CT-CT $g(r)$'s, where CT is the terminal carbon atom of the ethylammonium ethyl chains. Right panel: angular distribution functions of the N-H_{NH_3} $\cdots$O angle (θ) calculated from the MD simulations of pure EAN (blue line) and of the $Ce(NO_3)_3$ solution (red line).

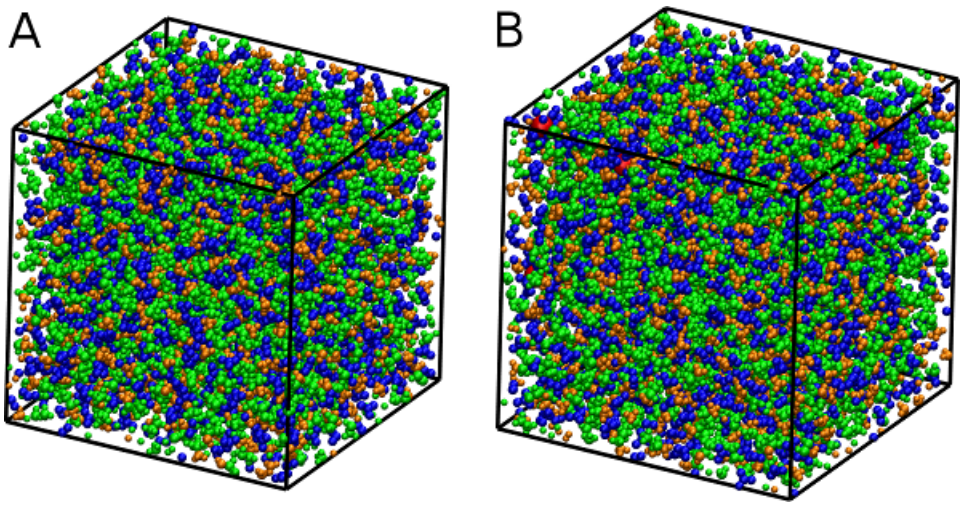

Figure 8.32: Snapshots of the MD simulation boxes of pure EAN (A) and of the $Ce(NO_3)_3$ solution (B). The Ce(III) ions are shown in red, the nitrate ions in blue, while the polar heads and the ethyl chains of the ethylammonium cation are colored orange and green, respectively.

previous results,[174, 176] that is also retained in the presence of $Ce(NO_3)_3$. Multiple acceptor atoms belonging to the polar domains interact with each

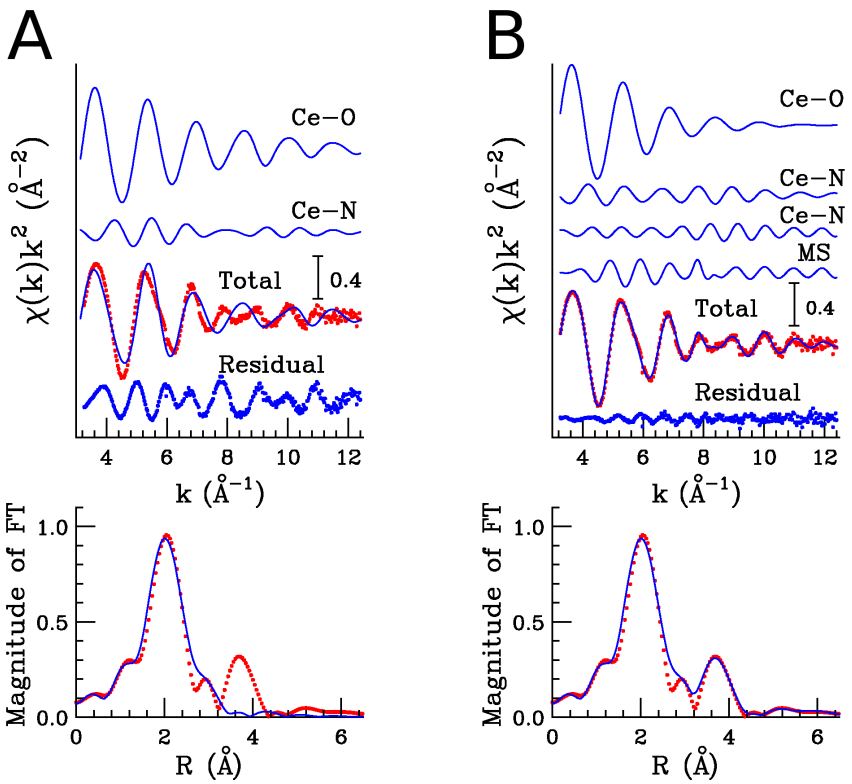

Figure 8.33: Upper panels: (A) Fit of the EXAFS spectrum of Ce(III) in EAN using the MD Ce-O and Ce-N $g(r)$'s as starting models. From the top to the bottom the following curves are reported: the Ce-O and Ce-N theoretical signals calculated from the MD Ce-O and Ce-N $g(r)$'s, the total theoretical signal (blue line) compared with the experimental spectrum (dotted red line) and the residual curve. (B) Fit of the EXAFS spectrum of Ce(III) in EAN by using the SS and MS signals associated with the Ce(III) icosahedral geometry. From the top to the bottom the following curves are reported: the first shell Ce-O theoretical signal, the Ce-N theoretical signals associated with the bidentate and monodentate nitrate ligands, respectively, the total MS contribution, the total theoretical signal (blue line) compared with the experimental spectrum (dotted red line) and the residual curve. Lower panels: nonphase-shift-corrected Fourier transforms of the experimental data (dotted red line) and of the total theoretical signals (blue line).

hydrogen donor forming a network of bifurcated hydrogen bonds.

All together our results show that in the presence of small amounts of $Ce(NO_3)_3$, the salt does not affect the EAN bulk structure, and the molecular arrangement of the pure IL is maintained both in the apolar and polar domains. Evidence for this can be also seen in the simulation boxes, depicted in Figure 8.32.

8.3.5 EXAFS analysis

In order to assess the reliability of the interaction potentials used in the simulations, we have compared the MD results with the EXAFS data. In a first step, we have calculated a $\chi(k)$ theoretical signal starting from the Ce-O

and Ce-N MD $g(r)$'s by means of eq. 2.6. This means that only the single scattering (SS) signals associated with the Ce-O and Ce-N two-body configurations have been considered. Least-squares fits of the EXAFS data have been carried out in the range k= 3.2-12.4 Å^{-1}, and the best-fit results are shown in panel A of Figure 8.33. Note that the MD structural parameters have been kept fixed during the analysis, and the only optimized parameters were S_0^2 and E_0, that were found equal to 0.9 and 2.5(0.5) eV above the first inflection point of the spectrum, respectively. As it can be seen, the agreement between theory and experiment is quite good, even if there is a residual curve showing an additional high frequency contribution, that has not been considered in the present analysis. This result is also evident from the corresponding k^2 weighted Fourier transform (FT) spectra, calculated with no phase shift correction applied, in the k-range 3.4-11.5 Å^{-1} and shown in the lower panel of Figure 8.33 A. In fact, while the experimental first peak is properly accounted for by the theoretical calculation, the higher distance peak (at about 3.8 Å) is absent in the theoretical spectrum. This result indicates that the first shell distances obtained from the simulations are correct, but in the experimental spectrum there is also a high frequency contribution due to multiple scattering (MS) signals originating from the icosahedral structure of the Ce(III) ion. In order to consider such MS contributions, we have performed an additional fitting procedure of the EXAFS data starting from the CDFs calculated from the SIM0 MD simulation. All the CDFs used for the EXAFS analysis are shown in Figure 8.34, while the corresponding structural parameters are collected in Table 8.13. In particular, we considered three SS contributions:
(i) a Ce-O path at 2.57 Å accounting for the 12 first shell oxygen atoms;
(ii) a Ce-N path at 3.10 Å associated with the 3 nitrogen atoms of the bidentate ligands;
(iii) a Ce-N path at 3.71 Å associated with the 6 nitrogen atoms of the monodentate ligands.
As regards the MS contributions, the relevant three-body configurations have been extracted from the CDF analysis. All the MS paths that provided a detectable contribution are listed in Table 8.13. In particular, the monodentate NO_3^- ligands give rise to 6 Ce-O_{1s}-N configurations with an intervening angle of 178° that provide the strongest MS contribution. Note that this path has a high multiplicity, it is almost linear and it is the shortest among all the MS contributions. In addition there are 6 linear and 30 bent (116°) O_{1s}-Ce-O_{1s} configurations associated with the first shell oxygen atoms. Longer paths that anyhow provide a detectable MS contribution are the Ce-N-O_{2s} and Ce-O_{1s}-O_{2s} involving a second shell oxygen atoms. The EXAFS minimizations have been carried out starting from the structural parameters collected in Table 8.13, and they have been varied less than 3% from the initial values. For each distance and angle, a Debye-Waller factor has been optimized and the best-fit structural parameters obtained from the EXAFS analysis are listed in Table 8.14. The S_0^2 and E_0 parameters were found equal to the previous determinations. Panel B of Figure 8.33 shows the best-fit results and, in particular, the first four curves from the top are the Ce-O, Ce-N_{bi}, Ce-N_{mono}

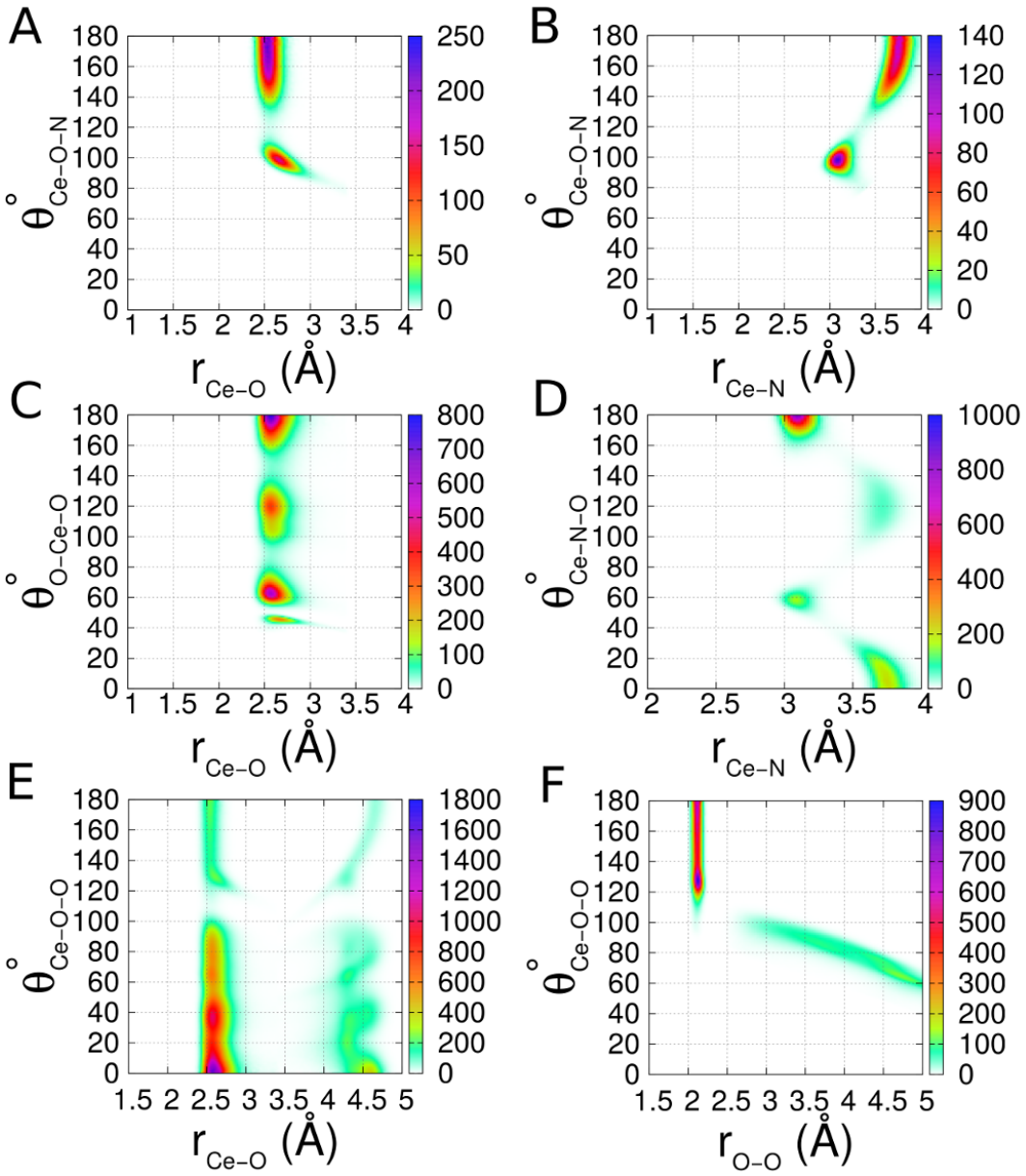

Figure 8.34: Combined distribution functions (CDFs) calculated from the MD simulation of $Ce(NO_3)_3$ in EAN for the box containing 5 Ce(III) ions (SIM0), used as starting model for the EXAFS analysis. (A,B) CDFs between Ce-O/Ce-N distances and Ce-O-N angles. (C) CDF between Ce-O distances and O-Ce-O angles. Only the oxygen atoms belonging to the Ce(III) ion first solvation shell have been included in the calculation. (D) CDF between Ce-N distances and Ce-N-O angles. (E) CDF between Ce-O distances and Ce-O-O angles. (F) CDF between O-O distances and Ce-O-O angles. Only the nitrogen and oxygen atoms of nitrate ions belonging to the Ce(III) first solvation shell have been included in the CDF calculation of panels D, E, F.

and the total MS contributions, while the reminder of the figure shows the comparison between the experimental spectrum and the total theoretical contribution together with the resulting residual. Now, we have obtained a very good agreement between the experimental and theoretical data. Taking into

Three-body configurations	N	R_1(Å)	R_2(Å)	$\theta°$	coordination mode
Ce-O_{1s}-N		Ce-O_{1s}	O_{1s}-N	Ce-O_{1s}-N	
	6	2.57	1.22	178	mono
O_{1s}-Ce-O_{1s}		Ce-O_{1s}	Ce-O_{1s}	O_{1s}-Ce-O_{1s}	
	30	2.57	2.57	116	mono & bi
	6	2.57	2.57	180	mono & bi
Ce-N-O_{2s}		Ce-N	N-O_{2s}	Ce-N-O_{2s}	
	12	3.71	1.22	120	mono
	3	3.10	1.22	180	bi
Ce-O_{1s}-O_{2s}		Ce-O_{1s}	O_{1s}-O_{2s}	Ce-O_{1s}-O_{2s}	
	6	2.57	2.12	129	bi
	8	2.57	2.12	129	mono
	4	2.57	2.12	176	mono

Table 8.13: Structural parameters obtained from the CDF analysis for the three-body configurations that have been used as starting values to calculate the EXAFS MS theoretical signals. R_1, R_2 are the two distances, θ is the intervening angle, O_{1s} and O_{2s} are the oxygen atoms belonging to the Ce(III) first and second shell, respectively, while N is the number of three-body paths.

account the MS contribution, the FT second peak is perfectly reproduced, proving the validity of the coordination model used in the analysis of the EXAFS data.

As previously mentioned, in all of the reported crystallographic structures of Ce(III) nitrate complexes, the Ce atoms are bonded to six bidentate nitrate groups, with 12 oxygen atoms in the first solvation shell arranged in an icosahedral fashion.[167, 168, 169] An example of the Ce(III) ion coordination geometry in the crystallographic structure of $[Mn_2O_2(bpy)_4]$-$[Ce(NO_3)_6]5H_2O$ is depicted in Figure 8.35. On the contrary, here we have shown that in liquid EAN the Ce(III) ion adopts an icosahedral first shell structure but it is surrounded by three bidentate and six monodentate nitrate ligands. In order to verify the reliability of our model we have carried out a further analysis of the EXAFS data starting from the crystallographic structure of Figure 8.35,[167] and by calculating all the SS and MS signals that involve the Ce(III) ion. In particular, the SS contributions are associated with 12 Ce-O

	R(Å)	σ_R^2 (Å^2)	θ°	σ_θ^2 ($^{\circ 2}$)
Ce-O_{1s}	2.62	0.0095(5)	-	-
Ce-N	3.11	0.0039(4)	-	-
Ce-N	3.73	0.0059(4)	-	-
N-O	1.22	0.0046(4)	-	-
O-O	2.10	0.0032(5)	-	-
Ce-O_{1s}-N	-	-	173.5	2.6(5)
O_{1s}-Ce-O_{1s}	-	-	123.5	7.6(5)
O_{1s}-Ce-O_{1s}	-	-	180.0	9.3(5)
Ce-N-O_{2s}	-	-	122.4	4.9(5)
Ce-N-O_{2s}	-	-	178.9	3.6(5)
Ce-O_{1s}-O_{2s}	-	-	129.2	5.4(5)
Ce-O_{1s}-O_{2s}	-	-	176.0	3.8(5)

Table 8.14: Best-fit structural parameters obtained from the minimization procedure carried out on the EXAFS spectrum of Ce(III) in EAN using the coordination structure obtained from the MD simulations.

distances at 2.64 Å and 6 Ce-N distances at 3.06 Å of the NO_3^- bidentate ligands. As far as the MS contributions are concerned, there are only four three-body configurations with angles bigger than 116° (namely, 6 linear and 6 bent O_{1s}-Ce-O_{1s} (132°) paths, 6 quasi-linear Ce-N-O_{2s} paths and 12 bent Ce-O_{1s}-O_{2s} (126°) paths) and the total MS contribution is expected to be lower than the previous model (see Table 8.15). The EXAFS minimization has been carried out starting from the structural parameters listed in Table 8.15 and they have been varied less than 3% from the initial values. The full list of parameters obtained from the fitting procedure is reported in Table 8.16, while the best-fit results are shown in Figure 8.35. Note that S_0^2 and E_0 were found equal to 0.9 and 1.5(0.5) eV above the first inflection point of the spectrum. It is clear that the agreement between the experimental and theoretical spectra is not very good and the residual curve shows a high frequency oscillation that is not accounted for in the theory. This finding is also evident from the corresponding k^2 weighted FT spectra where the second peak at 3.8 Å is not completely reproduced indicating that some high frequency contributions associated with the MS configurations have not been properly accounted for in the calculation. This result indicates that the structural model with six bidentate nitrate ligands is not compatible with the EXAFS experimental data of Ce(III) in EAN solution. The existence of monodentate

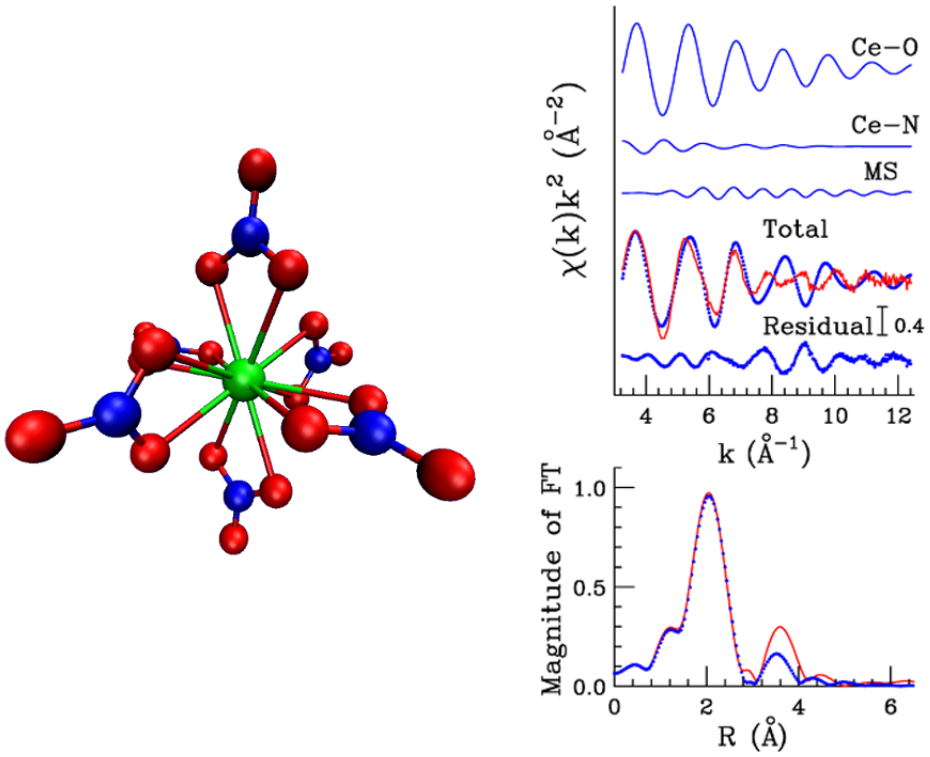

Figure 8.35: Left: Ce(III) ion coordination geometry in the crystallographic structure of $[Mn_2O_2(bpy)_4]$-$[Ce(NO_3)_6]5H_2O$. The cerium atom is colored in green, while the oxygen and nitrogen atoms of the nitrate anions are in red and in blue, respectively. Right: fit of the EXAFS spectrum of Ce(III) in EAN using the crystallographic structure of $[Mn_2O_2(bpy)_4]$-$[Ce(NO_3)_6]5H_2O$ as model. From the top to the bottom the following curves are reported: the Ce-O and Ce-N SS theoretical signals, the total MS contribution, the total theoretical signal (dotted blue line) compared with the experimental spectrum (red line) and the residual curve. Nonphase-shift-corrected Fourier transforms of the experimental data and of the total theoretical signals.

ligands in EAN can be due to the large number of nitrate ions present in solution that allows the formation of a more disordered coordination shell, as compared to the crystalline structures, that is typical of liquid systems, as already found in previous investigations. For example a recent study of Li(I) ion in EAN solution has shown that the Li(I) cation is coordinated by both monodentate and bidentate NO_3^- ligands, with a preferential monodentate coordination.[173, 177]

In conclusion, the results of this investigation show that the solvation behavior of EAN and water in the presence of a light lanthanoid ion is markedly different, notwithstanding the similarity in some properties of the two solvents. Understanding the dissolution of Ln(III) ions in complex liquid media can be an important starting point for the development of innovative solvents to be used, as an example, for the separation of these ions in nuclear waste.

Three-body configurations	N	R_1(Å)	R_2(Å)	θ°
O_{1s}-Ce-O_{1s}		Ce-O_{1s}	Ce-O_{1s}	O_{1s}-Ce-O_{1s}
	6	2.64	2.64	132
	6	2.64	2.64	180
Ce-N-O_{2s}		Ce-N	N-O_{2s}	Ce-N-O_{2s}
	6	3.06	1.23	175
Ce-O_{1s}-O_{2s}		Ce-O_{1s}	O_{1s}-O_{2s}	Ce-O_{1s}-O_{2s}
	12	2.64	2.17	126

Table 8.15: Structural parameters obtained from the crystallographic structure of solid $[Mn_2O_2(bpy)_4]$-$[Ce(NO_3)_6]5H_2O$ that have been used to calculate the EXAFS MS theoretical signals of the crystal. R_1, R_2 are the two distances, θ is the intervening angle, O_{1s} and O_{2s} are the oxygen atoms belonging to the Ce(III) first and second shell, respectively, while N is the number of three-body paths.

	R(Å)	σ_R^2 (Å^2)	θ°	σ_θ^2 ($^{\circ 2}$)
Ce-O_{1s}	2.64	0.0075(5)	-	-
Ce-N	3.06	0.0019(4)	-	-
N-O	1.26	0.0026(4)	-	-
O-O	2.17	0.0029(5)	-	-
O_{1s}-Ce-O_{1s}	-	-	132.9	7.1(5)
O_{1s}-Ce-O_{1s}	-	-	180.0	6.3(5)
Ce-N-O_{2s}	-	-	175.9	1.9(5)
Ce-O_{1s}-O_{2s}	-	-	126.2	4.9(5)

Table 8.16: Best-fit structural parameters obtained from the minimization procedure carried out on the EXAFS spectrum of Ce(III) in EAN using the crystallographic structure of $[Mn_2O_2(bpy)_4]$-$[Ce(NO_3)_6]5H_2O$ as model.

Chapter 9

Overall conclusions

In this work a detailed investigation of the structural organization of ILs, both monocationic and dicationic, and their water mixtures has been carried out by combining XAS spectroscopy and Classical MD simulations. The same joint XAS-MD approach has been also applied to the study of the solvation properties of Ln(III) salts dissolved in ILs.

As far as pure ILs are concerned, the combined use of XAS experimental data and MD simulations allowed us to carry out the structural characterization of 1-alkyl-3-methylimidazolium halide ILs, namely [C_6mim]I and [C_6mim]Br (with n = 5, 6, 8, 10), with the aim of shedding light on the structural changes that take place when either the halide ion or the alkyl chain is modified. Similarities and differences in the cation-anion local coordination have been found varying the nature of the IL anion ([C_6mim]Br and [C_6mim]I ILs). In both cases a well defined first coordination shell composed on average of 3.7 and 4.2 X^- ions in [C_6mim]Br and [C_6mim]I, respectively, has been found, with the anions preferentially coordinated with the three hydrogen atoms of the imidazolium ring. However, the combined and spatial distribution function analysis revealed that the three-dimensional arrangement of Br^- and I^- ions is different in the vicinity of the most acidic hydrogen atom of the imidazolium ring: I^- prefers to be above and below the ring plane and not coplanar with the plane itself, while Br^- has a high probability also to be coplanar with the imidazolium ring. While the nature of the IL anion alters the cation-anion local coordination, the local arrangement of cations around the Br^- ion in [$C_n$mim]Br ILs is not influenced by the length of the alkyl chain attached to the imidazolium ring. A local ordered structure has been evidenced with anions and imidazolium head groups interacting with each other and forming a local three-dimensional bonding pattern that is common to all the [$C_n$mim]Br IL family. Conversely, significant long-range structural changes take place when the alkyl chain length is modified. Theoretical X-ray structure factors have been calculated from MD simulations and a low q peak has been found, indicating the existence of long-range structural correlations. A quantitative analysis of the Br and I K-edge spectra of the investigated ILs has been carried out starting from the structural information derived from the MD simulations. The joint approach allowed us to reduce the number of

correlated model parameters required in the fitting of the experimental data and to increase the reliability of the EXAFS data analysis that represents a non-trivial task when dealing with disordered systems. Moreover, the very good agreement obtained between the experimental and theoretical EXAFS signals proves that the structural information derived from the MD simulations is reliable and that the force field is able to provide a correct description of the systems from a structural point of view.

Then we have carried out a thorough characterization of the structural properties of 1-hexyl-3-methylimidazolium iodide ($[C_6mim]I$)/water mixtures with molar ratios ranging from 1:1 to 1:200, and a clear picture of the arrangement of the water molecules inside the IL has been obtained from the synergic interpretation of the EXAFS and MD data. In all the solutions the water molecules were found to be preferentially coordinated with the I^- ion, even if a complex network of interactions among cations, anions and water molecules takes place. Both EXAFS and MD results show that the water molecules are placed next to the I^- ion, also for the $[C_6mim]I$/water mixture with 1:1 molar ratio, and the I^- hydration shell becomes more and more crowded with increasing water content. An interesting result is the presence of tight ion pairs in the mixtures with IL/water molar ratios between 1:1 and 1:12, and the absence of these ion pairs in the most diluted solutions, suggesting that the large size and the diffuse character of the I^- ion hamper the formation of strong cation-anion interactions. We have also investigated the aggregation behavior from the analysis of the MD trajectories, and the existence of long-range structural correlations has been highlighted for the IL/water mixtures with molar ratios from 1:1 to 1:12, with the apolar chains not completely segregated as expected for micelle-like structures. Conversely, the alkyl chains were found to be completely separated from each other for the 1:200 mixture, that is above the experimental critical aggregation concentration value. Also in this case the good agreement between the experimental and theoretical EXAFS spectra is a check of the validity of the force field used in the MD simulations for all the investigated solutions and the reliability of the structural MD results.

A complex network of interactions among cations, anions and water molecules has been also found in binary mixtures of water and geminal dicationic ILs, namely 1,n-bis[3-methylimidazolium-1-yl]bromide ($[C_n(mim)_2]Br_2$), whose properties have been studied as a function of both water concentration (DIL/water molar ratio from 1:16 to 1:400) and spacer chain length (n = 2, 3, 4, 6, 8, 9). Here the synergic experimental/theoretical procedure has been adopted at first to chose the best-performing Lennard-Jones parameters for the Br-water potential, and then to prove the transferability of the selected potential to the DIL/water mixtures. Water molecules were shown to be preferentially coordinated with the Br^- ion, and upon increasing the water fraction more and more water molecules enter the Br^- first coordination shell. On the other hand, the spacer chain length has an influence on both anion-water and cation-anion interactions. In particular, the interactions between dications and anions increase with the decreasing of the spacer chain length, since a

Br^- ion can simultaneously interact with the two imidazolium rings of the same $[C_n(mim)_2]^{2+}$ dication forming a bridge between them. Conversely, for long spacer chain DILs peculiar internal arrangements of the dications were found: one imidazolium ring tends to position itself above and below the other ring of the same dication forming π-π stacking interactions, and the spacer chains extend perpendicularly to the rings slightly hindering the approach of the Br^- ions towards the imidazolium rings. These distinguishing structural features of DILs could be at the origin of their peculiar properties such as increased thermal and chemical stability with respect to traditional monocationic ILs.

In the second part of the work the MD-EXAFS analysis have focused on the solvation properties of rare-earth metals dissolved in ILs. In order to address this issue we have first developed generic Ln-Ln Lennard-Jones parameters to be used in conjunction with force fields available in the literature to obtain pair potentials involving Ln(III) ions. We started from the optimization of the interaction potentials for Ln(III) ions in water, and this is the first time that new sets of Lennard-Jones and Buckingham parameters to be used in Classical MD simulations of Ln(III)-containing systems have been developed for the entire lanthanoid series by directly comparing the hydration structure obtained from the simulations with the EXAFS experimental data. In particular, the optimization procedure has been carried out in order to reproduce the Ln(III)-water EXAFS experimentally inferred mean distances, as they are the most accurate structural information that can be obtained from the EXAFS experimental technique. We have demonstrated that both the newly refined Lennard-Jones and Buckingham pair potentials are able to correctly describe the radial distribution of water molecules around the Ln(III) ions, the smooth decrease of the hydration number along the series, as well as the geometry of water molecules in the Ln(III) ion first hydration shell. Generic Ln-Ln Lennard-Jones parameters have been extrapolated by using the Lorentz-Berthelot mixing rules and they have been used in MD simulations of binary aqueous solutions of lanthanide salts and of a diluted solution of $Ce(NO_3)_3$ in the protic IL ethylammonium nitrate. In fact, from a theoretical point of view, the most straightforward way to study the solvation properties of Ln(III) ions in complex and disordered solvent media is to carry out Classical MD simulations without explicit polarization and describing the interactions among atoms by means of the computationally efficient Lennard-Jones potential.

The first investigated systems are aqueous solutions of two Ln(III) ions, La(III) and Dy(III), with triflate, bis(trifluoromethylsulfonyl)imide and nitrate as counterions in dilute conditions (0.1 M). Both MD simulations and EXAFS data indicate the substantially absence of inner-sphere $Ln(TfO)_3$, $Ln(Tf_2N)_3$ and $Ln(NO_3)_3$ complexes (in which Ln = La and Dy), making these anions and, in particular, the TfO^- and Tf_2N^- ones suitable to be used for experimental determinations of the Ln(III) structural properties in water. It is clear that they are non-complexing anions in high diluted conditions, as the one of the present investigation. In higher concentrated solutions (> 1

M) the anions could penetrate into the Ln(III) first coordination shell and form contact ion pairs due to the low number of water molecules that are not sufficient to complete the shell. Conversely, the anions have a strong affinity with water, which can explain several behaviors observed in systems based on such anions. For example, the Tf_2N^- ion is a component of many room-temperature ILs, of fundamental interest in pure and applied chemistry, which are soluble in water thanks to the favoured coordination of the Tf_2N^- anion with water. The good agreement between the experimental and theoretical results allowed us to validate the new set of Ln-Ln Lennard-Jones interaction potentials and to assess their capability to reproduce the structural properties of systems different from that for which they have been developed.

A diluted solution of $Ce(NO_3)_3$ in the protic IL ethylammonium nitrate has been taken as an example to disentangle the molecular interactions that take place between a lanthanoid ion and a protic IL. We have carried out two different sets of MD simulations of this system, with or without including explicit polarization. This is the first time, to the best of our knowledge, that explicit polarization was included in the classical force field to describe a heavy metal ion in a protic IL, but, at variance with water, it was found to be unessential. As expected, only nitrate ions, that are negatively charged, were found in proximity of the Ce(III) ion and the strong solvent-solvent interactions in the bulk drive the complex formation ability of this solvent. In particular, the first coordination shell of the Ce(III) ion is formed by 12 oxygen atoms belonging to the nitrate anions, with an equilibrium between monodentate and bidentate ligands existing in the solution. The analysis of combined distribution functions allowed us to unambiguously identify the peculiar coordination geometry of these 12 oxygen atoms, the icosahedron geometry, at variance with water where the Ce(III) ion adopts a tricapped trigonal prism structure. The combined MD-EXAFS approach allowed us to validate the theoretical force field used in the MD simulations, as well as to prove the importance of including multiple scattering signals originating from the icosahedral structure of the Ce(III) ion in the EXAFS analysis.

In conclusion, the combined XAS and MD approach used in this work allowed us to gain a clear picture of the structural organization of all of the investigated systems, both in the short- and long- distance range. Indeed, the structural characterization of liquid disordered systems is a quite challenging subject to be treated, and generally the use of a unique method of investigation does not allow to gain reliable information. The original application of EXAFS and MD simulations paves the route for the systematic use of an integrated approach, with increased reliability, in the structural investigation of ILs. All together these issues are expected to be of great help in the systematic design of IL systems to meet the requirements of key applications. In particular, in the field of lanthanide-based applications, ILs may be ideal alternatives for the dissolution of Ln(III) ions, and to select the best performing solvent or to develop new innovative solvents it is important to shed light on the molecular interactions taking place between the components of the mixture.

Bibliography

[1] M. Freemantle, *An Introduction to Ionic Liquids*, RSC Publishing, 2009.

[2] *Ionic Liquids IIIA: Fundamentals, Progress, Challenges, and Opportunities: Properties and Structure*, ed. R. Rogers and K. Seddon, American Chemical Society, Washington D.C., 2005, vol. 901.

[3] *Ionic Liquids IIIB: Fundamentals, Progress, Challenges, and Opportunities: Transformations and Processes*, ed. R. Rogers and K. Seddon, American Chemical Society, Washington D.C., 2005, vol. 902.

[4] R. D. Rogers and K. R. Seddon, *Science*, 2003, **302**, 792–793.

[5] H. Katayanagi, S. Hayashi, H. o Hamaguchi and K. Nishikawa, *Chem. Phys. Lett.*, 2004, **392**, 460–464.

[6] E. Bodo, L. Gontrani, A. Triolo and R. Caminiti, *J. Phys. Chem. Lett.*, 2010, **1**, 1095–1100.

[7] B. Aoun, A. Goldbach, S. Kohara, J.-F. Wax, M. A. González and M.-L. Saboungi, *J. Phys. Chem. B*, 2010, **114**, 12623–12628.

[8] A. E. Bradley, C. Hardacre, J. D. Holbrey, S. Johnston, S. E. J. McMath and M. Nieuwenhuyzen, *Chem. Mater.*, 2002, **14**, 629–635.

[9] Y. Umebayashi, H. Hamano, S. Tsuzuki, J. N. Canongia Lopes, A. A. H. Pádua, Y. Kameda, S. Kohara, T. Yamaguchi, K. Fujii and S.-i. Ishiguro, *J. Phys. Chem. B*, 2010, **114**, 11715–11724.

[10] B. Regan and M. Grätzel, *Nature*, 1991, **353**, 737–740.

[11] P. Bonhôte, A.-P. Dias, N. Papageorgiou, K. Kalyanasundaram and M. Grätzel, *Inorg. Chem.*, 1996, **35**, 1168–1178.

[12] N. Papageorgiou, Y. Athanassov, M. Armand, P. Bonhôte, H. Pettersson, A. Azam and M. Grätzel, *J. Electrochem. Soc.*, 1996, **143**, 3099–3108.

[13] W. Kubo, T. Kitamura, K. Hanabusa, Y. Wada and S. Yanagida, *Chem. Commun.*, 2002, 374–375.

[14] W. Kubo, S. Kambe, S. Nakade, T. Kitamura, K. Hanabusa, Y. Wada and S. Yanagida, *J. Phys. Chem. B*, 2003, **107**, 4374–4381.

[15] M. Shukla, N. Srivastava and S. Saha, *J. Mol. Struct.*, 2010, **975**, 349–356.

[16] R. Katoh, M. Hara and S. Tsuzuki, *J. Phys. Chem. B*, 2008, **112**, 15426–15430.

[17] M. H. Ghatee, A. R. Zolghadr, F. Moosavi and Y. Ansari, *J. Chem. Phys.*, 2012, **136**, 124706.

[18] S. Yeganegi, V. Sokhanvarana and A. Soltanabadi, *Mol. Sim.*, 2013, **39**, 1070–1078.

[19] S. M. Urahata and M. C. C. Ribeiro, *J. Chem. Phys.*, 2004, **120**, 1855–1863.

[20] M. Kohagen, M. Brehm, Y. Lingscheid, R. Giernoth, J. Sangoro, F. Kremer, S. Naumov, C. Iacob, J. Kärger, R. Valiullin and B. Kirchner, *J. Phys. Chem. B*, 2011, **115**, 15280–15288.

[21] M. H. Ghatee and Y. Ansari, *J. Chem. Phys.*, 2007, **126**, 154502.

[22] E. A. Turner, C. C. Pye and R. D. Singer, *J. Phys. Chem. A*, 2003, **107**, 2277–2288.

[23] O. Russina, A. Triolo, L. Gontrani and R. Caminiti, *J. Phys. Chem. Lett.*, 2012, **3**, 27–33.

[24] J. N. A. Canongia Lopes and A. A. H. Pádua, *J. Phys. Chem. B*, 2006, **110**, 3330–3335.

[25] H. V. R. Annapureddy, H. K. Kashyap, P. M. De Biase and C. J. Margulis, *J. Phys. Chem. B*, 2010, **114**, 16838–16846.

[26] J. L. Anderson, R. Ding, A. Ellern and D. W. Armstrong, *J. Am. Chem. Soc.*, 2005, **127**, 593–604.

[27] T. Payagala, J. Huang, Z. S. Breitbach, P. S. Sharma and D. W. Armstrong, *Chem. Mater.*, 2007, **19**, 5848–5850.

[28] H. Shirota, T. Mandai, H. Fukazawa and T. Kato, *J. Chem. Eng. Data*, 2011, **56**, 2453–2459.

[29] Q. Liu, F. van Rantwijk and R. A. Sheldon, *J. Chem. Technol. Biotechnol*, 2006, **81**, 401–405.

[30] J.-C. Xiao, and J. M. Shreeve, *J. Org. Chem.*, 2005, **70**, 3072–3078.

[31] X. Han, and D. W. Armstrong, *Org. Lett.*, 2005, **7**, 4205–4208.

[32] A. Chinnappan and H. Kim, *Chem. Eng. J.*, 2012, **187**, 283–288.

[33] G. Yu, S. Yan, F. Zhou, X. Liu, W. Liu and Y. Liang, *Tribol. Lett.*, 2007, **25**, 197–205.

[34] V. Jovanovski, V. González-Pedro, S. Giménez, E. Azaceta, G. Cabañero, H. Grande, R. Tena-Zaera, I. Mora-Seró and J. Bisquert, *J. Am. Chem. Soc.*, 2011, **133**, 20156–20159.

[35] H. Shirota and T. Ishida, *J. Phys. Chem. B*, 2011, **115**, 10860–10870.

[36] S. Yeganegi, A. Soltanabadi and D. Farmanzadeh, *J. Phys. Chem. B*, 2012, **116**, 11517–11526.

[37] S. Li, J. L. Bañuelos, P. Zhang, G. Feng, S. Dai, G. Rother and P. T. Cummings, *Soft Matter*, 2014, **10**, 9193–9200.

[38] S. Li, G. Feng, J. L. Bañuelos, G. Rother, P. F. Fulvio, S. Dai and P. T. Cummings, *J. Phys. Chem. C*, 2013, **117**, 18251–18257.

[39] K. R. Seddon, A. Stark and M.-J. Torres, *Pure Appl. Chem.*, 2000, **72**, 2275–2287.

[40] J. L. Anthony, E. J. Maginn and J. F. Brennecke, *J. Phys. Chem. B*, 2001, **105**, 10942–10949.

[41] A. R. Porter, S. Y. Liem and P. L. A. Popelier, *Phys. Chem. Chem. Phys.*, 2008, **10**, 4240–4248.

[42] I. Khan, M. Taha, P. Ribeiro-Claro, S. P. Pinho and J. A. P. Coutinho, *J. Phys. Chem. B*, 2014, **118**, 10503–10514.

[43] K. R. Seddon and A. Stark, *Green Chem.*, 2002, **4**, 119–123.

[44] L. Cammarata, S. G. Kazarian, P. A. Salter and T. Welton, *Phys. Chem. Chem. Phys.*, 2001, **3**, 5192–5200.

[45] A. Mele, C. D. Tran and S. H. De Paoli Lacerda, *Angew. Chem., Int. Ed.*, 2003, **42**, 4364–4366.

[46] M. Moreno, F. Castiglione, A. Mele, C. Pasqui and G. Raos, *J. Phys. Chem. B*, 2008, **112**, 7826–7836.

[47] M. Blesic, M. H. Marques, N. V. Plechkova, K. R. Seddon, L. P. N. Rebelo and A. Lopes, *Green Chem.*, 2007, **9**, 481–490.

[48] C. Spickermann, J. Thar, S. B. C. Lehmann, S. Zahn, J. Hunger, R. Buchner, P. A. Hunt, T. Welton and B. Kirchner, *J. Chem. Phys.*, 2008, **129**, 104505.

[49] V. Migliorati, P. Ballirano, L. Gontrani, O. Russina and R. Caminiti, *J. Phys. Chem. B*, 2011, **115**, 11805–11815.

[50] V. Migliorati, P. Ballirano, L. Gontrani and R. Caminiti, *J. Phys. Chem. B*, 2012, **116**, 2104–2113.

[51] V. Migliorati, A. Zitolo and P. D'Angelo, *J. Phys. Chem. B*, 2013, **117**, 12505–12515.

[52] B. L. Bhargava and M. L. Klein, *J. Chem. Theory Comput.*, 2010, **6**, 873–879.

[53] B. L. Bhargava and M. L. Klein, *J. Phys. Chem. B*, 2011, **115**, 10439–10446.

[54] S. Palchowdhury and B. L. Bhargava, *Phys. Chem. Chem. Phys.*, 2015, **17**, 11627–11637.

[55] Q. Q. Baltazar, J. Chandawalla, K. Sawyer and J. L. Anderson, *Colloids and Surfaces A: Physicochem. Eng. Aspects*, 2007, **302**, 150–156.

[56] Y.-S. Ding, M. Zha, J. Zhang and S.-S. Wang, *Colloids and Surfaces A: Physicochem. Eng. Aspects*, 2007, **298**, 201–205.

[57] K. Binnemans, *Chem. Rev.*, 2007, **107**, 2592–2614.

[58] X. Sun, H. Luo and S. Dai, *Chem. Rev.*, 2012, **112**, 2100–2128.

[59] A.-V. Mudring and S. Tang, *Eur. J. Inorg. Chem.*, 2010, **18**, 2569–2581.

[60] I. Billard, A. Ouadi and C. Gaillard, *Anal. Bioanal. Chem.*, 2011, **400**, 1555–1566.

[61] J. J. Rehr and R. C. Albers, *Rev. Mod. Phys.*, 2000, **72**, 621–654.

[62] R. de L. Kronig, *Z. Physik*, 1931, **70**, 317–323.

[63] D. Sayers, E. Stern and F. Lytle, *Phys. Rev. Lett.*, 1971, **27**, 1204–1207.

[64] E. Stern, *Phys. Rev. B*, 1974, **10**, 3027–3037.

[65] C. Natoli and M. Benfatto, *J. Phys. (Paris) Colloq.*, 1986, **48**, C8–11.

[66] M. Benfatto and C. Natoli, *J. Phys. (Paris) Colloq.*, 1987, **48**, C9–1077.

[67] A. Filipponi, A. Di Cicco and C. R. Natoli, *Phys. Rev. B*, 1995, **52**, 15122–15134.

[68] M. Allen and D. Tildesley., *Computer Simulations of Liquids*, Clarendon Press, Oxford, 1987.

[69] D. van der Spoel, E. Lindahl, B. Hess, A. van Buuren, E. Apol, P. Meulenhoff, D. Tieleman, T. Sijbers, K. Feenstra, R. van Drunen and H. Berendsen., *Gromacs User Manual version 3.3*, www.gromacs.org, 2005.

[70] P. Morse, *Phys. Rev.*, 1929, **34**, 57–64.

[71] L. Verlet, *Phys. Rev.*, 1967, **34**, 1311.

[72] R. Hockney and S. Goel, *J. Comp. Phys.*, 1974, **14**, 148–158.

[73] P. Ewald, *Ann. Phys.*, 1921, **64**, 253–287.

[74] T. Darden, D. York and L. Pedersen, *J. Chem. Phys.*, 1993, **98**, 10089–10092.

[75] U. Essmann, L. Perera, M. Berkowitz, T. Darden and L. P. H. Lee, *J. Chem. Phys.*, 1995, **103**, 8577–8593.

[76] J. Ryckaert, G. Ciccotti and H. Berendsen, *J. Comp. Phys.*, 1977, **23**, 327–341.

[77] H. Berendsen, J. Postma, W. van Gunsteren, A. D. Nola and J. Haak, *J. Chem. Phys.*, 1984, **81**, 3684–3690.

[78] S. Nosé, *Mol. Phys.*, 1984, **52**, 255–268.

[79] W. Hoover, *Phys. Rev. A*, 1985, **31**, 1695–1697.

[80] M. Parrinello and A. Rahman, *J. Appl. Phys.*, 1981, **52**, 7182–7190.

[81] M. L. K. S. Nosé, *Mol. Phys.*, 1983, **50**, 1055–1077.

[82] M. Salanne, L. J. A. Siqueira, A. P. Seitsonen, P. A. Madden and B. Kirchner, *Faraday Discuss.*, 2012, **154**, 171–188.

[83] A. Di Cicco, G. Aquilanti, M. Minicucci, E. Principi, N. Novello, A. Cognigni and L. Olivi, *J. Phys.: Conf. Ser.*, 2009, **190**, 012043.

[84] A. Filipponi and A. Di Cicco, *Phys. Rev. B*, 1995, **52**, 15135–15149.

[85] L. Hedin and B. I. Lundqvist, *J. Phys. C: Solid State Phys.*, 1971, **4**, 2064–2083.

[86] W. Smith and T. Forester, *J. Mol. Graphics*, 1996, **14**, 136–141.

[87] S. Nosé, *J. Chem. Phys.*, 1984, **81**, 511–519.

[88] D. J. Evans and B. L. Holian, *J. Chem. Phys.*, 1985, **83**, 4069–4074.

[89] U. Essmann, L. Perera, M. L. Berkowitz, T. Darden, H. Lee and L. G. Pedersen, *J. Chem. Phys.*, 1995, **103**, 8577–8593.

[90] J. N. Canongia Lopes, J. Deschamps and A. A. H. Pádua, *J. Phys. Chem. B*, 2004, **108**, 2038–2047.

[91] J. N. Canongia Lopes and A. A. H. Pádua, *J. Phys. Chem. B*, 2006, **110**, 19586–19592.

[92] W. L. Jorgensen, J. P. Ulmschneider and J. Tirado-Rives, *J. Phys. Chem. B*, 2004, **108**, 16264–16270.

[93] B. L. Bhargava and S. Balasubramanian, *J. Chem. Phys.*, 2007, **127**, 114510.

[94] H. J. C. Berendsen, J. R. Grigera and T. P. Straatsma, *J. Phys. Chem.*, 1987, **91**, 6269–6271.

[95] P. Mark and L. Nilsson, *J. Phys. Chem. A*, 2001, **105**, 9954–9960.

[96] C. J. Pings and J. J. Waser, *J. Chem. Phys.*, 1968, **48**, 3016.

[97] M. Brehm and B. Kirchner, *J. Chem. Inf. Model.*, 2011, **51**, 2007–2023.

[98] M. G. Del Pópolo, R. M. Lynden-Bell and J. Kohanoff, *J. Phys. Chem. B*, 2005, **109**, 5895–5902.

[99] S. Rivera-Rubero and S. Baldelli, *J. Phys. Chem. B*, 2006, **110**, 4756–4765.

[100] S. A. Katsyuba, E. E. Zvereva, A. Vidi and P. J. Dyson, *J. Phys. Chem. A*, 2007, **111**, 352–370.

[101] Z. Liu, S. Huang and W. Wang, *J. Phys. Chem. B*, 2004, **108**, 12978–12989.

[102] C. Hardacre, S. E. J. McMath, M. Nieuwenhuyzen, D. T. Bowron and A. K. Soper, *J. Phys.: Condens. Matter*, 2003, **15**, S159.

[103] K. Fumino, A. Wulf and R. Ludwig, *Angew. Chem., Int. Ed.*, 2008, **47**, 8731–8734.

[104] M. Chen, R. Pendrill, G. Widmalm, J. W. Brady and J. Wohlert, *J. Chem. Theory Comput.*, 2014, **10**, 4465–4479.

[105] G. Raabe and J. Khler, *J. Chem. Phys.*, 2008, **128**, 154509.

[106] P. D'Angelo, A. Zitolo, V. Migliorati, E. Bodo, G. Aquilanti, J. L. Hazemann, D. Testemale, G. Mancini and R. Caminiti, *J. Chem. Phys.*, 2011, **135**, 074505.

[107] H. Hamaguchi and R. Ozawa, *Adv. Chem. Phys.*, 2005, **131**, 85–104.

[108] C. Hardacre, J. D. Holbrey, C. L. Mullan, T. G. A. Youngs and D. T. Bowron, *J. Chem. Phys.*, 2010, **133**, 074510.

[109] A. Triolo, O. Russina, B. Fazio, R. Triolo and E. D. Cola, *Chem. Phys. Lett.*, 2008, **457**, 362–365.

[110] C. Chiappe, *Monatsh. Chem.*, 2007, **138**, 1035–1043.

[111] R.-S. Kühnel, N. Böckenfeld, S. Passerini, M. Winter and A. Balducci, *Electrochim. Acta*, 2011, **56**, 4092–4099.

[112] H. Shekaari, M. T. Zafarani-Moattar and N. J. Behrooz, *J. Chem. Thermodyn*, 2015, **86**, 188–195.

[113] M. M. Reif and P. H. Hünenberger, *J. Chem. Phys.*, 2011, **134**, 144104.

[114] V. Migliorati, F. Sessa, G. Aquilanti and P. D'Angelo, *J. Chem. Phys.*, 2014, **141**, 044509.

[115] K. Miki, P. Westh, K. Nishikawa and Y. Koga, *J. Phys. Chem. B*, 2005, **109**, 9014–9019.

[116] V. Migliorati, A. Serva, G. Aquilanti, L. Olivi, S. Pascarelli, O. Mathon and P. D'Angelo, *Phys. Chem. Chem. Phys.*, 2015, **17**, 2464–2474.

[117] I. Goodchild, L. Collier, S. L. Millar, I. Proke, J. C. Lord, C. P. Butts, J. Bowers, J. R. Webster and R. K. Heenan, *J. Colloid Interface Sci.*, 2007, **307**, 455–468.

[118] Y. Zhao, S. Gao, J. Wang and J. Tang, *J. Phys. Chem. B*, 2008, **112**, 2031–2039.

[119] F. Cesare Marincola, C. Piras, O. Russina, L. Gontrani, G. Saba and A. Lai, *ChemPhysChem*, 2012, **13**, 1339–1346.

[120] N. Vaghela, N. Sastry and V. Aswal, *Colloid Polym Sci*, 2011, **289**, 309–322.

[121] S. Misra, S. Naz, P. Kondaiah and S. Bhattacharya, *Biomaterials*, 2014, **35**, 1334–1346.

[122] Q. Huang, H. Chen, L. Zhou, J. Huang, J. Wu and X. Yu, *Chem. Biol. Drug Des.*, 2008, **71**, 224–229.

[123] S. Datta, J. Biswas and S. Bhattarcharya, *J. Colloid Interface Sci.*, 2014, **430**, 85–92.

[124] P. D'Angelo, A. Zitolo, G. Aquilanti and V. Migliorati, *J. Phys. Chem. B*, 2013, **117**, 12516–12524.

[125] P. D'Angelo, V. Migliorati and L. Guidoni, *Inorg. Chem.*, 2010, **49**, 4224–4231.

[126] K. Dong and S. Zhang, *Chem. Eur. J.*, 2012, **18**, 2748–2761.

[127] S. V. Eliseeva and J.-C. G. Bunzli, *Chem. Soc. Rev.*, 2010, **39**, 189–227.

[128] H. Dong, S.-R. Du, X.-Y. Zheng, G.-M. Lyu, L.-D. Sun, L.-D. Li, P.-Z. Zhang, C. Zhang and C.-H. Yan, *Chem. Rev.*, 2015, **115**, 10725–10815.

[129] R. D. Teo, J. Termini and H. B. Gray, *J. Med. Chem.*, 2016, **59**, 6012–6024.

[130] N. Rathore, A. M. Sastre and A. K. Pabby, *J. Membr. Sci.*, 2016, **2**, 2–13.

[131] S. O. Odoh, G. D. Bondarevsky, J. Karpus, Q. Cui, C. He, R. Spezia and L. Gagliardi, *J. Am. Chem. Soc.*, 2014, **136**, 17484–17494.

[132] P. D'Angelo, A. Zitolo, V. Migliorati, G. Chillemi, M. Duvail, P. Vitorge, S. Abadie and R. Spezia, *Inorg. Chem.*, 2011, **50**, 4572–4579.

[133] M. Duvail, A. Ruas, L. Venault, P. Moisy and P. Guilbaud, *Inorg. Chem.*, 2010, **49**, 519–530.

[134] S. Galera, J. M. Lluch, A. Oliva, J. Bertran, F. Foglia, L. Helm and A. E. Merbach, *New J. Chem.*, 1993, **17**, 773–9.

[135] S. L. Mayo, B. D. Olafson and W. A. Goddard III, *J. Phys. Chem.*, 1990, **94**, 8897–8909.

[136] T. Kowall, F. Foglia, L. Helm and A. E. Merbach, *J. Am. Chem. Soc.*, 1995, **117**, 3790–3799.

[137] M. Duvail, P. Vitorge and R. Spezia, *J. Chem. Phys.*, 2009, **130**, 104501.

[138] M. Duvail, M. Souaille, R. Spezia, T. Cartailler and P. Vitorge, *J. Chem. Phys.*, 2007, **127**, 034503.

[139] P. D'Angelo and R. Spezia, *Chem.- Eur. J.*, 2012, **18**, 11162–11178.

[140] T. Kowall, F. Foglia, L. Helm and A. E. Merbach, *J. Phys. Chem.*, 1995, **99**, 13078–13087.

[141] I. Persson, P. D'Angelo, S. De Panfilis, M. Sandström and L. Eriksson, *Chem. - Eur. J.*, 2008, **14**, 3056–3066.

[142] P. D'Angelo, S. De Panfilis, A. Filipponi and I. Persson, *Chem. - Eur. J.*, 2008, **14**, 3045–3055.

[143] H. J. C. Berendsen, D. van der Spoel and R. van Drunen, *Comput. Phys. Commun.*, 1995, **91**, 43–56.

[144] J. N. Canongia Lopes and A. A. H. Pádua, *J. Phys. Chem. B*, 2004, **108**, 16893–16898.

[145] K. Djanashvili, C. Platas-Iglesias and J. A. Peters, *Dalton Trans.*, 2008, 602–607.

[146] A. M. van Loon, H. van Bekkum and J. A. Peters, *Inorg. Chem.*, 1999, **38**, 3080–3084.

[147] W. W. Rudolph and G. Irmer, *Dalton Trans.*, 2015, **44**, 295–305.

[148] C. Bonal, J.-P. Morel and N. Morel-Desrosiers, *J. Chem. Soc., Faraday Trans.*, 1998, **94**, 1431–1436.

[149] S. Andersson, K. Eberhardt, C. Ekberg, J.-O. Liljenzin, M. Nilsson and G. Skarnemark, *Radiochim. Acta*, 2006, **94**, 469–474.

[150] M. Duvail, A. Ruas, L. Venault, P. Moisy and P. Guilbaud, *Inorg. Chem.*, 2010, **49**, 519.

[151] T. Yaita, H. Narita, S. Suzuki, S. Tachimori, H. Motohashi and H. Shiwaku, *J. Radioanal. Nucl. Chem.*, 1999, **239**, 371–375.

[152] R. W. Impey, P. A. Madden and I. R. McDonald, *J. Chem. Phys.*, 1983, **87**, 5071–5083.

[153] R. Caminiti, G. Licheri, G. Piccaluga and G. Pinna, *J. Chem. Phys.*, 1978, **68**, 1967–1970.

[154] L. X. Dang, T.-M. Chang, M. Roeselova, B. C. Garrett and D. J. Tobias, *J. Chem. Phys.*, 2006, **124**, 066101.

[155] J. Thøgersen, J. Réhault, M. Odelius, T. Ogden, N. K. Jena, S. J. K. Jensen, S. R. Keiding and J. Helbing, *J. Phys. Chem. B*, 2013, **117**, 3376–3388.

[156] M. B. Oliveira, M. Domínguez-Pérez, M. G. Freire, F. Llovell, O. Cabeza, J. A. Lopes-da Silva, L. F. Vega and J. A. P. Coutinho, *J. Phys. Chem. B*, 2012, **116**, 12133–12141.

[157] M. Tariq, P. J. Carvalho, J. A. Coutinho, I. M. Marrucho, J. N. C. Lopes and L. P. Rebelo, *Fluid Phase Equilib.*, 2011, **301**, 22–32.

[158] P. Walden, *Bull. Russ. Acad. Sci.: Phys.*, 1914, **1800**, 405–422.

[159] K. Fumino, A. Wulf and R. Ludwig, *Angew. Chem., Int. Ed.*, 2009, **48**, 3184–3186.

[160] E. Bodo, *J. Phys. Chem. B*, 2015, **119**, 11833–11838.

[161] T. L. Greaves, A. Weerawardena, C. Fong, I. Krodkiewska and C. J. Drummond, *J. Phys. Chem. B*, 2006, **110**, 22479–22487.

[162] F. Martelli, Y. Jeanvoine, T. Vercouter, C. Beuchat, R. Vuilleumier and R. Spezia, *Phys. Chem. Chem. Phys.*, 2014, **16**, 3693–3705.

[163] E. Bodo, V. Macaluso and R. Spezia, *J. Phys. Chem. B*, 2015, **119**, 13347–13357.

[164] T. Yan, Y. Wang and C. Knox, *J. Phys. Chem. B*, 2010, **114**, 6905–6921.

[165] T. L. Greaves and C. J. Drummond, *Chem. Rev.*, 2008, **108**, 206–237.

[166] M. Salanne, C. Simon, P. Turq and P. A. Madden, *J. Phys. Chem. B*, 2008, **112**, 1177–1183.

[167] D. Ramalakshmi and M. V. Rajasekharan, *Acta Crystallogr. Sect. B*, 1999, **55**, 186–191.

[168] N. Audebrand and D. Louër, *Acta Crystallogr. Sect. C*, 2000, **56**, 913–915.

[169] A. R. Biju and M. V. Rajasekharan, *Cryst. Growth Des.*, 2010, **10**, 426–429.

[170] Y. Zhu, W. S. Liu, M. Tan, T. Jiao and G. Tan, *Polyhedron*, 1993, **12**, 939–944.

[171] S.-P. Ji, M. Tang, L. He and G.-H. Tao, *Chem.-Eur. J.*, 2013, **19**, 4452–4461.

[172] P. D'Angelo, A. Zitolo, F. Ceccacci, R. Caminiti and G. Aquilanti, *J. Chem. Phys.*, 2011, **135**, 154509.

[173] T. Mendez-Morales, J. Carrete, O. Cabeza, O. Russina, A. Triolo, L. J. Gallego and L. M. Varela, *J. Phys. Chem. B*, 2014, **118**, 761–770.

[174] R. Hayes, S. A. Bernard, S. Imberti, G. G. Warr and R. Atkin, *J. Phys. Chem. C*, 2014, **118**, 21215–21225.

[175] T. Murphy, S. K. Callear, G. G. Warr and R. Atkin, *Phys. Chem. Chem. Phys.*, 2016, **18**, 17169–17182.

[176] R. Hayes, S. Imberti, G. G. Warr and R. Atkin, *Angew. Chem., Int. Ed.*, 2013, **52**, 4623–4627.

[177] O. Russina, R. Caminiti, T. Mendez-Morales, J. Carrete, O. Cabeza, L. J. Gallego, L. M. Varela and A. Triolo, *J. Mol. Liq.*, 2015, **205**, 16–21.

List of Publications

1. Combining EXAFS spectroscopy and molecular dynamics simulations to understand the structural and dynamic properties of an imidazolium iodide ionic liquid.
   V. Migliorati, A. Serva, G. Aquilanti, L. Olivi, S. Pascarelli, O. Mathon, P. D'Angelo.
   Phys. Chem. Chem. Phys., **17** 2464, (2015).

2. Local order and long range correlations in imidazolium halide ionic liquids: a combined molecular dynamics and XAS study.
   V. Migliorati, A. Serva, G. Aquilanti, S. Pascarelli, P. D'Angelo.
   Phys. Chem. Chem. Phys., **17** 16443, (2015).

3. Structural properties and aggregation behavior of 1-Hexyl-3-methylimidazolium iodide in aqueous solutions.
   P. D'Angelo, A. Serva, G. Aquilanti, S. Pascarelli, V. Migliorati.
   J. Phys. Chem. B, **119** 14515, (2015).

4. Structural properties of geminal dicationic ionic liquid/water mixtures: a theoretical and experimental insight.
   A. Serva, V. Migliorati, A. Lapi, G. Aquilanti, A. Arcovito, P. D'Angelo
   Phys. Chem. Chem. Phys., **18** 16544, (2016).

5. Unveiling the complex network of interactions in ionic liquids: a combined EXAFS and molecular dynamics approach.
   A. Serva, V. Migliorati, A. Lapi, P. D'Angelo.
   J. Phys.: Conf. Ser., **712** 012135, (2016).

6. Development of Lennard-Jones and Buckingham potentials for lanthanoid ions in water.
   V. Migliorati, A. Serva, F. Maria Terenzio, P. D'Angelo.
   Inorg. Chem., **56** 6214, (2017).

7. How does Ce^{III} nitrate dissolve in a protic ionic liquid? A combined molecular dynamics and EXAFS study.
   A. Serva, V. Migliorati, R. Spezia, P. D'Angelo.
   Chem. Eur. J., **23** 8424, (2017).

8. On the coordination of Zn^{2+} ion in $Tf2N^{-}$ based Ionic Liquids: Structural and dynamic properties depending on the nature of the organic cation.
   F. Sessa, V. Migliorati, A. Serva, A. Lapi, G. Aquilanti, G. Mancinci P. D'Angelo.
   Submitted to Phys. Chem. Chem. Phys..

9. Aqueous solutions of lanthanide salts: inner- vs outer sphere complexation.
   A. Serva, V. Migliorati, F. Sessa, A. Lapi, P. D'Angelo.
   In preparation.